Trinity College Dublin
Coláiste na Tríonóide, Baile Átha Cliath
The University of Dublin

Design and development of a hydrogel formulation with nanoparticles for the treatment of glioblastoma multiforme

A dissertation submitted for the degree of
Doctor of Philosophy
at the School of Pharmacy & Pharmaceutical Sciences,
Trinity College Dublin,
the University of Dublin, Ireland

by Luiza Erthal Cardoso dos Santos

Under the supervision of

Dr. Eduardo Ruiz-Hernandez and Dr. Oliviero Gobbo

March 2021

Declaration

I declare that this thesis has not been submitted as an exercise for a degree at this or any other university. A small proportion of the work described in this thesis was carried out in collaboration with other researcher and this is duly acknowledged in the text wherever relevant. This includes the experiments with neuron cultures outlined in Chapter 3 and Chapter 4, which were conducted in conjunction with Yuliia Rakovets. I declare that all other work is entirely my own.

I declare that part of this thesis was published as a Review Paper in the journal Acta Biomaterialia.

I agree to deposit this thesis in the University's open access institutional repository or allow the Library to do so on my behalf, subject to Irish Copyright Legislation and Trinity College Library conditions of use and acknowledgement.

Luiza Erthal Cardoso dos Santos

Table of Contents

Abstract

Glioblastoma multiforme (GBM) is the most aggressive form of brain tumours. GBM treatment is challenging because tumours are highly invasive and it is difficult to achieve effective therapeutic doses of drugs into the brain. Indeed, the Blood Brain Barrier (BBB) impairs most of the anti-cancer drugs to reach the tumour site. To overcome this problem, different drug delivery methods, such as the direct delivery of drugs into the brain after tumour removal surgery, have been proposed. Biomaterials are in the front line of the research focus for new treatment options. Especially, biocompatible polymers have been proposed in hydrogel-based formulations aiming at injectable and localized therapies. These formulations can comprise chemotherapeutic drugs, nanoparticles, cells, nucleic acids, and diagnostic agents. In this thesis, a hydrogel-based formulation containing free drug and drug-loaded stimuli-responsive nanoparticles was developed and tested for the treatment of GBM. Specifically, in Chapter 2 a detailed description of the materials and methods used in this work is presented. In Chapter 3, the first specific objective was the synthesis and characterization of the stimuli-responsive mesoporous silica nanoparticle capped with polyethylene glycol (MSN-PEG). This was followed by the evaluation of two loaded chemotherapeutic drugs, temozolomide (TMZ) and paclitaxel (PTX) concerning the loading capacity, release profile and *in vitro* effect on U-87 GBM cells and healthy neurons. In addition, the stability of the nanoparticles was analysed to support the interpretation of all these data. In Chapter 4, three gels (two thermoresponsive and one chemically crosslinked) were evaluated for the combination with the nanoparticle with or without the stimuli-responsive modification. The release profile of these nanoparticles and free drugs (temozolomide, paclitaxel and carmustine) from the gels was thoroughly analysed to increase the understanding on the behaviour of the combination as a drug delivery system. This shed light on the promising materials to be used as the delivery platform for the nanoparticles developed on Chapter 3. Moreover, gel degradation was also evaluated. Through a step by step screening process, the crosslinked (CX) hydrogel was selected to compose the final formulation (GlioGel) together with free TMZ and PTX-loaded nanoparticles. In Chapter 5, the efficacy of the combination therapy was evaluated in a 3D *in vitro* model and the final formulation was implanted *in vivo* in an animal model of GBM. We used tumour spheroids as a 3D platform to evaluate the effect of the formulation *in vitro* regarding cytotoxicity and nanoparticles

penetration. In addition, the formulation combining free TMZ and PTX-loaded MSN-PEG into the CX hydrogel was implanted in U-87 tumour-bearing mice after resection surgery to evaluate treatment efficacy *in vivo*. Finally, Chapter 6 is a general discussion of the research developed in this project, including the main findings of each part of the work and future research that can be conducted based on these project findings. In conclusion, a hydrogel-based formulation loaded with free chemotherapeutics and loaded nanoparticles was developed. *In vivo* results showed efficacy against GBM tumours after surgical resection in mice. Therefore, the GlioGel formulation is a viable option to treat GBM and improve the current chemotherapy outcomes in those patients.

Acknowledgements

Publications and Presentations

Publications:

1. **LUIZA C. S. ERTHAL;** OLIVIERO L. GOBBO; EDUARDO RUIZ-HERNANDEZ. Biocompatible copolymer formulations to treat glioblastoma multiforme. *Acta Biomaterialia,* v.121, p.89-102, 2020.

2. MARINA MARTÍNEZ-CARMONA; QUI P. HO; JÉRÉMY MORAND; ANA GARCÍA; ENRIQUE ORTEGA; **LUIZA C. S. ERTHAL**; EDUARDO RUIZ-HERNANDEZ; M. DOLORES SANTANA; JOSÉ RUIZ; MARIA VALLET-REGÍ; YURII GUN'KO.
Amino-Functionalized Mesoporous Silica Nanoparticle-Encapsulated Octahedral Organoruthenium Complex as an Efficient Platform for Combatting Cancer. *Inorg. Chem.* v.59, p.10275–10284, 2020.

3. NAM, L.; COLL, C.; **ERTHAL, L.;** DE LA TORRE, C.; SERRANO, D.; MARTÍNEZ-MÁÑEZ, R.; SANTOS-MARTÍNEZ, M.; RUIZ-HERNÁNDEZ, E.
Drug Delivery Nanosystems for the Localized Treatment of Glioblastoma Multiforme. *Materials.* v.11, p.779, 2018.

Poster Presentations:

1. Poster presentation at the **Controlled Release Society Virtual Annual Meeting, 2020.**
Luiza C. S. Erthal, Yuliia Rakovets, Andrew Harkin, Oliviero L. Gobbo, Eduardo Ruiz-Hernandez
In vivo evaluation of a hydrogel-nanoparticles formulation to treat glioblastoma multiforme.

2. Poster presentation at the **Controlled Release Society Annual Meeting, Valencia, Spain, 2019.**
Luiza C. S. Erthal, Oliviero L. Gobbo, Eduardo Ruiz-Hernandez
Controlled release of a chemotherapeutic drug from a stimuli responsive nanoparticle incorporated in an injectable hydrogel for the treatment of solid

tumours.

3. Poster presentation at the **Multidisciplinary Research Showcase -TCD, Dublin, Ireland, 2018.**

Luiza C. S. Erthal, Carmen Coll, Oliviero L. Gobbo, Eduardo Ruiz-Hernandez

Design and characterization of a chemotherapeutic delivery system based on gated-nanoparticles.

4. Poster presentation at the **United Kingdom and Ireland Controlled Release Society Symposium**, **Belfast, Northern Ireland, 2018.**

Luiza C. S. Erthal, Carmen Coll, Tomás Ó hOistín, Oliviero L. Gobbo, Eduardo Ruiz-Hernandez

Gated nanoparticles incorporated in injectable hydrogels for localized chemotherapeutic delivery.

Oral Presentations:

1. Oral presentation at the **1st COST Action CA17140 Conference - Cancer Nanomedicine: from the bench to the bedside, Riga, Latvia, 2019.**

Luiza C. S. Erthal, Oliviero L. Gobbo, Eduardo Ruiz-Hernandez

Controlled release of a chemotherapeutic drug from a stimuli responsive nanoparticle incorporated in an injectable hydrogel for the treatment of solid tumours.

2. Oral presentation at the **41st All Ireland Schools of Pharmacy Conference, Dublin, Ireland, 2019.**

Luiza C. S. Erthal, Oliviero L. Gobbo, Eduardo Ruiz-Hernandez

Development of injectable hydrogels combined with stimulus-responsive nanocarriers for the treatment of glioblastoma multiforme.

List of Figures

List of Tables

List of Abbreviations

1p19q - Short arm chromosome 1 and long arm of chromosome 19

ACN- Acetonitrile

ANOVA - Analyses of variance

APTES - (3-Aminopropyl)triethoxysilane

ATP - Adenosine triphosphate

ATR - Attenuated total reflection

ATRX - Alpha thalassemia/mental retardation syndrome X

BBB – Blood brain barrier

BCNU - Bis-chloroethyl nitrosourea or carmustine

BET model - Brunauer-Emmett-Teller model

BJH model - Barrett-Joyner-Halenda model

BLI - Bioluminescence imaging

BRAF - B-Raf Proto-oncogene, serine/threonine kinase

BSA- Bovine serum albumin

BTB – Blood tumour barrier

CCK-8 – Cell-counting kit 8

CDK4 - Cyclin-dependent kinase 4

CDKN2A - Cyclin-dependent kinase inhibitor 2A

CED - Convection enhanced delivery

Chr – Chromosome

CMC - Critical micelle concentration

CMT - Critical micellar temperature

CNA - Copy number alterations

CNS - Central nervous system

CpG - 5'—C—phosphate—G—3'

CPT - Camptothecin

CTABr - Cetyltrimethylammonium bromide

CTLA - Cytotoxic T-lymphocyte-associated protein 4

CUR - Curcumin

CX – Crosslinked gel

DAPI - 4′,6-diamidino-2-phenylindole

DCM - Dichloromethane

DHA - Docosahexaenoic acid

DHLA - Dihydrolipoic acid

DLS - Dynamic light scattering

DMEM - Dulbecco's modified eagle medium

DMSO - Dimethyl sulfoxide

DOX - Doxorubicin

DTT - Dithiothreitol

ECM – Extracellular matrix

EDTA - Ethylenediaminetetraacetic acid

EGFR - Epidermal growth factor receptor

EPHA3 - Ephrin type-A receptor 3

EPI - Epirubicin

Epo - Erythropoietin

EPR effect - Enhanced permeation and retention effect

FBS – Fetal bovine serum

FDA – Food and Drug Administration

FITC - Fluorescein isothiocyanate

FR - Folate receptor

FTA - Farnesylthiosalicylic acid

FTIR - Fourier-transform infrared spectroscopy

FVII - Coagulation factor VII

Gal-1 - Galectin-1

GBM – Glioblastoma multiforme

GCIMP - Glioma CpG island methylator phenotype

GemC12 - Lauroyl-gemcitabine

GO- Graphene oxide

GSH- Glutathione

HA- Hyaluronic acid

HDAC - Histone deacetylase

HEMA - 2-hydroxyethyl methacrylate

HLB - Hydrophilic-lipophilic balance

HNPs - Hybrid nanoparticles

HPLC – High performance liquid chromatography

HPMA- 2-hydroxypropylmethacrylate

IC50 - half maximal inhibitory concentration

IDH - Isocitrate dehydrogenase

IL-10 - Interleukin 10

IR - Infrared

IR820 - Dye new indocyanine green

KIT - Proto-oncogene, receptor tyrosine kinase

LCST - Lower critical solution temperature

LCT - Liquid crystal templating

LDH - Lactate dehydrogenase assay

LOD- Limit of detection

LQP4 – Liquid polymer 4

Lucirin TPO - (2,4,6-trimethylbenzoyldiphenyl phosphine oxide)

LVR- Linear viscoelastic region

MAP2 - Microtubule associated protein 2

MAPK - Mitogen-activated protein kinase

MCF - Mesoporous cellular foam

MCM - Mobil composition of matter

MDR - Multi drug resistant

ME - Microemulsions

MEM - Minimum essential medium

MGMT - O-6-methylguanine-DNA methyltransferase

MLT - Melatonin

MLTH - Monitor long term therapeutic hydrogel

MMP - Matrix metalloproteinase

MRI – Magnetic resonance imaging

MRT- Magnetic resonance tomography

MSN – Mesoporous silica nanoparticles

MTT - 3-(4,5-dimethylthiazol-2-yl)-2,5-diphenyltetrazolium bromide

MTX - Methotrexate

MYCN - Proto-oncogene, N-myc protein

NAD - Nicotinamide adenine dinucleotide

NADH - Nicotinamide adenine dinucleotide + hydrogen

NBM - Neurobasal media

NF1 - Neurofibromin 1

NF-Kb - Nuclear factor kappa-light-chain-enhancer of activated B cells

NI2 - Nestin intron 2

NK cells – Natural killer cells

NOS - Nitric oxide synthase gene

NP - Nanoparticles

NTA - Nanoparticle tracking analysis

PARP - Poly-ADP ribose polymerase

PBS – Phosphate buffered saline

PBS-T - Phosphate buffered saline with tween

PCLA - Polycaprolactone-co-lactide

PDGFRA - Platelet derived growth factor receptor alpha

PDI - Polydispersity index

PDL1- Programmed death ligand-1

PEG - Polyethylene glycol

PEG-DMA - Polyethylene dimethacrylate

PEGDVS - PEGdivinyl sulfone

PEI - Polyethylenimine

PEO - Poly(ethylene oxide)

PEPE -Polyether-co polyester

PET- Positron emission tomography

PFA - Paraformaldehyde

PgP- P-glycoprotein efflux pump

pH – Hydrogen ion concentration

PI3K - Phosphoinositide 3-kinase

PIK3C2B - Phosphatidylinositol-4-phosphate 3-kinase C2 domain-containing beta polypeptide

PIK3CA - Phosphatidylinositol-4,5-bisphosphate 3-kinase catalytic subunit alpha

PIK3R1 - Phosphoinositide-3-kinase regulatory subunit 1

PKC - Protein kinase C

PLA- Polylactic acid

PLGA - Poly(lactic-co-glycolic acid)

PMMA - Poly(methyl methacrylate)

Poly-NIPAM – Poly (N-isopropylacrylamide)

PPO - Poly(propylene oxide)

PTEN - Phosphatase and tensin homolog

PTX - Paclitaxel

PXRD - Powder X-ray diffraction

RAS/RAF - Rat sarcoma/Rapidly accelerated fibrosarcoma

Rb – Retinoblastoma protein

RB1 - Retinoblastoma gene

RGD - Arginyl-glycyl-aspartic acid (RGD) tri-peptide

ROI - Region of interest

ROS - Reactive oxygen species

RT – room temperature

SBA-15 - Santa Barbara amorphous-15

SEM – Scanning electron microscopy

SEM – Standard error of the mean

SMOs - Sulfamethazine oligomers

STAT - Signal transducer and activator of transcription protein

TBE - Temozolomide ester

TCGA - The Cancer Genome Atlas

TEM – Transmission electron microscopy

TEOS - Tetraethyl orthosilicate

TERT - Telomerase reverse transcriptase

Tf - Transferrin

TGA - Thermogravimetric analysis

TGF-β - Transforming growth factor beta

TGP - Thermo-reversible gelation polymer

TMC - N-trimethylated chitosan

TMV - Tobacco mosaic virus

TMZ - Temozolomide

TP53 - Tumour protein p53 gene

TRAIL - Tumour necrosis factor α-related apoptosis-inducing ligand

TUNEL - Terminal deoxynucleotidyl transferase dUTP nick end labelling

UV – Ultraviolet

VEGF - Vascular endothelial growth factor

VLPs - Virus-like particles

VPA - Valproic acid

WHO – World Health Organization

WT – Wild type

CHAPTER 1: GENERAL INTRODUCTION

1.1 Glioblastoma multiforme (GBM)

According to the World Cancer report from the World Health Organization (WHO)[1], cancers from the brain and central nervous system were the 17th most common type of cancer in 2018. In this category, malignant gliomas are tumours that originate in glial cells and represent the most common type of primary brain tumours. Among them, glioblastoma multiforme (GBM) is the most prominent and aggressive brain tumour with a higher incidence in males than in females (1.6 times) at a median age of 64 years old[2]. Despite the treatment approach, GBM has a poor survival prognosis of less than one year[3]. This prognosis of GBM is not only due to the severity of the disease but also to the hurdles of the treatment imposed by the localization and biological characteristics of this type of tumour.

1.1.1 Molecular and cellular classifications of GBM

1.1.1.1 GBM cell populations

The brain is composed by a structural or connective tissue, which includes blood endothelial cells, fibroblasts and epithelial cells[4], and by a functional tissue composed of two types of cells, neurons (or nerve cells) and glial cells (or neuroglia). While the neurons are responsible for the electrical and chemical signalling throughout the brain, the glial cells maintain the optimal function of the brain supporting and protecting the neurons[5].

GBM originates from astrocytes, a type of glial cells. Nevertheless, different subpopulations of brain cells can be found in the tumour mass. GBM heterogeneity is influenced by these different cell subpopulations inside the tumour. Through a comprehensive genetic analysis of GBM samples from the TCGA (The Cancer Genome Atlas), it was demonstrated that four different cell states can be present in the same GBM tumour[6]. These cell states have similarity with normal developing brain cells which are the neural progenitor cells, oligodendrocytes progenitor cells, astrocytes and mesenchymal cells.

Importantly, these subpopulations are stimulated to develop in the tumour due to genetic alterations and microenvironment characteristics. Each of them has a specific genetic marker, that is platelet-derived growth factor receptor A

(PDGFRA) amplification for oligodendrocytes progenitors, cyclin-dependent kinase 4 (CDK4) amplification for neural progenitors, epidermal growth factor receptor (EGFR) amplification for astrocytes progenitors and neurofibromin 1 (NF1) alteration for mesenchymal progenitors **(Figure 1.1)**. The evolution between these cell states correlates with tumour progression.
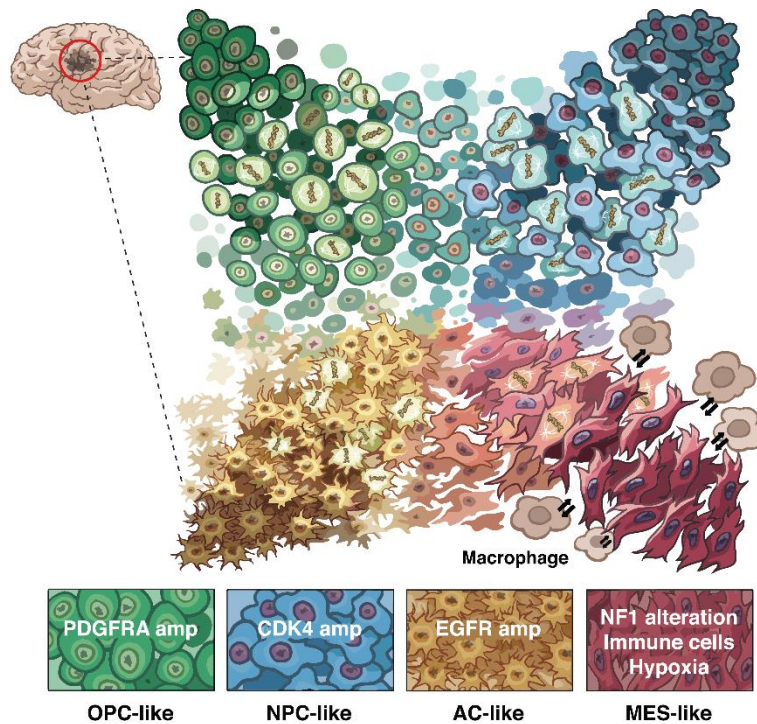
Figure 1.1: Cell types presenting in GBM and the characteristic molecular feature: oligodendrocyte-progenitor-like (OPC- like), neural-progenitor-like (NPC-like), astrocyte-like (AC-like), mesenchymal-like (MES-like). Reprinted with permission from ref [6]. PDGFRA- platelet-derived growth factor receptor A, CDK4- cyclin-dependent kinase 4, EGFR- epidermal growth factor receptor, NF1- Neurofibromin 1.

Moreover, stem cells are one of the most important subtypes in the tumour mass. They are self-renewal cells that can be quiescent or highly proliferative and are present in different organs[7]. Glioblastoma stem cells can proliferate and maintain the tumour. Therefore, cancer stem cells are frequently associated with GBM recurrence and resistance to different chemotherapy regimens[8,9]. These cells can originate from neural progenitors (neural stem cells) or from a differentiated cell that acquires oncogenic alterations and develop into the stem-like phenotype[10]. In the first scenario, it is believed that in the proneural subtype common signalling pathways that direct brain development, such as Notch and NF-κB, contribute to the activation of cancer stem cells which favours tumorigenesis.[11] For example, the

Notch pathway that inhibits neuronal differentiation during neural development can be disrupted and induce cancer stem cells to differentiate and progress the tumour.[12]

Cancer stem cells are also important because they can play a role in the immune suppression in GBM[13]. For instance, they can interact with immune cells through secreted factors such as IL-10 and TGF-β[14]. Alterations on the immune cells present in the tumour microenvironment, such as T lymphocytes, macrophages, dendritic cells and natural killer (NK) cells, make the immune response generated in the body against the tumour very weak[15]. In addition, the tumour produces low amounts of neo-antigens that can stimulate an immune response[16]. Thus, brain tumours are known to be immunologically 'cold', which means that they do not respond well to the patient immune system.

The understanding of tumour microenvironment is essential for a better management of the disease. The interactions between GBM tumour cells, endothelial cells, pericytes, astrocytes, stromal cells, immune cells, GBM cancer stem cells and the extracellular matrix that are present in the tumour mass and in the peritumoural tissue, can help with the prediction of treatment efficacy or resistance and also with the selection of multi-target therapies to combat this disease.

1.1.1.2 GBM molecular features

Initially, GBM was mainly diagnosed and classified based on histopathological characteristics. As such, the tumour was stratified as grade IV by the WHO[17] and it was further categorized as a primary or secondary malignancy. Primary GBM originated directly in the brain as a very aggressive tumour while secondary GBM is either an evolution from lower grade gliomas (astrocytomas grade II or III) or metastasis-competent cells from a primary tumour that achieved the brain. However, GBM tumours have both inter-tumour and intra-tumour heterogeneity, and usually show different clinical signs and symptoms among patients.

For this reason, the WHO has revised its classification system to include molecular features combined with the histology for tumour type determination. The molecular and cellular characteristics of a tumour are very important to estimate prognosis and choose the most suitable treatment options. Several efforts were

made in glioblastoma research to differentiate histologically similar tumours based on expression of specific genes previously related to the disease (including IDH, PIK3C2B, MDM4, MYCN, PIK3CA, PDGFRA, KIT, EGFR, BRAF, PIK3R1, PTEN, RB1, TP53, NF1and ATRX).

GBM was the first tumour type analysed by the Cancer Genome Atlas (TCGA) program (https://portal.gdc.cancer.gov/projects/TCGA-GBM). The beginning path along the identification of different molecular features of GBM was comprehensively reviewed by Eder and Kalman[18]. Many factors contribute to glioblastoma heterogeneity including DNA aberrations, DNA methylation and gene expression patterns, immune heterogeneity, cancer stem cell populations, microenvironment components and miRNA expression.

The main genetic alterations observed in GBM patients are DNA methylation, copy number alterations (CNA) such as deletions and fusions, and gene mutations[19]. Specifically, molecular markers of GBM include isocitrate dehydrogenase (IDH) mutation, 1p/19q codeletion, the ATRX (Alpha Thalassemia Mental Retardation X-linked gene) mutation, TP53 mutation, O6-methylguanine DNA methyltransferase (MGMT) promoter methylation, telomerase reverse transcriptase (TERT) promoter mutation, epidermal growth factor receptor (EGFR) gene mutation among others[20].

The main genetic marker used to classify GBM tumours is the IDH mutation status. Therefore, the tumour can be divided into IDH wildtype, IDH mutant and the tumours not otherwise specified (NOS). When the mutation is not present, the tumour is said primary or de novo GBM while in the presence of mutation it is called secondary GBM and it is less aggressive with better prognosis.

The molecular classification considers changes in gene expression and genetic aberrations that alters signalling pathways and, consequently, affect the clinical development of gliomas. These molecular characteristics were considered in order to expand GBM classification in the molecular subtypes: proneural, mesenchymal and classical **(Figure 1.2)**. The proneural subtype is correlated with better prognosis while the others have shown poor prognosis. The median survival estimation for the subtypes are 11.5 months for the mesenchymal, 14.7 months for the classical and 17 months for the proneural subtype[21]. It is important to note that this subtype classification is based only on the analysis of malignant cells. Nevertheless, the microenvironment cells, which include the immune cells, play a role in the subtype plasticity that occurs mainly after treatment in recurrent tumours.

In addition, it was estimated that 55% of GBM tumours retain their subtype during disease progression.
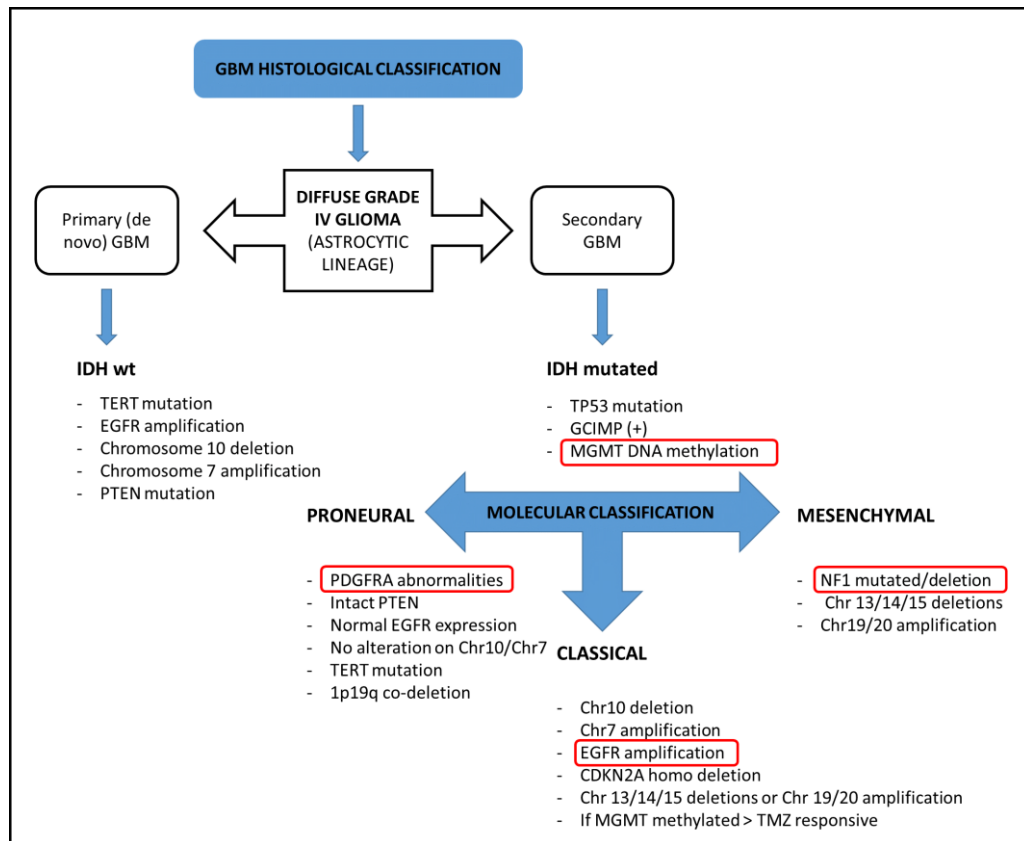
Figure 1.2: GBM classification and molecular features. (Abbreviations: wt = wild-type, IDH= isocitrate dehydrogenase, TERT= telomerase reverse transcriptase , EGFR = epidermal growth factor receptor , PTEN = Phosphatase and tensin homolog, TP53 = tumour protein p53 gene, GCIMP= cytosine-phosphate-guanine (CpG) island methylator phenotype, MGMT= O[6]-methylguanine-DNA methyltransferase, PDGFRA = platelet-derived growth factor receptor A, 1p19q = short arm chromosome 1 (i.e. 1p) and the long arm of chromosome 19 (i.e. 19q), NF1=Neurofibromin 1, CDKN2A= cyclin-dependent kinase inhibitor 2A, Chr= Chromosome). The red circles indicate characteristic molecular alteration of each subtype. Ref [15,18].

The main goal of a specific molecular categorization is to guide and personalize as much as possible the treatment decision. However, this approach is still controversial. Although each subtype has at least one characteristic molecular alteration that may be used to predict treatment outcome and disease progression, GBM heterogeneity is very high. As mentioned before, different cell populations in the tumour microenvironment also play a role in the clinical development of GBM.

Epigenetics also plays an important role in glioblastoma prognosis and clinical characteristics. Hypermethylation of specific promoter areas in the DNA causes the silencing of the associated gene. For example, to date the most consistent biomarker used clinically (in tissue biopsy) to address GBM therapy in a molecular level is the MGMT (O[6]-methylguanine-DNA methyltransferase) methylation status. The methylation of the MGMT promoter combined with an IDH wild type tumour is used as predictive marker of benefit from alkylating therapy, such as temozolomide[22,23].

Most of the genetic alterations in GBM affect genes and proteins related to signalling pathways important to cell survival, proliferation and cell cycle regulation[20]. Two types of signalling cascades affected are the tumour suppressor pathways and the oncogenic pathways. The tumour suppressor signalling from p53 and Rb are inactivated in GBM[24]. This leads to uncontrolled cell division, and cell survival and proliferation irrespective of the presence of mutations in the DNA.

On the other hand, the constitutive activation of EGFRvIII, a common mutation in GBM[25], affects both the hyperactivation of the phosphatidylinositol-4,5-bisphosphate 3-kinase/Protein Kinase B (PI3K/AKT) pathway and the VEGF expression that act on its receptor contributing to survival and invasion of GBM tumours. Other signalling pathways downstream of EGFR such as the RAS/RAF mitogen-activated protein kinase (MAPK), the signal transduction and transcription activator (STAT) and the protein kinase C (PKC) pathway are also affected in GBM favouring tumour progression, survival and migration.[26]

Besides the genetic alterations that originate GBM tumours, mutations that occur over time and due to the microenvironment and disease progression are also important and can influence the treatment outcomes. For instance, the expression of protein transporters on tumour cell surface are responsible for the extracellular acidification[27] and resistance to chemotherapeutic drugs[28–30].

Although a great advance was made on the molecular and transcriptional classification of GBM, its clinical translation is still incipient. The interconnection between signalling pathways in the molecular level and the presence of multiple mutations in the same tumour combined with different cell populations is yet a huge challenge for GBM diagnosis and treatment.

1.1.2 GBM management

The standard of care for GBM comprises surgery for tumour resection followed by radiotherapy and chemotherapy regimens[31]. Although this approach has been used for more than 20 years, it is not sufficient to combat GBM and new treatment options are needed. Two main factors contribute to challenges in the treatment of GBM: the achievement of therapeutic doses in the brain and tumour resistance to chemotherapeutic agents. These factors are heavily influenced by the presence of the Blood Brain Barrier (BBB) and the Blood Tumour Barrier (BTB).

Normally, the BBB impairs most of molecules to penetrate the brain[28]. However, both the BBB and the BTB integrity are compromised in glioblastoma. The heterogeneity on these barriers interferes with treatment effectiveness by influencing drug permeability and transport in and out of the brain[32], affecting glioblastoma progression and treatment results.

Treatment approaches aiming to overcome these challenges are increasingly related to methods of drug administration that can be, systemic or local. Systemic delivery includes intravenous injection, oral intake of chemotherapeutic drugs or even intranasal delivery, which bypasses the BBB[33]. Local delivery involves the direct injection of drugs into the brain using different strategies such as convection enhanced delivery. Moreover, radiation therapy is a non-invasive treatment that can be delivered both systemically and locally[34].

In GBM, these two methods of delivery (systemic and local) are frequently used simultaneously after tumour resection to increase the treatment rate of success. Besides that, other treatments are being researched, for example thermal therapies such as hyperthermia[35] and thermal ablation[36,37], tumour treating fields[38], and electric field-mediated drug delivery[39].

1.1.2.1 Systemic treatment versus local treatment

Systemic treatments of neurological disorders are very challenging due to the presence of the BBB, which impairs the penetration of drugs into the brain. One of the mechanisms responsible for the BBB selective permeability is the presence of protein transporters (also known as efflux pumps) that move several molecules, including hydrophobic drugs and chemotherapeutics, across the cell membranes and outside the brain in an ATP-dependent manner[30,40]. Both the permeability of the BBB and the existence of efflux pumps are responsible for the difficulty to achieve

an effective concentration of drug in the brain[41]. Moreover, systemic chemotherapy imposes many severe side effects to patients. For this reason, the standard of care for GBM still needs to be refined to provide better outcomes associated with improvement of quality of life, e.g. less systemic side effects. In addition, episodes of recurrence and resistance to the chemotherapeutic drug are very common[42]. Therefore, to avoid all these problems and increase treatment safety and efficacy, new local drug delivery strategies have been proposed against GBM[43].

One of the local delivery methods developed for drug administration to the brain is the Ommaya reservoir[44]. It delivers drugs into the intraventricular space direct into the cerebrospinal fluid, what can also be achieved through intrathecal and intraparenchymal injections.

In 1996, a localized treatment for GBM was approved with the commercial name Gliadel[45,46]. This drug delivery device consists in wafers of Polifeprosan 20 embedded with carmustine (bis-chloroethylnitrosourea, BCNU). Its development intended to improve the treatment outcome and decrease the side effects experienced by patients following systemic chemotherapy. Since then, in some cases the surgical resection of the tumour is followed by the local implantation of these wafers. However, the use of Gliadel presents some challenges related to the resection area, which is not effectively covered by the wafers, and the low amount of drug that can diffuse into the brain reaching the cancer cells[47,48]. For this reason, other local delivery approaches to the brain, such as hydrogels, are under investigation to improve GBM treatment **(Figure 1.3).**
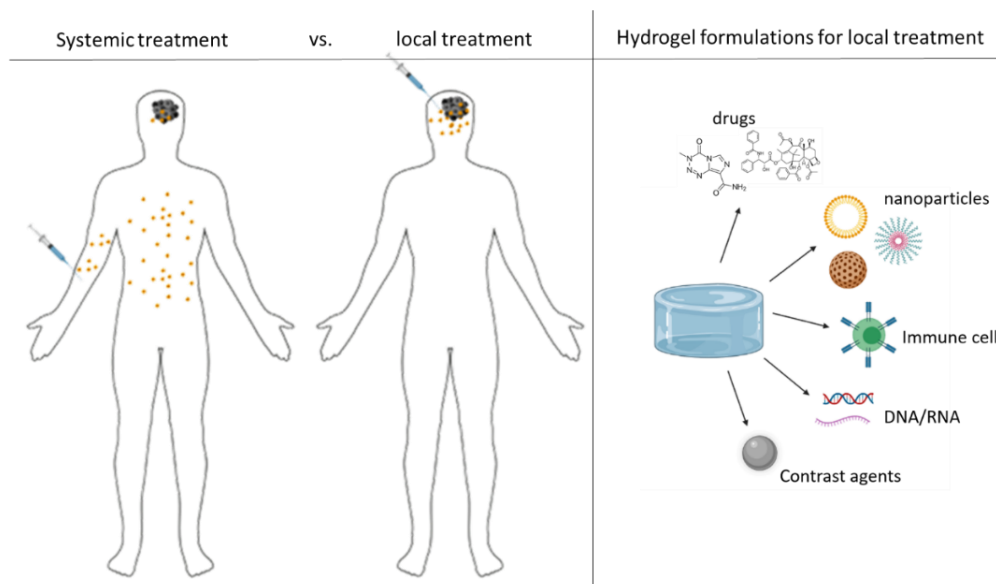
Figure 1.3: Systemic vs local treatments of GBM. Hydrogel formulations for the local treatment of GBM may contain free drugs, different types of drug-loaded nanoparticles such as liposomes and polymeric or inorganic nanoparticles, immune cells, nucleic acids and contrast agents.

In addition to the likelihood to decrease side effects, local therapy seems convenient for GBM since most of the patients will undergo surgery as one of the first steps of their treatment. In this scenario, formulations consisting of copolymers forming hydrogels or polymeric nanoparticles (hydrogel nanoparticles, nanospheres, nanocapsules, microspheres and micelles) and nanocarriers including metal and inorganic nanoparticles, liposomes, polymeric micelles and microspheres are gaining more attention as possible alternatives in the development of a localized treatment[49].

The incorporation of drugs into nanoparticles protects them from degradation while it can also provide targeted and controlled release of drugs depending on the characteristics of the nanodelivery system. Moreover, the combination of nanoparticles into hydrogels adds the possibility to combine drugs and to control the delivery not only of drugs, but also of nanoparticles from the hydrogels. Therefore, alternative routes of drug administration are under investigation such as the in situ injection of chemotherapeutic drugs formulated into nanosystems and/or hydrogels, intranasal delivery and convection enhanced delivery. Importantly, the specific formulation of the chemotherapeutics play a crucial role to improve treatment outcomes.

1.1.2.2 Convection enhanced delivery

The Convection enhanced delivery (CED) of drugs into the brain was proposed back in 1994[50]. This technique differs from simple diffusion of drugs into the brain because it uses a pump to infuse drug in an active manner. To achieve this, a catheter needs to be implanted in the brain of the patient configuring an invasive method.

An advantage of CED is the higher amount of drug that can penetrate the tumour tissue. However, this depends on several parameters of the treatment design. It is possible to have one or more catheters; the infusion can be done intratumourally or peritumourally and the infusion parameters (flow rate, total volume infused, the number of infusions and the duration) also play a crucial role[51]. Some disadvantages of CED are the side effects such as edema, tissue damage, bleeding and infection[52].

Several aspects of the technique, including canula design and placement, reflux and the chosen agent to be delivered, need to be carefully determined so that it can be translated successfully to the clinical setting[53]. After the treatment, the monitoring using MRI is also important to ensure that the drug was delivered and distributed throughout the brain. Indeed, this is considered to be critical for the optimization and clinical translation of this treatment method. Thus, Stephen *et al.* suggested the use of iron-oxide nanoparticles as both imaging tracer and delivery system to better monitor drug distribution in the brain parenchyma[54]. Using time-resolved MRI to monitor the volume of distribution of target and non-target nanoparticles, they demonstrated that nanoparticles containing chlorotoxin on the surface as a target molecule had 3.4 times higher volume distribution compared to the non-target nanoparticle after 24 h of injection.

Different drug formulations and nanocarriers are being developed and improved to be specifically delivered through CED. Liposomal formulations with different surface charges, PEGylation and transition temperature were tested *in vitro* for cellular uptake, tissue distribution and retention into the brain[55]. The liposomal formulation with an specific molar ratio of PEG and cationic lipids (76.15 : 20 : 3.85 of L-α-phosphatidylcholine : 1,2-dioleoyl-3-trimethylammonium-propane : PEG) showed a higher degree of internalization by GL261 cells *in vitro* and almost 4-times higher retention in the brain tumour *in vivo* after CED. Thus, specific formulations may improve the efficiency of this delivery method in treating brain tumours.

Another type of nanocarrier that can be used to deliver drugs through CED are virus-like particles (VLPs). Three different VLPs, bacteriophage MS2 spheres, tobacco mosaic virus (TMV) disks and nanophage filamentous rods, were developed and studied for their potential use in CED to treat glioblastoma[56]. All three VLPs modified with doxorubicin decreased GBM cell viability *in vitro* similarly to free drug. However, only TMV disks improved the survival of U-87-glioma bearing mice after CED delivery treatment.

Formulations containing hydrophobic drugs that do not cross the BBB when administered systemically are candidates to be delivered locally, for example through CED. Pluronic nano-micelles loaded with a histone deacetylase (HDAC) inhibitor distributed well in the brain of rats and remained in the brain up to 48 h after CED infusion. Indeed, the formulation significantly increased the survival time of syngeneic Fischer344/F98-Luc orthotopic rat glioma model compared to both untreated and vehicle only groups[57]. Platinum drugs that are also very insoluble in aqueous solutions could be used in CED when formulated accordingly. Zhang *et al.* formulated a cisplatin-loaded nanoparticle coated with PEG that was able to penetrate deeper in the brain parenchyma and significantly increased the median survival time of rats bearing orthotopic glioma (median survival not reached) compared to non-coated loaded nanoparticle[58].

Finally, formulations carrying EGFR target antibodies are also being developed to be delivered through CED. An EGFR antibody conjugated with iron oxide nanoparticles delivered through CED enhanced tumour radiosensitivity by both inhibiting DNA repair and increasing ROS formation. In addition, animal survival was improved by 5 times compared to the control group[59]. Another formulation composed of an EGFR-targeted immunotoxin showed promising results in mouse and rat models for anti-tumour effects and toxicity safety and entered in a Phase I/II clinical trial[60] (https://clinicaltrials.gov/ct2/show/NCT02303678).

1.1.2.3 Intranasal delivery of agents for brain targeting

The intranasal route has been explored for the delivery of drugs that suffer from lack of permeability through BBB and that present fast degradation rates systemically. The drugs have to be specially formulated to take advantage of the nose-to-brain route[61]. Thus, intranasal formulations include nasal solutions, gels and spray systems.

In the nose-to-brain administration method the nasal mucosa plays a crucial role for the drug transport to the brain. Two pathways have been proposed for transport: the perivascular channels in the mucosa and the intracellular/extracellular mechanisms in the olfactory and trigeminal nerves[61].

Some strategies are used to increase the effectiveness of intranasal formulations. These include the use of nanocarriers such as liposomes and polymer-based nanoparticles incorporating small drugs. The entrapment of drugs in nanocarriers can prevent the degradation of drugs in the nasal mucosa. Therefore, formulations containing loaded nanoparticles are attractive for the intranasal delivery route. In addition, different polymers, enzymatic inhibitors of prodrugs and excipients are used to increase the efficiency of the formulation.

PLGA nanoparticles loaded with paclitaxel and surface modified with Arginyl-glycyl-aspartic acid (RGD) tri-peptide that target glioblastoma tumour cells were tested for their effectiveness in delivering drugs intranasally to the brain[62]. The nanoparticles released the drug in a sustained manner over 4 days after a burst release of 30% in the first 30 min, and decreased the viability of both human and rat cells *in vitro* (U-87 and C6 cells). Furthermore, the drug was increasingly deposited in the glioma region after intranasal delivery (48 h) compared to intravenous administration that caused a high offsite deposition of the drug. In both rat (using C6 cells) and mice (using U-87 cells) models of GBM, the RGD-NP-PTX decreased tumour volume by up to 72% and 75% respectively compared to controls.

The delivery of a temozolomide ester (TBE) intranasally using a targeted PLGA nanoparticle (P-NP) has also been studied[63]. The nanoparticle was coated with N-trimethylated chitosan (TMC) as an adhesive agent and functionalized with anti-EPHA3 (Ephrin type-A receptor 3), a receptor that is overexpressed in glioma vasculature. The anti-EPHA3-T/P-TBE-NPs increased the median survival time of rats bearing tumours by 1.5 times compared to control group, also increasing the apoptosis level in glioma cells. Moreover, the nanoparticle distribution was higher in the brain after intranasal administration when compared to intravenously.

Another group has developed polycaprolactone nanoparticles to deliver melatonin (MLT-NP) via intranasal route to treat GBM[64]. These nanoparticles sustained the release of melatonin over 48 h with an initial burst release (30%) in the first 6 h. A comparison between oral and intranasal administration showed enhanced MLT concentration in the brain (9-fold and 18-fold percentage) at 0.5 h

after intranasal administration using the NP formulation when compared to oral and intranasal delivery of free drug, respectively.

Hybrid nanoparticles have also been explored for intranasal delivery. For example, farnesylthiosalicylic acid (FTA) loaded (lipid-cationic) lipid-PEG-PLGA hybrid nanoparticles (HNPs) were tested for antitumour efficacy[65]. After repetitive treatments, FTA loaded HNPs administered intranasally or intravenously equally decreased tumour area. However, only when administered intranasally, FTA accumulated in the brain and remained present until 120 h. These results highlight a major advantage of the intranasal route that decreases the systemic distribution of drugs.

Bypassing the BBB is another advantage of intranasal administration. For this purpose, the formulations can also include components that act as mediators for the transport. Shinde & Devarajan prepared microemulsions (ME) of curcumin (CUR) and tested the role of docosahexaenoic acid (DHA) in mediating bypass of BBB[66]. Curcumin concentration in the brain after intravenous administration was higher for CUR DHA ME formulation compared to CUR solution (8-fold higher) and CUR Capmul ME (2-fold higher). In addition, the highest CUR concentration in the brain was observed for the intranasal administration of CUR DHA ME. These results clearly confirm the impact of DHA on the BBB target.

Delivery of oligonucleotides, which are not able to cross the BBB upon systemic administration, can be achieved through the nose-to-brain route as well. This approach was used to silence Galectin-1 (Gal-1) gene in mice to sensitize the tumour to chemo and immunotherapy[67]. Tumour-bearing mice were treated intranasally with siRNA targeting Gal-1 (siGal-1) loaded on chitosan nanoparticles, and Gal-1 expression was reduced by 40% leading to a higher median survival and lower levels of tumour cell proliferation. However, no changes in apoptosis were observed. Immune activation was shown when Gal-1 was silenced with increasing amounts of lymphocytes and macrophages type I (pro-inflammatory). Combination therapy with TMZ increased the median survival from 32 days (TMZ only) to 53 days (TMZ + siGal-1). Besides immune activation, this effect was ascribed to vasculature normalization due to Gal-1 silencing.

1.2 Applications of biomaterials in GBM research

1.2.1 Stimuli-responsive Mesoporous Silica Nanoparticles (MSN)

Nanotechnology approaches have been investigated for the treatment of different types of cancer, since they can be explored for localized and targeted therapy, reducing side effects and ineffective treatment. Among the nanosystems under development, mesoporous silica nanoparticles (MSNs) are being widely explored in their ability to constitute an active targeting system for GBM treatment. MCM-41, a type of MSN, was first described in 1992 as one member of the silicate/aluminosilicate molecular sieves family. These materials were characterized by regular and hexagonal pores and were synthetized by a procedure called liquid crystal templating using surfactants[68] **(Figure 1.4)**.
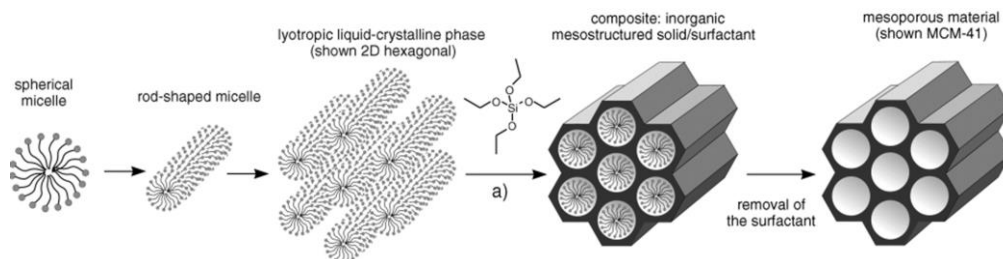
Figure 1.4: Liquid Crystal template method to synthetize MSNs[69] (CC licence).

This synthesis procedure can originate different types of MSNs by tailoring the surfactant concentration. Moreover, the surfactant chain length changes the pore size of the material obtained[70]. Due to the easy synthesis and the possibility to change some parameters to obtain the desirable product, MCM-41 has been extensively studied. More importantly, its chemical and structural properties make them a very attractive material to be used in targeted and stimuli-responsive delivery nanosystems[71].

Using mesoporous silica nanoparticles, it is possible to develop a gated system in which the nanoparticle pores are capped with a compound that blocks the pore, impairing the cargo release until a stimulus, such as temperature, pH or changes in enzyme or reducing agents concentration in the medium, triggers the release. The capping molecules can be peptides, proteins, antibodies among others[72–76].

The stimuli-sensitive delivery of drugs is an important approach in cancer treatment since it is an effective way to avoid the severe side effects of chemotherapy. Mesoporous silica nanoparticles can be multi-functionalised with different molecules that can target specific cell components and be triggered by different mechanisms to deliver chemotherapeutic drugs increasing the likelihood of a successful therapy. In addition, contrast agents can also be delivered in response to stimulation to monitor the efficacy of the treatment **(Figure 1.5)**.
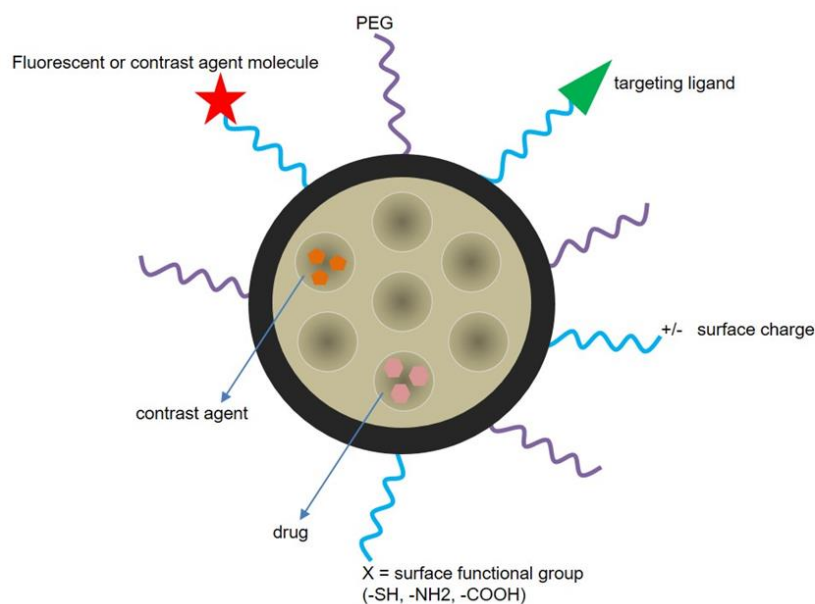
Figure 1.5: MSNs surface can be multi-functionalized to develop a target and stimuli responsive delivery system. The types of functionalization include the attachment of PEG, fluorescent or contrast agent molecule, a targeting ligand (e.g. protein, peptide, antibody), changes in surface charge and different functional groups (-SH, -NH$_2$, -COOH). Image from ref. [77]

Moreover, it is possible to take advantage on tumour cell microenvironment characteristics. For example, differences in pH between normal cells and tumour cells are well stablished[78] and extensively used as a strategy to trigger drug delivery in many types of cancers. Ahmadi Nasab *et al.*[79] used this principle in the design of a silica nanoparticle loaded with curcumin and coated with chitosan. They showed that at pH 7.4 the release of the drug from the nanoparticle was lower than at pH 5.5 in the presence of the polymer coating. In addition, the IC50 of curcumin in U-87 cells was also decreased when delivered by this pH sensitive nanosystem. Li *et al.*[80] used MSNs to develop a delivery system combining the release of camptothecin (CPT) and doxorubicin (DOX) in response to the acidic pH in tumour

cells. Briefly, MSNs were loaded with CPT and surface functionalized with DOX through a hydrazone bond that could be hydrolysed at pH 6.5. *In vitro* tests of this system in U-87 cells confirmed the synergistic effects between CPT and DOX as well as the improvement in the chemotherapeutic effect provided by the pH-sensitive release.

Another important characteristic of mesoporous silica nanoparticles is that their size can be tuned to achieve the desired therapeutic effect. Mo *et al.*[81] explored the particle size tailoring of MSN and evaluated its effect on the nanosystem performance. They tested nanoparticles of 20, 40 and 80 nm for the internalization and retention by cells as well as the ability to cross the blood brain barrier applying a co-culture model. The MSNs loaded with doxorubicin with an average size of 40 nm were more extensively internalized, and also presented a higher ability to cross the blood brain barrier cell model decreasing the cell viability. Moreover, they showed that the decrease in cell viability was caused by the overproduction of reactive oxygen species (ROS) and the disruption of vasculogenic mimicry capacity of glioma cells.

MSNs can also take advantage of the enhanced permeation and retention (EPR) effect[82]. According to this concept, large molecules and small particles are more prone to accumulate in the tumour tissue rather than the normal tissue due to the enhanced and leaky vascularization[83,84]. In both targeted and non-targeted nanocarriers, the drug is protected from degradation and elimination having a bigger circulation time in the body. Thus, the EPR effect is favoured through the use of nanocarriers. It is important to note that the aforementioned modifications on the surface of mesoporous silica nanoparticles can also contribute to the biodistribution, biocompatibility[85] and the EPR effect[86].

In summary, the modifications that can be applied to mesoporous silica nanoparticles make them a very attractive material to be differentially designed and developed to treat GBM. The stimulus-sensitive and targeting approaches are being explored and they can contribute to a great improvement in patient's treatment.

1.2.2 Hydrogels

The use of hydrogels in healthcare devices has many technical advantages. Firstly, many of them allow the solubilization of hydrophobic drugs. For instance, as demonstrated by Zentner *et al.*[87], the incorporation of paclitaxel (PTX), a highly

hydrophobic drug, in a biodegradable triblock copolymer significantly increased drug solubility and stability, providing a sustained release during approximately 6 weeks. Secondly, encapsulation in hydrogels protects drugs from phagocytic cells and disfavourable environmental factors that can promote drug degradation. Thus, hydrogel formulations can increase the half-life of chemotherapeutic drugs while reducing the frequency of drug administration and improving patient compliance [88,89].

To design a suitable hydrogel formulation for drug delivery, some materials characteristics are important, specifically viscoelasticity and swelling capacity, encapsulation stability and minimal toxicity. Other characteristics that may be tuned and improved include the response to stimulus, passive and active targeting, controlled and sustained drug release[90].

Many polymers are available to be used in local treatment formulations as hydrogels. Some examples of hydrogel formulations developed for GBM therapy includes poly-NIPAM (poly N-isopropylacrylamide)[91], alginates[92,93], chitosan[94] and PEI (polyethylenimine)[95]. Specifically, block copolymers derived from the combination of two or more polymers can also be used as hydrogel formulations. Copolymers design considering characteristics such as hydrophobic/hydrophilic ratio, block length and molecular weight, influence gel formation, release profiles, degradation and biocompatibility, which can be tuned based on hydrogel composition[96]. In addition, the sol-gel transition of hydrogels, for example, can be controlled by changing the block lengths, the polymers ratio and concentration[97]. Therefore, these design possibilities make copolymer hydrogels interesting materials for the development of an in situ delivery formulation.

1.2.2.1 Thermo-responsive block copolymers

Hydrogels can be classified according to their structure, mechanical properties, method of preparation and responsiveness to an external stimulus. The ones in the latter category are known as stimuli-sensitive hydrogels and they can be responsive to pH, light, redox environment, magnetic field, temperature among others[98]. Specifically, thermo-responsive hydrogels are formed in response to changes in the local temperature and can be used to deliver drugs and/or diagnostic agents in a controlled and sustained manner.

The hydrogel chemical and physical properties influence the loading and delivery of compounds. Different mechanisms are responsible for the delivery of a drug from a hydrogel and the most important is passive diffusion. However, there are different models to predict release profiles from hydrogels, and these models are classified in three categories: (1) diffusion-controlled, (2) swelling-controlled, and (3) chemically controlled. Moreover, the structure and consequently the release characteristics of a hydrogel can be tuned by monomer composition, different degrees of crosslinking and the intensity of external stimuli[99]. Therefore, the possibility to build different formulations to achieve the desired delivery profile has estimulated an increased research in this area, specially for biomedical applications[100].

For drug delivery purposes, the use of *in situ* forming hydrogels is favorable since this type of gels offers a number of benefits; namely, they can be administered in liquid state in the absence of a trigger mechanism, and can rapidly undergo gelation after injection[101]. In this way, implantation by invasive surgical procedures is avoided. Furthermore, the incorporation of different types of drugs to the polymer solution can be achieved by simple physical mixing[102]. Thermosensitive hydrogels that can undergo an *in situ* gelation process at body temperature have received significant attention for the design of local depots for anticancer drugs due to their ease of preparation and administration. In this section, some types of block copolymers **(Figure 1.6)** and different formulations that were built focused on the treatment of GBM are summarised.
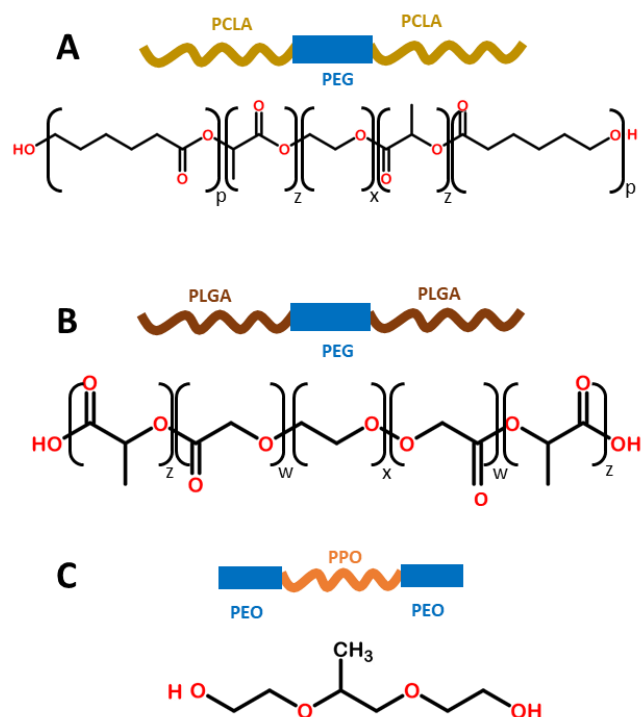
Figure 1.6: Representative thermosensitive tri-block copolymers and their chemical structures. **A-** PCLA-PEG-PCLA, **B-** PLGA-PEG-PLGA, **C-** PEO-PPO-PEO (Pluronic) These polymers were used in different formulations for the local treatment of GBM due to their temperature sensitivity and favourable chemical characteristics to incorporate drugs and nanocomposites. PCLA- Polycaprolactone-co-lactide, PEG- Polyethylene glycol, PLGA- Poly(lactic-co-glycolic acid), PEO- Poly(ethylene oxide), PPO- Poly(propylene oxide).

1.2.2.1.1 PCLA-PEG-PCLA

Copolymers of PCLA-PEG-PCLA (poly(ε-caprolactone-co-lactide)-b-poly(ethylene glycol)-b-poly(ε-caprolactone-co-lactide)) have been used as drug delivery systems in different biomedical formulations since they are biodegradable and biocompatible and therefore suitable for *in vivo* use. This triblock copolymer has thermosensitive properties which contributes to tuning the loading and release of small molecules. Besides that, the rheological properties of this hydrogel can be improved to make them more suitable for drug delivery applications.

Several studies investigated and compared the PCLA-PEG-PCLA properties after chemical modification on the polymer chain by different capping systems and through blending of the modified systems. Xun *et al.* synthetized a peptide functionalized hydrogel (KRGDKK- PCLA-PEG-PCLA- KRGDKK) that kept the

thermosensitive properties while presenting improved rheological characteristics[103]. The peptide added to the structure contributed with hydrogen bonds to the formation of stronger gels at lower temperatures and this characteristic is important to facilitate the use of the hydrogels for implantation. Another important improvement was the sustained and more prolonged release (over 1 month vs. 10 days) of doxorubicin which was also attributed to the presence of the peptide moiety on the hydrogel structure.

Petit *et al.* studied PCLA-PEG-PCLA aqueous solution of uncapped (hydroxyl-terminated), hexanoyl[104], acetyl and propionyl-capped[105] copolymers regarding the gelation and degradation behaviours. The degradation and sol-gel transition are very important characteristics for the material applicability and, in these studies, the possibility to modify and mix thermosensitive triblock copolymers to build the desired drug delivery formulation was demonstrated. They showed that the hydrogel degradation occurred through dissolution rather than hydrolysis over 280 days depending on the hydrogel composition, with the most hydrophobic and semi-crystalline copolymers having a slower dissolution. Moreover, the composition of the block copolymers provides the possibility to tune the temperature for sol-gel transition.

Besides the thermosensitive property, this copolymer can be functionalized to present other stimuli responsive characteristics such as pH sensitivity[106,107]. Shim *et al.* were able to both tune the pH sensitivity and the biodegradability of PCLA-PEG-PCLA polymers by adding pH-sensitive sulfamethazine oligomers (SMOs) to either end of the block polymer. The constructed polymer undergoes sol-gel transition at physiological conditions (pH 7.4 and 37 °C). This modified hydrogel was then tested for the ability to incorporate and deliver PTX to tumour-bearing mice through subcutaneous injections[108]. The effect of drug incorporation on the hydrogel properties was studied, and it was shown that regardless of the PTX amount loaded into the hydrogel, the sustained drug release was maintained although the gelation temperature shifted to lower temperatures in high loaded gels (10 mg/mL PTX). These characteristics are important regarding the practical aspect of administration in a clinical setting. Therefore, the formulation containing 5 mg/mL PTX which maintained the sustained drug release and the sol-gel transition similar to the unloaded gel was considered the most suitable for an injectable treatment. *In vivo* evaluation of the formulations in C57BL/6 male mice bearing tumours in the left flank showed a significant decrease in tumour volume compared to the control group

(saline – 17cm^3) and PTX hydrogel treated groups (smaller than 7 cm^3) after 2 weeks of treatment. This result was confirmed by TUNEL analysis of apoptotic cells that were very prominent in PTX hydrogel treatment but not in the control group.

1.2.2.1.2 PLGA-PEG-PLGA

Poly(D,L-lactic-co-glycolic acid)-(polyethylene glycol)-poly(D,L-lactic-co-glycolic acid) (PLGA-PEG-PLGA) polymers have been extensively studied as drug delivery systems for poorly water soluble drugs and drug combination therapy. In this class of polymers, the triblock thermosensitive copolymer named ReGel™ is one of the most commonly studied. This hydrogel has been investigated as a potential drug delivery vehicle against various solid tumours such as breast cancer, oesophageal cancer, spinal cancer, peritoneal and ovarian cancer, and high-grade gliomas[109].

Regarding GBM, ReGel™ was loaded with PTX originating a commercial product named OncoGel™, which is in clinical trials[110]. OncoGel™ has been studied as a monotherapy and as combination therapy with TMZ or radiation **(Figure 1.7)**. For instance, Tyler *et al.* treated mice intracranially implanted with 9L gliosarcoma cells with different OncoGel formulations or ReGel (with no drug, as negative control) to investigate the synergistic effects of OncoGel and radiation therapy in comparison with each therapy alone[111]. The results demonstrated that the group treated with OncoGel had extended survival periods compared with the group treated with ReGel. Moreover, the authors demonstrated that the group treated with both OncoGel and radiotherapy had the longest survival period (31 days), improving the results obtained with OncoGel (17 days) or radiotherapy alone (26 days). In another study with 9L gliosarcoma xenografts, Vellimana *et al.* treated mice with an individual therapy of OncoGel, TMZ (oral therapy or poly (1,3-bis-[p-carboxyphenoxy propane]-co-[sebacic anhydride]) local implant), radiotherapy or combinations of these therapies[112]. It was shown that the combination of OncoGel and TMZ was more effective than the individual treatments. Moreover, the addition of radiotherapy to the combination treatment with oral TMZ significantly improved the therapeutic outcome, as 100% of the animals were alive at the end of the study (120 days). Furthermore, a similar outcome was obtained for the group treated with OncoGel and an intracranial implant of TMZ.
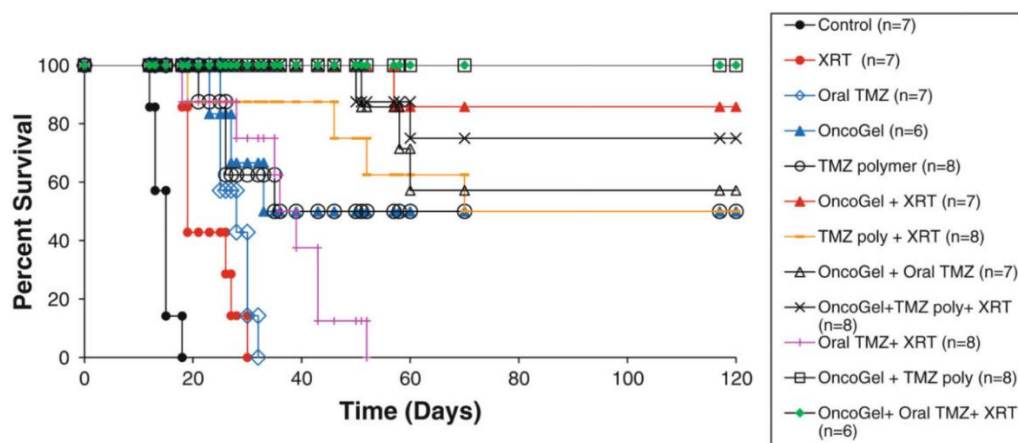
Figure 1.7: Oncogel *vs* TMZ/radiation therapies. Efficacy of intracranial TMZ or oral TMZ in combination with OncoGel with or without radiation on Fischer-344 rats. Median survivals: Control- 15 days; Radiation Day 5- 19 days; Oral TMZ on Days 5-9- 28 days; OncoGel 6.3 on Day 0- 33 days; TMZ polymer Day 5 –35 days; OncoGel 6.3 + radiation- 85% long term survivors; TMZ polymer + radiation- 70 days; OncoGel 6.3 + oral TMZ 57% long-term survivors; OncoGel 6.3 + TMZpolymer + radiation –75% long-term survivors; Oral TMZ + radiation –35 days; OncoGel 6.3 + TMZ polymer and OncoGel 6.3 + oral TMZ + radiation – 100% long-term survivors. From Ref [112].

1.2.2.1.3 Pluronics

Linear Pluronics, also known as poloxamers, are non-ionic amphiphilic triblock copolymers. They are composed of poly(ethylene oxide) and poly(propylene oxide) ordered as an ABA triblock copolymer (PEO-PPO-PEO) with thermo-reversible properties in aqueous solutions. Pluronics can be used as hydrogels in injectable and topical formulations. For instance, a thermogel application of Pluronic copolymers include vaginal formulation to deliver amphotericin B locally, taking advantage of the relative *in vivo* stability of this system[113] . They can also form and are most used as micellar systems for drug delivery[114].

Pluronic copolymers can self-assemble into polymeric micelles above their critical micellar temperature (CMT) forming nano-delivery systems. The polymeric micelles formed can incorporate hydrophobic drugs and this is directly dependent on the copolymer composition. The size and composition ratio between the hydrophilic (PEO) and the hydrophobic (PPO) chains influence the solubilisation of different types of drugs as well as their release characteristics[115]. Drug release is also controlled by polymer dissolution rate which can be tuned by the polymer

concentration[116]. Some types of poloxamers and their physicochemical characteristics are summarized in **Table 1.1**.

Table 1.1: Physicochemical characteristics of some Pluronic copolymers[117–119].

Pluronic copolymers	Molecular weight	HLB [a]	CMC (M) [b]
F 127	12,600	22	2.8×10^{-6}
P 85	4,600	16	6.5×10^{-5}
P 103	4,950	9	6.0×10^{-6}
P105	6,500	15	6.2×10^{-6}
P 123	5,750	8	4.4×10^{-6}

[a] HLB: hydrophilic-lipophilic

balance

[b] CMC: critical micelle

concentration

The encapsulation of drugs in the core of these polymers allows delivering hydrophobic drugs to tumour sites while the hydrophilic surface protects the drug from degradation and inactivation. Therefore, hydrophobic drugs, such as genistein, PTX and quercetin were already incorporated in different Pluronic micelles[120]. The solubility of these drugs was higher in moderately hydrophobic Pluronics, P103 and P123, and was favoured by increased temperature and salt concentration. The release of the drugs from the micelles fits on a first-order model equation. Therefore, the drugs are released in a sustained manner from the micelles mainly through diffusion **(Figure 1.8)**. Pluronics have also been applied as gene delivery systems and it has been proposed that both physical forms of the material, the micellar solution and the gel, can contribute differently to the gene transfection capability of the system[121].
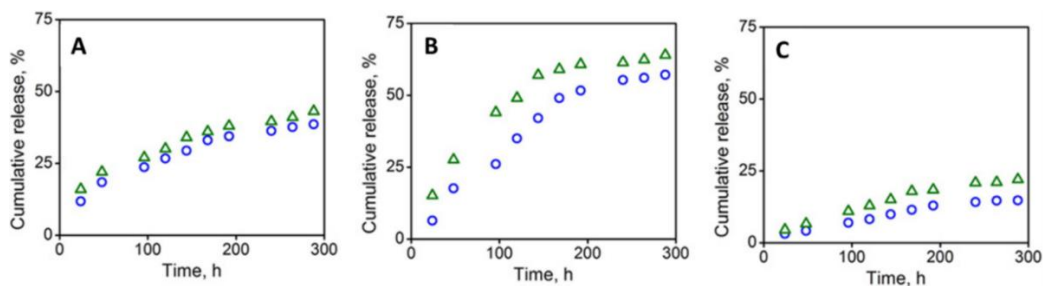
Figure 1.8: Release of hydrophobic drugs from Pluronic micelles. Release profiles of (a) genistein, (b) paclitaxel, and (c) quercetin from 1% (○) P103 and (Δ) P123 at 37 °C. From Ref [120]

Some studies have shown that Pluronic copolymers are not inert drug delivery vehicles **(Figure 1.9)**. The effect of Pluronic administration on several cell processes includes inhibition of efflux transport, activation of glutathione/glutathione S-transferase detox system and drug sequestration on vesicles, among others[122]. For example, Batrakova *et al.* showed that Pluronic P85 acts as a chemosensitizer agent in multi drug resistant (MDR) cancer cells, making them more sensitive to doxorubicin (DOX). Using Pgp expressing membranes, they demonstrated that the Pluronic effect is due to both ATP depletion and Pgp ATPase activity inhibition[123]. Importantly, the authors highlight that the drug resistant mechanisms in these cells are coupled with other factors, such as activation of glutathione/glutathione S-transferase detoxification system, that dramatically increases the energy requirements of these cells, also contributing to the Pluronic cytotoxic effects observed.
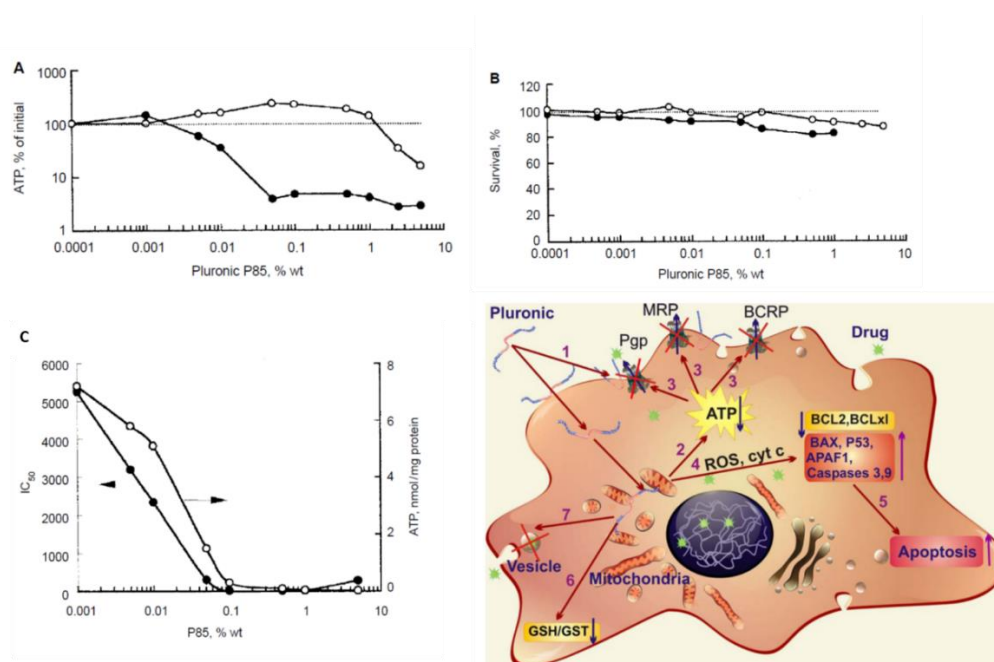
Figure 1.9: Pluronic copolymers are not inert drug delivery vehicles. Effects of P85 on (**A**) intracellular ATP levels; and (**B**) cell survival in resistant MCF-7/ADR (filled circles) and sensitive MCF-7 (empty circles) (**C**) Effects of P85 on IC50 of doxorubicin (filled symbols) and ATP intracellular levels (empty symbols) in KBv cells. (D)Schematic on the Pluronic copolymer effects in MDR cells. Ref [122] and [123].

Besides the ability to take advantage of passive targeting due to their nanometric size, Pluronic polymeric micelles have been engineered as targeted drug delivery systems able to cross the BBB. Niu *et al.* designed Pluronic P105 micelles with two targeting moieties, glucose and folic acid, and evaluated the dual-targeting system loaded with DOX (GF-DOX) in brain tumour models[124]. While glucose can increase the BBB penetration through the glucose receptor in the brain, folic acid can target its receptor present in glioma cells. Using an *in vitro* BBB model of murine brain microvascular endothelial cells (BMVECs), they observed a 5 times higher transportation of the glucose modified micelles loaded with DOX (GP-DOX) compared to free DOX and a decrease in transport when an excess of glucose was present. Moreover, rat C6 glioma cells showed higher uptakes of folic acid modified micelles (FP-DOX) compared to non-modified micelles (P105-DOX) and GP-DOX. The dual-target micelles (GF-DOX) decreased C6 cell viability *in vitro* by more than 80% and, after an intravenous administration in C6 intracranial tumour model, they significantly decreased the tumour volume compared to mice treated with P105-DOX, GP-DOX and FP-DOX (approximately 7.5, 3.5 and 4 times smaller).

In another example of active targeting with Pluronics, Zhang *et al.* proposed a folate functionalization of Pluronic P123/F127 mixed micelles (FPF)[125]. The functionalized micelles loaded with paclitaxel (FPF-PTX) showed higher cell uptake of drug compared to the non-functionalized micelles, while also increased the blood circulation time compared to the free drug. Interestingly, the authors observed the co-localization of the uptaken micelles and mitochondria, organelles important for both cell metabolism and cell death. Therefore, the co-localization of Pluronic micelles with mitochondria highlights the dual effect of the targeted micelles interfering on cell metabolism and cell death induction through mitochondria sensing and protein release. Finally, in the *in vivo* efficacy test against MDR tumour bearing mice, FPF-PTX showed superior results regarding inhibition of tumour growth, likely due to both active targeting and the chemosensitization effect of the Pluronic system. Additionally, Pellosi *et al.* demonstrated that Pluronics can be used as delivery systems of both drugs and photosensitizer molecules, which normally are very poorly soluble in water[126]. In this report, Pluronic P123/F127 micelles loaded with the isomer mixture of benzoporphyrin derivatives (BPDMA and BPDMB) showed photo-toxicity against HeLa and A549 cells.

1.2.2.2 Chemically crosslinked hydrogels

The aforementioned thermosensitive hydrogels are formed in situ through physical crosslinking due to changes in the temperature. The thermosensitivity is a very useful characteristic because the body has a specific temperature that can be used to favour gel formation. Nonetheless, there is another mechanism that can be employed to form hydrogels from the starting polymers, and it is based on chemical crosslinking.

Chemically crosslinked hydrogels are formed by the mix of polymers with a chemical crosslinker, which can be of different types such as azide-alkyne, thyol-ene, Diels-Alder and oxime crosslinkers. Some building blocks used for the hydrogel preparation include hyaluronic acid, chitosan, alginate, poly(ethylene) glycol, poly(N-isopropyl-acrylmide) among others. These types of hydrogels are mostly used in GBM research as 3D matrices to understand cell proliferation, migration, invasion, gene expression and to develop 3D cultures of GBM cells.

To better understand the interaction of GBM with the extracellular matrix, Xiao *et al.*[127] developed a new 3D platform based on thiolated- Hyaluronic Acid (HA)

crosslinked with PEG via a Michael type addition-reaction to encapsulate GBM cells derived from patients. They showed that the procedure of crosslinking and cell encapsulation is quick and does not affect the viability of the cells. Moreover, the 3D network is suitable to the incorporation of ECM peptides and proteins to study the effects of different components on the cell behaviour. Finally, they demonstrated that the 3D culture can be analysed by the most common used techniques, namely flow cytometer, confocal and light microscopy, western blotting and immunofluorescence staining.

A similar hydrogel network formed with HA and gelatin using PEG as a crosslinker and the same reaction on the previous work was used to develop a method to quantify proliferation and invasiveness of GBM spheroids[128]. Different physical and chemical characteristics of the biomaterial were tuned to determine the factors that contribute to invasiveness. Firstly, PEGdivinyl sulfone (PEGDVS) was chosen as the crosslinker due to the higher stability over cell secretion of enzymes during invasiveness. Secondly, the stiffness of the gel was tailored so that it is favourable to cell invasion. The higher the polymer concentration and crosslinking density, the higher the stiffness, which results in a decreased invasive behaviour. They stated that the optimal stiffness for biologically relevant analyses would be between 1 and 5 kPa and that this corresponds to their developed 3D network.

Following the same principle of achieving a biologically relevant 3D hydrogel support to culture GBM cells and study tumour proliferation and invasiveness, the degradability of a PEG-based hydrogel was evaluated[129]. It was shown that at least 50% degradability by matrix metalloproteinases was required to support tumour spreading, and that this did not influence cell proliferation.

With regards to tumour migration analysis, collagen hydrogels crosslinked with 8S-StarPEG reduced U-87 microtumour cells migration *in vitro* compared to the non-crosslinked collagen[130]. These results reinforce the general observation that increasing the crosslinking density, and consequently the viscosity, influences migration characteristics of tumour models. Furthermore, it was observed that this behaviour correlates with a lower expression of some enzymes that are known to favour this process (metalloproteinases, urokinase plasminogen activator, and tissue plasminogen activator).

It is known that cell spheroids usually show greater resistance compared to monolayer cultures. For this reason, they are models that better reflect the clinical manifestation of cancer. Therefore, crosslinked polymers are also used to grow

tumour spheroids in order to compare drug cytotoxicity with monolayer cultures and perform drug screenings. In this sense, chitosan-PEG hydrogel (CSPG gel) crosslinked with genipin was tested, and showed cell morphology favoured towards spheroids while cells were more undefined and spread on uncrosslinked gel and Matrigel[131]. Importantly, the spheroids formed on CSPG gels were more resistant to TMZ and BCNU likely due to the upregulation of ATP transporters and downregulation of DNA repair proteins compared to Matrigel.

It is of note that chemically crosslinked hydrogels can also be explored as injectable gels that will form *in situ* and deliver drugs and drug-loaded nanosystems to treat GBM locally. However, this approach has not been widely explored for this type of gels.

1.2.2.3 Applications of hydrogels formulations

For biomedical applications, hydrogels are being used to develop several formulations with enhanced physicochemical, mechanical and biological properties. These formulations can include not only drugs but also NPs, cells, nucleic acids and diagnostic agents **(Table 1.2)**. For instance, the combination of two drug delivery platforms, hydrogel and NPs, may prevent the burst release of encapsulated drugs and extend the release period, thus decreasing potential adverse effects and increasing drug bioavailability[132]. Moreover, the incorporation of nanostructures into hydrogel matrices may alter the hydrogel physicochemical properties, providing tailored functionalities and improved drug delivery efficiency of the composite[133]. A significant advantage of hydrogel formulations, and specifically of thermosensitive hydrogels, is the formation of a localized therapeutic depot that can be implanted after surgical resection of a tumour for combating residual tumour cells and for the prevention of metastasis or recurrence.

Recently, hydrogel research for GBM treatment has been focused on two main areas, hydrogel formulations for treatment and hydrogels for brain tumour cell culture[134]. In the latter approach, hydrogels are being used in the development of *in vitro* models to understand the blood brain barrier[135], to develop test platforms for different therapeutic modalities such as photothermal therapy[136] and to establish 3D models of tumours[137,138] using patient derived cells or established cell lines aiming to understand tumour development and drug resistance in a mimic tumour microenvironment.

Regarding the therapeutic application, hydrogels are mainly used as drug delivery systems. Specially, hydrogels are used in drug combination therapies such as the most recent development of an enzyme responsive hydrogel loaded with TMZ and an MGMT inhibitor (O^6-benzylamine) that sensitizes TMZ resistant cells after resection surgery *in vivo*, thus decreasing recurrence[139]. Besides combination therapies, drug penetration into the brain parenchyma is another concern and hydrogels are being designed to help solve this problem. Wang *et al.*[140] designed a hydrogel based on a penetrating cyclic peptide and two camptothecin drug molecules, which can also encapsulate other drugs for combined therapy. The formulation improves penetration and antitumour effect *in vitro* on spheroids and *in vivo*. Other recent developments include a copolymer formulation that maintains high local concentrations of paclitaxel *in vivo*[141] and a camptothecin-based self-assembling hydrogel[142]. These formulations, applied locally after tumour resection, showed effect on supressing tumour recurrence and prolonging survival in GBM mouse models.

Table 1.2: Hydrogel formulations tested for GBM treatment in *in vitro* and *in vivo* models.

Polymer composition	Formulation additives			*in vitro* tested cell line	*in vivo* model	Reference
	nanoparticle/ nanocomposite	drugs/small molecules/ genetic material	cells			
PCLA-PEG-PCLA end capped with the pH-sensitive sulfamethazine oligomers (SMOs)	-	paclitaxel	-	-	C57BL/6 male mice bearing tumours in the left flank	108
PLGA -PEG -PLGA (Regel)	-	paclitaxel/temozolomide	-	9L gliosarcoma cells	Female Fischer-344 rats intracranially implanted with 9L gliosarcoma cells	111
Oncogel (PLGA -PEG - PLGA)	-	paclitaxel	-	-	Female Fischer-344 rats implanted with 9L gliosarcoma cells	112
Pluronic P85	-	doxorubicin	-	multi drug resistant cancer cells (MDR cells)	-	123
Pluronic P105	-	doxorubicin	-	Murine brain microvascular endothelial cells (BMVECs) and rat C6 glioma cells	Male Institute of Cancer Research (ICR) mice implanted with C6 cells	124
Pluronic P123/F127 micelles mixture	-	paclitaxel	-	KBv and KB cells and A-549 cells	mice subcutaneously implanted with KBv cells on the flank	125

PEG and poly-N-isopropylamide	-	doxorubicin	-	T98 and U-87 GBM cell lines	Male BALB/c nude mice model with a subcutaneous U-87 grafted tumour	[143]
PLGA with different common plasticizers	-	temozolomide	-	C6 and U-87 GBM cell lines	Adult PRKDC CB-17 mice model with subcutaneous U-87 cell grafted tumour and Adult Wistar rats with C6 cells intracranial tumour	[144]
Triglyceride core surrounded by a shell containing two surfactants (Span 80 and Kolliphor HS15)	-	lauroyl-gemcitabine(GemC$_{12}$)	-	U251, T98-G and U-87 glioma cells	nude mice and NMRI mice	[145,146]
Phospholipid based gel system	-	paclitaxel	-	-	Male Balb/c mice intracranially implanted with C6 cells	[147]
PEG hydrogel	PEG particles surface functionalized with MMP2 as well as RGDS peptide	quinacrine loaded particles and free TRAIL	-	U-87 cells	-	[148]
Alginate gel matrix	PLGA microspheres	paclitaxel	-	C6 cells	BALB/c nude male mice subcutaneously injected with C6 cells	[149]
PLGA (Poly Lactic-co-Glycolic Acid)	PLGA nanofiber discs	paclitaxel	-	-	BALB/c nude mice intracranially implanted with U-87 MG-luc2	[150]

Polyethylene glycol (PEG) and poly-N-isopropylacrylamide	PLGA microspheres	camptothecin and vincristine	-		mice models bearing C6 glioma tumours (Male Sprague–Dawley rats)	151,152
poly(N-isopropylamide-co-n-butylmethacrylate) (poly(NIPAAm-co-BMA) and PEG	polymeric microspheres or liposomes	doxorubicin	-	U-87, LN229 and G55 cells	nude mice subcutaneously implanted with U-87 cells	153
PEG-dipalmitoyl-phosphatidyl-ethanolamine (m-PEG-DPPE)	calcium phosphate nanoparticles (NPs)	paclitaxel and temozolomide	-	C6 cells	SPF male Wistar rats bearing C6 gliomas (after resection)	154
poly(ethylene glycol) dimethacrylate and Lucirin-TPO, a photoiniator	PEG-PCLA micelles	temozolomide	-	-	female athymic nude subcutaneously injected with U-87 cells	155
poly(ethylene glycol)-g-chitosan hydrogels	-		T-lymphocyte cells	U-87 cells	-	94
cellulose nanocrystals functionalized with a copolymer of N-isopropylacrylamide and N,N′-dimethyl-amino-ethyl methacrylate	-	-	fibroblasts and T-cells	-	-	156
nanogel of cholesteryl pullulan (CHP)	-	peptide antigen	-	-	Female BALB/c mice subcutaneously injected with the vaccine	157

cationic polymer composed of RGD peptide and Polyethylenimine (PEI) (RGD-PEG-SS-PEI)	-	pDNA complexes	-	U-87 cells	nude mice intracranially implanted with U-87 cells	[158]
dexamethasone-conjugated-polyethylenimine (PEI-Dexa)	-		-	C6 and U-87 GBM cell lines	subcutaneous (Balb/cSlc nude mice) and intracranial (male Sprague−Dawley rats) models of GBM	[159]
mPEG-PEI polymers	-	target peptide sequence (retro-inverso CendR peptide (D(RPPREGR))	-	U-87 cells	Male BALB/c nude mice intracranially implanted with U-87 cells	[95]
Poly (organophosphazene) hydrogel	cobalt ferrite nanoparticles	7-ethyl-10-hydroxycamptothecin (SN-38)	-	NIH3T3 mouse embryo fibroblast cells and U-87 cells	6-week-old female BALB/c-nu mice (U-87 ectopic xenograft model and orthotopic brain tumour model)	[160]
carboxymethyl cellulose (CMC)-grafted poly (N-isopropylacrylamide co-methacrylic acid)	albumin nanoparticles loaded with paclitaxel	gadolinium/epirucibin (EPI)	-	MBR 614 human brain tumour cell	C57BL/6 and Nu/Nu mice subcutaneously implanted with MBR-614 or U-87 cells	[161]

1.2.2.3.1 Hydrogels loaded with drugs

One of the earliest studies to investigate the potential of *in situ* forming thermoresponsive hydrogels as local depots to deliver a chemotherapeutic drug is the research work by Arai *et al.*[143]. They incorporated DOX in a thermoresponsive hydrogel composed of PEG and poly(N-isopropylamide), and the anticancer effect of the formulation was tested in T98 and U-87 GBM cell lines as well as in a mice model with a subcutaneous U-87 xenograft. The hydrogel triggered significant apoptosis on both cell lines *in vitro* and decreased the tumour weight when locally injected in mice.

In an attempt to develop a novel local drug delivery system, Akbar *et al.* designed a hydrogel system composed of PLGA with different common plasticizers, to locally deliver TMZ to tumour cells following tumour resection surgery[144]. In the study, U-87 cells were implanted intracranially in mice and after 35 days the tumours were surgically removed followed by the hydrogel injection in the resected area. There were no significant differences in adverse effects between control groups and groups treated with TMZ-loaded hydrogels. However, in terms of treatment efficacy, the tumour weight in groups injected with hydrogels decreased up to about 95%.

Another innovative system, based on a lipid nanocapsule hydrogel composed of a triglyceride core surrounded by a shell containing two surfactants (Span 80 and Kolliphor HS15) and the chemotherapeutic agent lauroyl-gemcitabine (GemC$_{12}$), was developed to be locally delivered in the treatment of brain tumours[145,146]. The intratumoural injection of the hydrogel formulation was well tolerated in the GBM *in vivo* models used (nude mice and NMRI mice). Furthermore, a significant increase in the median survival of groups treated with the hydrogel (62 days) compared to control groups (no treatment – 35.5 days) was observed as well as a lower rate of tumour recurrence. The group of Chen *et al.* reported on a different phospholipid based gel system aimed to deliver PTX[147]. The formulation, liquid at room temperature, turns into a gel upon injection into the tumour due to difusion of the ethanol that is included in the formulation. PTX was delivered in a sustained manner, and the gel was well tolerated and significantly increased the median survival of U-87 tumour bearing mice compared to mice receiving no treatment (26.5 days versus 15.5 days) or local injections of free drug (18 days).

Erkoc *et al.* proposed a dual therapy for GBM through the combination of a degradable hydrogel loaded with free TRAIL (tumour necrosis factor α-related

apoptosis-inducing ligand) and a TRAIL sensitizer drug, quinacrine[148]. The hydrogel is formed through the crosslinking of PEG particles using visible light. The hydrogel was sensitive to matrix-metalloproteinases, secreted by the tumour cells, and was functionalized with targeting RGDS peptides. The authors proved the *in vitro* synergistic effect between the quinacrine-loaded hydrogel and TRAIL, also showing that the treatment induces apoptosis specific gene expression in U-87 cells.

1.2.2.3.2 Hydrogels loaded with micro/nanoparticles incorporating drugs

The properties and applicability of drug-loaded hydrogel formulations can be improved by the combination with different types of particles. The addition of a particulate component opens the possibility to combine different chemotherapeutic agents in the same formulation and allows the exploitation of additional ways to control and target the drug release **(Figure 1.10)**. For instance, Ranganath *et al.* developed an implant formed by an alginate gel matrix entrapping PTX-loaded PLGA microspheres[149]. The incorporation of microspheres in a gel matrix resulted in formulations with a highly sustained *in vitro* release profile of PTX of more than 60 days at a near-constant rate and with a minimum initial burst. Moreover, when implanted subcutaneously in mice it reduced the tumour volume more effectively than Taxol, demonstrating their potential as a local chemotherapy for glioma treatment.

The same group compared these PTX-loaded PLGA microspheres entrapped in alginate hydrogel matrices with PTX-loaded PLGA nanofiber discs[150]. At this time, the formulations were intracranially implanted in BALB/c nude mice with glioblastoma xenografts (U-87-luc2). They observed that the nanofiber discs formulations had the higher release rate *in vitro* and provided deeper penetration of drug in the tumour, inhibiting tumour growth *in vivo* more effectively compared to the formulations developed previously. This result was attributed to a higher drug concentration at the implant surface. In a typical post-surgical chemotherapy regimen, the initial tumour growth inhibition will be critical to slow down the rate of glioma recurrence, thereby inhibiting migration and invasion into healthy brain tissue. Thus, the authors concluded that these implants could improve the treatment outcome for recurrent GBM.

Using a similar approach, Ozeki *et al.* designed a system in which PLGA microspheres loaded with camptothecin were mixed with a thermosensitive polymer composed of PEG and poly-*N*-isopropylacrylamide[151]. The *in vivo* assessment using mice models bearing C6 glioma tumours showed that the formulation significantly increased the survival period of animals compared with both the hydrogel alone (placebo) and drug-loaded hydrogel without the microspheres. It was shown that the formulation with microspheres had higher retention times up to 14 days, which could contribute to enhance therapeutic outcome. They also showed that the microsphere-hydrogel composites may act as local depot after tumour resection surgery and different chemotherapeutic drugs can be incorporated into the gel, for example, camptothecin and vincristine, improving the survival period of the *in vivo* model (male Sprague–Dawley rats bearing C6 intracranial tumours)[152,162].

Another example of hydrogel nano/micro-composites was developed by Arai *et al.* combining polymeric microspheres or liposomes loaded with DOX with a thermo-reversible gelation polymer (TGP), composed of poly(*N*-isopropylamide-*co-n*-butylmethacrylate) (poly(NIPAAm-co-BMA) and PEG[153]. *In vitro* results using U-87, LN229 and G55 cells confirmed that TGP alone is non-toxic to glioma cell lines and that the DOX released from the TGP, liposomes and spheres retains its biological effect. In subsequent *in vivo* studies, the antitumour effect was evaluated in subcutaneous human glioma xenografts in nude mice. The free DOX entrapped in TGP was released faster than from the TGP combined with DOX-loaded spheres (2.5x times) or liposomes (4.3x times), which presented a more sustained drug release up to 30 days and, therefore, inhibited tumour growth up to 32 and 38 days, respectively.

More recently, Ding *et al.* developed an injectable thermoresponsive hydrogel based on PEG-dipalmitoyl-phosphatidyl-ethanolamine (m-PEG-DPPE) and calcium phosphate NPs that provided a sustained and local delivery of both PTX and TMZ[154]. The formulation was able to inhibit C6 cell proliferation *in vitro* and significantly increased the survival rate of rats bearing C6 gliomas, which were injected with the hydrogel formulation after tumour resection.
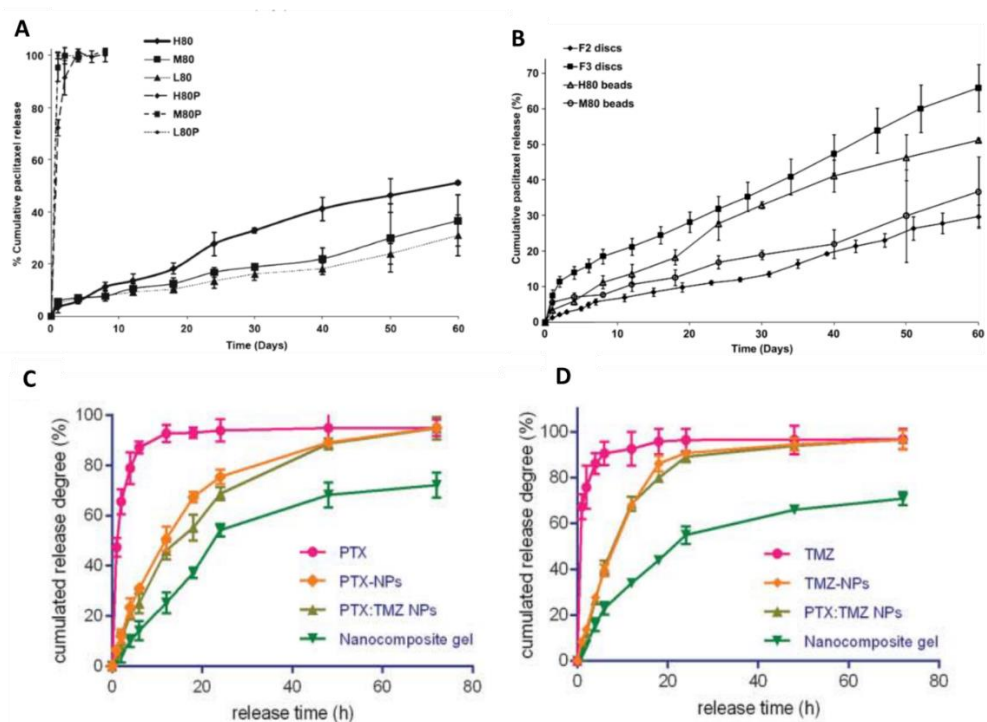
Figure 1.10: Nanoparticles loaded into hydrogels provide a more sustained release of drugs over time. **(A)** *In vitro* release of paclitaxel from different formulations of alginate beads. 80% (w/w) microsphere-loaded alginate beads and paclitaxel-loaded beads; The prefixes H, M and L refer to the extent of crosslinking in the beads, (high, medium and low). H80P, M80P, L80P refers to paclitaxel-loaded beads with equivalent amount of paclitaxel as compared to its microsphere loaded beads. Ref[149] **(B)** *in vitro* release of paclitaxel from 9.1% paclitaxel-loaded F3 discs, 9.1% paclitaxel-loaded F2 discs, H80 and M80 beads [From previous Ref.[149]] and Ref[150]. **(C)** Cumulative release profiles of PTX from PTX NPs, PTX:TMZ NPs and nanocomposite gel. **(D)** Cumulative release profiles of TMZ from TMZ NPs PTX:TMZ NPs and nanocomposite gel (Ref[154]).

Photopolymerization methods have also been used to design hydrogel-nanostructure composites for the treatment of GBM. In the research by Fourniols *et al.*, PEG (Poly(ε-caprolactone-cotrimethylene carbonate) micelles loaded with TMZ were added to a polymer solution containing poly(ethylene glycol) dimethacrylate and Lucirin-TPO as photoiniator[155]. The formulation was locally injected in female athymic nude mice and UV light was applied to induce the polymerization reaction, forming the local gel depot at the tumour site. The *in vivo* results showed that the tumours from mice treated with the hydrogel-nanostructure formulation were significantly lighter, and a higher extent of apoptosis was observed compared to mice treated with systemic TMZ.

Taken together, these results confirm the advantages of a localized and combined strategy. On one hand, local administration can ensure the therapeutic

dose maintenance at the tumour site. On the other hand, the NPs ensure a sustained and prolonged release of drugs to remaining or recurrent tumour cells. Therefore, this combination holds significant promise in the treatment of GBM.

1.2.2.3.3 Hydrogels for cancer immunotherapy

Immunotherapy is a modern and attractive approach in cancer treatment that attempts to stimulate or help the patient immune system to specifically reject and destroy tumours with minimal harm to healthy tissues[163]. Thermosensitive hydrogels are not only able to carry small molecules and micro or nanoparticles but have also been reported to act as depots for immune cells-based therapy. Tsao *et al*. designed a thermosensitive poly(ethylene glycol)-g-chitosan hydrogel that was able to support the penetration of T-lymphocyte cells[94]. The hydrogel showed better compatibility for the infiltration and release of T-lymphocyte cells when compared to Matrigel likely due to its bigger pore size (0.5−1µm vs 0.1-0.5 µm pore size distribution). Moreover, the cells retained their cytotoxic activity against U-87 glioblastoma cell line. Although *in vivo* studies were not carried out, these results may lead to the development of a novel localized immunotherapy for glioblastoma or other CNS disorders.

Similarly, Thérien-Aubin *et al*. developed a thermosensitive nanofibrillar hydrogel composed of cellulose nanocrystals functionalized with a copolymer of N-isopropylacrylamide and N,N′-dimethyl-amino-ethyl methacrylate which was able to encapsulate fibroblasts and T-cells[156]. The system was evaluated for the ability to form gels at physiological temperature and to support *in vitro* cell culture development. Moreover, physical characteristics of the gels (structure and mechanical properties) could be tuned through changes in composition, and the material did not show toxicity for the cells tested (NIH 3T3 fibroblast and EL4 T cells). The authors suggested that the system can be used as an injectable therapy or as an artificial matrix to 3D cell culture. Although this system was not evaluated against cancer cells, it constitutes an interesting approach to immunotherapy applications using hydrogels.

Another immunotherapeutic approach studied for cancer treatment is the development of vaccines. Cancer vaccines aim to stimulate the immune system to act against cancer cells. However, some improvements are needed to get the desired immunogenicity for the formulations[164,165]. Muraoka *et al*. developed a cancer vaccine using a nanogel of cholesteryl pullulan[157]. The nanogel loaded with

a peptide antigen was selectively internalised in macrophages in lymph nodes of female BALB/c mice subcutaneously injected with the vaccine. In addition, they showed that the macrophages could present the antigen to T cells, triggering the immune response against syngeneic tumours transplanted in the mice. Importantly, this nanogel system was already tested in clinical trials that confirm its safety and efficacy.

The abovementioned research works introduce new developments regarding immunotherapy and cell therapy against cancer. They show that hydrogels can be used both as cell supporting systems *in vitro* and as cell delivery vectors. The biocompatibility of these materials would allow their incorporation into new treatments for GBM and other tumour types.

1.2.2.3.4 Hydrogels loaded with DNA/RNA

Different strategies to deliver gene sequences have been developed and evaluated in the past years[166]. Polymers have been presented as a feasible strategy to increase the transfection efficiency of gene therapies, exploring stimuli-responsive and targeting mechanisms. For this purpose, oligonucleotides have been loaded or attached to hydrogel NPs using a range of approaches. For instance, Ma *et al.* attached siRNA to hydrogel NPs via disulphide bonds to improve the systemic and controlled delivery of gene therapy[167]. In this design, the siRNA release is responsive to reductive conditions. The developed material was tested *in vitro* using luciferase-expressing HeLa cells, and the inhibition of luciferase expression was observed upon treatment with the siRNA conjugated hydrogel NPs. *In vivo* tests were conducted with C57BL/6 mice, showing the efficiency of transfection (at both mRNA and protein level) through gene silencing of the Coagulation factor VII (FVII) produced by hepatocytes. Exploring the same principle with disulphide linkages, Lei *et al.* developed a non-viral gene delivery vector aimed to treat GBM[158]. A cationic polymer composed of RGD-PEG linked to polyethyleneimine (PEI) through a disulphide bond (RGD-PEG-SS-PEI) was synthesized. The PEG moiety was used to both decrease the polymer toxicity and increase the transfection efficiency. The superior performance of the reducible targeted gene vector was confirmed *in vitro* in U-87 cells, and *in vivo* after intravenous administration in nude mice bearing U-87 tumours. The analysis of

reporter gene systems in the mice organs after polymer administration showed an efficient targeting to the brain.

Alternative stimuli-responsive strategies that take advantage of pathological characteristics of the tumour, such as hypoxic conditions, have been reported. Using dexamethasone-conjugated PEI as plasmid carrier, Kim *et al.* developed a specific therapy for GBM that combines two different regulatory elements, the nestin intron 2 (NI2) which has increased gene expression in glioblastoma and the erythropoietin (Epo) enhancer which has increased expression under hypoxia, to deliver a suicide gene to the tumour[159]. They confirmed the specificity of their constructs and the cytotoxicity promoted by the delivered gene in C6 and U-87 GBM cell lines. Moreover, *in vivo* subcutaneous and intracranial models of GBM showed response to this gene delivery therapy. Indeed, the study showed that the combination between the polymer carrier and the gene vector was more effective in reducing the tumour volume compared to the polymer alone (three times less effective) or combined with a non-specific plasmid sequence (twice less effective).

A polymer based on mPEG-PEI was reported by Wang *et al.* to deliver gene sequences to GBM tumour cells using a retro-inverso CendR targeting peptide (D(RPPREGR)), known to increase cell penetration through binding the neuropilin-1 receptor[95]. Enhanced cell uptake and tumour spheroid penetration of the fluorescent peptide FITC-D(CRPPREGR) were achieved, as well as higher transfection using the gene delivery system both *in vitro* (almost 2-fold targeting enhancement in U-87 cells) and *in vivo* in nude mice bearing U-87 tumours.

In summary, polymer based formulations are showing promising results as gene delivery systems for GBM therapy and the use of polymers as non-viral delivery vectors is a very promising area of research to be expanded.

1.2.2.3.5 Theranostic hydrogels

The combination of therapeutic and diagnostic approaches, known as "theranostics", has also been reported in the field of hydrogels. In this case, the polymer matrix contains both a chemotherapeutic and a contrast agent that allows the treatment monitoring in real time. As an example of nanotheranostic formulation, the "MRI-monitor long term therapeutic hydrogel" (MLTH) system consists of a thermosensitive poly(organophosphazene) hydrogel, cobalt ferrite NPs and the chemotherapeutic drug 7-ethyl-10-hydroxycamptothecin (SN-38)[160], which is the

active metabolite of irinotecan. MLTH systems with different amounts of SN-38 were tested in U-87 ectopic xenograft mice models to determine the MRI-enhancing effect and anticancer efficacy of the formulations. The hydrogel formulations generated higher inhibition effects on tumour growth (up to 48% decrease) compared with the chemotherapeutic drug only. Moreover, the cobalt-ferrite NPs in the composite had suitable MRI contrast-enhancing effects to distinguish between the untreated and treated areas in the brain. The MLTH system has been presented as an alternative approach to treat malignant brain tumours without any surgical resection.

Other formulations propose benefits following tumour resection and claim to impair tumour recurrence. This is the case of the recently reported theranostic hydrogel formulation with rapid gelation ability that is composed of carboxymethyl cellulose-grafted poly(*N*-isopropylacrylamide co-methacrylic acid) and the MRI agent gadolinium, loaded with a free drug, epirucibin (EPI), and PTX-loaded albumin NPs [161]. *In vivo* studies with mice bearing gliosarcoma tumours of MBR-614 or U-87 cells showed that the theranostic formulation increases the average survival compared to the control group from 18 to 63 days (MBR-641 models) and from 27 to 69 days (U-87 models). *In vivo* MRI of the group that received local administration of the hydrogel formulation showed a bright contrast at the site of implantation, and the signal intensity gradually decreased in 21 days, corresponding to the degradation and clearance of the hydrogel depot. The theranostic ability of this type of hydrogels could significantly improve treatment monitoring in the clinical setting **(Figure 1.11)**.
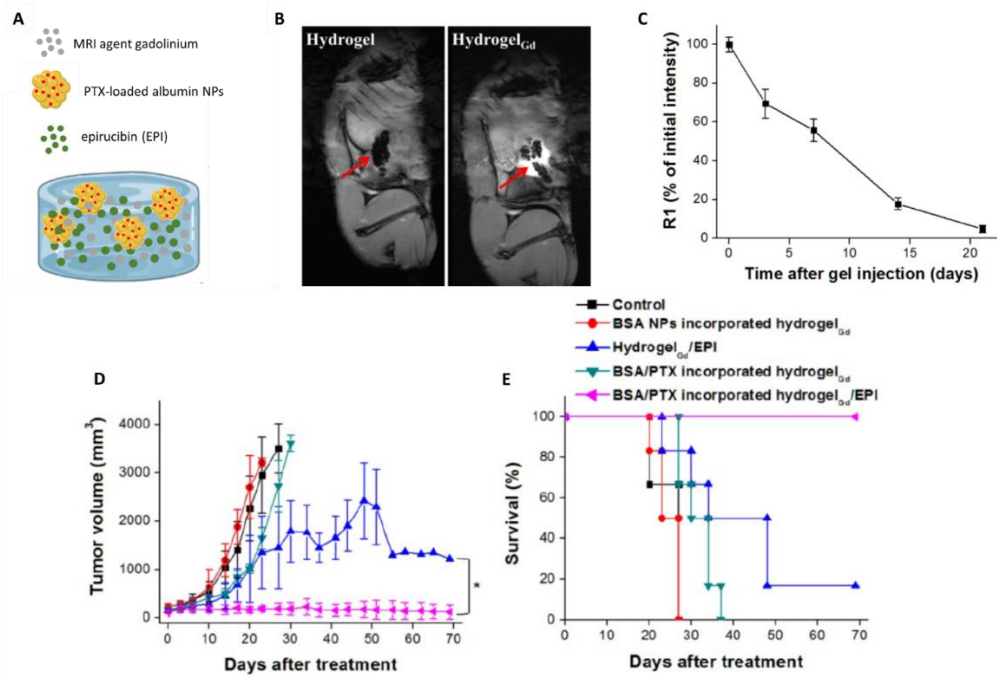
Figure 1.11: Theranostic hydrogels. (A) Schematic illustration of the theranostic formulation proposed by Lin *et al.*[161]. (B) MRI contrast-enhanced T1 images of (left) hydrogel and (right) hydrogelGd implanted in tumour-bearing mice. (C) The reduction of MR T1 intensity of BSA NPs-incorporated hydrogelGd in tumour site. (D) Tumour growth curves of mice bearing U-87 tumours after surgical operation then treatment with bovine serum albumin (BSA) NPs incorporated hydrogelGd or hydrogelGd/EPI or BSA/PTX NPs incorporated hydrogelGd or BSA/PTX NPs incorporated hydrogelGd/EPI implantation. (E) Survival curves of mice bearing U-87 tumours after different treatments. MRI- Magnetic Resonance Image, Gd-Gadolinium, EPI- Epirubicin, NPs-Nanoparticles.

1.3 Project aims

The treatment of GBM patients has followed the same standard of care protocol over 20 years while the improvement in survival time and quality of life has been very poor. New approaches to treat this disease are urgently needed. Important characteristics of the disease, such as the tumour localization, can be used to guide the development of new approaches.

Based on the rationale of combination therapy already used in GBM (surgery, radiotherapy and combination of chemotherapeutic regimens), I hypothesized that the application of a local therapy after tumour resection would improve the treatment outcomes. Moreover, this would be achieved by the local controlled release of drugs in a hydrogel formulation with nanoparticles. Thus, the main objective of this project is to develop a formulation for the local treatment of GBM. This formulation, named

GlioGel, will be a biomaterial combining an injectable gel with stimuli-responsive nanoparticles and free drug to treat brain tumours. The rapid release of the free drug will correspond to a first line of treatment towards residual tumour cells, followed by the later and more controlled release of drug-loaded nanoparticles as a second line of treatment.

This thesis will describe all the process since the selection and characterization of new biomaterials, analysis of their combinations and effects until the final formulation was chosen and tested *in vitro* and *in vivo*. A detailed *in vitro* analysis was performed for each of the formulation components, the gels and nanoparticles, using a GBM cell line and normal brain cells. Then, the combination of both components was also evaluated. Finally, the selected combination was analysed more in depth for the *in vitro* and *in vivo* performance.

CHAPTER 2: MATERIAL AND METHODS

2.1 Materials

Fetal bovine serum (FBS), fluorescein isothiocyanate (FITC), Safranin O, glutathione (GSH), L-glutamine solution, Minimum Essential Medium Eagle (MEM), Pluronic F-127, poly(ethylene glycol) (PEG) methyl ether thiol, sodium hydroxide (NaOH), temozolomide (TMZ), paclitaxel (PTX), tetraethyl orthosilicate (TEOS), trypsin-EDTA solution 0.25%, 2,2-dipyridyl disulphide (Aldithriol-2), (3-mercaptopropyl) trimethoxysilane, (3-Aminopropyl)triethoxysilane (APTES), iron III chloride hexahydrate, ammonium thiocyanate, sodium acetate, triton x-100, tween 80 and p-nitrophenil phosphate were purchased from Sigma- Aldrich Ireland. Carmustine (BCNU) was purchased from Tokyo Chemical Industry (TCI) Europe. Cetyltrimethylammonium bromide (CTABr) was purchased from ThermoFisher Scientific, Ireland. CCK-8 kit was purchased from Dojindo, Europe. Ultra-pure distilled water was prepared by the PURELAB Option system (ELGA LabWater, UK).

The Liquid Polymer 4 (LQP4) gel was provided by InGell Labs company and the Crosslinked (CX) gel was provided by Dr. Yang Shi, Group Leader in the Polymeric Nanomedicines Group at Aachen University in Germany.

2.2 Methods

2.2.1 Mesoporous silica nanoparticle (MSN) synthesis

The synthesis of the mesoporous silica nanoparticles was performed through the mechanism called "Liquid crystal templating" (LCT) in which a surfactant served as a template for the formation of the porous matrix. Briefly, 1 g of cetyltrimethylammonium bromide was solubilized in 500 mL of distilled water at 30 °C. When it was perfectly dissolved, 3.5 mL of NaOH 2M were added and the solution was heated until 80 °C. At this temperature, the stirring was increased and 5 mL of tetraethyl orthosilicate were added. This mixture was stirred for 2 h until full hydrolysis and condensation of the silica precursor, and the resulting nanoparticles were kept on the bench to cool until room temperature. Finally, the nanoparticle dispersion was centrifuged at 5000 rpm for 20 min to isolate the MSN, washed twice

with distilled water and once with ethanol. Then the material was kept in ethanol until surfactant extraction.

In order to synthesize fluorescently labelled nanoparticles (MSN-FITC), fluorescein isothiocyanate (FITC) was put to react with 3-aminopropyltriethoxysilane (APTES) for 2 h, protected from light. Then, this reaction mixture was added together with tetraethyl orthosilicate in the condensation reaction so the FITC was incorporated into the silica matrix.

An acidic extraction was performed to remove the surfactant from the material. The nanoparticles (1 g) were re-suspended in 1M HCl in ethanol (100 mL) and put in a reflux system under agitation and heating to 80 °C overnight. After that, the material was washed with distilled water four times and one time with ethanol and kept in ethanol until further use.

2.2.2 Mesoporous silica nanoparticle loading and functionalization

To load the nanoparticles with Safranin O, a ratio of 0.8mmol of the dye per gram of nanoparticles was used. The mixture of Safranin O and nanoparticles in water was stirred overnight at room temperature. The nanoparticles were loaded with TMZ by impregnation and transiently under vacuum following adaptations to a previously described method[168]. 20 mg of MSNs were put under vacuum for 2 h. Afterwards, 6 mL of 2.5 mg/mL TMZ in methanol were added to the material under vacuum and the vacuum was released. This mixture was kept stirring overnight at room temperature. To load the nanoparticles with PTX, the drug was solubilized in dichloromethane (2.5 mg/mL) and 10 mL of this solution were added to 75 mg nanoparticles[169]. This mixture was also kept stirring overnight at room temperature. Before proceeding with PEG functionalization, the loaded nanoparticles were collected by centrifugation and resuspended in acetonitrile (ACN) in the presence of an excess of Safranin O,TMZ or PTX, and 3 mmol of (3-mercaptopropyl) trimethoxysilane was added. This mixture was stirred for 5 h 30 min at room temperature. After this period, 3 mmol of 2,2'-dipyridyl disulphide (Aldrithiol) was added to the reaction mixture and kept stirring overnight at room temperature. Then, the sample was centrifuged and dried under vacuum at room temperature. The dried solid and poly (ethylene glycol) methyl ether thiol were resuspended in ACN in the presence of an excess of Safranin O, TMZ or PTX and the mixture was stirred

overnight. The final material, MSN-Saf-PEG, MSN-TMZ-PEG or MSN-PTX-PEG, was isolated by centrifugation, washed and dried under vacuum[170].

2.2.3 Drug loading estimation by High Performance Liquid Chromatography (HPLC)

The encapsulation efficiency (EE%) and loading capacity (LC%) were estimated using drug solution aliquots before and after the loading procedure. The encapsulation efficiency is the percentage of drug successfully loaded into the nanoparticle, while the loading capacity is the amount of drug loaded per mg of nanoparticle expressed as a percentage of nanoparticle mass that corresponds to drug loaded.

They are calculated using the following formulas:

$$EE\% = \frac{amount\ of\ drug\ in\ MSNs}{total\ amount\ of\ drug}\ x\ 100$$

$$LC\% = \frac{amount\ of\ drug\ in\ MSNs}{total\ nanoparticle\ weight}\ x100$$

Drug quantification was performed by UV light absorbance detection using a Gemini 5µm C18 column (110 Å, 250 x 4.6 mm) attached to a Waters Alliance High Performance Liquid Chromatography (HPLC) System following previously described methods for TMZ[171], BCNU[172] and PTX[173].

For TMZ, the mobile phase consisted in 10% acetonitrile/ 90% water (v/v), the flow rate was 1 mL/min and the detection wavelength was 316 nm. For BCNU, the mobile phase was 50% acetonitrile/ 50% water (v/v), the flow rate was 1.2 mL/min and the detection wavelength was 230 nm. For PTX, a mobile phase consisting of 70% acetonitrile/ 30% water (v/v) was used with a flow rate of 1 mL/min and detection wavelength was 227 nm.

2.2.4 PEG quantification on MSN

Aliquots from the washing samples after the PEGylation process were used to perform an indirect quantification of the amount of PEG on the surface of the nanoparticles using a colorimetric assay[174]. A biphasic system consisting of 0.5 mL ammonium ferrothiocyanate and 0.5 mL chloroform was prepared in Eppendorf tubes and 50 µL of each wash sample were added to one tube. The samples were mixed for 30 min in a shaker, then centrifuged at 3000g for 2 min. The chloroform

layer was separated and its absorbance was measured at 510 nm using a glass cuvette in a Shimadzu UV-1700 Spectrophotometer. A calibration curve of PEG was measured in different solvents (water, ethanol and acetonitrile) to match the solvent used in the washing steps.

The amount of PEG on the surface of the nanoparticles was calculated by subtracting the total amount of PEG added from the amount measured in the assay. Then, the value was converted in a percentage of the total amount added per mg MSN in the functionalization process.

2.2.5 Mesoporous silica nanoparticle characterization

2.2.5.1 Particle size and surface charge analysis

The particle size distribution and zeta potential were determined using a Zetasizer Nano series Nano-ZS ZEN3600 fitted with a red laser light beam (λ=633 nm) (Malvern Instruments Ltd., UK). The equilibration time was set to 2 min at 25 °C. Measurements for each sample were taken in triplicate. The mesoporous silica nanoparticles were characterized before and after functionalization with PEG. A suspension of nanoparticles was prepared in water at 1 mg/mL final concentration. The samples were stirred and sonicated when necessary to avoid aggregates that could interfere in the final result. Data for diameter (nm) and ζ-potential (mV) represent the average of independent experiments with each nanoparticle batch. The average size of the nanoparticles was also evaluated using TEM images measuring with ImageJ software.

2.2.5.2 Thermogravimetric analysis

Thermogravimetric analysis of the material was performed using a TGA Q50 (TA Instruments, USA) to check the composition of the nanoparticles before and after extraction. The mesoporous silica nanoparticles were heated up to 600 °C at a rate of 5 °C/min. The material weight/mass were measured and plotted in relation to temperature increase. The percentage of weight loss was then calculated.

2.2.5.3 Powder X-ray diffraction (PXRD)

The powder X-ray diffraction (PXRD) pattern of the synthesized nanoparticles was acquired in a Rigaku Miniflex II diffractometer with a Cu Kα

radiation X-ray source. The dried nanoparticles were mounted on the sample holder and scanned over a 2θ range of 2-10 degrees; step width of 0.01; count time 1; 30 kV and 15 mA.

2.2.5.4 Fourier-transform infrared spectroscopy (FTIR)

The infrared (IR) spectra of the materials were recorded using a Perkin-Elmer Spectrum 100 spectrometer with an attenuated total reflection (ATR) accessory attached to it. The spectral range recorded was from 4000 cm^{-1} to 600 cm^{-1}.

2.2.5.5 Surface area

The surface area and the pore size distribution of the nanoparticles were analysed by nitrogen (N_2) adsorption-desorption porosimetry. The isotherm was measured on a Gemini VI (Micromeritics Instrument Corporation, USA) surface analyser. The nanoparticle powder was degassed overnight at 120 °C before analysis. The surface area was determined through the Brunauer-Emmett-Teller (BET) model[175] using the adsorption isotherm data at P/P^0 from 0.1 to 0.6. The average pore diameter was calculated using the adsorption data applying the Barrett-Joyner-Halenda (BJH)[176] model.

2.2.5.6 Electron microscopy

The MSN were visualized by transmission and scanning electron microscopy (TEM and SEM) before and after the surface functionalization. For TEM, MSN suspension in ethanol was dropped into holey carbon coated 200 mesh copper grids and subsequently left to dry at room temperature. The images were acquired in a JEOL 2100 microscope operating at 200 kV. For SEM analysis, the MSN suspension was dropped in a metal stub and left to dry at room temperature. After that, the samples were coated with a thin layer of gold/palladium under vacuum to increase image contrast, minimize damage to the samples and image artefacts. The secondary electron images were acquired in a Zeiss ULTRA plus instrument operating at 3 kV.

The crosslinked hydrogel was visualized through Cryo-SEM in its 'natural' hydrated state. The hydrogel piece was cooled in liquid nitrogen and transferred under vacuum into the SEM chamber. The surface of the hydrogel piece was cut to

reveal the internal structure and was imaged in the vacuum chamber at a low temperature.

2.2.6 Release studies

2.2.6.1 Drug release from MSN

The loaded nanoparticles were suspended in distilled water or PBS pH 7.4 (with 0.5% Tween-80 for PTX release) and kept under stirring. At predetermined time points the sample was centrifuged and the supernatant was collected for analysis.

The stimulus was added at t = 30 min to the drug-loaded nanoparticles and at t = 60 min to the Safranin-O loaded nanoparticles. After that, PBS pH 7.4 with 10 mM GSH was replaced at each time to keep the GSH concentration constant.

Uncapped nanoparticles and nanoparticles in PBS pH 7.4 without GSH were used as positive and negative controls, respectively. Safranin-O release was monitored by UV spectrophotometry at 520 nm and TMZ or PTX release was monitored by HPLC as previously described.

2.2.6.2 MSN incorporation and release from gels

The thermoresponsive hydrogel Pluronic F-127 was prepared by dissolving the polymer in water for a final concentration of 20%w/v. The thermoresponsive Liquid Polymer (LQP4) was used as received from InGell Labs company. The hydrogels (50 μL) were mixed with 1 mg MSN or MSN-PEG. After that, the mixture was placed in a 24-well cell insert and into the cell plate at 37 °C to form the gel.

The crosslinked hydrogel, kindly provided by Dr. Yang Shi, Group Leader in the Polymeric Nanomedicines Group at Aachen University in Germany, was prepared by dissolving the polymer in water for a final concentration of 4%w/v after mixing with the crosslinker. After complete hydrogel solubilisation, 25 μL were added to 1 mg MSN or MSN-PEG. The crosslinker solution was prepared separately in water (24.3 mg/mL) and mixed with the hydrogel/nanoparticle solution to give a 100% crosslinked gel. The mixture (50 μL) was added to a 1 mL syringe tip as a mould to have the final hydrogel piece used in the release.

To start the release, 0.2 mL PBS was gently added to the insert containing the material (hydrogel + MSN or MSN-PEG) and 1 mL was added to the bottom of

the well. At predetermined time points, 1mL PBS was collected from the bottom of the well and the same amount of fresh PBS was added back.

The collected sample was kept in the freezer until the concentration of nanoparticles was measured by Nanoparticle Tracking analysis (NTA) using a Nanosight NS300. The aliquots from the gel release were placed in the Nanosight directly or after dilution when needed, and a laser source was applied to visualize the particles. Concentrations ranging 10^6-10^9 particles/mL of particles with diameters between 10 and 2000 nm can be visualized by this technique. Each sample was measured three times and a mean percentage release ± Standard Error of the Mean (SEM) is reported. A detailed description of the percentage calculation from the value measured on the NTA is available on **Appendix 3.**

2.2.6.3 Drug incorporation and release from gels

The thermoresponsive gels Pluronic F-127 and LQP4 were prepared as described in the previous section. The gels (50 µL) were mixed with TMZ (11 mg), BCNU (2 mg) or PTX (2 mg) in an Eppendorf tube and the mixture was incubated at 37 °C for 15 min to form the gel. After that, 1.7 mL of PBS or PBS + 0.5% Tween 80 (for PTX release) pH 7.4 were gently added to the tube to avoid the disruption of the gel, and the tube was placed in an incubator at 37 °C to start the release study. At predetermined time, 850 µL of the supernatant were collected from the tube containing the sample and the same amount of fresh PBS was added to the tube. The collected 850 µL were kept in the freezer until analysis.

The crosslinked hydrogel was prepared as described in the previous section and the same amount of drug was incorporated into the gel as in the thermoresponsive materials. The drug release assay was performed in PBS pH 7.4 (with 0.5% Tween 80 for PTX release) at 37 °C in 30-35 mL of release media. At each time point, 1 mL aliquot was taken and 1 mL fresh PBS was added back. The aliquots were stored at -20 °C until HPLC analysis as previously described.

Drug release from the GlioGel final formulation was also tested *in vitro*. The gel was prepared as described for the *in vivo* experiment (section 2.2.12.4) and put into PBS pH 7.4. At predetermined time points 1 mL aliquot was taken and fresh PBS was added. The TMZ release from GlioGel was measured through HPLC.

A mathematical fitting was performed for all hydrogel releases (drugs and MSN) to evaluate the main mechanisms of release: Zero-order, First-order, Higuchi and Korsmeyer-Peppas models **(Appendix 2 and Appendix 4).**

2.2.7 Nanoparticle stability

Nanoparticle stability was studied by resuspending the material at 1 mg/mL in PBS pH 7.4 and incubating at 37 °C. At pre-determined time points, aliquots were withdrawn for the preparation of TEM grids, PXRD or porosimeter analysis. All the analyses were performed as described before for the nanoparticle characterization.

2.2.8 Hydrogel degradation

The hydrogels were prepared as described previously and the dry weights were recorded. For Pluronic F-127 and LQP4, the weight of tube + gel was used. The gels were incubated in PBS pH 7.4 at 37 °C and at pre-determined time points the liquid was removed and the material weight was recorded. The weight change over time was plotted.

2.2.9 Hydrogel rheology

The rheological properties of hydrogels were assessed using oscillatory measurements on AR-2000 Rheometer (TA instruments) coupled with a parallel plate- (diameter 40 mm or 8 mm).

The thermoresponsiveness of the Pluronic F-127 gel was assessed as a function of temperature, with storage modulus (G') being used as an indicator of gel structure. The temperature was increased by 1 °C/min using a temperature sweep mode extended between 20 and 38 °C at a frequency of 0.1 Hz.

The viscoelastic properties of CX gel were measured at 25 °C in the pre-formed gel at 1 Hz frequency and the storage modulus G' and loss modulus G'' were measured as a function of the stress. For the Pluronic F-127, the same analysis was performed on pre-formed gels at 37 °C and 0.15 Hz frequency.

2.2.10 *In vitro* 2D cell assays

2.2.10.1 Cell culture conditions

U-87 human glioblastoma cell line was cultured in Minimum Essential Medium Eagle (MEM) (Sigma-Aldrich, Ireland) supplemented with 10% FBS and 1% L-glutamine under humidified atmosphere of 5% CO_2 at 37 °C.

Primary rat neurons were cultured in Neurobasal media (NBM) supplemented with 1% (v/v) penicillin-streptomycin, 0.1% (v/v) fungizone, 1% (v/v) glutaMax and 1% B-27 (referred to as complete NBM (cNBM)). The primary culture was performed by Yuliia Rakovets, from Prof. Harkin's laboratory in the School of Pharmacy and Pharmaceutical Sciences (Trinity College Dublin, Dublin, Ireland).

Prior to cell culture, glass coverslips (13 mm) were placed in the wells of a 24-well plate followed by sterilisation under UV light for 60 min in a laminar flow hood. The coverslips were coated by placing a drop of Poly-D-lysine solution (75 µL; 50 µg/mL; filter-sterilised) on the centre of each coverslip and incubating for 45 min. This facilitates the adhesion of neurons to the coverslip. After coating, the coverslips were washed twice with sterile tissue culture grade water and left to dry fully for approximately 2 h in a laminar flow hood. Any remaining droplets were removed by aspiration. Once dried, plates were either directly used for the cell culture or parafilmed and stored in the fridge for up to two weeks or at -80 °C for up to two months. Primary cortical neuronal cultures were prepared as previously described[177,178] from postnatal day 1-2 (P1-2) neonate Wistar rat pups under sterile conditions in a laminar flow hood. Neonates were decapitated, the skin was cut along the midline, and finally the skull was also cut along the midline. The brain was carefully removed from the skull and placed onto a sterile Petri dish. The evident blood vessels, surrounding meninges, olfactory bulbs and the cerebellum were removed from the brain and the cortical tissue from both hemispheres was placed in a drop of pre-warmed cNBM. The cortical tissue was cut using a scalpel and transferred into 5 mL of Trypsin-EDTA for 4 min at 37 °C. Following this, 5 mL of DMEM was added to deactivate trypsin and centrifuged for 3 min at 2000 rpm at 21 °C. The cell pellet was resuspended in 5 mL DMEM, passed through a cell strainer with a 40 µm filter and centrifuged at 2000 rpm for 4 min at 21 °C. The pellet was then resuspended in 1 mL of pre-warmed cNBM and gently triturated until a homogenous cellular suspension was obtained. The resulting neuronal cell

suspension was counted using the trypan blue exclusion method. For all experiments, 3 x 10^4 cells were seeded and incubated at 37 °C in a humidified, 5% CO_2 atmosphere for a minimum of 2 h to allow adherence of neurons before being topped up with 200 µL of pre-warmed cNBM. Neurons were left to grow on the coverslip for at least 14 days to mature.

2.2.10.2 Half maximal inhibitory concentration (IC50)

U-87 cells were seeded on 24-well plates in an initial density of 25000 cells/well and left to attach for 24 h. Subsequently, the cells were treated with increasing concentrations of TMZ or PTX. The controls correspond to cells growing without any treatment or in the presence of 1% DMSO (amount present in each condition due to drug solubilization on this solvent).

After the incubation period (72 h), the cell viability was evaluated using the Cell Counting Kit-8 (CCK-8) (Dojindo, United Kingdom). The reagent was directly mixed with fresh media and put in contact with the cells for 1 h at 37 °C. After that, the absorbance at 450 nm was read. The viability was plotted as percentage (%) of absorbance normalized for the control. The IC50 was calculated by plotting log[drug] x % viability and fitting the curve with a non-linear regression function and variable slope on GraphPad Prism 5.

2.2.10.3 Cell viability

The cell viability was determined using a colorimetric assay kit through UV measurement to quantify the number of live cells. U-87 cells were seeded on 24-well plates in an initial density of 25,000 cells/well and left to attach for 24 h. Subsequently, the cells were treated with increasing concentrations of empty MSN or MSN-PEG, MSN loaded with TMZ or PTX (MSN-TMZ and MSN-PTX), MSN loaded with PTX and functionalized with PEG (MSN-PTX-PEG) and the hydrogels (50 µL).

Primary neurons were cultured as described previously and 3 x 10^4 cells were seeded for the viability tests. Rat neurons were treated with 50 µL hydrogels and fixed concentrations of nanoparticles (250 µg/mL MSN or MSN-PEG and 875 µg/mL MSN-PEG).

For the hydrogel treatment, the material was placed in a cell insert and 0.2 mL cell media was gently added on top (in the insert) and 1 mL media was added

to the bottom of the well. The nanoparticles were mixed with media in the corresponding concentration and dispersed using an ultrasonic bath for 2 min. After that, the media containing the nanoparticles was added to the cells.

The same cells growing without any treatment were used as control. After the incubation period (72 h) the cell viability was evaluated using the Cell Counting Kit-8 (CCK-8) (Dojindo, United Kingdom). The reagent was directly mixed with fresh media and put in contact with the cells for 1 h at 37 °C. After that, the absorbance at 450 nm was read. The viability was plotted as percentage (%) of absorbance normalized for the control.

2.2.10.4 Flow cytometer analysis

To monitor the nanoparticle internalization by U-87 glioblastoma cells, fluorescently labelled nanoparticles were used. The cells were seeded on 6-well plates in an initial density of 50,000 cells/well and left to attach for 24 h. Subsequently, the cells were treated with 50 μg/mL MSN-FITC or MSN-FITC-PEG. The same cells growing without any treatment were used as control. After 24 h, the medium was removed, and the cells were harvested with trypsin by centrifugation and then resuspended in PBS. The single cell suspension was analysed in a BD Accuri™ C6 (BD Biosciences) before and after the addition of 50 μL trypan blue, as a FITC quenching agent[179,180]. Three experiments were performed in triplicates and 10,000 events per sample were recorded. The percentage of fluorescent cells before and after trypan blue addition was plotted and analysed in GraphPad Prism 5.

2.2.10.5 Confocal Fluorescence Microscopy

The nanoparticle internalization was further analysed by confocal microscopy. The cells were seeded on μ-Slide 8 well chambered coverslip (Ibidi) in an initial density of 12000 cells/well and left to attach for 24 h. Subsequently, the cells were treated with 50 μg/mL MSN-FITC or MSN-FITC-PEG. The same cells growing without any treatment were used as control. After 24 h, the non-internalized nanoparticles were removed, the cells were fixed with 10% formalin and stained with Phalloidin (actin cytoskeleton) and Hoechst (nucleus), then fresh medium was added and the cells were imaged at a Leica SP8 confocal inverted microscope (Leica Microsystems).

2.2.10.6 Neuron staining with MAP2 for the Sholl analysis

Neurons were treated with MSN (250 µg/mL), MSN-PEG (875 µg/mL), Pluronic F-127 hydrogel (50 µL) and crosslinked hydrogels (50 µL). After 72 h, the medium was removed and the cells were fixed in 4% paraformaldehyde (PFA) in PBS for 20 min at room temperature, followed by 3 washing cycles with PBS. After that, non-specific interactions were blocked at room temperature for 2 h using a blocking buffer (2% normal goat serum (NGS), and 2% BSA in PBS containing 0.1% Triton-X (PBS-T). Then, 200µl of primary antibody anti-microtubule associated protein 2 (MAP2, [mouse; M1406]) in blocking buffer (1:1000) were added and left overnight at 4 °C. The primary antibody was removed, and the cells were washed three times in PBS. Secondary antibody Alexa Fluor 546 [goat anti-mouse; A11003] in PBS-T (1:500) was added and left for 2 h at room temperature protected from light. Finally, cells were washed three times with PBS and glass coverslips were removed from plates and mounted onto microscope glass slides for imaging and Sholl analysis.

The coverslips were mounted onto microscope glass slides (1-1.2 mm) using Vectashield fluorescent mounting media containing DAPI (4´,6-Diamidino-2-phenylindole dihydrochloride) and kept in the dark at 4 °C. The slides were visualised using an AxioImager Z1 epifluorescent microscope with a Zeiss AxioCam HR camera and AxioVision 4.8.2 software at 20X magnification. In order to be included in the analysis, the slides had to display a healthy neuronal network throughout the visual field. Seven individual images were taken per coverslip and 6 coverslips per experimental condition were typically collected for analysis. Where possible, experimenter was blind to treatment, and cells were selected in the DAPI channel to avoid bias.

2.2.10.7 Sholl analysis

Sholl analysis is a widely used method for quantifying and graphically representing various parameters of neuronal complexity following treatment. The simplified version of this protocol (Fast Sholl) was adapted from Sholl[181] and Gutierrez and Davies[182]. This analysis involves placing 25 concentric rings with regular 10 µm radial increments around the neuron and quantifying the number of neurites intersecting each ring using the following equation: $x_i = x_{i-1} + b_i - t_i$, where "$x_i$" is the number of neurites for the "ith" segment, "b_i" is the number of branches

occurring in the "ith" segment and "ti" the number of terminations in that segment. This equation was programmed into Matrix Laboratory (MATLAB, R2012b) to follow a semi-automated procedure. The number of neuritic branches, relative neuritic length, number of primary neurites and Sholl profile were determined for each neuron. The Sholl profile represents the number of neuritic branches at each radial distance from the cell soma. These analyses were performed by Yuliia Rakovets.

2.2.11 *In vitro* 3D spheroids assays

U-87 spheroids were grown *in vitro* using a liquid overlay system on the Nunclon Sphera low-attachment surface 96-well plate (ThermoFisher Scientific). Different initial amounts of cells (250, 500 and 1000 cells/well) were compared in the analysis of spheroids growth in the presence and absence of 1% DMSO. The spheroids were imaged at days 1,2,3,4,5 and 7 using an AxioCamERc5s coupled to Nikon Diaphot 300 Inverted Phase Contrast Microscope and using Zeiss Zen 3.1 software. The spheroid growth was monitored through diameter measurement using ImageJ software and the growth rate was calculated using the following equation:

$$Growth\ rate\ (\%) = \frac{(final\ diameter\ -\ initial\ diameter)}{initial\ diameter} \times 100$$

The 1000-cell spheroids growing for 2 days or 4 days were treated with different concentrations of free drug, MSN-PEG, MSN-PTX-PEG and a mix of free drug + MSN-PTX-PEG for 72 h. The spheroids viability was measured by Acid Phosphatase assay[183,184] and plotted as percentage (%) of absorbance at 405 nm normalized for the control (spheroids growing without treatment).

The spheroids diameter was monitored at day 2 or 4 (before treatment) and day 5 or 7 (after treatment). The growth ratio was calculated using the following equation:

$$Growth\ ratio = \frac{diameter\ (t + 3)}{diameter\ (t)}$$

Where *t* is the time of growth in days in which the spheroid was measured.

2.2.11.1 Nanoparticle penetration on 3D spheroids

The nanoparticle penetration on 3D spheroids was analysed by confocal microscopy. The 1000-cell spheroids were grown on the Nunclon Sphera low-attachment surface 96-well plate (ThermoFisher Scientific) for 2 days or 4 days. Subsequently, the spheroids were treated with 100 µg/mL MSN-FITC or MSN-FITC-PEG. After 24 h and 72 h, the spheroids were fixed with 10% formalin and stained with Phalloidin (actin cytoskeleton) and Hoechst (nucleus). Then, 15 to 20 image stacks (5 µm) of each spheroid were taken at a Leica SP8 confocal inverted microscope.

The area of nanoparticles in the spheroids and the total area of the spheroid were estimated using ImageJ software. Then, the proportion of nanoparticles area in relation to the spheroid total area was calculated and plotted as mean ± SEM.

2.2.12 *In vivo* studies

2.2.12.1 Animals

The experimental protocols employed in this study were approved by the local Animal Research Ethics Committee and Health Products Regulatory Authority (HPRA) Ireland, in accordance with the guidelines of the Animal Ethics Committee Trinity College Dublin and the European Council Directive 1986 (86/806/EEC). The use and treatment of mice throughout the study was performed within the Three R's guidelines for ethical animal testing. The Three R's: Replacement, Reduction and Refinement, first described by Russell and Burch[185] and also by Tannenbaum and Bennett[186] aims to improve animal welfare during scientific studies.

The mice strain used for the establishment of the GBM tumour model was the CIEA NOG mouse® developed by Mamoru Ito of the Central Institute for Experimental Animals (CIEA) in Japan. The CIEA NOG mice are an excellent system for tumour engraftment since they have impaired T and B cell lymphocyte development. Moreover, the CIEA NOG background additionally results in deficient natural killer (NK) cell function. Thus, it is a refined strain to grow a xenograft tumour model.

Female mice (22 ± 3 g) were housed in groups of 4 and kept under standard housing conditions at a constant temperature (20 ± 2 °C) and standard lighting conditions (12 h light: 12 h dark cycle). Food and water were available *ad libitum.*

2.2.12.2 GBM tumour model

Mice were anesthetized using 2% isoflurane and maintained in an anaesthetised state at 1.5%. Afterwards, they were transferred to a stereotactic frame under anaesthesia with 1.5% isoflurane. The scalp hair at the surgical site was removed with a depilatory cream and the skin was treated with an alcoholic solution. An incision along the midline was made in the right frontal lobe and a small hole was drilled to expose the brain, 0.5 mm posterior and 2.5 mm lateral to the bregma. $3x10^4$ U-87 GBM cancer cells in complete cell culture media (2.5 μL) were injected into the brain at a depth of 1.5 mm. After complete injection over 5 min, the needle was kept in place for 5min and then removed to avoid cells going back to the needle. The wound was closed with 4/0 interrupted simple sutures and cleaned with alcohol and iodine. During the procedure the mouse body temperature was monitored and maintained at 37–38.0 °C using a heating pad.

2.2.12.3 Tumour growth monitored by Magnetic Resonance Imaging (MRI)

All magnetic resonance imaging was carried out on a dedicated rodent Bruker Biospec system (Bruker Biospin, Germany) with a 7 Tesla magnet and a 30 cm diameter bore, equipped with a 20 cm actively shielded gradient system. A pair of actively decoupled 12 cm Helmholtz transmit, and 3 cm surface quadrature receive coils (Bruker Biospin, Germany) were used for signal transmission and reception respectively.

The animals were initially anaesthetized using 2% isoflurane and maintained in an anaesthetised state at 1.5%. They were subsequently placed onto a custom-built fiberglass cradle and temperature was maintained using a warming surface that was controlled by a water pump-driven temperature regulator (SA Instruments Inc., Stony Brook, NY, USA). A mechanical ventilator (Ugo Basile, Comerio, VA, Italy) was used to deliver an adequate flow of gas to the facemask and the respiration signal was monitored using customised hardware and software (SA Instruments Inc., Stony Brook, NY, USA). Anaesthetic depth was controlled by maintaining a respiration rate between 60 and 75 breaths per minute.

The animal's brain was scanned at days 14, 21 and 26 after cell injection to monitor the tumour growth. Coronal brain images were acquired successively using a two-dimensional multi slice T1-weighted FLASH, 10 averages with TE = 2.461 ms, TR = 326.837 ms, a flip angle of 60°, field of view of 2 cm × 2 cm (voxel size: 0.156

x 0.156 x 0.5 mm^3). For each animal, 30 consecutive coronal sections of 0.5 mm thickness were acquired (interslice distance of 0.55 mm). The total acquisition time was 4 min 41s 79 ms. Images were reconstructed with Paravision 6.0 software (Bruker Biospin, Germany).

The tumour volumes were calculated using MIPAV software by manually drawing the region of interest (ROI). The curve was fitted with an exponential growth equation.

2.2.12.4 Resection surgery and hydrogel implantation

The presence and size of tumour was evaluated by MRI at day 19 after tumour cell injection. The resection surgery was performed on day 23 and the procedure followed a previously reported protocol[187] with some adaptations. Briefly, a mouse was anesthetized using 2% isoflurane and maintained in an anaesthetised state at 1.5%. Afterwards, they were transferred in a stereotactic frame under anaesthesia with 1.5% isoflurane. An incision on the same directions used in the injection was made exposing the skull. A hole was drilled and a vacuum pump was used to remove the tumour. After the resection, the animals were divided in two groups receiving: 1) a piece of hydrogel only (4-5 μL – n=5); 2) a piece of hydrogel (4-5 μL) containing the dose of 0.6 mg/kg free TMZ and 0.3 mg/kg PTX (loaded on MSN-PEG) (n=4). To repair the cranial defect, bone wax was placed on top and the skin was closed with 4/0 interrupted simple sutures and cleaned with alcohol and iodine.

2.2.12.5 Animal welfare

Animals were monitored daily for any sign of pain and/or distress during the experiment period. Each animal was closely monitored following surgery to detect immediate adverse effects and to ensure full recovery after anaesthesia.

Additionally, they were monitored twice a day for 3 days after surgery (cell injection and tumour resection). We used the grimace score sheet to evaluate specifically their suffering.

All daily monitoring, scoring, weights, supportive care and treatment were recorded in score sheets **(Appendix 5)**. In circumstances where profound discomfort is observed, or when a mouse has exceeded 20% weight loss, the animal is humanely euthanized by CO_2 inhalation.

2.2.12.6 Histological analysis

Animal brain was harvested when the mouse died or reached a humane endpoint and was euthanized, or 5 weeks after the resection surgery to finalize the experiment. The brain was fixed in 4% PFA at 4 °C for approximately 24 h, or until they sink and dehydrated in 20% sucrose in PBS at 4 °C until sectioning in a vibratome. Slices between 50 – 90 µm were cut, mounted in slides and stained with Haematoxylin/Eosin. The slides were imaged in an Olympus BX51 upright microscope.

2.2.13 Statistical analysis

All experiments were done in triplicates (3 independent experiments) and the data in the thesis were plotted as mean ± Standard Error of the Mean (SEM). The results were analysed using GraphPad Prism 5. Analyses of variance (ANOVA) followed by Tukey's post-test (comparing all treatment groups) or Dunnett's post-test (treatment groups against the controls) were performed where relevant. Data were considered significant when $P < 0.05$ (*), $P < 0.01$ (**) or $P < 0.001$ (***).

For the *in vivo* pilot study, the Kaplan-Meier survival curves were analysed with a log rank test (Mantel-Cox test). The multiple comparison was corrected by the Bonferroni threshold with significance level set at 0.05. The tumour volume after resection (recurrence) was compared through a Mann Whitney test.

The number of animals selected for the pilot study was based on Workman *et al.*[188], which suggests that the number of animals per group should be between 5 and 10 for a pre-clinical pilot study.

CHAPTER 3: MESOPOROUS SILICA NANOPARTICLES AS STIMULI RESPONSIVE DELIVERY SYSTEMS OF CHEMOTHERAPEUTIC DRUGS

3.1 Introduction

Nanotechnology has been investigated to improve conventional therapeutic and diagnostic strategies in cancer. Different types of nanocarriers such as liposomes, polymeric nanoparticles and inorganic nanoparticles **(Figure 3.1)** are being developed for cancer treatment [189–191].
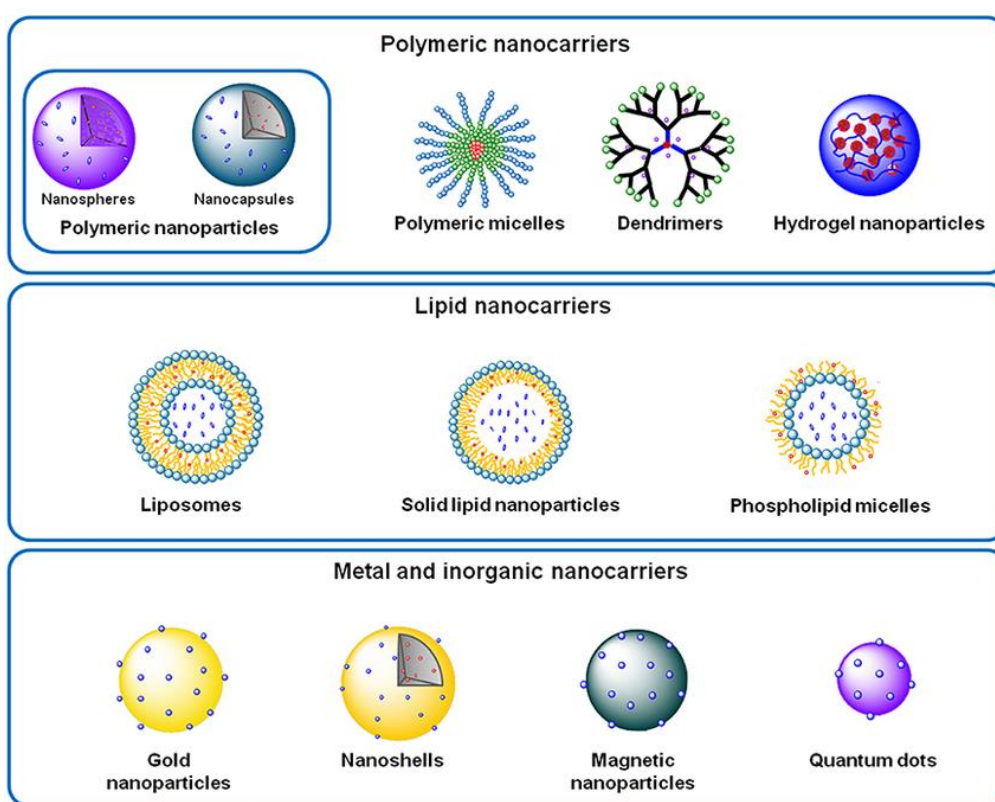
Figure 3.1: Types of nanoplatforms. Reproduced from ref[192].

Among the inorganic nanocarriers, the M41S family of mesoporous silica nanoparticles (MSN) includes various types of mesoporous materials named after Mobil Composition of Matter (MCM), particularly MCM-48, MCM-50 and MCM-41. All M41S mesoporous materials have ordered and uniform pores. However, slight differences in the synthesis process will change the material characteristics. MCM-41 is the nanoparticle used in this work and it is hexagonally ordered, while MCM-48 is cubic and MCM-50 is lamellar **(Figure 3.2)**.

Figure 3.2: Schematic diagram of the M41S materials, MCM-50 (layered), MCM-41 (hexagonal) and MCM-48 (Cubic). Reproduced from ref [193].

MCM-41 have some advantageous characteristics for the development of nanodelivery systems including high surface area and porosity, thermal stability and high loading capacity[194]. Therefore, these nanoparticles can be loaded with different types of drugs and surface-modified with many different molecules, such as peptides, proteins, antibodies or nucleic acids[72–76] to form a responsive drug delivery and diagnostic system[195,196].

Different nanosystems with theranostics functionalities composed of MSN have been proposed for GBM treatment[77]. For example, MSN loaded with zero-valent Fe were developed to act both as a treatment and imaging tool against GBM[197]. The nanoparticles could be monitored by MRI and it was shown that they crossed the BBB and accumulated into the brain of rats bearing C6 orthotopic tumours inducing oxidative stress with consequent cellular toxicity.

The accumulation of MSN in tumour tissue can also be explored to stimulate the development of radiosensitizer nanosystems such as the folate-VPA-MSN, which is targeted to cancer cell through the folate receptor (FR) and is loaded with the radiosensitizer valproic acid (VPA) [198]. This proposed dual functional MSN improved the radiation toxicity in cells while decreasing the radiosensitizer dose needed, being beneficial to decrease potential damage to healthy tissue.

In some strategies to accumulate into tumour tissue, the nanosystem needs to cross BBB and this is another functionality that can be built and improved in MSN nanoparticles. For instance, the surface modification of MSN with RGD peptides increased the penetration of the nanoparticle through a BBB co-culture model *in vitro* and this was accompanied by an increase in toxicity of a novel selenium compound against U-87 cells[199]. Importantly, the effect of the modified MSN was

targeted to cells with high integrin expression thus avoiding side effects on normal cells.

Combining theranostics with targeting is another interesting approach. Heggannavar et al.[200] proposed a magnetic MSN loaded with doxorubicin, coated with Pluronic F-127 and conjugated with transferrin (Tf) to increase BBB penetration and target cancer cells. The developed MSN showed enhanced BBB permeability after magnetic field application and anti-cancer effect compared to free drug. A Vascular Endothelial Growth Factor (VEGF)-MSN loaded with sunitinib, an anti-VEGFR drug, and surface functionalized with ^{64}Cu radioisotope was developed and tested for simultaneous imaging and treatment of U-87 tumour bearing mice. The targeted nanoparticles showed 3 times higher tumour accumulation when compared to non-targeted nanoparticles[201].

MSNs can also be designed to increase the penetration in certain tissues[81], to be hidden from the immune system[202] and also to be responsive to different types of stimuli such as environmental pH[79,80] and redox conditions[203]. The responsiveness to different environment conditions is an advantage to strategically close the pores and entrap a drug until a stimulus is present and to target the therapy to specific sites. Specifically, redox responsive nanomaterials, including MSN, have been reported by several groups. Overall, these studies highlight the exploration of cell redox characteristics as a tool for more effective therapies. For instance, the specific delivery of drugs inside the cells using the reductive stimulus was proposed as a way to overcome cell drug resistance[204].

Other examples include a poly(ethylene glycol)-b-poly(L-lysine)-b-poly(L-phenylalanine) (PEG-b-PLysb-PPha) core-shell micelle with a crosslinked-disulphide PEG on the outer surface, which releases the cargo and exerts the toxicity effect in the presence of glutathione (GSH)[205]. Another (PEG-b-PLysb-PPha) copolymeric micelle in which the PEG was attached by a disulphide bond on the outer surface was successfully internalized into HeLa cells delivering the drug while minimal amounts were lost in the outside environment[206].

A polymersome composed of poly(ethylene glycol)-b-poly(lysine)-b-poly(caprolactone) with a disulphide link between the PCL chain and the PEG-Plys chain was proposed as a dual-drug delivery system[207]. Camptothecin (CPT) was incorporated into the membrane of the polymersome while doxorubicin (DOX) was encapsulated in the core. The drug delivery system releases both drugs in the presence of a reductive environment *in vitro* and inside cancer cells.

Besides polymeric micelles, a model drug delivery system was proposed using gold nanoparticles linked through a disulphide bond to a fluorescent dye[208]. This proposed system releases the attached molecule (a drug or a dye) when in the presence of GSH in high concentrations characteristic of the cell cytoplasm. Following this same idea, the delivery of cysteine (Cys) from mesoporous silica nanoparticles was proposed using a disulphide bond to link Cys on the surface of MSN[209]. The detachment of Cys from the nanoparticles was shown *in vitro* using several reductive agents such as nicotinamide adenine dinucleotide + hydrogen (NADH), dithiothreitol (DTT), dihydrolipoic acid (DHLA) and GSH, showing similar potency to break the link and release Cys. Importantly, the internalization of the nanoparticles and the release in the cytoplasm of HeLa cells was shown by confocal fluorescence microscopy.

Therefore, using the concept of PEG-capped pores proposed by Giménez *et al.*[170], my work aims to expand the application of this capped system by analysing the loading and release of different chemotherapeutics, and proposing the combination of these nanoparticles with a hydrogel to build a new drug delivery formulation for GBM (GlioGel). Specifically, in this chapter we show the synthesis and characterization of MSN, its loading with a dye model molecule and two different chemotherapeutic drugs (temozolomide and paclitaxel) and the surface functionalization of the nanoparticles with the redox-responsive moiety to have a preferential release of the chemotherapeutic drug from the mesoporous matrix in the intracellular environment. The *in vitro* release and cytotoxic effect of these nanoparticles on a GBM cancer cell are shown and discussed. In addition, the nanoparticle stability was studied in order to correlate and understand its influence on the proposed application of the material. Finally, the effect of the nanomaterial on neurons was also evaluated to give insights on the effect on healthy brain.

3.2 Results and discussion

3.2.1 MSN synthesis and characterization

Mesoporous silica nanoparticles (MCM-41 type) synthesis is a process well described in the literature and very reproducible[194]. Using the liquid crystal template method and keeping constant parameters such as temperature, reaction time, type of surfactant and extraction process, it is possible to obtain very similar batches of nanoparticles with the desired characteristics. During this work, reproducible and

comparable batches of MSN were synthesized and used in the experiments. Thus, the characterization showed in this section corresponds to a representative nanoparticle batch and the description includes the range of values measured for the batches.

Several techniques were used to check and perform a quality control of the nanoparticles after synthesis. Firstly, the surfactant was removed from the pores by an acid extraction. The extraction process was chosen over calcination to avoid additional silica condensation on the surface, leaving a high number of silanol groups to react in the functionalization step. To ensure that this procedure was effective, a thermogravimetric analysis (TGA) was performed **(Figure 3.3A)**. From TGA curves, the weight loss until 100 °C corresponds to the loss of water from the material, between 100 °C and 500 °C the surfactant (CTABr) is burned, and from then up to 600 °C we can observe the condensation of silanol groups on the surface of the particles with concomitant water loss which causes a very small change in weight. Usually, the proportion of surfactant in the material before the extraction ranges from 35% to 48%, and after the procedure, it decreased significantly to around 3% to 6% which is considered acceptable as a residual content.

The removal of the surfactant is a critical process in MSNs synthesis because it prepares the material for the subsequent experiments in which the nanoparticle pores will be loaded with the molecule of interest. Moreover, the presence of high amounts of surfactant can impact on cell experiments by causing undesired cell toxicity.

The surface area and pore size of MSNs are important characteristics of these materials that give them pronounced advantages over other materials in drug delivery applications. The high loading capacity and the possibility to tune the size of the pores during the synthesis make these particles very useful for the loading of different drugs ranging from small molecules to nucleic acids and antibodies.

The MSNs surface area was analysed by N_2 adsorption-desorption porosimetry. In this technique, N_2 is adsorbed inside the nanoparticle pores and is subsequently taken out through a consecutive increase and decrease in the gas pressure. This is described by an adsorption/desorption isotherm shown in **Figure 3.3B**. At low relative pressures, N_2 is adsorbed in the micropores (under 2 nm), while between 0.1 and 0.6 relative pressures the mesopores (2-50 nm) are filled[194]. A surface area ranging from 887 to 1575 m^2/g and an average pore diameter ranging from 2.1 to 2.7 nm were calculated for the different batches using the adsorption

isotherm. Moreover, the nanoparticles presented a narrow pore size distribution **(Figure 3.3B)**.

MSNs are amorphous materials that show some ordered arrangements in the pore organization. This important characteristic can be observed through powder X-ray diffraction analysis (PXRD). Due to their amorphous nature, MSNs do not show any peaks at high diffraction angles. The peaks found at low diffraction correspond to the pore organization[194].

The pores in MCM-41 mesoporous silica nanoparticles are periodically arranged in a hexagonal structure and the distance between the pores can be estimated from the X-ray diffraction peaks **(Figure 3.3C)**. Four peaks were observed at low angle for the material corresponding to the pore planes of the mesoporous silica nanoparticle (100), (110), (200) and (210) at 2.1°, 3.6°, 4.2° and 5.7° respectively. Finally, the spherical morphology of these nanoparticles was confirmed by scanning electron microscopy **(Figure 3.3D)**.
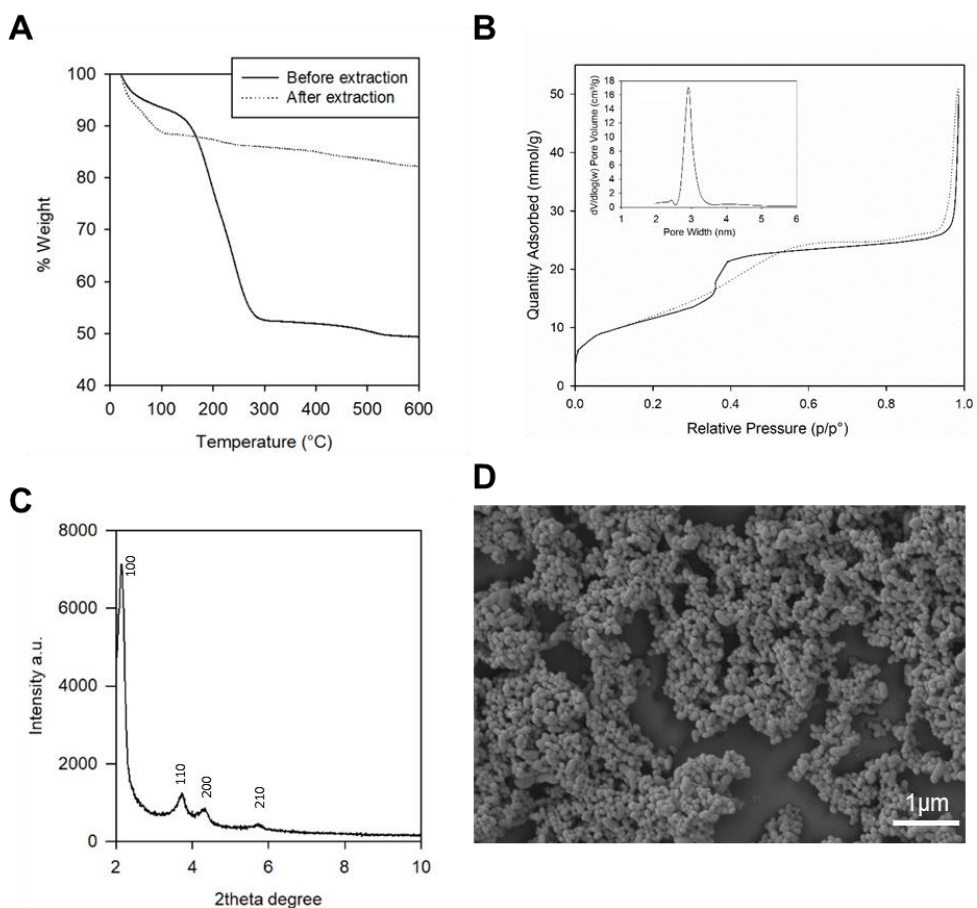
Figure 3.3: MSN structural and textural characterization. The nanoparticles were characterized to determine the hexagonal pore organization, pore volume and size, surface area and morphology. **A-** Thermogravimetric analysis before and after surfactant extraction. **B-** N_2 adsorption-desorption porosimetry isotherm and pore size distribution (inset). **C-** Powder X-ray diffraction pattern of MSN at low angle. **D-** Representative scanning electron microscopy image of the nanoparticles.

3.2.2 MSN surface functionalization

After the synthesis and surfactant template extraction, the MSNs were loaded with either safranin-O, a model dye molecule, or chemotherapeutic drugs (temozolomide or paclitaxel) **(Figure 3.4)**.
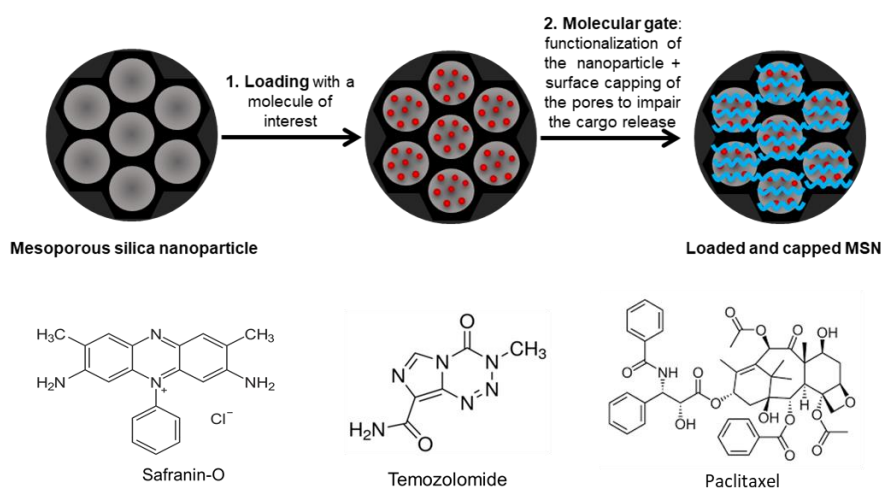
Figure 3.4: MSN loading and surface functionalization process. The nanoparticles were loaded with either a dye model molecule (Safranin O) or temozolomide or paclitaxel. Then, the surface of the nanoparticles was functionalized with PEG, which was attached through a disulphide bond building a redox-responsive molecular gate.

In order to build a redox-responsive gate system on the MSN surface, the loaded nanoparticles were functionalized with PEG through a disulphide bond[170]. For this purpose, a series of chemical reactions were used starting by the addition of 3-mercaptopropyl trimethoxy-silane, which interacts with the silanol groups on the surface of the nanoparticle through the silicon atom, leaving a sulfhydryl group on the surface of the material. Then, the 2,2´-dipyridyl disulfide (or aldithriol) was coupled to the nanoparticle surface through a disulphide bond (S-S). Finally, the polyethylene glycol methyl ether thiol was attached to the particle surface through a thiol-disulphide exchange reaction[210] **(Figure 3.5)**.
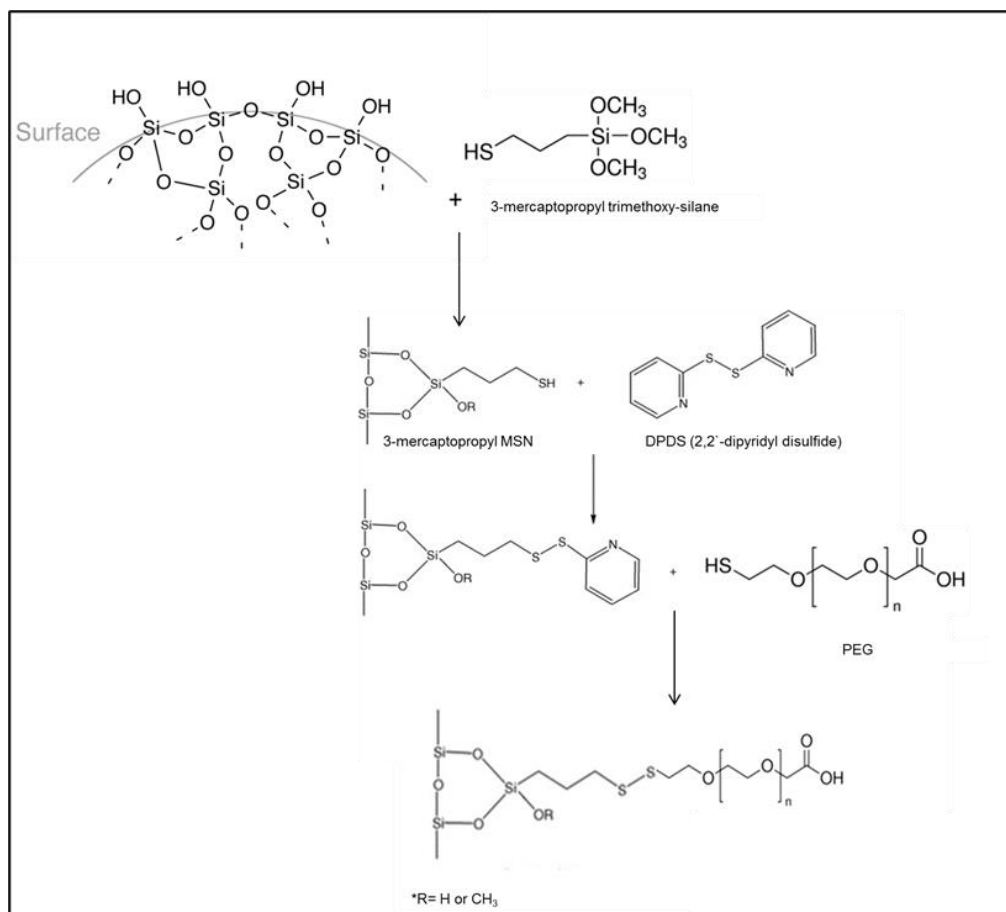
Figure 3.5: Chemical reactions for the MSN surface functionalization with PEG to block the nanoparticle pores.

This PEG-based surface functionalization was chosen for different reasons. Firstly, the disulphide bond attachment on the surface allows the use of reductive stimulus for the nanoparticle cargo release. In addition, differences in reductive environment conditions can be explored in cell compartments and in different cells, e.g. differences between normal cells and tumour cells[211,212]. Secondly, the PEG groups help the particles to evade the immune system once administered[202].

The loading and functionalization did not affect the morphology of the nanoparticles **(Figure 3.6A and 3.6B)**. The average size of the non-functionalized nanoparticles as observed by TEM was 137 ± 55 nm. The hydrodynamic size of the nanoparticles in aqueous dispersion was 291 ± 19 nm, with a polydispersity index (PDI) of 0.31 ± 0.03, as measured by dynamic light scattering (DLS). After the addition of PEG, the size observed by TEM did not significantly change (133 ± 30 nm), and a smaller size was found in dispersion (193 ± 18 nm, PDI 0.42 ± 0.05) as compared to the non-functionalized MSN. Both nanoparticles had similar values of

surface charge (-18 ± 5 and -21 ± 4 mV for MSN and MSN-PEG, respectively) **(Figure 3.6C and 3.6D)**.
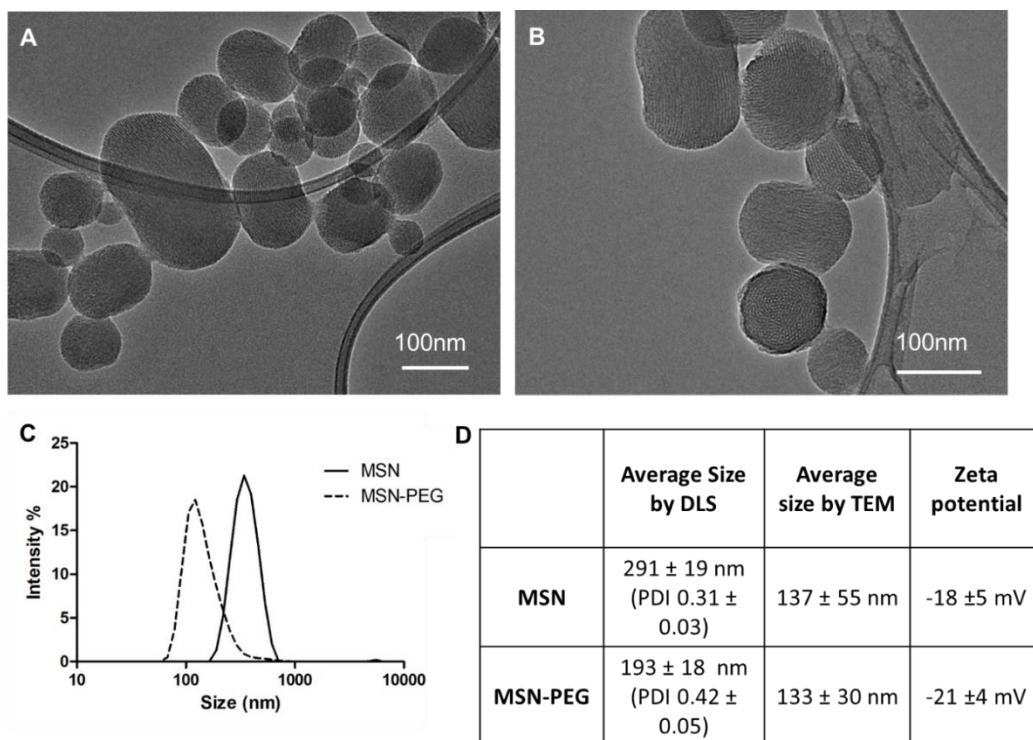
Figure 3.6: The morphology of the MSN did not change after functionalization with PEG. The average size and the zeta potential change slightly after PEG addition. **A-** TEM image of MSN. **B-** TEM image of MSN-PEG. **C-** Size distribution (% intensity) for MSN (solid line) and MSN-PEG (dotted line) by DLS. **E-** Table with average size measured by DLS and by TEM (using ImageJ software), and MSN zeta potential.

DLS measurements are based on the Brownian motion of particles and determine the hydrodynamic diameter of particles in suspension. The intensity of the light scattered by a particle is proportional to its size because this determines the Brownian movement speed. Small particles move faster and scatter less light than bigger particles[213]. Therefore, bigger particles have a higher contribution to the particle size as measured by DLS, which can explain the higher average size measured by intensity through DLS. Moreover, MSNs are prone to aggregation due to their surface area, and the aggregates can influence the final size measured by DLS. Another factor that influences the size measurement by DLS is the water/solvent-material interaction. Thin layers of water can be formed on the surface of the particles contributing to the hydrodynamic diameter measured. An

overestimation of mesoporous silica nanoparticles size measured through DLS compared to TEM estimation is already documented in the literature[214].

In addition, the surface charge characterized by the zeta potential can influence particle stability and the aggregation propensity. The PEG on the surface of the nanoparticles may promote steric hindrance between the particles and improve nanoparticle suspension in water, as seen in the DLS distribution. Indeed, Cauda *et al.* demonstrated that three different types of PEGylated mesoporous silica nanoparticles had improved suspension in water and biological media compared to uncoated nanoparticles, and both the uncoated and PEGylated nanoparticles had similar average size measured by TEM[215].

The presence of PEG on the surface of the nanoparticles was confirmed by Fourier-transform infrared (FTIR) spectroscopy **(Figure 3.7)**, where the bands corresponding to C-H stretching (2900-2800 cm^{-1}) were identified after functionalization. Moreover, the characteristic bands of Si-O-Si (1064 cm^{-1}) and Si-OH bonds (962 and 799 cm^{-1}) were also identified. The amount of PEG on the surface of the nanoparticles was estimated by a colorimetric test[174], and the percentage of PEG attached to the surface of the particles in relation to the amount added was 82% ± 6%.
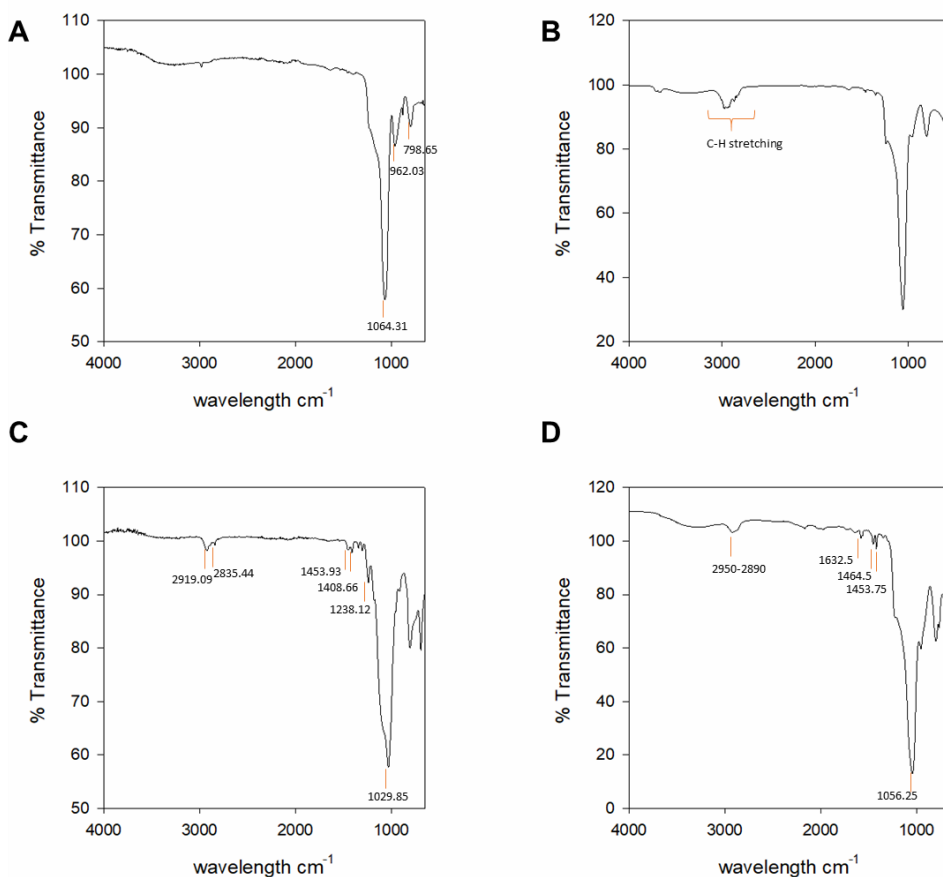
Figure 3.7: The presence of PEG on the MSN was evaluated by FTIR. **A-** FTIR spectrum of MSN shows bands correlated with Si-O-Si stretching (1064 cm^{-1}) and Si-OH stretching (962 798 cm^{-1}). **B-** FTIR spectrum of MSN-PEG shows new bands correlated with C-H stretching (2840-2970 cm^{-1}). **C-** FTIR spectrum of MSN-TMZ-PEG shows bands correlated with C-H stretching (2919, 2835 cm^{-1}) and N-H stretching (1238, 1408 and 1453 cm^{-1}). **D-** FTIR spectrum of MSN-PTX-PEG shows bands correlated with C-H stretching (2950 - 2890 cm^{-1}) and N-H stretching (1632, 1464,1453 cm^{-1}).

The release of Safranin-O was used as proof of concept for the PEG molecular gate. The MSN-Saf-PEG only release the payload after the addition of 10 mM glutathione in the release media (water or PBS) **(Figure 3.8)**. In the absence of a stimulus, a basal leaking of 18% (water) and 26% (PBS) is observed over 4 h of experiment. Thus, the PEG molecular gate was functional and responsive in both media tested.
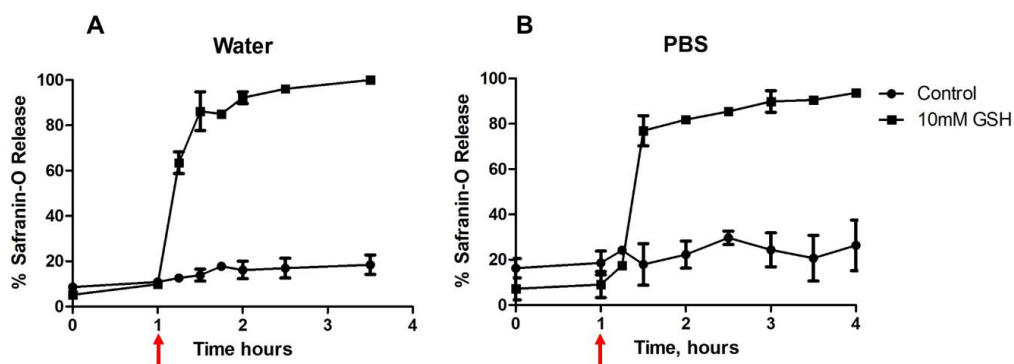
Figure 3.8: The successful formation of the responsive gate was confirmed by the release study. The MSN-PEG only release their payload after the addition of glutathione (GSH) as a reductive stimulus (red arrows). **A-** Safranin-O release in water. **B-** Safranin-O release in PBS pH 7.4, both at room temperature. The results were normalized for the highest amount released (results are presented as mean ± SEM of 2 independent measurements).

3.2.3 Chemotherapeutic drug loading and *in vitro* release

After the extensive characterization of the material and the molecular gate proof of concept, the nanoparticles were loaded with temozolomide or paclitaxel by impregnation. The process of TMZ loading was done at room temperature and partially under vacuum conditions to maximize the diffusion of the drug into the pores. The loading process yielded an encapsulation efficiency of 29% ± 6% w/w for TMZ and 67% ± 12% for PTX, while the loading capacity was similar for both drugs, 22% ± 5% w/w for TMZ and 18% ± 3% for PTX **(Figure 3.9)**.
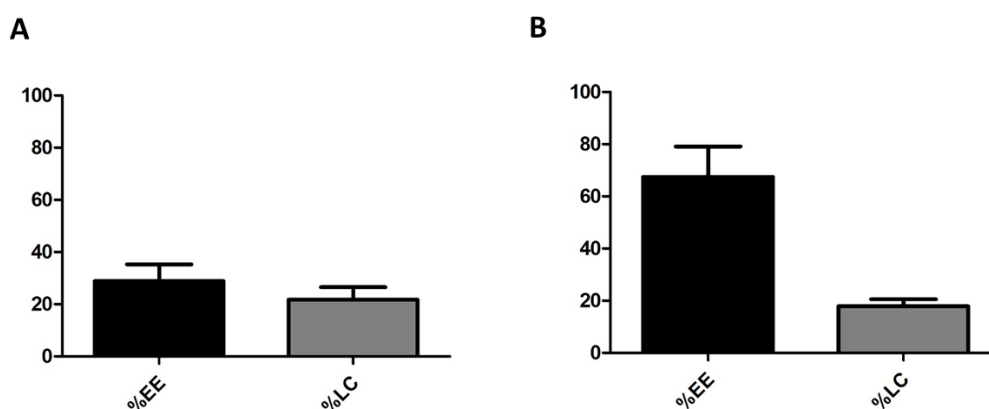
Figure 3.9: MSN encapsulation efficiency (%EE) and loading capacity (LC%) for **A-** Temozolomide and **B-** Paclitaxel. Values are represented as Mean ± SEM.

Drug loading into nanoparticles adds several benefits to disease treatment such as increased drug solubility[169], protection of drug from degradation[216], a decrease in the dose needed and in the potential side effects[217].

Many papers describe the loading of temozolomide on nanoparticles[168,218–221], while few of them report on the release of such drug. Moreover, the solvents used in the loading process vary for each approach, which also yields a range of loading capacities and encapsulation efficiencies for each combination of nanocarrier/solvent used. Thus, after some trials with different solvents (DMSO, acetonitrile, ethanol and PBS) we were able to reproduce the loading described by Bertucci *et al.*[168] while adapting it with the addition of vacuum on the process to maximize drug diffusion into the nanoparticle pores.

Similarly, the loading of paclitaxel in different nanoparticles has also been reported in the literature. Some examples include liposomes[222], PLGA nanoparticles[223], mesoporous titania[224] and MSN[225–229]. Indeed, a high number of reports using MSN and describing different loading approaches are available since MSNs are highly used to deliver hydrophobic drugs[230] as is the case of paclitaxel. The most frequently used solvents to load paclitaxel are chloroform and dichloromethane (DCM) giving encapsulation efficiencies higher than 60% based on previous papers. He *et al.* compared the effect of solvents (DCM, DMSO and ethanol), ratio of drug/carrier and time on the MSN loading of PTX, verifying that loading with dichloromethane for 24 h and a drug/carrier ratio of 1:3 yielded the best encapsulation efficiency and loading capacity in MSN. Thus, following the proposed method, we achieved a comparable loading of PTX into our MSN.

Our system presents a specific release profile due to the stimulus sensitivity. The effect of GSH addition observed in the MSN-Saf-PEG release was reproduced in the drug-loaded MSN release **(Figure 3.10)**. The basal release from MSN-PEG is around 15% of the total release over time for both drugs. Regarding TMZ, the drug loaded in the nanoparticle is promptly released when no molecular gate (no PEG) is present, with more than 80% being released in the first 4 h. In the presence of the molecular gate and a constant GSH concentration in the release media, almost 40% is progressively released over 24 h. The MSN-PTX nanoparticles released more than 90% of the drug in the first 4 h while MSN-PTX-PEG also released almost 40% over 24 h when the stimulus was added.
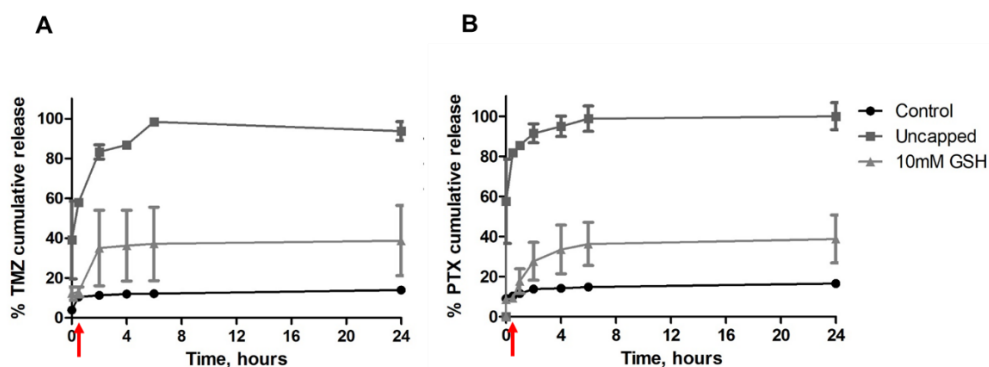
Figure 3.10: Drug release from MSN (uncapped) and MSN-PEG (after the addition of 10 mM GSH as a reductive stimulus – red arrow). **A-** TMZ release. **B-** PTX release. The results were normalized for the highest amount released (results are presented as mean ± SEM of at least 2 independent measurements).

Regarding the release profile, TMZ has a very short half-life in PBS[231] making the detection challenging over time. Some publications show the measurement of its degradation products[221], while others only use model molecules (such as fluorescent molecules) to prove the concept on the nanocarrier[168,232], leaving the effect of the drug-loaded delivery system to cell assays. For PTX, the release is usually measured in PBS with the addition of tween-80, as we performed here. Different amounts of tween-80 increase both the solubility and stability of the drug in the media facilitating the observation of drug release[222,233].

Importantly, the *in vitro* release was set in PBS pH 7.4 although upon the addition of glutathione, to simulate the high reductive environment inside cancer cells, the pH may decrease due to glutathione chemical characteristics[234]. This event does not compromise the analysis of data and can even be beneficial as both drugs are more stable at acidic pH[231,235–237].

Furthermore, due to cancer cells metabolism, an acidic environment is more common in the tumour proximity compared to physiological conditions[238,239] and the levels of reducing agents are much higher inside cancer cells than outside or in normal cells[211,240]. Based on these assumptions, the developed nanosystem would be able to deliver its cargo preferentially in the cancer cells. Previous publications have already described systems that rely on the redox-responsive molecular gate to be applied in different types of cancer[170,203,241]. These publications are a proof of concept for their proposed systems using PEG or collagen attached to the surface of MSN through different reaction steps.

Finally, the release behaviour for the uncapped MSN was similar for both drugs while the expected effect of capping the pores was also observed. A lower drug release was seen for the particles in which the PEG was attached to the surface and blocked the pores. In this case, the immediate release was prevented, and the amount released did not increase as observed for the uncapped but a steady release over time was displayed instead. The release study was designed so that the amount of drug being released did not exceed the solubility limit. Thus, the impairment in the release due to saturation can be discarded as a factor affecting the drug dissolution. Some drug degradation may occur during the measurement of the release. However, this is not expected to have a large effect in the release profile since a cumulative release is calculated summing up progressively all release time points. Therefore, we speculate that the PEG attachment on the surface is breaking slowly to release the drug originating the controlled release.

The responsiveness of the nanosystem and the sustained release over time is essential for GlioGel formulation. The nanoparticle component aims to treat remaining tumour cells left post-surgery for an extended period.

3.2.4 Cell studies

3.2.4.1 U-87 cells

3.2.4.1.1 Cytotoxicity assays

In addition to the controlled release, the biological effect of the developed nanoparticles is highly important for the success of the GlioGel formulation. Therefore, an *in vitro* biological evaluation of free drugs and drug loaded nanoparticles was performed.

In vitro evaluation of TMZ cytotoxic effect against U-87 glioblastoma cell line indicated a very high IC50 of 832.5 µM **(Figure 3.11A)**. Importantly, MSN and MSN-PEG alone had a minor effect on U-87 cells, decreasing the viability to 84% and 77%, respectively **(Figure 3.12A and B),** for the concentration range tested. On the contrary 250 µg/mL nanoparticles loaded with TMZ at a drug concentration corresponding to 260 µM, decreased the cell viability to 21% **(Figure 3.11B and 3.11C)**. In comparison, the same amount of free drug (260 µM) did not show a significant effect on these cells, decreasing the cell viability to 81%. Even lower concentrations of drug loaded into nanoparticles, such as 100 µM TMZ, decreased

the cell viability to 53% which was significantly different from 100 µM free TMZ **(Figure 3.11C)**. The results suggest that MSN-TMZ is decreasing the amount of drug needed to exhibit an effect on cell viability compared to the free drug.
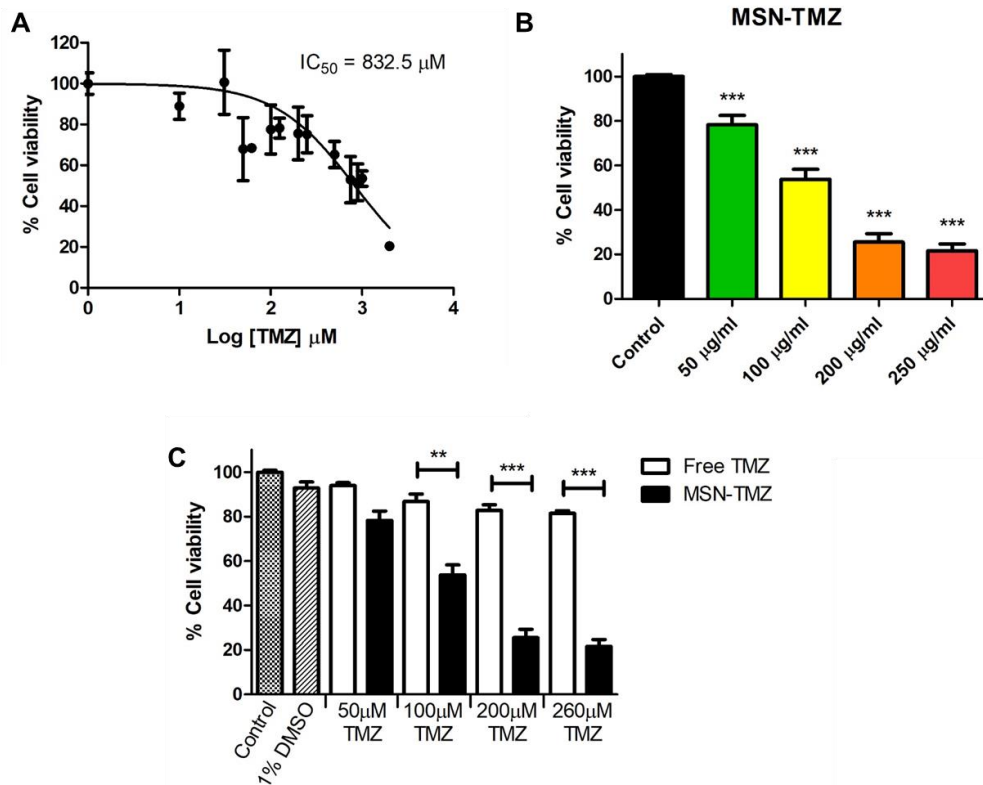
Figure 3.11: The MSN-TMZ exerted an *in vitro* cytotoxicity effect on U-87 glioblastoma cells. **A-** TMZ IC50 in U-87 cells (72 h). **B-** U-87 cell viability assay upon treatment with TMZ loaded MSN for 72 h (mean ± SEM). The x-axis corresponds to MSN concentration. For the corresponding amount of drug loaded, see (C) or Appendix 1. **C-** Comparison of U-87 cell viability upon treatment with free TMZ and MSN-TMZ with corresponding drug concentrations. One-way ANOVA with Dunnett's post-test **(A)** and Tukey's post-test **(C)**. p <0.05 (*), p <0.01 (**) and p <0.001 (***).
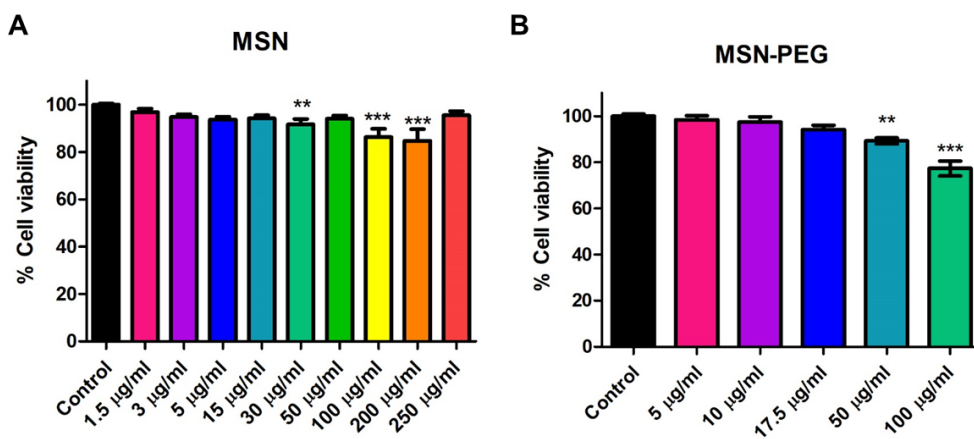
Figure 3.12: U-87 cell viability assay upon treatment with **A-** MSN and **B-** MSN-PEG, for 72 h (mean ± SEM). One-way ANOVA with Dunnett's post-test. $p < 0.05$ (*), $p < 0.01$ (**) and $p < 0.001$ (***) vs control.

As observed in the IC50 assay, TMZ is not a potent drug to kill U-87 cells. In addition, the reported sensitivity of some GBM cell lines to temozolomide varies enormously[242]. The low cytotoxicity of the free TMZ observed in the U-87 cells viability test may be explained by cell resistance.

Glioblastoma cells can develop different molecular and cellular mechanisms of resistance to chemotherapeutic drugs that include overexpression of membrane transporters[26]. In fact, TMZ binding sites on P-glycoprotein efflux pump (P-gp) was already reported in the literature and correlated with drug resistance in GBM cells[243]. Thus, if free drug was actively taken out from the cells, this could explain the low toxicity and high IC50. On the contrary, the chemotherapeutic drug inside the nanoparticles (MSN) may not be recognized at first as a harmful agent to the cancer cells. The internalization of the nanoparticles into cancer cells with a controlled release of therapeutics, decreases drug efflux and consequently reduces drug resistance[204]. Here, MSN loading a concentration three times lower than the IC50 of TMZ was able to kill almost 80% of the U-87 cells.

The importance of inhibiting tumour cell membrane transporters has led to the development of different nano-delivery systems that co-load an anti-cancer drug and an inhibitor[244,245]. Additionally, in some cases, the nano-delivery system itself showed an effect. For instance, a biosurfactant nanoparticle loaded with doxorubicin showed higher toxicity than the free drug, and the authors suggested that the nanoparticle could affect the expression of P-glycoprotein efflux pump[246].

Furthermore, the possible interactions of different types of nanoparticles with ABC transporters were reviewed, and inorganic nanoparticles were pointed as competitive inhibitors of these transporters[247].

Another mechanism of acquired drug resistance in GBM cells is the overexpression of proteins directly or indirectly related to DNA repair[248,249]. It was already shown that drug resistance due to upregulation of dihydropyrimidine dehydrogenase gene expression was overcome by a hollow mesoporous silica nanoparticle targeted to a colorectal cancer cell line via the epidermal growth factor[250]. The authors suggest that the observed effect is due to the high intracellular drug concentration provided by the nano-delivery system. This hypothesis resonates with the possible reason proposed here for TMZ loaded nanoparticles.

The effect of both PEGylated and non-PEGylated drug-loaded MSN on U-87 cell viability (**Figures 3.13A and B)** was evaluated using paclitaxel (IC50 27.7 nM) **(Figure 3.13C)**, a more potent chemotherapeutic drug compared to TMZ (IC50 of 832.5 µM) **(Figure 3.11A)**. Paclitaxel concentrations higher than the IC50 had very similar effects on U-87 cells if the drug was loaded into either MSN or MSN-PEG, decreasing the viability by up to 20% (MSN-PTX) and 24% (MSN-PTX-PEG). Importantly, the free drug had a reduced effect at a concentration 25-times (7 µM) higher than the IC50 **(Figure 3.13D)**. In this case, the incorporation of PTX into the nanoparticles is an advantage over the use of the free drug.

The inverse effect of higher paclitaxel concentrations on cell viability at 24 h, 48 h and 72 h was previously reported for different cancer cell lines[251]. In addition, it was shown that the diluent commonly used with this drug (Cremophor) had an antagonist behaviour with paclitaxel. Therefore, the use of nanoparticles to deliver this drug and prolong the time of contact with the cells through a sustained release seems a promising strategy over the use of the common diluent.

Taken together, these results highlight the benefits of the incorporation of TMZ and PTX into the nanoparticles for the improvement of cytotoxic effects upon U-87 cells. This is an important benefit to be considered in the final GlioGel formulation.
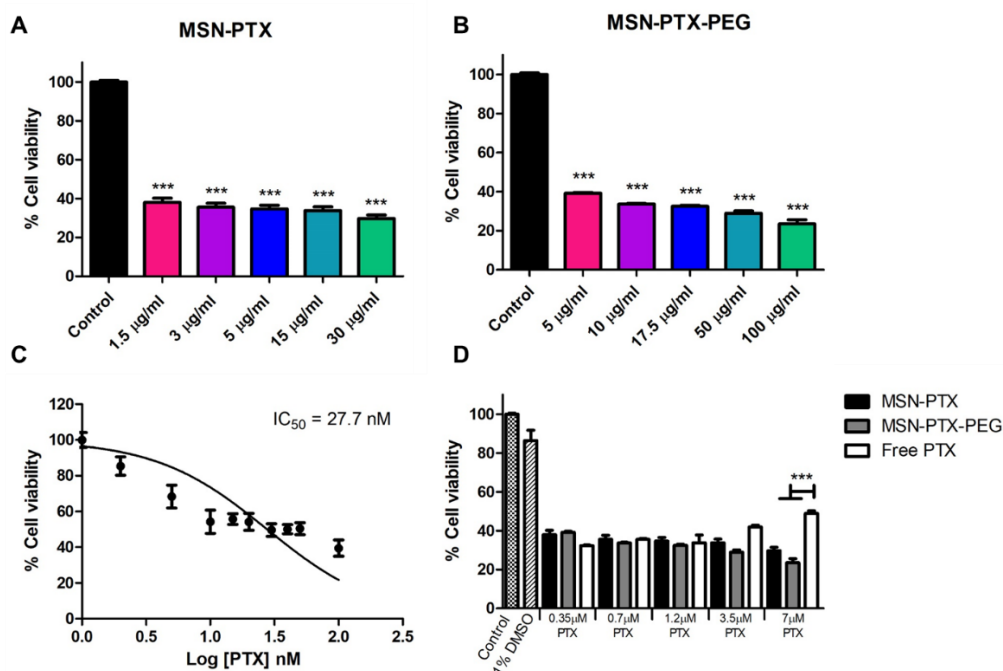
Figure 3.13: The MSN-PTX exerted an *in vitro* cytotoxicity effect on U-87 glioblastoma cells. **A-** U-87 cell viability assay upon treatment with MSN loaded PTX and **B-** MSN-PTX-PEG for 72 h (mean ± SEM). The x-axis corresponds to MSN concentration. For the corresponding amount of drug loaded, see (D) or Appendix 1. **C-** PTX IC50 in U-87 cells (72 h). **D-** Comparison of U-87 cell viability upon treatment with free PTX, MSN-PTX and MSN-PTX-PEG with corresponding drug concentrations. One-way ANOVA with Dunnett's post-test **(A and B)** and Tukey's post-test **(D)**. $p < 0.05$ (*), $p < 0.01$ (**) and $p < 0.001$ (***).

3.2.4.1.2 MSN internalization

The effect of nanoparticles on the cells can be understood by means of both pore opening for drug release in the media and nanoparticle internalization. Nanoparticle internalization by the cells after 24 h is shown by confocal microscopy images and flow cytometry using nanoparticles functionalized with fluorescein isothiocyanate (FITC), which is a model fluorescent dye. Qualitative analysis of nanoparticle internalization through fluorescent microscopy images showed that cells incubated with MSN-FITC-PEG presented a higher density of nanoparticle spots (green colour) into the cells compared to MSN-FITC images **(Figure 3.14)**.

| Control | MSN-FITC | MSN-FITC-PEG |
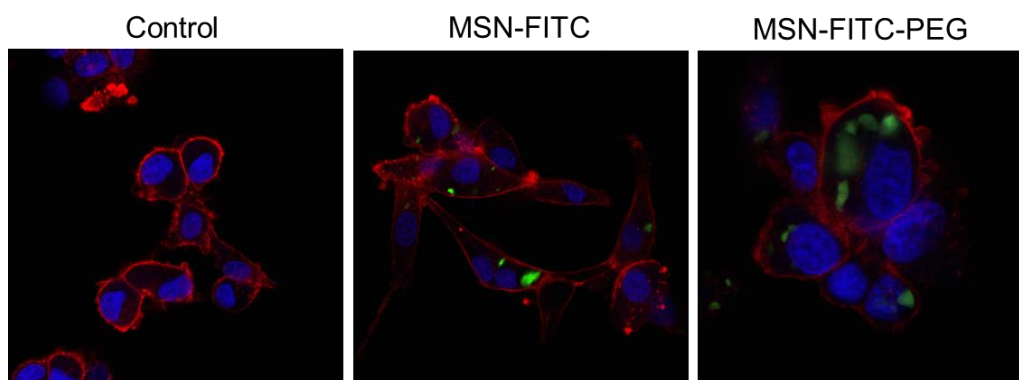
Figure 3.14: Confocal fluorescence microscopy of U-87 cells after 24 h treatment with 50 µg/mL MSN-FITC and MSN-FITC-PEG. Red- Phalloidin-TRITC staining cytoskeleton; blue – Hoechst staining cell nucleus; green- nanoparticles functionalized with fluorescein isothiocyanate (FITC). Magnification 40x.

The quantification of the nanoparticles internalization by flow cytometer analysis confirmed this previous observation. Only 6% of the cells were fluorescent when nanoparticles were not added to the media (controls) while 93% of cells treated for 24 h with MSN-FITC-PEG and 91% treated with MSN-FITC were fluorescent, which indicates the nanoparticles internalization **(Figure 3.15A)**.

In the flow cytometry experiments, trypan blue was added to the cell suspension to avoid unspecific fluorescence from nanoparticles adsorbed on the surface of the cells[179,180]. The flow cytometer results before and after the addition of trypan blue for one of the experiments replicates are shown in **Appendix 1**. After the addition of trypan blue, the fluorescence decreased slightly for the MSN-FITC treated cells (89%) while for the cells treated with MSN-FITC-PEG, 92% were still fluorescent **(Figure 3.15B)**.
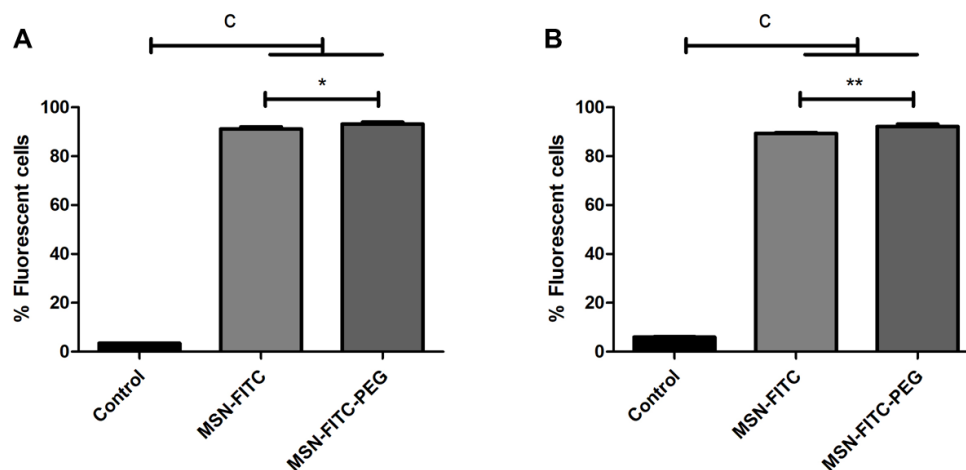
Figure 3.15: Fluorescent cells detected by flow cytometry after 24 h treatment with 50 µg/mL MSN-FITC and MSN-FITC-PEG. **A-** Before addition of trypan blue. **B-** After addition of trypan blue. Control = cell only without treatment with MSN. One-way ANOVA with Tukey's post-test. Differences to the control are represented as c = $p < 0.0001$. Differences between MSN-FITC and MSN-FITC-PEG is represented as $p < 0.05$ (*), $p < 0.01$ (**) and $p < 0.001$ (***).

The PEGylation of nanoparticles can be a double-edged sword in the design of nanodelivery systems. The addition of PEG was shown to decrease the adsorbance of human serum albumin on MSN almost by 7 times, and reduces to a minimum of 0.1% the nanoparticle phagocytosis[252]. Thus, the prevention of phagocytosis may increase nanoparticle circulation time facilitating internalization while the reduction on protein adsorption can impair nanoparticle uptake.

Our results show that the PEGylation did not impair nanoparticle internalization by U-87 after 24 h in contact with the cells. This result is supported by previous observations of PEGylated PLGA-based nanoparticles internalization in HeLa cells verified by flow cytometry (up to 24 h incubation)[173], brain endothelial cells uptake of PEGylated silica nanoparticles observed by confocal fluorescence microscopy (4 h incubation)[253] and MSN capped with PEG through a disulphide link internalized in MCF7 cells after 24 h incubation[203].

Nanoparticle internalization by U-87 cells, especially after the functionalization with PEG, not only justifies the effect of drug-loaded nanoparticles on cell viability but also supports the use of MSN-PEG on the GlioGel.

3.2.4.2 Primary rat neuron culture: viability and complexity

The GlioGel formulation, which will be composed of a gel, free drug and drug-loaded nanoparticles, is intended to be administered directly into the brain after tumour resection surgery. Therefore, this formulation will be in close contact with the remaining tumour cells but also with healthy brain tissue. To understand how the nanoparticles affect healthy neurons, we evaluated the viability and complexity of primary rat neurons in the presence of MSN and MSN-PEG. Neither MSN nor MSN-PEG in the highest concentrations tested in the cancer cells affected the viability of neurons **(Figure 3.16)**.
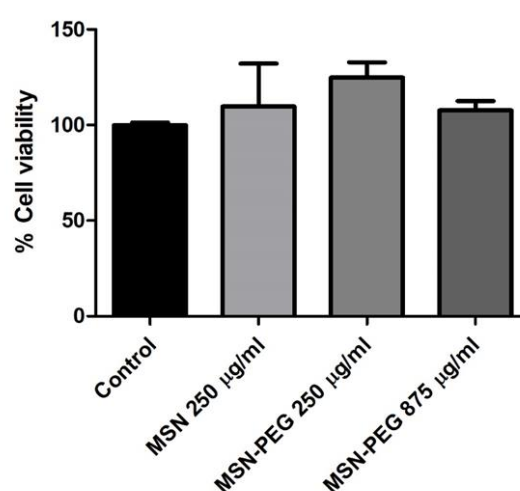
Figure 3.16: Primary rat neurons viability after MSN and MSN-PEG treatment for 72 h. One-way ANOVA with Tukey's post-test. There was no statistical difference ($p > 0.05$).

Following the treatment with MSN and MSN-PEG, we marked the neurons with the Microtubule Associated Protein 2 (MAP-2) antibody and stained the nucleus with DAPI. MAP-2 is a protein expressed only in the cell body of a neuron (the perikarya) and in the dendrites, being a good marker to study neurons morphology using the Sholl analysis.

The Sholl analysis was developed by Dr. Sholl to compare the morphology of different types of neurons in cats[181]. It is a quantitative analysis to characterize neurons morphology, especially dendritic complexity, that can be performed either manually or automated[254]. The analysis consists in applying concentric rings spaced 10 μm apart centred on the soma on a neuron image and count the number of intersections, branches, primary neurites and neuritic length **(Figure 3.17)**.
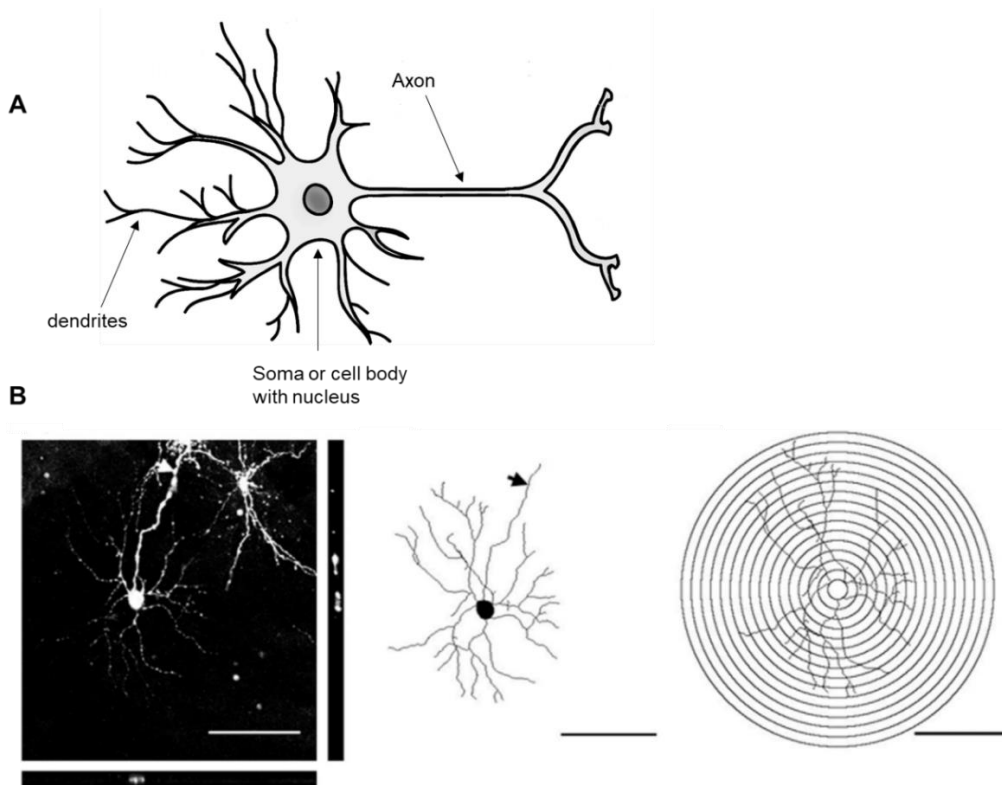
Figure 3.17: Sholl analysis. **A-** Schematic of a neuron showing the soma or cell body with nucleus and the neurites (dendrites and axon) **B-** Example of Mouse Retinal Ganglion cell projected z-stack image with orthogonal views, the corresponding 8-bit tracing constructed using the Fiji plugin Simple Neurite Tracer and 8-bit tracing with digitally applied concentric rings spaced 10 μm apart centred on the soma centre. Scale bar: 100 μm. Axons indicated by arrows. Image from ref[254].

After marking and imaging the neurons treated with MSN (250 μg/mL), we did not observe the presence of neurites, thus MSN treatment altered neurons complexity **(Figure 3.18A)** and the Sholl analysis was not possible in these samples. Conversely, MSN-PEG treatment did not affect the presence of neurites and neurons had the same morphological aspect compared to normal neurons **(Figure 3.18B)**. The Sholl profile indicated that slightly more intersections are observed in these neurons near to the cell body, which can be interpreted as more branches up to 100 μm distance from the soma and also slightly less branches far from the soma **(Figure 3.18C)**. Overall the number of branches **(Figure 3.18D)** and the neuritic length **(Figure 3.18E)** were similar to control neurons, while a significantly higher number of primary neurites was observed **(Figure 3.18F)**.
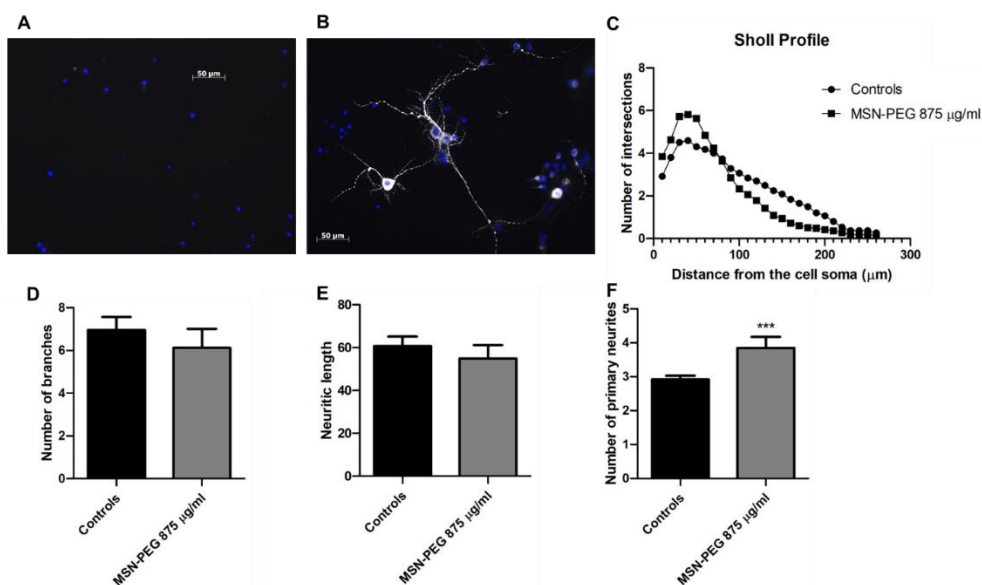
Figure 3.18: The MSNs effect on Primary rat neurons. MAP2 staining of neurons after treatment (72 h) with **A-** MSN (250 µg/mL) and **B-** MSN-PEG (875 µg/mL). **C-** Sholl Profile **D-** Number of branches **E-** Neuritic length **F-** Number of primary neurites for MSN-PEG. Unpaired t test p <0.05 (*), p <0.01 (**), p < 0.0001 (***) vs control.

Overall, our results indicated that the nanoparticles did not affect the viability of neurons and the PEG is being protective regarding the neuron development of normal morphology. Orlando *et al.*[255] showed that MSNs of 30 and 250 nm did not affect the viability of neuronal cells evaluated in terms of mitochondrial activity (MTT assay) and membrane integrity (LDH assay). More importantly, they showed that up to 250 µg/mL of MSN increased the excitability of neuronal cells but did not affect the viability even though they did not propose any mechanism responsible for these observations.

Another study evaluating the effect of MSN (50 µg/mL) loaded with Nerve growth Factor (MSN-NGF) in the differentiation of Neuron-Like PC12 Cells showed that non-loaded MSN did not induce neurites outgrow in these cells[256]. This may correlate with our observation of neurites absence in our MSN treated neurons although it did not explain the possible inhibition effect. Notably, different examples in the literature show the non-toxic nature of MSNs (up to 400 µg/mL) in neuron cell lines and their use as drug delivery agents in molecular and gene therapy aiming to promote neuritic growth in neurons[257,258] as well as to reprogram fibroblast into dopaminergic neurons[259].

Neuronal complexity is the measurement of the degree of interaction between neurons in a neural system[260]. Although the evaluation of neural complexity

by Sholl analysis permits the morphological quantification of any treatment alteration, other aspects can also be analysed in neural networks including criticality and neuronal avalanches, which are dynamic and time-ordered[261], and neuronal molecular variability[262]. Altogether, these analyses would give a broader view about neural networks and the effect of any specific treatment, for example of biomaterials to be used in the brain.

The analysis of biomaterial interactions with neurons are important when they are intended to be administered directly into the brain. Any deleterious effect on healthy brain would be prohibitive on the use of such material. Besides that, the interconnection between neurons and cancer cells is also an important factor. It was already reported that interactions between neurons and cancer cells can induce tumour growth. Cancer cells can develop cell-membrane protrusions called tumoural microtubes that facilitate tumour infiltration[263]. Moreover, it was demonstrated that glioma cells have the ability to respond to electrical signals coming from surrounding neurons leading to migration and increased invasiveness[264]. Thus, an analysis on co-cultures of neurons and glioma cells can also improve the understanding on the effects of biomaterials, such as nanoparticles, in these systems.

Our results based on the Sholl analysis suggest again that the use of MSN-PEG on the GlioGel formulation is preferred over the use of MSN that affected neurons complexity.

3.2.5 MSN stability

To understand how the nanoparticles change over time in the media when they release their cargo, we studied their stability *in vitro*. After incubation for 7 days in PBS pH 7.4 at 37 °C, the powder X-ray analysis did not show the characteristic peaks related to the hexagonal organization of the pores **(Figure 3.19A)**. At the same time, a change in the N_2 adsorption-desorption porosimetry isotherm was observed and a reduced surface area of 170 g/cm^3 was measured **(Figure 3.19B)**. In addition, the nanoparticles did not show the same characteristic pore distribution in the mesopores range. The pore size distribution determined with the adsorption curve did not show any peak, while taking the desorption curve, it shows a peak and average pore diameter of 23 nm.
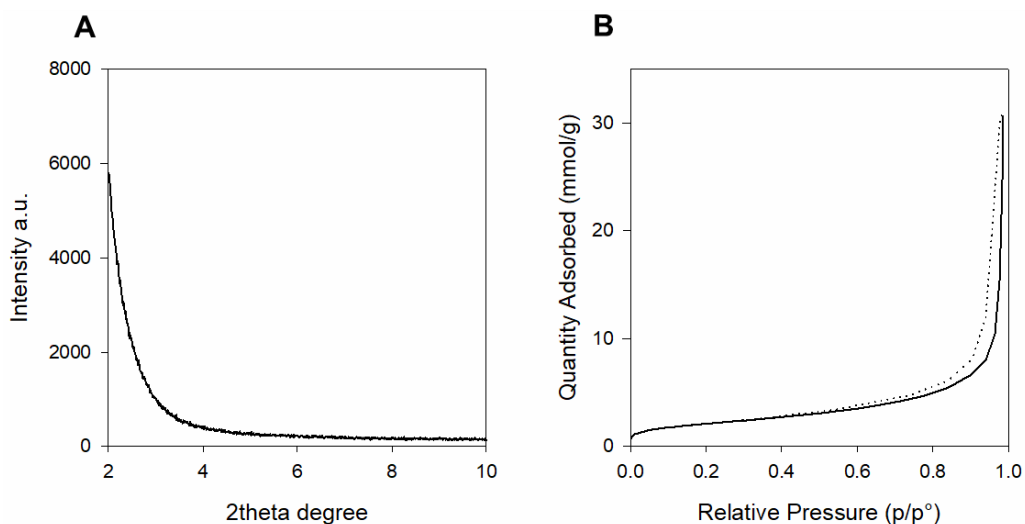
Figure 3.19: Nanoparticle stability. **A-** Powder X-ray diffraction pattern at low angle **B-** N_2 adsorption- desorption porosimetry isotherm of MSN after incubation 37 °C in PBS pH 7.4 for 7 days.

As shown before in the MSN characterization, the common isotherm for mesoporous silica is type IV. Besides that, there are other five types of isotherms described[193] (Types I, II, III, V and VI) as shown in **Figure 3.20**. The observed isotherm after MSN incubation corresponds to type III and is characteristic of slit-shaped pores. This type of isotherm is seen on mesoporous cellular foam (MCF), which has very large mesopores, and titanate nanotubes that is a tubular shape material[194].
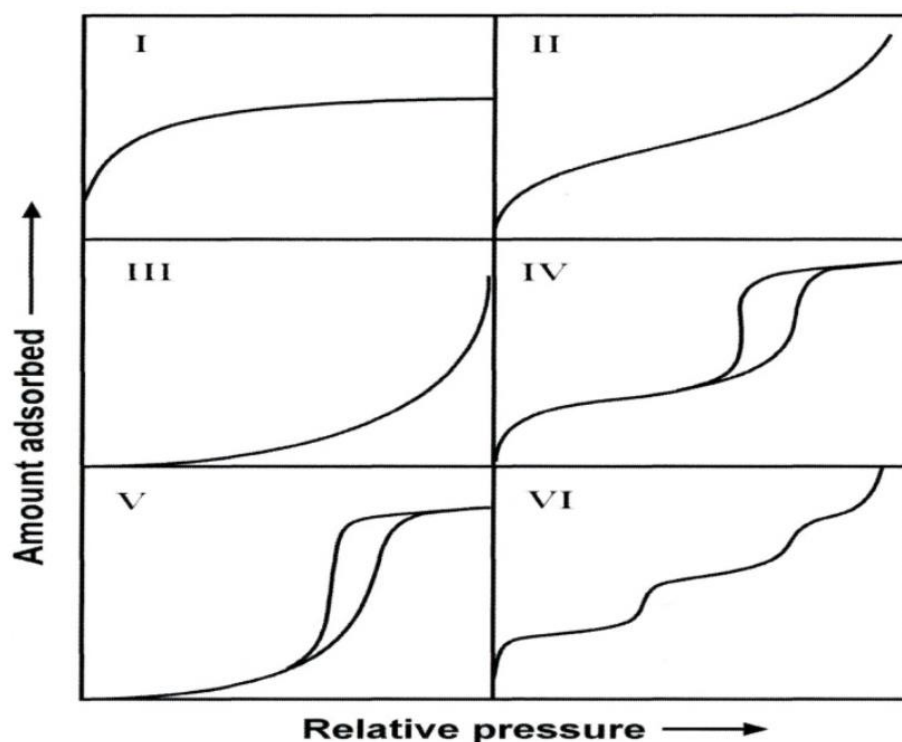
Figure 3.20: Types of adsorption isotherms showing both the adsorption and desorption curves. Type I is characteristic of microporous materials. Types II, III and VI are characteristic of nonporous or macroporous materials and types IV and V of mesoporous materials. From ref [193].

These results indicate that the nanoparticles surface is being degraded over time with a subsequent increase in the pore diameter and loss of the hexagonal pore arrangement. Similar results on silica degradation were observed for pure silica films and films mixed with metal oxides, such as zirconia or alumina, and SBA-15 particles[265]. Partial degradation occurs rapidly, followed by structure stabilization and then complete depletion of silica resulting in materials with bigger pores after 1 h exposure to PBS for the films and 5 h for the particles. Of note, SBA-15 materials are similar to our MCM-41 nanoparticles having a hexagonal pore organization but with bigger pores and thicker walls.

As observed by TEM **(Figure 3.21)**, the nanoparticle degradation is more pronounced at 37 °C compared to room temperature (25 °C). After 1 day of incubation, a pronounced change in the nanoparticle structure was already observed and maintained until 7 days. Importantly, it was demonstrated that PEGylated mesoporous silica nanoparticles have a slower degradation in simulated body fluid compared to non-functionalized nanoparticles. They kept a stable

structure for at least 4 days and have a detectable surface area and pore volume after 1 month[266].
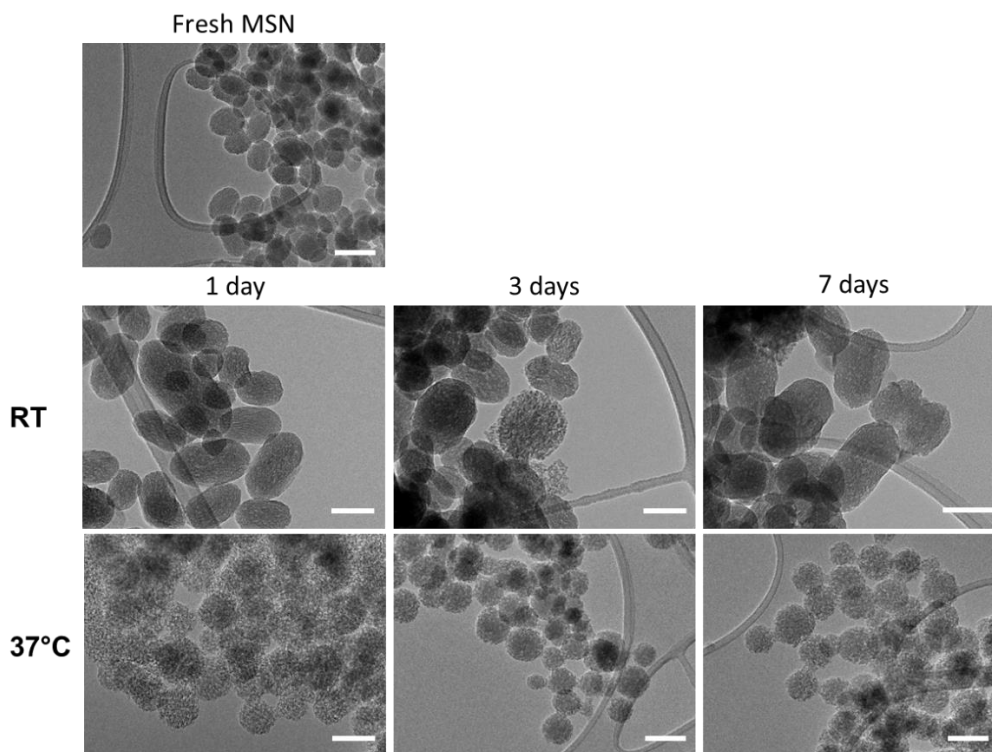
Figure 3.21: Nanoparticle stability. Structural and morphological analysis by TEM after incubation at room temperature (RT) and 37 °C in PBS pH 7.4. Scale bars = 100 nm.

The degradation of MSN structure over time at physiological conditions (pH 7.4 and 37 °C) is combined with relative nanoparticle stability. An increase in the pore size is observed without the complete dissolution of the material. Indeed, the dissolution of silica from MSN was analysed before, and less than 5% was measured after 2 h in simulated intestinal fluid[267]. Therefore, this degradation/stability characteristic is interesting for our delivery system contributing to a sustained but constant release of drug even after the molecular capping is broken.

3.3 Conclusions

The rationale for the use of nanoparticles relies on the possibility to protect drugs until they arrive to their point of action, control the delivery of drugs to specific cells or organs and decrease the dose needed to achieve the therapeutic effect while reducing side effects.

In this chapter, a nanodelivery system based on mesoporous silica nanoparticles was developed and tested against U-87 cells, a model glioblastoma cell line. Moreover, the effects of the nanoparticles on healthy neurons were also evaluated. Finally, the stability of these nanoparticles was studied and correlated with the overall performance of the nanodelivery system.

Mesoporous silica nanoparticles were able to accommodate high amounts of the drugs tested, TMZ and PTX, while only releasing them after a redox stimulus was added into the release media breaking the molecular capping composed of a disulphide attachment between PEG and the surface of the material.

The drug-loaded MSN showed pronounced effects against glioblastoma cells *in vitro* decreasing the IC50 of a less effective chemotherapeutic drug (temozolomide) and maintaining the effect of a more potent drug (paclitaxel). This effect was attributed to nanoparticle internalization into the cells shown by flow cytometry and confocal images. Moreover, after breaking the PEG attachment and opening the pores, the nanoparticles degrade over time losing their ordered pore structure and increasing the pore diameter. This process can also contribute to the delivery of drugs in an extended time period besides the opening of the pores.

The PEG functionalization proved to be an important characteristic of the developed material. Firstly, its attachment resulted in a responsive and controlled delivery of the loaded drug. Secondly, its presence on the surface of the nanoparticle facilitates the internalization, which is an important factor for therapeutic effect. Finally, the presence of PEG on the nanoparticles seemed to be protective regarding the maintenance of neurons complexity and viability.

In conclusion, PEGylated mesoporous silica nanoparticles loaded with a chemotherapeutic drug and responsive to a redox stimulus are internalized by glioblastoma cells and improve drug cytotoxicity effect *in vitro*, constituting a promising drug delivery system to be used in the GlioGel formulation to treat GBM locally.

CHAPTER 4: A NEW FORMULATION APPROACH TO GBM: INJECTABLE GELS COMBINING DRUGS AND NANODELIVERY SYSTEMS

4.1 Introduction

The use of hydrogels is being researched for different biomedical applications[87,97,98]. Hydrogels are largely used in contact lens[268,269], hygiene products[270,271], wound dressings[272–274] and they have also been explored in tissue engineering scaffolds[275] and drug delivery systems[276].

Hydrogels are 3D networks of polymer chains in which water is the dispersion medium. Depending on the way the network is formed, hydrogels can be classified as 'reversible or physical' gels and 'permanent or chemical' gels. Physical or self-assembling gels are formed by the spontaneous molecular interaction of polymer chains through ionic, H-bonding or hydrophobic forces. Chemical gels are formed through covalent bonds between polymeric chains most commonly using a crosslinker[277] **(Figure 4.1)**.
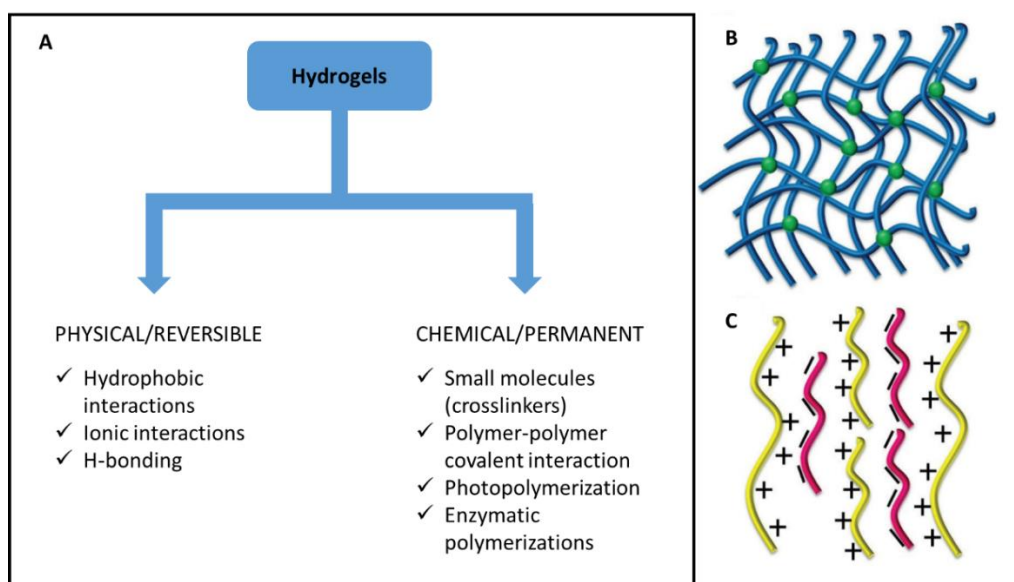
Figure 4.1: Types of Hydrogels. **A-** Hydrogel classification based on the process of network formation (Adapted from[277]) and schematic representation of **B-** Chemical hydrogels and **C-** Physical hydrogels (Adapted from[278]).

Both types of hydrogels have advantages and disadvantages. For instance, chemical hydrogels have a high shape stability while physical hydrogels have a

limited shape stability. This is related to the mechanical properties of hydrogels, which are an important characteristic for implantable devices[279]. On the other hand, physical gels can be thermoresponsive, a characteristic that can contribute to their functionality. For example, the thermoresponsive polymers composed of poly(ethylene oxide) (PEO) and poly(propylene oxide) (PPO) copolymer chains (PEO-PPO-PEO), and commercially available under the name of Pluronics or Poloxamers are very versatile due to this characteristic. This polymer follows two steps in the gel formation, firstly it forms micelles in a temperature and concentration dependent manner and then, with further temperature increase, it undergoes gelation[114] **(Figure 4.2).** Hence, the structures involved in the hydrogel formation process contribute to the incorporation and release characteristics of this material.
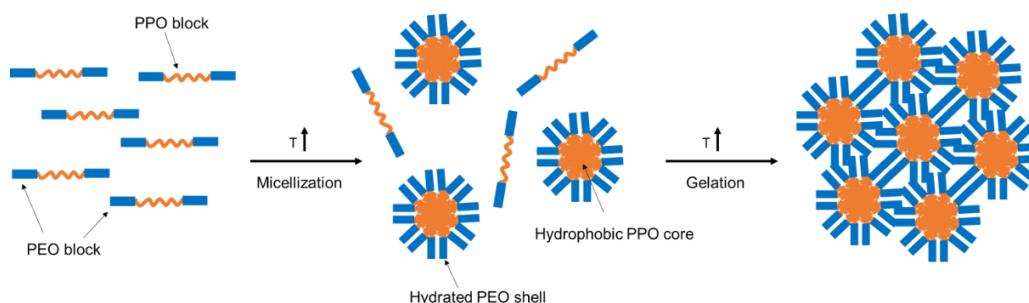
Figure 4.2: Pluronic gelation steps (Adapted from [114]).

Other examples of polymers that can form thermoresponsive hydrogels are poly(lactic acid) (PLA), poly(glycolic acid) (PGA), poly(caprolactone-co-lactide) (PCLA), poly(ethylene glycol) (PEG) and the derived copolymers. Besides that, acrylate polymers such as 2-hydroxyethyl methacrylate(HEMA), 2-hydroxypropylmethacrylate (HPMA), acrylamide, acrylic acid, N-isopropylacrylamide can form chemical hydrogels through the use of different crosslinkers[280].

In cancer research, the use of hydrogels for drug delivery has many technical advantages. Firstly, many of them allow the incorporation of hydrophobic drugs due to the presence of hydrophobic blocks. For instance, as demonstrated by Zentner *et al.*, the incorporation of paclitaxel (PTX), a highly hydrophobic drug, in a biodegradable triblock copolymer significantly increased drug solubility and stability, providing a sustained release during approximately 6 weeks[87]. Secondly, encapsulation in hydrogels protects drugs from phagocytic cells and disfavourable environmental factors that can promote drug degradation. Thus, hydrogel

formulations can increase the half-life of chemotherapeutic drugs while reducing the frequency of drug administration and improving patient compliance.

Particularly, these materials have shown promising results in the treatment of solid tumours. Yang *et al.*[281] used a thermosensitive hydrogel to incorporate gemcitabine, an anti-tumour and radiosensitizer drug, and developed a formulation able to release the drug over a 1-month period. When injected in tumour bearing mice, the formulation inhibited the tumour growth and a synergistic effect with X-ray therapy was observed. Furthermore, PCLA-PEG-PCLA polymers were used to form nanocapsules that incorporate paclitaxel, iron-oxide nanoparticles and IR820, an imaging molecule useful for phototherapy[282]. The formulation controlled the release of both PTX and IR820 showing synergistic results (chemotherapy and phototherapy) *in vitro* and *in vivo* together with imaging capabilities.

Specifically for brain tumours, a range of hydrogels are being tested aiming to improve treatment outcomes through a localized therapy[49]. For example, the most frequently used drug in the treatment of GBM, temozolomide (TMZ), can benefit from hydrogel incorporation due to its low stability in physiological conditions and the poor BBB penetration. In fact, temozolomide loaded into amphiphilic diblock copolypeptide hydrogels of 180-poly-lysine and 20-poly-leucine (K180L20) was more effective both *in vitro* and *in vivo* on GBM models compared to local treatment with free drug[283]. The formulation significantly enhanced the survival time of mice bearing intracranial tumour after resection surgery and treatment from 20 days (controls) to 38 days.

Moreover, hydrogel formulations can be used to deliver a combined treatment to tumours. Indeed, combination therapy using different hydrogels has been proposed such as a chitosan hydrogel loaded with TMZ and a radioactive isotope (iodine) aiming to combine chemotherapy and radiotherapy[284]. The formulation was effective in decreasing tumour size in a subcutaneous brain tumour model due to 10-times higher chemotherapeutic drug accumulation compared to systemic treatment with free drug.

Besides the local and combined treatment, the use of hydrogels enables the development of nanocomposite formulations, which are characterized by the combination of polymers with nanostructures such as nanoparticles. Recently, a thermosensitive hydrogel based on PCLA-PEG-PCLA copolymer was used in the development of a nanocomposite formulation for glioma treatment[285]. The hydrogel was used to incorporate and deliver curcumin-loaded nanopolymersomes, which

were able to significantly sustain the drug release compared to curcumin directly loaded into the hydrogel. In addition, the hydrogel nanocomposite was 3-times more effective in reducing the tumour volume in an ectopic glioma model.

Finally, the use of Pluronic polymers to treat glioblastoma has been proposed both in the form of micelles and hydrogels. The micelle formulations are mainly developed aiming to improve the blood brain barrier penetration. Examples of this approach include a chitosan-Pluronic micelle incorporating myricetin[286] and cyclic arginine-glycine-aspartic acid peptide-decorated Pluronic micelles loaded with doxorubicin and paclitaxel (RGD-PF-DP)[287]. Both micelle constructs showed higher *in vivo* penetration into the brain compared to free drugs after systemic administration and *in vivo* effects regarding decrease in tumour volume (myricetin loaded micelles) and 1.6-fold survival time increase (paclitaxel and doxorubicin micelles). Pluronic F-127 (15.5 wt%) has been proposed to form injectable hydrogels, and the combination with particles, such as alginate microparticles, can improve the polymer functionality making the release more sustained compared to the free loading system[288].

In summary, the two main advantages of using hydrogels to treat brain tumours, such as GBM, is the possibility to have a local treatment and a drug combination therapy. These approaches may improve treatment results by increasing the effective dose reaching the tumour site and possibly decreasing the side effects.

Therefore, in this chapter two physical thermosensitive gels and one chemical hydrogel will be evaluated to compose the injectable gel drug delivery system (GlioGel) for the treatment of GBM. The gels will be analysed for the drug delivery capabilities as well as for the ability to incorporate and deliver the responsive nanoparticles developed in the previous chapter.

4.2 Results and discussion

4.2.1 Gels and chemotherapeutic drugs

Having developed a responsive nanoparticle able to carry chemotherapeutic drugs and exert an *in vitro* cytotoxicity effect on U-87 glioblastoma cells, we advanced into the development of a formulation (GlioGel) that would combine an injectable gel with free drug and drug-loaded responsive nanoparticles for the treatment of GBM.

To start the development of this gel formulation, we followed a screening process in which three different gels and three drugs were chosen and analysed step by step allowing the determination of a final formulation, which has the most suitable characteristics for the intended use. These characteristics are the sustained release of nanoparticles and drug aiming a first pronounced release of free drug followed by the release of nanoparticles. Hence, the combination therapy could act both immediately to eliminate remaining cancer cells and in an extended time frame to target recurrent tumour cells.

The gels that entered the screening process were two thermosensitive tri-block copolymers, a PCLA-PEG-PCLA gel (named LQP4, which stands for Liquid Polymer and the weight ratio of hydrophobic to hydrophilic blocks) and a PEO-PPO-PEO hydrogel (specifically based on the Pluronic F-127), and a chemically crosslinked hydrogel based on poly(methyl methacrylate) (PMMA) (named Crosslinked (CX) gel). Importantly, these gels have different characteristics related to polymer composition, physical appearance, hydrophilicity as well as the method of depot formation, which influence the preparation and the behaviour of the final formulation **(Figure 4.3).**
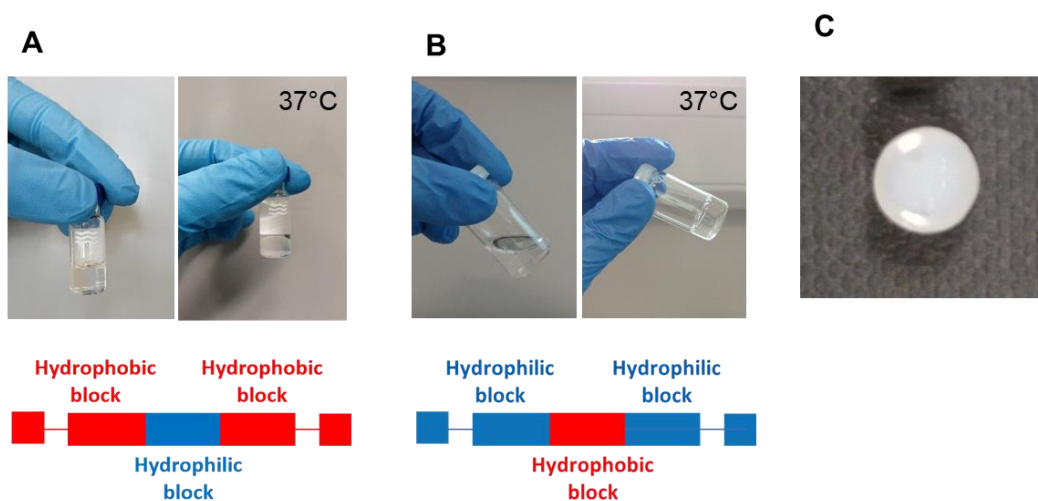
Figure 4.3: Structure and physical appearance of the gels tested. **A-** Liquid Polymer 4 (LQP4). **B-** Pluronic F-127. **C-** Crosslinked gel after complete crosslinking at room temperature.

The LQP4 has a hydrophilic block based on PEG (MW 200 Da), two hydrophobic blocks composed of ε-caprolactone, L-lactide and an hexanoyl end-capping. On the other hand, the Pluronic F-127 is a co-polymer composed of two hydrophilic blocks of poly(ethylene oxide (PEO) flanking one hydrophobic block of

poly(propylene oxide (PPO). The proportion of hydrophobic to hydrophilic units in the PF-127 is 1:3. Therefore, the hydrophobicity is higher in the LQP4 than in the PF-127 hydrogel. Finally, the CX gel is based on the PMMA but with an amide and a ketone modification facilitating the crosslinking through a hydrazide compound, specifically the adipic acid dihydrazide.

Besides their polarity, the physical appearance of these gels also varies. All three polymers are liquids at room temperature and present different degrees of viscosity, with the LQP4 being the most viscous with a honey-like consistency. After the addition of PBS and incubation at 37 °C, the LQP4 undergoes gelation and becomes opaque **(Figure 4.3A),** while the PF-127 also undergoes gelation when heated at 37° but remains clear **(Figure 4.3B)**. The CX gel forms upon the addition of the crosslinker becoming an opaque white piece with the shape according to the mould used in the gel preparation **(Figure 4.3C)**.

Three drugs were chosen to be analysed in the incorporation and release from the gels. The two drugs used in the standard of care for GBM, temozolomide (TMZ) and carmustine (BCNU), and a third chemotherapeutic drug, paclitaxel (PTX), that has been used in the treatment of different types of cancer.

TMZ and BCNU are alkylating agents already in use to treat brain tumours that have the same mechanism of action interacting with the DNA to prevent replication and transcription[289–291]. Oral or intravenous temozolomide is indicated in the treatment of newly diagnosed glioblastoma patients as a monotherapy or combined with radiotherapy[292], while carmustine is mainly used in recurrent GBM as a biodegradable disc implant after tumour resection surgery[293]. PTX is a drug that targets the microtubules affecting cell replication by interfering with the polymerization/depolymerisation of tubulin[294]. Thus, the treatment with paclitaxel causes defects on the chromosome segregation and mitotic spindle formation, which impairs cell division.

4.2.2 Drug releases from gels

With the aim to develop the drug delivery formulation combining drug-loaded hydrogels and the previously described responsive nanoparticles, the release profiles of TMZ, BCNU and PTX from the gels were evaluated. The drugs were incorporated in the thermoresponsive polymer PF-127, the liquid polymer LQP4 and the crosslinked CX gel. All gels are liquid and injectable at room temperature.

The release profiles of all drugs from the hydrogels are very similar, presenting an immediate release in the first 4 h **(Figure 4.4 A, B and C).** The LQP4 is the gel with the lowest burst release while the CX gel is the hydrogel with the highest burst. However, the main difference between the gels is the total release proportion for each drug **(Figure 4.4 D, E and F)**. Over 14 days, the Pluronic F-127 has the highest release proportion of drug (35% of PTX) while the LQP4 has the lowest release proportion (4.6% of PTX). The highest proportion of BCNU is released from the Pluronic F-127 (26%) as compared to LQP4 and CX gel (7.5% and 5% respectively). The release proportion of TMZ is very similar between all three gels with 16% release from Pluronic F-127, 17% from LQP4 and 22% from CX gel **(Table 4.1)**.

It is important to highlight that the degradation of these drugs during the *in vitro* study may affect the release proportions measured. However, this would not affect the release profiles observed. Moreover, the intended local application of the GlioGel formulation can partially overcome the influence of the degradation factor into the treatment performance. Of note, the most unstable drug is BCNU with a half-life of 50 min (PBS pH 7.4) [295], followed by TMZ (~1.24 h in PBS pH7.4)[296] and PTX (~43 h in PBS pH 7.4)[233]. A correlation between the half-life and the release proportion is not evident, which reinforces the possibility to evaluate the gel performance based on this parameter. Therefore, it is still possible to use the release proportions and profile to guide the comparisons and choice between the drugs.
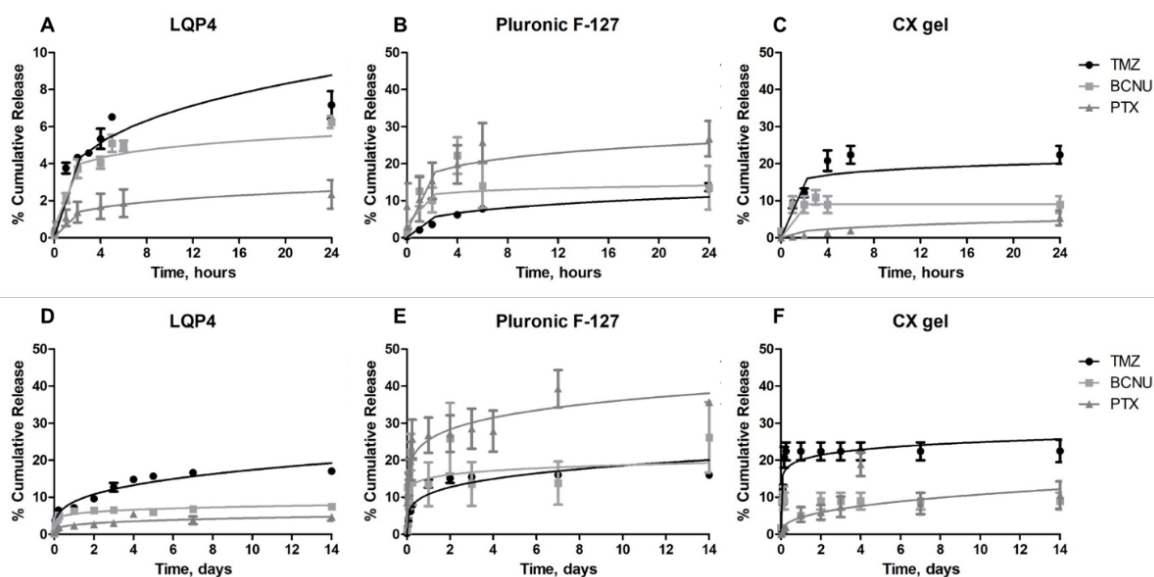
Figure 4.4: Drug release profiles from the Liquid Polymer 4 **(A and D)**, Pluronic F-127 hydrogel **(B and E)** and the crosslinked gel **(C and F)** in the first 24 h and over 14 days. The gels (50 µL) were loaded with 11 mg TMZ, 2 mg BCNU and 2 mg PTX. These weights were used to calculate the proportion (%) of cumulative release. Results are plotted as mean +/- SEM and fitted with the Korsmeyer-Peppas mathematical model.

Table 4.1: Drug release proportions from gels in the first 4 h and in 14 days.

Drug releases from gels						
	Burst (first 4 h)			14 days		
	LQP4	PF-127	CX gel	LQP4	PF-127	CX gel
TMZ	5.3%	6.2%	20.8%	17.0%	16.0%	22.0%
BCNU	4.0%	22.0%	8.9%	7.5%	26.0%	8.9%
PTX	1.7%	19.8%	1.3%	4.6%	35.0%	10.5%

The release of drugs from therapeutic systems such as gels can be related to many different factors including the physicochemical characteristics of gel and drugs, depot structure and depot degradation[96]. The first approach used to analyse the release profile and the impact of the gel depot characteristics was the application of mathematical models on the obtained drug release kinetics.

Overall the best fit for the release profiles was the Korsmeyer-Peppas model, including TMZ and BCNU releases from all gels that correlate with a quasi-Fickian mechanism and the PTX release from CX gel, which better correlates with an anomalous transport, meaning that the release occurs due to a combination of drug

diffusion and solvent penetration into the matrix[297] **(Table 4.2).** The respective graphs originated from the application of the mathematical model analysis can be seen on **Appendix 2**.

The Korsmeyer-Peppas model with a quasi-Fickian mechanism means that a combination of factors, such as diffusion and structural properties of the material, are influencing the release[297]. As stated by Hamidi *et al.*[99], a diffusion-controlled release follows the Fick`s law of diffusion in which the release depends mainly on the structural characteristics of the hydrogel, for example the mesh size, that can be modified by chemical functionalization and monomer composition.

The release profiles of PTX from LQP4 and Pluronic F-127 are slightly better fitted by the Higuchi model. However, one assumption of this model is that the matrix does not swell or dissolve during drug release[298], which may not be the case for these gels. Therefore, it is clear that the use of mathematical models is not conclusive and other analyses related to gel degradation and structure will be presented to help explain the release profiles and their implications on the final formulation.

Table 4.2: Mathematical model fitting parameters of drug releases from gels at 37 °C. R^2 is the correlation coefficient. The release rate constants (K_0, K_1 and K_H) and the release exponent (n) were calculated from the slopes of the respective mathematical models.

		Zero-Order		First-Order		Higuchi		Korsmeyer-Peppas		
	Mathematical Models									
		R^2	K_0	R^2	K_1	R^2	K_H	R^2	n	Release mechanism
LQP4	**TMZ**	0.689	1.17	0.702	0.005	0.906	0.005	**0.988**	0.254	quasi-Fickian
	BCNU	0.384	0.317	0.392	0.001	0.603	1.436	**0.971**	0.209	quasi-Fickian
	PTX	0.567	0.267	0.566	0.119	**0.771**	1.139	0.749	0.105	quasi-Fickian
PF127	**TMZ**	0.426	0.972	0.433	0.004	0.708	4.543	**0.921**	0.245	quasi-Fickian
	BCNU	0.162	0.718	0.171	0.003	0.163	2.611	**0.653**	0.120	quasi-Fickian
	PTX	0.530	1.647	0.563	0.009	**0.754**	7.166	0.713	0.076	quasi-Fickian
CX	**TMZ**	0.072	0.557	0.066	0.002	0.212	0.002	**0.901**	0.162	quasi-Fickian
	BCNU	0.101	0.202	0.105	0.0009	0.046	0.496	**0.444**	0.063	quasi-Fickian
	PTX	0.363	0.805	0.343	0.003	0.568	3.676	**0.890**	0.670	Anomalous

To further evaluate the releases, the degradation of the gels was studied. The LQP4 is the only gel that presents a swelling process, which is very pronounced in the first 2 h and then a slighter swelling was displayed until 7 days. After that, only 8% of weight is lost in 58 days **(Figure 4.5A and B)**.The observation of matrix swelling did not correspond to the assumptions made on the Higuchi model and therefore, this model cannot be accepted as an explanation of PTX release from this gel. In this case, the Korsmeyer-Peppas model has to be considered.

Moreover, the low degradation of the gel over time can explain the low release proportion for the three drugs. The PCLA-PEG-PCLA polymer used here is modified with an hexanoyl end-capping that prevents the rapid degradation in PBS at 37 °C[104]. Therefore, the degradation rate of this polymer is very low and influences the release kinetics.

The Pluronic F-127 hydrogel dissolves in PBS very quickly. Thus, almost 50% of the weight is lost in 2 h and the depot disappears in 6 h **(Figure 4.5C)**. This also ruled out the Higuchi model for these hydrogel releases, specifically the PTX release.

The Pluronic F-127 polymer is a surfactant with thermosensitive properties. Thus, in concentrations higher than the CMC (critical micellar concentration), which is 0.7% w/v at 25 °C and 0.025% w/v at 35 °C[299], it forms micelles and upon temperature increasing higher than the lower critical solution temperature (LCST) these micelles are packed forming a gel.

The 20% w/v Pluronic F-127 hydrogel used in this work has a sol-gel transition between 26 °C and 28 °C depending on the solvent (water or PBS)[300]. Thus, at 37 °C the polymer undergoes a sol-gel transition and entraps the drug. As observed in the degradation assay, the aqueous solvents destabilize the interactions between the PEO chains dissolving the gel depot, while the micelles are still present in the solution until a concentration lower than the CMC is reached[299]. Therefore, even after 6 h, we still observe a gradual and sustained release of the drugs from the micelles.

The CX gel exponentially degrades with 55% weight loss in 7 days and more than 80% weight loss in 58 days **(Figure 4.5D)**. Although the degradation rate is relatively quick for this gel in the first 2 days, after that the process slows down correlating to the sustained release for the three drugs.
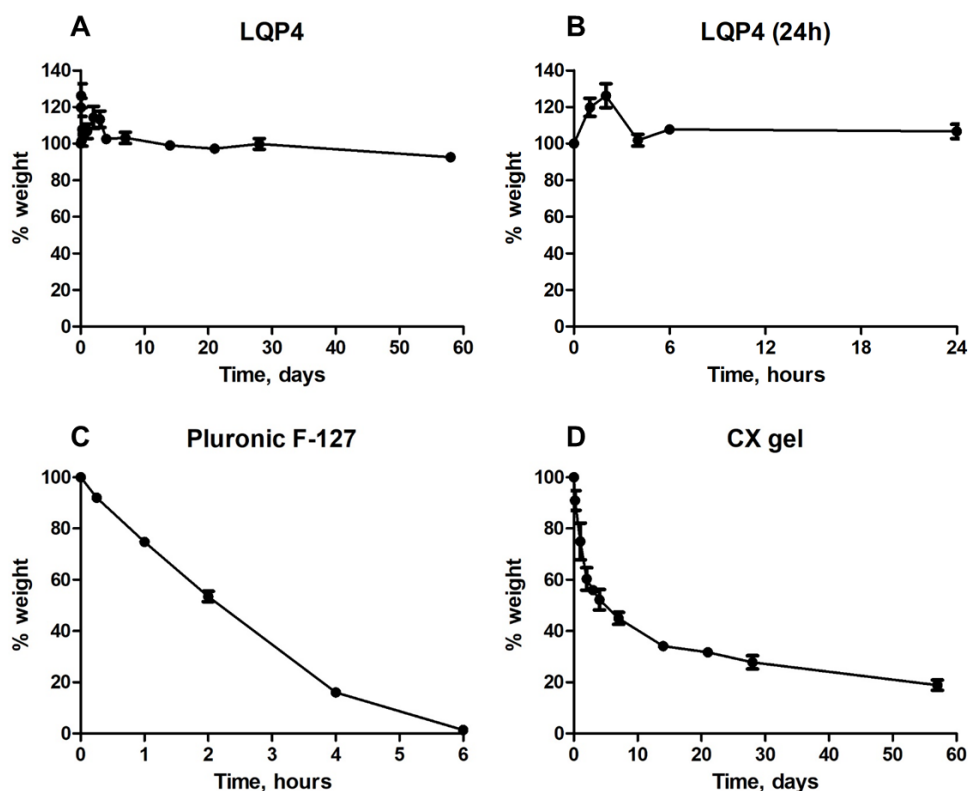
Figure 4.5: Gel degradation in PBS pH 7.4 at 37 °C. **A-** Liquid polymer 4 (LQP4) degradation over 58 days. **B-** Liquid polymer 4 (LQP4) degradation in the first 24 h. **C-** Pluronic F-127 20%w/w **D-** Crosslinked gel (40 mg/mL). Results are presented as mean ± SD of 3 independent measurements.

Overall, drug release seems to be influenced by both drug diffusion and matrix degradation or dissolution in different degrees. In the case of the CX gel, the cryo-SEM images indicate a highly porous network that may be contributing to the sustained release through drug diffusion despite the fast gel degradation **(Figure 4.6)**.
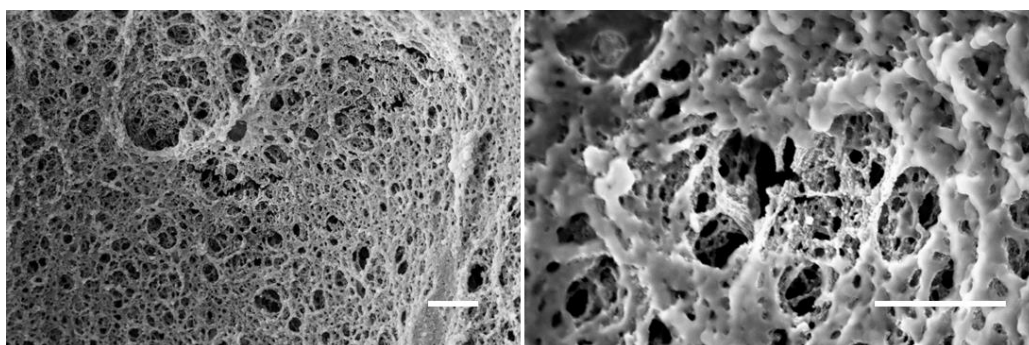
Figure 4.6: Crosslinked gel structure by Cryo-SEM. Scale bar = 1 μm.

The effect of gel dissolution on the drug release from Pluronic F-127 gels was previously proposed by Anderson *et al.*[116]. Additionally, the drug release observed despite the fast dissolution of the Pluronic F-127 suggests that the drugs are incorporated into the micelles to a certain degree[301]. In previous reports, the Pluronic F-127 micelles were modelled to elucidate the polymer chain interactions and the overall structure in which the PPO (hydrophobic) chain forms the core of the micelle and the PEO (hydrophilic) chains are exposed to the aqueous environment[302]. These micelles have a smaller hydrophobic core and an expanded hydrophilic surface compared to the Pluronic L-64, which is less hydrophilic **(Figure 4.7)**.

F127 micelle

L64 micelle
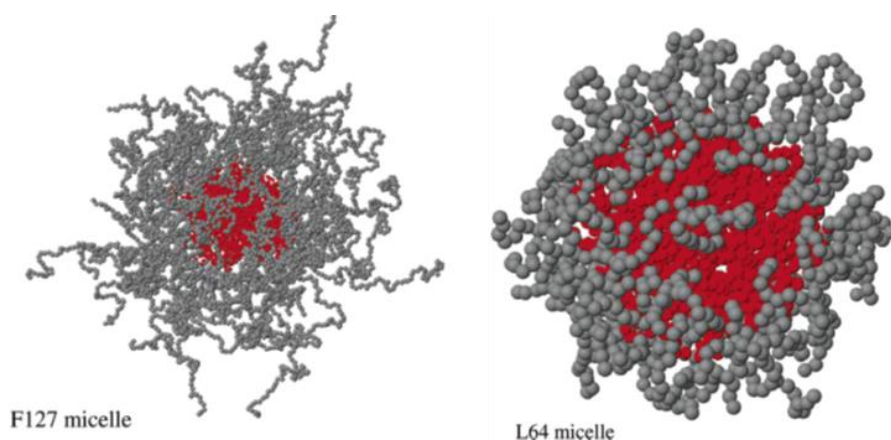
Figure 4.7: Representative snapshots of L64 and F127 micelles models. Reprinted with permission from[302].

Taking this into account, we can assume that the Pluronic F-127 micelles can incorporate a limited amount of hydrophobic drug in the core[301]. Interestingly, the two most hydrophobic drugs, BCNU and PTX are showing the highest release in this gel, possibly due to this poor incorporation. Conversely, a more efficient incorporation of BCNU and PTX in the LQP4 may be responsible for a lower and much prolonged release, which depends on the hydrogel swelling and drug diffusion over time.

Of note, the release of BCNU from the CX gel stops after the burst and even for the other gels an increment of only 4% release is observed from 4 h until the end of the experiment. This may be explained by a very low release from these gels after 4 h that limits the detection of the drug or the fast degradation of BCNU, which has an estimated half-life at pH 7.4 of 50 min[295,303].

Moreover, the similar burst release of TMZ from the LQP4 and Pluronic F-127 hydrogel may indicate that this drug is well incorporated by these gels and the release occurs mainly by diffusion, without a heavy influence of the polymer

composition. On the other hand, the higher burst release of TMZ from the CX gel compared to the other gels indicates an inferior incorporation. However, the pore structure of the CX gel contributes to sustain the release of that fraction of the drug that remains in the gel after the initial burst.

Taken together, these results suggest that both the Pluronic F-127 and the CX gel release proportions can result in a first high local dose of drug (burst) in the tumour area, specifically in the case of PTX and TMZ. The burst release may contribute to the immediate effect of the formulation after the resection surgery and hydrogel implantation. However, a long-term drug presence in the brain is desirable to combat possible recurrent tumour cells. This can be addressed through the incorporation of nanoparticles into the gel originating a nanocomposite formulation.

4.2.3 Release of nanoparticles from gels

The formulation we aim to develop will also consist of drug-loaded nanoparticles, specifically the mesoporous silica nanoparticles developed in Chapter 3. The incorporation of nanoparticles in the formulation enables the use of combined therapy and includes another level to control the drug release[304]. Thus, the release of MSN and MSN-PEG from the three gels was evaluated in order to determine which gel is able to control the release of the responsive system as well as the proportion of nanoparticle being released over time **(Appendix 3 - Calculation of MSN percentage release from gels)**.

Pluronic F-127 solution becomes a cloudy liquid when the MSN are added **(Figure 4.8A)**, and undergoes gelation when heated at 37 °C **(Figure 4.8B)**. After MSN incorporation, LQP4 solution remains clear. It undergoes gelation and becomes opaque when incubated in PBS at 37 °C for 24 h **(Figure 4.8C and D)**. The CX gel conserves the same appearance before **(Figure 4.8E)** and after **(Figure 4.8F)** MSN incorporation without changes in the crosslinking procedure.
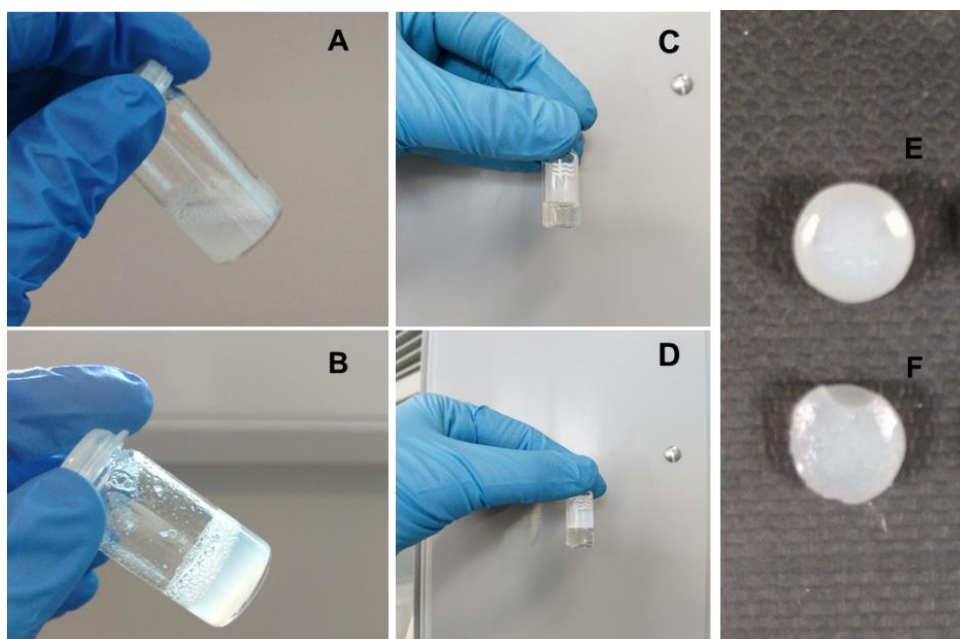
Figure 4.8: The MSN were mixed with the gels to build an injectable formulation. **A-** Pluronic F-127 20% w/w + 20 mg/mL MSN in PBS at room temperature. **B-** Pluronic F-127 20% w/w + 20 mg/mL MSN in PBS at 37 °C. **C-** LQP4 gel at room temperature. **D-** LQP4 gel after 24 h in PBS at 37 °C. **E-** Crosslinked gel. **F-** Crosslinked gel + 20 mg/mL MSN.

Analysing the release profiles, we observed that both MSN and MSN-PEG are released in a controlled manner from the LQP4 gel over 14 days and no significant burst release effect was observed **(Figure 4.9A)**. On the contrary, the Pluronic F-127 has an immediate release of MSN-PEG corresponding to 50% and a more sustained release of MSN up to 36% in 14 days **(Figure 4.9B)**. The CX also controls the release of MSN and MSN-PEG over 14 days **(Figure 4.9C)**. Therefore, both the LQP4 and the CX gel present a controlled release of MSN-PEG. However, the proportion of nanoparticles released from LQP4 (4.4% of 1 mg nanoparticles loaded into the gel) is much lower compared to the CX gel (13.8% of 1 mg nanoparticles loaded into the gel).
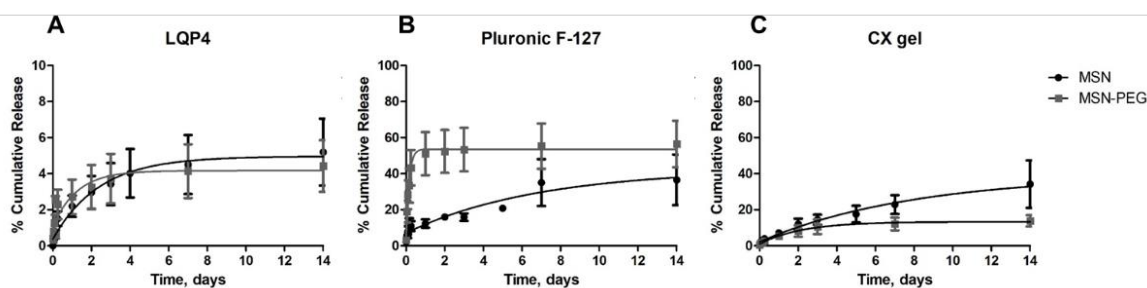
Figure 4.9: MSN and MSN-PEG release profiles from **A**- Liquid Polymer 4 (LQP4). **B**-Pluronic F-127 hydrogel and **C**- crosslinked gel (CX gel). The gels (50 µL) were loaded with 1 mg MSN or MSN-PEG. This weight was used to calculate the proportion (%) of cumulative release. See also Appendix 3 for further explanation on the calculations.

The same aspects considered for the evaluation of drug release can be used for the nanoparticles release, specifically the best mathematical model fit, the degradation profile of the gels and the possible nanoparticle-gel interactions.

According to the mathematical models **(Table 4.3)**, the release of MSN-PEG follows the Higuchi model in all the gels. However, as we determined before, this model is not a good fit for our systems due to its required assumptions. Besides that, the MSN-PEG release from the Pluronic F-127 is very poorly fitted in all the models. For MSN release from LQP4 and CX gel, the Korsmeyer-Peppas model with anomalous (non-Fickian) transport mechanism[305] is suggested by the data. In summary, it was not possible to correlate well the mathematical models with the experimental data.

Table 4.3: Mathematical model fitting parameters of MSN and MSN-PEG release from gels at 37 °C. R^2 is the correlation coefficient. The release rate constants (K_0, K_1 and K_H) and the release exponent (n) were calculated from the slopes of the respective mathematical models.

	Mathematical Models									
		Zero-Order		First-Order		Higuchi		Korsmeyer-Peppas		
		R^2	K_0	R^2	K_1	R^2	K_H	R^2	n	Release mechanism
LQP4	**MSN**	0.713	0.365	0.718	0.001	0.932	1.520	**0.934**	0.533	Anomalous
	MSN-PEG	0.594	0.253	0.599	0.001	**0.805**	1.09	0.754	0.322	quasi-Fickian
PF127	**MSN**	0.845	2.376	0.863	0.013	**0.917**	8.950	0.898	0.293	quasi-Fickian
	MSN-PEG	0.476	2.800	0.592	0.019	**0.644**	0.120	0.265	0.355	quasi-Fickian
CX	**MSN**	0.946	2.376	0.969	0.012	0.991	8.823	**0.993**	0.498	Anomalous
	MSN-PEG	0.824	0.940	0.838	0.004	**0.967**	3.756	0.886	0.523	Anomalous

Nevertheless, some conclusions can be drawn if we consider the degradation of the gels over time and the possible interactions of nanoparticles with the gel structures. Regarding the interaction of the nanoparticles with the Pluronic micelles, it is expected that the more hydrophilic MSN-PEG would be freely dispersed between the micelles in contact with the hydrophilic chains composed of poly(ethylene oxide). Indeed, it was shown before that PEG polymer solutions can favour the formation of micelle clusters of Pluronic F-127 and that PEG is separated from the micellar phase[306]. On the contrary, non-PEGylated MSN may present a lower dispersibility in the presence of Pluronic F-127, which can explain the differences in the release profiles observed between MSN-PEG and MSN.

Compared to the Pluronic hydrogel, the LQP4 displays a higher weight ratio of hydrophobic:hydrophilic polymer chains in the composition, meaning a larger water-free surrounding area for the cargo loaded into the gel[104]. The lack of significant differences between the release profiles obtained for MSN and MSN-PEG can be related to the limited dispersion of both types of nanoparticles into the gel network.

A uniform distribution of nanoparticles into the CX gel can be assumed to originate the sustained release from this gel. Furthermore, the porous gel structure

also contributes to the release profile with the nanoparticles diffusing into the highly porous network and delaying the release while the gel degrades.

The incorporation of nanoparticles into gels may add considerable benefits to drug delivery strategies. Formulations using drug-loaded Pluronic micelles[57,287,307,308] or based on PCLA-PEG-PCLA copolymer[103,108] incorporating drugs were already reported. However, using nanoparticles, a combination therapy composed of free drugs and drug-loaded nanoparticles into the gels can be proposed. Moreover, a two-step release may be achieved with first and immediate release of the free drug followed by the release of the drug loaded into the nanoparticles after being exposed to an environmental stimulus.

Taking together the analysis of the release profiles of both drugs and nanoparticles, we could make an informed decision about the combination of gel/drug/nanoparticles that is expected to follow the intended release pattern for the GlioGel. The LQP4 was the gel with the lowest release for both drugs and nanoparticles, while the Pluronic F-127 and the CX hydrogels released amounts of drugs that can generate an immediate presence of chemotherapy locally. This makes these hydrogels an interesting option for the final formulation. Thus, both hydrogels (Pluronic F-127 and CX) will be further evaluated regarding other essential characteristics of the final GlioGel formulation, including the maintenance of nanoparticles responsiveness, rheological properties and cytotoxicity effects.

4.2.4 Effect of the incorporation of nanoparticles on the redox-sensitive molecular gate

To successfully formulate the MSNs inside the hydrogels it is necessary that they keep their designed properties, namely the stimuli responsiveness of the molecular gate. This was addressed in gel release studies with MSN-PEG loaded with Safranin O (MSN-Saf-PEG), used as a model cargo.

The MSN-Saf-PEG nanoparticles were incorporated into the Pluronic F-127 and the CX gel, and the release was tested in the presence and absence of glutathione, which acts as the stimulus to open the nanoparticle pores.

We observed a burst release on the Pluronic F-127 gels and a more sustained release on the CX gel for Safranin-O, while the controls (without glutathione) showed a basal release of Safranin-O up to 24% (Pluronic F-127) and

32% (CX gel) **(Figure 4.10)**. This basal release is similar to the basal release observed for MSN-Saf-PEG, as shown in Chapter 3.
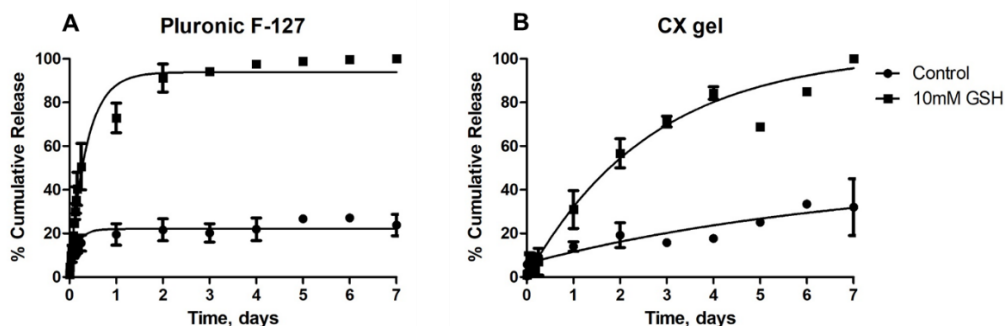
Figure 4.10: Safranin-O release from MSN-PEG incorporated into **A**-Pluronic F-127 hydrogel and **B-** Crosslinked gel (CX gel).

From this analysis, we showed that after incorporation into the gels and release from them, the nanoparticles were still able to respond to the reducing environment, opening the pores and releasing their cargo. Therefore, we can conclude that the disulphide PEG attachment is not affected by the nanoparticle incorporation into these gels. This is essential for the success formulation of the GlioGel.

4.2.5 Rheological properties of hydrogels

An important characteristic of hydrogels intended to be implanted in the body is their mechanical properties. The hydrogel behaviour upon an applied stress can show if the hydrogel will deform or break, and to what extent this will occur. Then, this information can be correlated with the same parameters of the tissue where the material will be implanted. Specifically, the GlioGel formulation is being designed for implantation in the brain, and the Pluronic F-127 and the CX gel were analysed and compared to the brain tissue.

The hydrogel stiffness was analysed through oscillatory rheological measurements of the storage modulus (G') and the loss modulus (G'') as a function of shear stress (amplitude sweep). The storage modulus describes the stiffness of the solid-like part of the material while the loss modulus describes the stiffness of the liquid-like part, and the total stiffness is given by the complex modulus[309].

From the amplitude sweep experiment, the linear viscoelastic region (LVR) of deformation of the Pluronic F-127 and CX gel was determined at increasing shear

stress. This is the range in which the hydrogel structure is maintained intact during the measurement.

For the CX gel, the range goes from 1 Pa up to 350 Pa at a frequency of 1 Hz **(Figure 4.11A)**, after which both the storage and the loss moduli decrease sharply. This decrease corresponds to changes occurring in the hydrogel microstructure. Because the decrease in the storage and loss moduli occur at the same value of shear stress, we can infer that the structure is breaking[310,311]. For the Pluronic F-127 gel, the LVR corresponds to 1 to 100 Pa at a frequency of 0.15 Hz **(Figure 4.11B)**.

In both hydrogels, the G' is greater than the G'', indicating that the sample has a gel-like or solid structure[311]. They are, therefore, viscoelastic solid materials. The highest value obtained for the CX gel on storage modulus is 24×10^3 Pa and for the Pluronic F-127 gel is 12×10^3 Pa, which means that the CX gel is stronger compared to the Pluronic F-127.
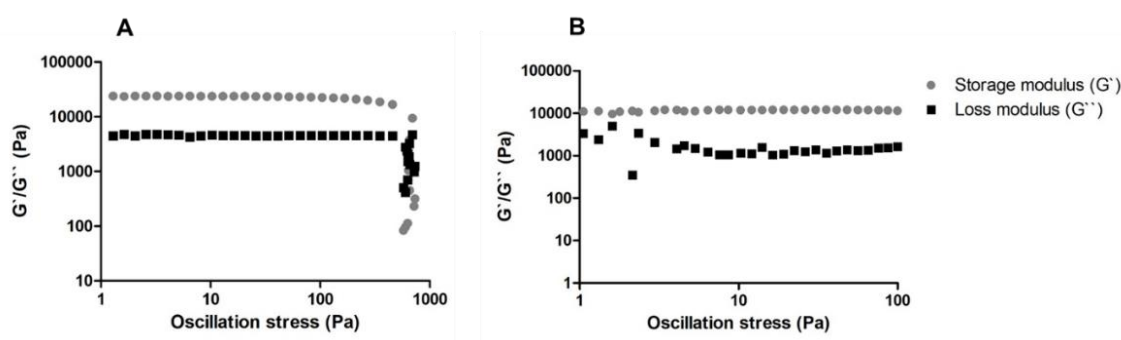
Figure 4.11: Amplitude sweep measurement of the gels. **A-** Crosslinked gel (CX) **B-** Pluronic F-127.

These measurements can also indicate if the stiffness of the hydrogels is close to that of the central nervous system tissues. This is an important aspect considering that our hydrogel formulation will be injected into the brain. Early studies on *in vitro* human brains reported a storage modulus (G') range between 600 and 1100 Pa and a loss modulus (G'') between 350 and 600 Pa[312]. However, rheological measurements are very dependent on the technique used and parameters such as the frequency applied. A more recent study measured the brain stiffness *in vivo* as around 12000 Pa for the white matter and 8000 Pa for the grey matter[313]. Studies using hydrogels for the analysis of glioblastoma cell behaviour frequently report material stiffness that is considered suitable and comparable to the brain tissue

between the range of 1000 to 5000 Pa [128,129]. In these cases, the hydrogel stiffness was able to induce cell proliferation and invasion in 3D cultures.

Therefore, the data reported on brain rheological properties can vary by more than two orders of magnitude between them[314]. Nonetheless, they all indicate a solid-like behaviour of the brain tissue. Our materials also have a solid-like behaviour with the Pluronic F-127 having the most similar stiffness to the data reported by McCracken *et al.*[313] on human brains, while the CX gel has twice the rigidity.

Finally, in a temperature sweep experiment we can observe the hydrogel thermosensitive properties and determine the exact temperature where the sol-gel transition occurs. This is the case of the Pluronic F-127 hydrogel, which shows a sol-gel transition starting at 23 °C. This is the intersect point between the storage and the loss modulus. After that, the storage modulus is always higher than the loss modulus, indicating a solid-like structure. The storage modulus increases until 28 °C, when it stabilizes as a gel at higher temperatures.
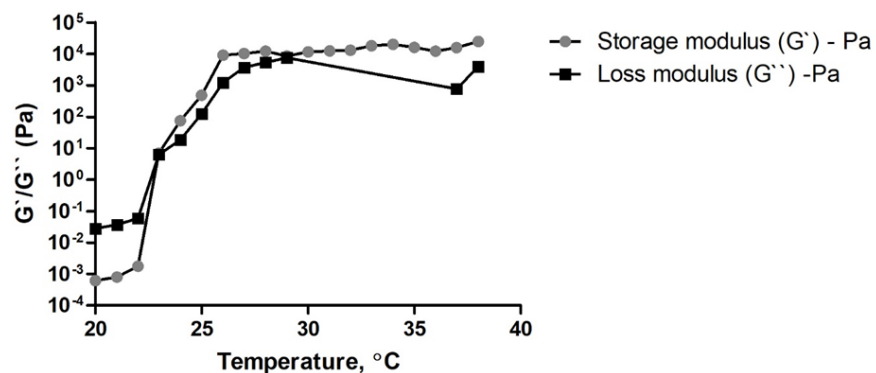
Figure 4.12: Temperature sweep measurement of Pluronic F-127 gel from 20 °C to 38 °C.

The Pluronic F-127 is available commercially and its characterization regarding both the temperature transition and stiffness was previously reported by several groups[300,315–317]. Conversely, acrylic based hydrogels comprise a range of materials with different structures that can also be combined with other polymers. Rheological characterization of some acrylic based gels was already reported but, as expected, they vary according to the materials specificity[318,319].

In conclusion, both the CX and the Pluronic F-127 gels present the solid-like behaviour characteristic of the brain tissue. Particularly, the higher rigidity of the CX

gel is not expected to compromise the GlioGel formulation performance on GBM treatment.

4.2.6 Cell studies

4.2.6.1 Cytotoxicity

To understand the effect of the hydrogels on cells, we analysed the viability of U-87 cells and primary neurons upon treatment with these materials *in vitro*. The Pluronic F-127 had a remarkable cytotoxic effect on U-87 cells, decreasing the viability to less than 50% while the CX gel was inert to these cells **(Figure 4.13A)**. Interestingly, none of the gels showed cytotoxic effects on primary neurons **(Figure 4.13B)**. Notably, a slight increase in viability was observed on neurons treated with the CX gel. Since neurons do not proliferate in culture[320], this increase in viability could be attributed to an increase in cell metabolic activity[321] or to the proliferation of remaining glial cells that were not completely removed in the process to establish the primary culture[322].
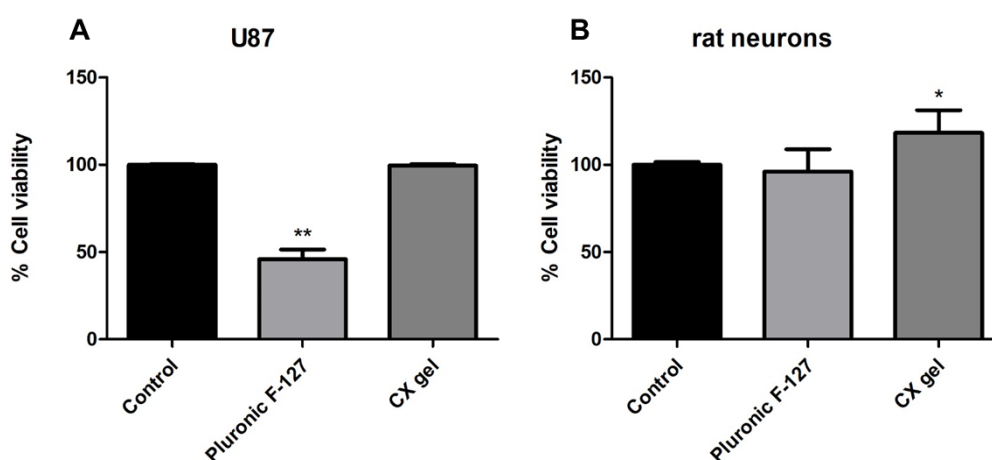
Figure 4.13: A- U-87 cells viability **B-** Primary rat neurons viability after treatment with 50 µl Pluronic F-127 gel and 50 µL piece of CX gel for 72 h. One-way ANOVA with Dunnet's post-test p <0.05 (*) and p <0.01 (**) vs control.

The effect of Pluronic copolymers on multiresistant cells were already reported[323,324]. Specifically, these effects are related to the cell energy metabolism[325] and they are intensified by the expression of drug efflux transporters such as P-glycoproteins[326]. One of the mechanisms of resistance to chemotherapeutic drugs in GBM cells is the overexpression of these membrane

transporters[26]. Therefore, we hypothesize that the cytotoxicity effect of Pluronic F-127 on U-87 cells may be related to membrane transporters expression.

On the other hand, hydrogels have been used to generate 3D models of neuronal cells showing good support in terms of cell-cell interaction and functional networks. For example, neurons were cultured on top of a synthetic hydrogel based on collagen-like peptide coupled to PEG and containing the integrin binding motif RGD. In these conditions, the neurons showed more neurite growth and formation of active neuronal networks compared to conventional culturing conditions and were able to form functional organoids[327].

Pluronic F-127 successfully improved the adhesion of neurons to polydimethylsiloxane on micro-chip devices[328]. Importantly, neuron network formation with dendritic differentiation and axon growth was three times higher compared to the surface without Pluronic F-127, possibly due to a better adhesion.

Co-culture conditions of neurons and glial cells have also been analysed with hydrogels. For instance, in the work by Evans *et al.*[329], primary cortical neurons and glial cells seeded in soft collagen hydrogels were viable for 8 days and presented a complex neurite network besides the characteristic neuronal electrical responses.

Based on the above reports, it seems that hydrogels used to support culture of neuronal cells can favour neuron network development, while some hydrogels can have an impact on cancer cell viability such as Pluronic gels. Both effects are acceptable in the GlioGel formulation if they do not affect the viability of healthy cells. Our results do not show any detrimental effect on neurons cell viability upon treatment with the Pluronic F-127 and the CX gel. Thus, we then evaluated the effect of these hydrogels on neuronal network development by means of neuronal complexity.

4.2.6.2 Neuronal complexity

Neurons complexity is important to maintain the physiological structure and function of the brain. Besides that, the GlioGel formulation to treat brain tumours should be effective against malignant cells but have minimal to no effect on the brain tissue. As we analysed for the nanoparticles, we also tested the effect of the hydrogels on neurons complexity.

The basics of this analysis are explained on Chapter 3. In summary, after treatment with the hydrogels, neurons were marked with the Microtubule Associated

Protein 2 (MAP-2) antibody and the nucleus was stained with DAPI **(Figure 4.14 A and B)**. This enables the analysis of the cell body and dendrites of neurons after treatment, because MAP2 is only expressed in these parts of the neuron. The analysis is based on the quantification of dendrite (or neurite) characteristics, particularly the number of primary neurites, branches, and intersections formed and the neuritic length.

Although the Pluronic F-127 did not show a cytotoxic effect on primary neurons, it significantly decreased the neuronal complexity in terms of number of branches **(Figure 4.14C)** and neuritic length **(Figure 4.14D)** formed by these cells *in vitro*. Neurons treated with Pluronic F-127 hydrogel have essentially the same number of primary neurites **(Figure 4.14E)** but their development was compromised. The CX gel also did not alter the number of primary neurites **(Figure 4.14E),** and it slightly reduced the neuritic length **(Figure 4.14D)** and the number of branches on the neurons **(Figure 4.14C)**.
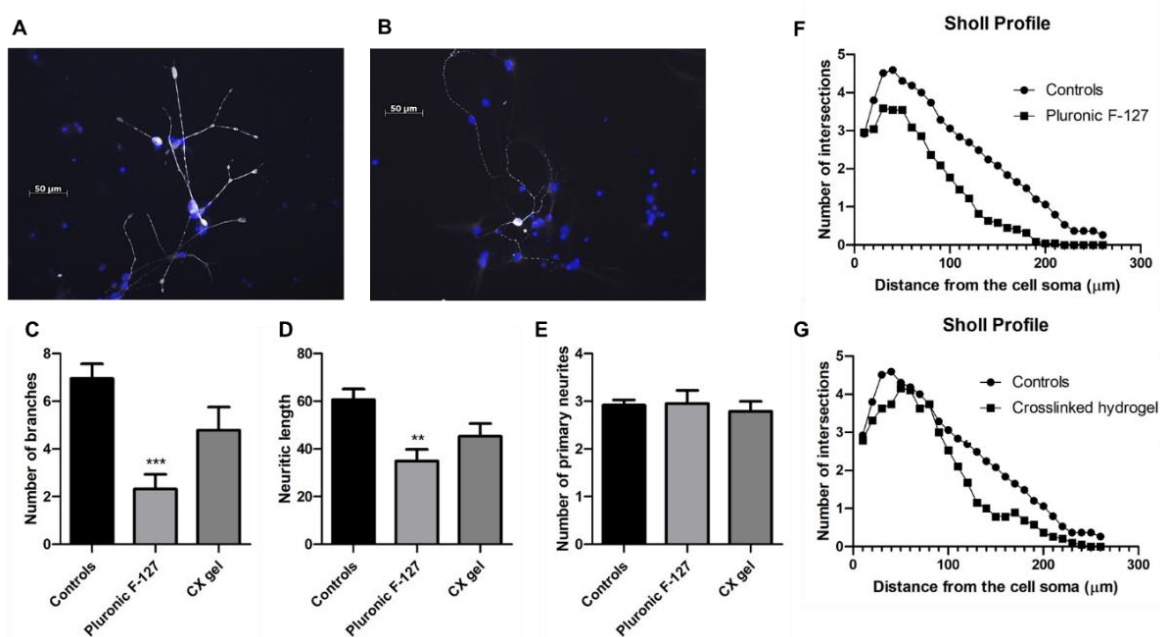
Figure 4.14: The hydrogel effect on primary rat neurons. MAP2 staining of neurons after treatment (72 h) with **A-** Pluronic F-127 and **B-** Crosslinked gel. **C-** Number of branches **D-** Neuritic length **E-** Number of primary neurites **F-** Sholl Profile for Pluronic F-127 and **G-** Sholl Profile of Crosslinked gel. One-way ANOVA with Dunnet's post-test $p < 0.01$ (**), and $p < 0.001$ (***) vs control.

The decrease in the number of branches is reflected in the Sholl Profile of both hydrogels **(Figure 4.14F and G)**. In the Sholl Profile of the Pluronic F-127 gel,

we observe a decrease in the number of neurite intersections on the neurons treated compared to the controls. This lower number is observed along all the extension analysed, starting from the cell body (soma) up to 260 µm. Analysing the Sholl Profile of the CX gel, we observe that the neurons formed similar number of intersections near the cell body, while it decreases compared to the controls from distances higher than 100 µm.

Sutachan *et al.*[330] reported an effect of Pluronic F-127 (0.02%) on neuronal depolarization induced by Ca^{2+} signalling, even though they did not observe any cell toxicity effect related to the polymer. This observation may be related to our observation of normal neuronal viability despite the neuronal complexity alteration. Moreover, the CX gel results are supported by the literature reports mentioned previously[327–329], which show hydrogels favouring neuronal development in 3D cultures.

These results support the use of the CX gel in the GlioGel formulation, considering that this gel did not affect the viability of healthy neurons and displayed a lower effect on the neurons complexity compared to the Pluronic F-127 gel.

4.3 Conclusions

The use of hydrogels to formulate a local delivery system against GBM has many advantages over current treatments. Of those, we highlight the possibility to incorporate both drugs and nanoparticles into the hydrogels and derive a combined treatment. This approach could expand the possibility of synergistic treatments that are usually essential for successful outcomes in GBM therapy.

In this chapter, we evaluated several aspects of the hydrogel performance that are crucial to build the GlioGel formulation to treat GBM. A sustained release of drugs and nanoparticles was observed for all the gels studied. However, only two of them (Pluronic F-127 and CX gel) released a proportion of drugs that may have a positive effect of immediate treatment upon injection after GBM surgery. These hydrogels were also able to release the nanoparticles in a sustained manner while they did not compromise the sensitivity of the molecular gate.

The use of a disulphide bond to attach PEG on the surface of nanoparticles and control the release of drugs via a redox stimulus brings two important advantages to the formulation. Firstly, the nanoparticles can deliver their cargo in selected environments decreasing unspecific and uncontrolled release. Secondly,

the presence of PEG on the surface of nanoparticles can improve the penetration in the brain tissue[331]. For this reason and considering our previous results on the redox-responsive nanoparticles, the use of MSN-PEG in our formulation is considered an advantage.

Of note, the CX gel was more effective in controlling the release of MSN-PEG compared to the Pluronic F-127 gel. This gel also showed better results regarding cell viability and neurons complexity, and a higher robustness considering both the degradation profile and rheological measurements. These aspects may be relevant for a one-time therapy in which an extended treatment window need to be covered.

The analysis of the hydrogels and the nanoparticles presented on the previous Chapters (Chapter 3 and 4), pointed to a GlioGel formulation composed of CX gel incorporating free TMZ and PTX-loaded nanoparticles. This is supported not only by the results presented, but also by a previous publication that highlights the benefit of combining TMZ and PTX for GBM therapy[332]. Importantly, the dose proposed in this study (0.6 mg/kg of TMZ and 0.3 mg/kg of PTX) is feasible to be reproduced in our formulation, enabling the *in vivo* evaluation of GlioGel with a safe dose that was previously tested.

In summary, the proposed formulation will expand the use of hydrogels for drug delivery applications by adding drug release mediated by the nanoparticles. Thus, the composite formulation could be injected in the tumour cavity after surgical resection and release the loaded nanoparticles over a period of several weeks. The nanoparticles then deliver their drug content upon redox stimulus, preferentially inside the cancer cells, at the same time that free drug is present in the tumour resection area to combat remaining cancer cells immediately after the surgery.

CHAPTER 5: THE EFFECT OF THE NEW GLIOGEL FORMULATION ON 3D *IN VITRO* AND *IN VIVO* MODELS

5.1 Introduction

The efficacy evaluation of new treatments for complex diseases such as cancer has to be performed as close as possible to reality. In this regard, several cancer disease models exist and can be divided into two main types, *in vitro* and *in vivo* models. While the *in vitro* approach will compose the initial evaluation and will permit a comparison and an informed selection of the best new treatment option, *in vivo* models can deepen the understanding related to efficacy and safety.

Cell culture using either immortalized or patient-derived cells is the most common *in vitro* model to test new cancer treatments[333,334]. Several immortalized cells of GBM origin have been used in GBM research and the classical ones include U-87[335,336], T98G[337] and U-251[338] from human origin and C6, a rat glial tumour cell line[339].

The main advantages on the use of cell culture are the simplicity of the model, which facilitates the analysis of different factors that can influence tumour progression, and the possibility to reduce the number of animals used in future *in vivo* studies. However, the genetic alteration imposed to the cells due to culture conditions is the major criticism of these models[340]. Despite that, the use of immortalized cell lines is still highly spread in scientific research.

These cell models evolved from 2D to 3D culturing aiming more complex and similar structures to real tumours[341]. Nowadays, the use of 3D models and patient-derived cells is increasing in an attempt to rely on a model more closely related to the clinical reality. Examples of 3D GBM models include spheroids and organoids that can fill the gap between the 2D cell culture and *in vivo* models[342] **(Figure 5.1)**.
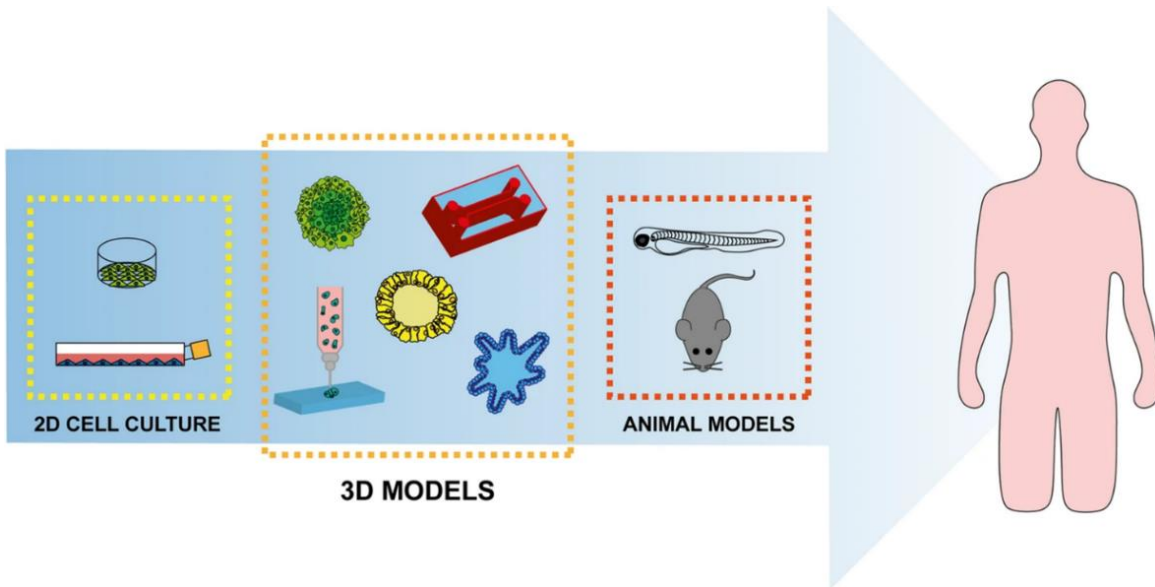
Figure 5.1: 3D cultures including spheroids, organoids and organ-on-a-chip may fill in the gap between 2D *in vitro* cell culture and animal models to accelerate the clinical translation of new treatments. Reproduced from [342] (open access article distributed under the terms and conditions of the Creative Commons Attribution (CC BY) license).

Spheroids are traditional 3D systems derived from a cell line monoculture while organoids are derived from different stem cell types and better recapitulate organ physiology[343]. Therefore, organoids are used to study organ development and disease modelling, specifically tumour biology and mutational signatures[344]. Spheroids are generally developed for high-throughput analysis and screening of new drugs[345] **(Figure 5.2)**.
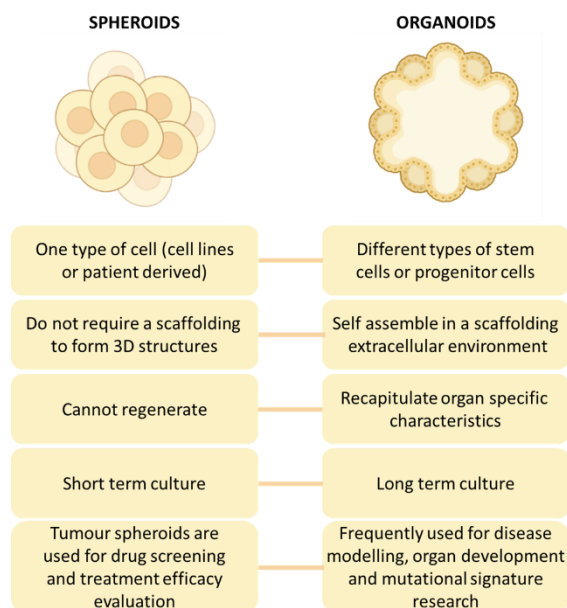
Figure 5.2: Differences and applications of spheroids and organoids.

There are mainly two approaches in the culture of 3D spheroids, namely the culture of established cell lines and the culture of patient-derived tumour cells. Moreover, different methods can be used for spheroids formation, such as pellet culture, liquid overlay, hanging drop and spinner cultures[346] **(Figure 5.3)**.
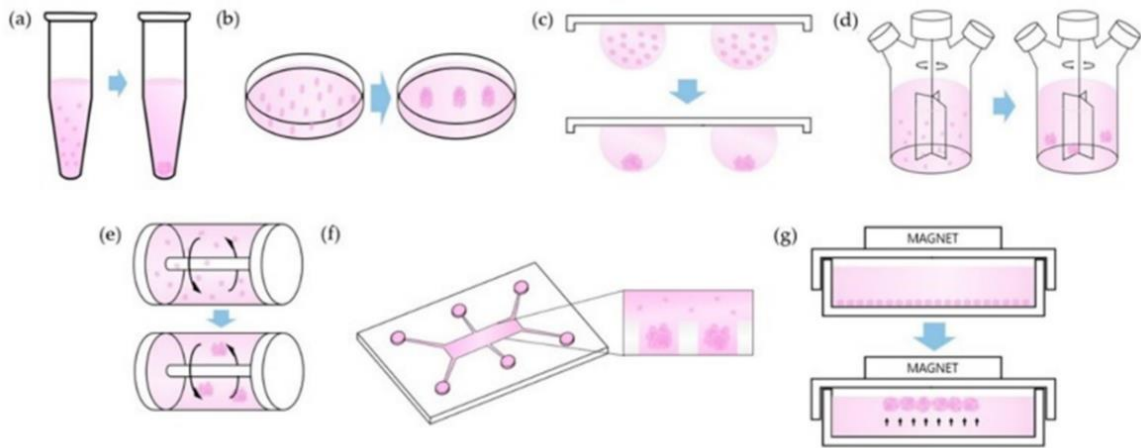
Figure 5.3: Methods of spheroids preparation: a- Pellet culture, b- liquid overlay, c- hanging drop, d-spinner culture, e-rotating vessel, f- microfluidics, g- magnetic levitation. Reproduced from[346] (open access article distributed under the terms and conditions of the Creative Commons Attribution (CC BY) license).

GBM spheroids of different cells have been used as 3D *in vitro* models to study several aspects of glioma disease as well as new treatments **(Table 5.1)**. For instance, an early study used U-251 spheroids to analyse glioma angiogenesis[347]. The spheroids were prepared in flasks coated with agar for 7 to 10 days until they reached 300 μm, when they were implanted in rat brains to study the vascularization process.

Spheroids have also been used to study glioma invasion. Stein *et al.*[348,349] proposed a mathematical model of tumour invasion based on *in vitro* data from U-87 spheroids. The U-87 spheroids were grown from an initial cell number of 500 cells for four days before being transferred to collagen gels used as 3D support. With this model, they showed that U-87 cells without EGFR mutation have a faster rate of cell migration away from the spheroid core. In addition, the authors compared the EGFR mutated and wild type U-87 cell regarding the growth of the spheroid core and the invasion radius, which are important parameters for a model development.

Other groups used GBM spheroids to test several aspects of new drugs or treatment formulations. For example, a poly(ether)-co-poly(ester) (PEPE) dendrimer

developed as a drug carrier against gliomas was tested for the ability to penetrate U-87 glioma tumour spheroids[350]. The dendrimers loaded with methotrexate (MTX) penetrate the spheroids within 12 h and the spheroids volume significantly decreased by around 80% of control spheroids volume with increasing drug concentrations.

Nanoparticles penetration on U-87 spheroids and the effect on the growth was also evaluated by Gao *et al.*[351] to prove the effect of their formulations on a 3D model. The synthesized poly(ethylene glycol)-poly(ε-caprolactone) nanoparticles functionalized with aptamers showed higher uptake into U-87 spheroids compared to non-functionalized nanoparticles. Moreover, the nanoparticles were able to inhibit tumour spheroids growth up to 80% compared to the control that doubled in volume over 5 days.

The combined effect of X-ray radiation, topotecan (topoisomerase I inhibitor) and A-966492 (PARP inhibitor) was evaluated in U-87 spheroids showing a radio- and chemo-sensitizer enhancement measured by surviving fraction in a clonogenic assay[352]. Berthier *et al.*[353] analysed the effect of sodium selenite (SS) on spheroids of different GBM cell lines (LN-229, T98G and U-87 cells) showing that this drug is more potent than the standard TMZ in the 3D spheroids culture. Furthermore, increasing concentrations of SS inhibit spheroid growth monitored by spheroid diameter measurement. Bayat *et al.* proposed a 3D culture system of U-87 cells on fibrin gel to study the effect of atorvastatin[354,355]. In this model, they showed a spheroid growth inhibition and an increase in apoptotic cells for increasing concentrations of drug.

Finally, in a recent work, Lázaro *et al.*[356] studied the interaction of graphene oxide (GO) flakes with U-87 spheroids. Interesting, they showed that the treatment with GO flakes induced spheroid growth but decreased cell proliferation. In addition, the material was able to penetrate the spheroids but remained outside the cells. The *in vivo* analysis of the same material in mice bearing U-87 tumours did not show any impact on tumour growth and progression.

Table 5.1: Key parameters and applications of spheroids derived from GBM cell lines used to study the effect of drugs and new treatments.

Spheroid cell line	Initial number of cells	Spheroid size	Growth time	Growing method	Measurements	Reference
U-251 cells	5×10^6	300 µm	7-10 days	Liquid overlay in 75 cm^2 flasks coated with agarose	angiogenesis	[347]
U-87 cells	500	not mentioned	4 days	Hanging drop method followed by growth in a collagen 3D gel	cell invasion	[348,349]
U-87 cells	1×10^5	not mentioned	7 days	Liquid overlay in plates coated with agarose	Growth inhibition, cell viability, diffusion of dendrimers into the spheroids	[350]
U-87 cells	2×10^3	1000 µm (from confocal microscopy image)	7 days	Liquid overlay in 48-well plates coated with agarose	Growth inhibition and drug uptake by spheroids	[351]
U-87 cells	5×10^5	300 µm	19 days	Liquid overlay in 25 cm^2 flasks coated with Poly-HEMA	Effect of radiation therapy on spheroids viability	[352]

LN-229, T98G and U-87 cell lines	3×10^3	Approximately 350 µm	3 days	Liquid overlay in a 96-well plate uncoated U-bottom	Drug uptake, spheroids viability and invasiveness	[353]
U-87 cells	not mentioned	Approximately 100 µm	4 days	Liquid overlay in non-adherent 8-well plate followed by culture on fibrin gel	Apoptosis by TUNEL assay, proliferation and cell cycle analysis	[354,355]
U-87 cells	1×10^4	500 µm	3 days	Liquid overlay in 96-well plates coated with agarose	Spheroid growth and proliferation, material penetration	[356]

Following the *in vitro* analysis of new treatments, the logical procedure includes the evaluation in pre-clinical studies. For these, *in vivo* models of GBM have been used **(Table 5.2).** Several of these models explore the use of intracranial administration of chemotherapy. Upadhyay *et al.*[357] compared the intracranial delivery of TMZ loaded into microcapsules and oral TMZ in F344 rats bearing a metastatic adenocarcinoma in the brain. The intracranial delivery was superior to the systemic delivery, increasing the overall survival by almost three times. Importantly, they showed that TMZ delivered intracranially distributes better in the brain and induces apoptosis.

Combination therapies are also explored in GBM animal models of local treatment. For instance, chitosan lipid nanoparticles loaded with siRNA anti-EGFR and anti-Galectin-1, administered through convection enhanced delivery (CED) into the brain of mice bearing U-87 tumours in combination with systemic TMZ, showed that treatment resistance could be overcome[358]. Specifically, the combination therapy significantly enhanced the mean survival time of mice from 34 days (individual treatments) to 39 days (combination). Another example is the combination of TMZ and PTX in a local treatment proposed by Zhao *et al*[332]. Particularly, they showed a synergistic effect between TMZ and PTX (drug ratio of 1:2) *in vitro* using U-87 glioblastoma cells. In addition, they analysed the combination therapy *in vivo* for safety and efficacy. The combination dose of 0.6 mg/kg TMZ and 0.3 mg/kg PTX administered in the brain of mice after tumour resection was safe and effective, significantly increasing the survival when compared to the resected but untreated group.

Local treatments using hydrogels can enormously benefit from the use of orthotopic *in vivo* models of GBM that comprise a resection surgery. Firstly, it is proven that tumour removal contributes to improve survival outcomes in patients[359]. Secondly, the resection step leaves an empty cavity where the treatment can be applied directly after the surgery procedure. Therefore, hydrogel formulations evaluated in pre-clinical models that use resection surgery have a higher potential for clinical translation because the surgical benefits are considered since the pre-clinical evaluation.

Examples of *in vivo* models that use a resection surgery step includes the one developed by Sweeney *et al.*[360] in athymic nude rats. In this model, the U-87 tumour grows during 4 weeks (1 x 10^5 cells injected), and then it is resected, leaving the cavity protected by a coverslip where a local therapy can be applied or the

recurrence can be monitored through bioluminescence imaging (BLI). Subsequently, another model using BLI monitoring was proposed for athymic mice by Kim *et al.*[361]. Different amounts of U-87 cells (1×10^4, 1×10^5 and 3×10^5) were injected into the brain and the tumour growth was monitored over 4 weeks through BLI, confirming a time dependent increase in both tumour volume and bioluminescence intensity. However, a resection was not proposed in this case.

In the past years, an orthotopic model comprising resection in athymic nude mice using U-87 cells was proposed by Bianco *et al.*[187]. In this model, the tumour resection was performed with a biopsy punch to specifically create a cavity where a local treatment can be applied. In addition, the tumour growth kinetics of U-87 cells in this mice strain was proposed along with tumour recurrence monitored by magnetic resonance imaging (MRI). This model was used to evaluate the effect of a local treatment based on a photopolymerizable hydrogel containing PTX-loaded PLGA nanoparticles[362]. A significant increase in the survival time and delay of tumour recurrence was observed in the treatment group compared to the controls (more than 50% long term survivals up to 150 days).

It is important to note that all models have limitations. One important drawback is related to the lack of cellular heterogeneity in tumour xenografts, especially the absence of immune cells. The use of immunocompetent models[363] is the way to overcome this restriction. In addition, immunocompetent models are interesting to investigate the role of the immune system in the treatment. For instance, oncolytic virus Delta24-RGD treatment in a murine model of GL261 tumour cells in C57BL/6 mice showed effect only when the immune response was intact[364,365]. The recruitment of macrophages and T cells was elicited after tumour cells infection with the virus and this was impaired by co-treatment with dexamethasone. Nonetheless, the use of immunocompetent mice is less common than the immunocompromised counterparts. This is due to the common use of human cells in animals, which requires the suppression of their immune response.

Considering the advantages and limitations of the models, we can still analyse treatment efficiency and draw conclusions using these pre-clinical models aiming the clinical translation of the proposed formulations.

Table 5.2: *In vivo* models of GBM.

In vivo model	Cell line	Tumour growth time	Treatment	Tumour monitoring	Reference
F344 rats bearing a metastatic adenocarcinoma in the brain	CRL1666 cells (rat mammary adenocarcinoma – 7.5×10^4 cells injected into the brain)	not measured	intracranial delivery of TMZ loaded into microcapsules and oral TMZ	n/a	[357]
female athymic Swiss nude mice	U-87 cells (3×10^4 cells injected into the brain)	14 days	chitosan lipid nanoparticles loaded with siRNA anti-EGFR and anti-Galectin- 1 in combination with systemic TMZ	Magnetic Resonance Imaging (MRI)	[358]
athymic nude rats	U-87 (1×10^5 cells injected into brain)	4 weeks	n/a	bioluminescence imaging (BLI)	[360]
athymic nude mice	U-87 cells (1×10^4, 1×10^5 and 3×10^5 cells injected into the brain)	4 weeks	n/a	bioluminescence imaging (BLI)	[361]

athymic nude mice	U-87 cells (3×10^4 cells injected into the brain)	13 days	photopolymerizable hydrogel containing PTX-loaded PLGA nanoparticles	Magnetic Resonance Imaging (MRI)	**187,362**
C57BL/6 mouse	GL261 cells (1×10^5, 1×10^4, 1×10^3 and 1×10^2 cells injected intracranially or subcutaneously)	not measured	n/a	n/a	363
C57BL/6 mouse	GL261 cells (5×10^4 cells injected into the brain)		oncolytic virus Delta24-RGD treatment and combined treatment with dexamethasone	Histology	364,365

(n/a = not applied)

In the previous chapters, the development of a new biomaterial formulation to treat GBM was shown. This formulation combines a hydrogel, which will fill the cavity left by the resection of the tumour, free drug and drug-loaded nanoparticles, designed to be able to release a chemotherapeutic drug in a controlled and sustained manner. The results in the previous chapters using 2D cell culture were used to direct the selection of the most promising formulation to proceed in the 3D spheroids model test and the *in vivo* experiment.

This chapter focuses on the tests of the lead formulation (GlioGel), consisting of the CX gel with free TMZ and MSN-PTX-PEG, both in 3D spheroids and in an *in vivo* animal model of GBM. We specifically evaluated the effect of the combination treatment on the viability, size and morphology of 3D spheroids of U-87 cells, and the nanoparticles ability to penetrate these structures. In addition, a pilot *in vivo* experiment was performed aiming to test the efficacy of the new formulation. For this, the tumour growth kinetics *in vivo* was monitored to achieve similar tumour sizes in all animals, followed by resection surgery and direct treatment of the area with the GlioGel formulation.

5.2 Results and discussion

5.2.1 GlioGel *in vitro* release

The lead GlioGel formulation comprises the CX gel loaded with free TMZ and PTX-loaded MSN-PEG. As mentioned before, a safe dose previously tested for this combination treatment in mice[332] was chosen to be used in the *in vivo* evaluation of the GlioGel. This dose corresponds to 0.6 mg/kg TMZ and 0.3 mg/kg PTX. According to our loading efficiency, the calculated dose of nanoparticles corresponding to the PTX dose is 4 mg/kg MSN-PTX-PEG. Finally, considering the maximum volume of injection in the mice brain of 5 µL, the GlioGel formulation would contain 3 mg/mL TMZ and 20 mg/mL MSN-PTX-PEG.

The *in vitro* release of TMZ from the CX gel was evaluated when the drug was co-loaded with MSN-PTX-PEG at the specific dose determined for the *in vivo* assay (3 mg/mL TMZ and 20 mg/mL MSN-PTX-PEG). In the GlioGel formulation, incorporating both the drug and the nanoparticles, the CX gel presented the same appearance and undergone the same sol-gel process as previously observed. A higher proportion of TMZ release was observed for the GlioGel formulation when compared to the release of TMZ incorporated alone in the gel **(Figure 4.4F)**.

Surprisingly, the immediate release (burst) was also faster, occurring in the first hour, followed by a sustained release up to 40% in 14 days **(Figure 5.4).**
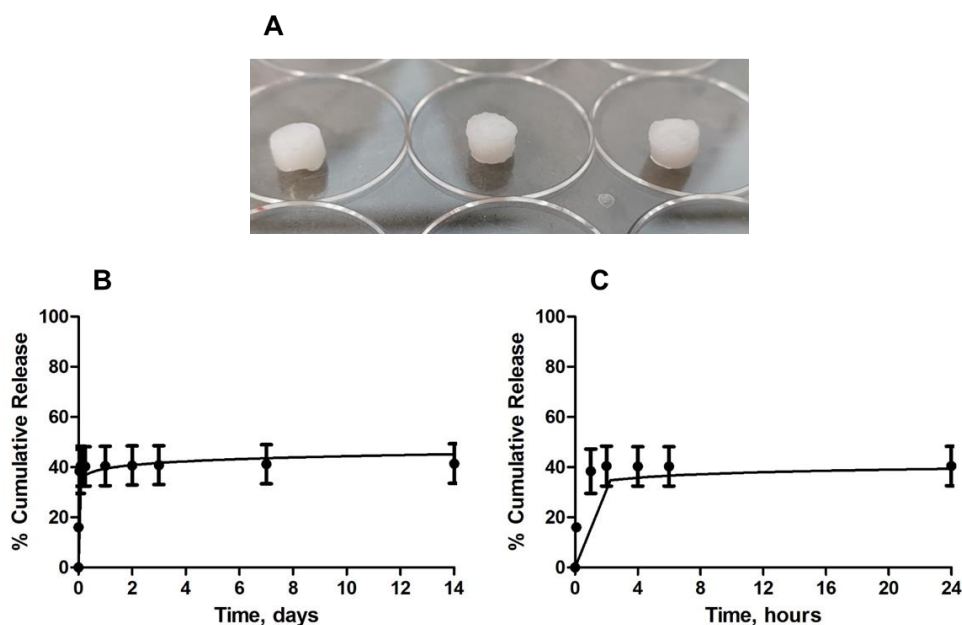
Figure 5.4: TMZ release from GlioGel formulation. **A-** CX gel (50 µL) was formulated with 150 µg TMZ and 1 mg MSN-PTX-PEG (corresponding to 270 µg PTX). **B-** TMZ release from GlioGel over 14 days **C-** The first 24 h of TMZ release.

This can be related to both the presence of nanoparticles and the lower dose of TMZ incorporated into the gel. A total of 150 µg TMZ was present in the analysed formulation combined with 1 mg of MSN-PTX-PEG, corresponding to 270 µg of PTX. Of note, the mathematical models of the release suggest the same release mechanism of the TMZ alone in the gel that is the diffusion-controlled release described by the Korsmeyer-Peppas equation[297]. The respective graphs and parameters originated from the application of the mathematical models can be seen on **Appendix 4**.

Due to health and safety reasons regarding the use of chemotherapeutic drugs, the analysis of nanoparticles release from the gel via NTA in the presence of free TMZ was not performed. However, it is important to highlight the correlation between the performance of the two releases aiming to understand the formulation behaviour. The total amount of TMZ released from the hydrogel formulation containing nanoparticles corresponds to 300 µM. Taken the estimated proportion of MSN-PEG released from the CX gel of 13.8%, which corresponds to 9.8 µM PTX, an estimated combination of 1 to 30 µM PTX:TMZ is expected in the release treatment over the 14 days.

It is important to consider the possible effects of this drug combination, specially related to effective cytotoxicity both *in vitro* and *in vivo*. Besides that, the expected fate of each formulation component has to be considered. While the free drug can exert an immediate effect, it is metabolized faster compared to the drug encapsulated in the nanoparticles. The nanoparticles may have more time to penetrate the tissue and exert their effect over a longer period of time. All these factors will influence the drug ratio in the *in vivo* scenario. Therefore, we proceeded with an *in vitro* evaluation of this drug combination using a 3D cell culture system, which is considered a more clinically relevant model.

5.2.2 3D *in vitro* cell culture: U-87 cells spheroids

The use of 2D cultures for *in vitro* experiments has been an established laboratory practice for many years. However, the resemblance of the cell in a 2D system with the clinically relevant conditions found in patients are intensely discussed, especially for cancer cell lines. Therefore, we also analysed the GlioGel formulation *in vitro* using a 3D culture of U-87 cell spheroids.

We opted for a scaffold free approach using a specialized culture plate that prevents cell attachment to generate tri-dimensional U-87 cells spheroids. This approach was preferred over the use of a scaffold-based system, such as collagen gels, to facilitate the drug treatment evaluation. Scaffold-based systems may require protocol adaptations, different viability kits or even removal of the scaffold for proper viability and imaging evaluation[366]. Despite the fact that U-87 cells are able to spontaneously stick to each other forming spheroids, the methods followed in this regard are very diverse. Thus, we firstly established our own protocol by testing different initial amounts of cells and monitoring the growth over a week period.

The shape of the final spheroids was very similar in spite of the absence of an artificial scaffold to help their formation. However, we identified some key parameters that influence the spheroids formation and uniformity. For example, the addition of 1% DMSO from day 0 seems to impair cell cluster formation, delaying the spheroid growth rate and originating smaller spheroids compared to the condition in the absence of 1% DMSO **(Figure 5.5 and Table 5.3)**. Moreover, irrespective of the initial amounts of cells, the spheroid diameters were very similar at day 7 in the presence of DMSO (251 µm, 292 µm and 382 µm in average for 250, 500 and 1000 cells, respectively).

Table 5.3: Spheroid growth rate**.**

Growth rate without DMSO

	Day 2 to day 5	Day 2 to day 7	Day 4 to day 7
250 cells	58 ± 34%	90 ± 21%	42 ± 12%
500 cells	69 ± 45%	131 ± 54%	55 ± 19%
1000 cells	68 ± 43%	116 ± 57%	49 ± 26%

Growth rate with DMSO

	Day 2 to day 5	Day 2 to day 7	Day 4 to day 7
250 cells	36 ± 37%	40 ± 25%	17% ± 15%
500 cells	51 ± 38%	83 ± 61%	35 ± 31%
1000 cells	44 ± 37%	48 ± 32%	26 ± 27%

In the absence of DMSO, the sizes of the spheroid on day 1 were very similar for all three initial amounts of cells. However, some individual cells and small fragments were still present for 250 and 500-cell spheroids conditions. This was improved on day 2. Hence, a minimum of 2 days is advised in order to have uniform and perfectly formed spheroids for further analysis.

The growth rate for all three conditions was similar and bigger spheroids were obtained after 7 days with increasing number of initial cells seeded. Furthermore, the bigger the spheroid gets, the denser and compact it becomes. Highly dense and compact U-87 cell spheroids from 1×10^5 cells growing for 7 days were reported previously[350]. Bayat *et al.*[355] reported spheroids grown for 4 days and then encapsulated in fibrin gels that are morphologically more similar to our spheroids. Unfortunately, the initial number of cells used in this case was not disclosed.
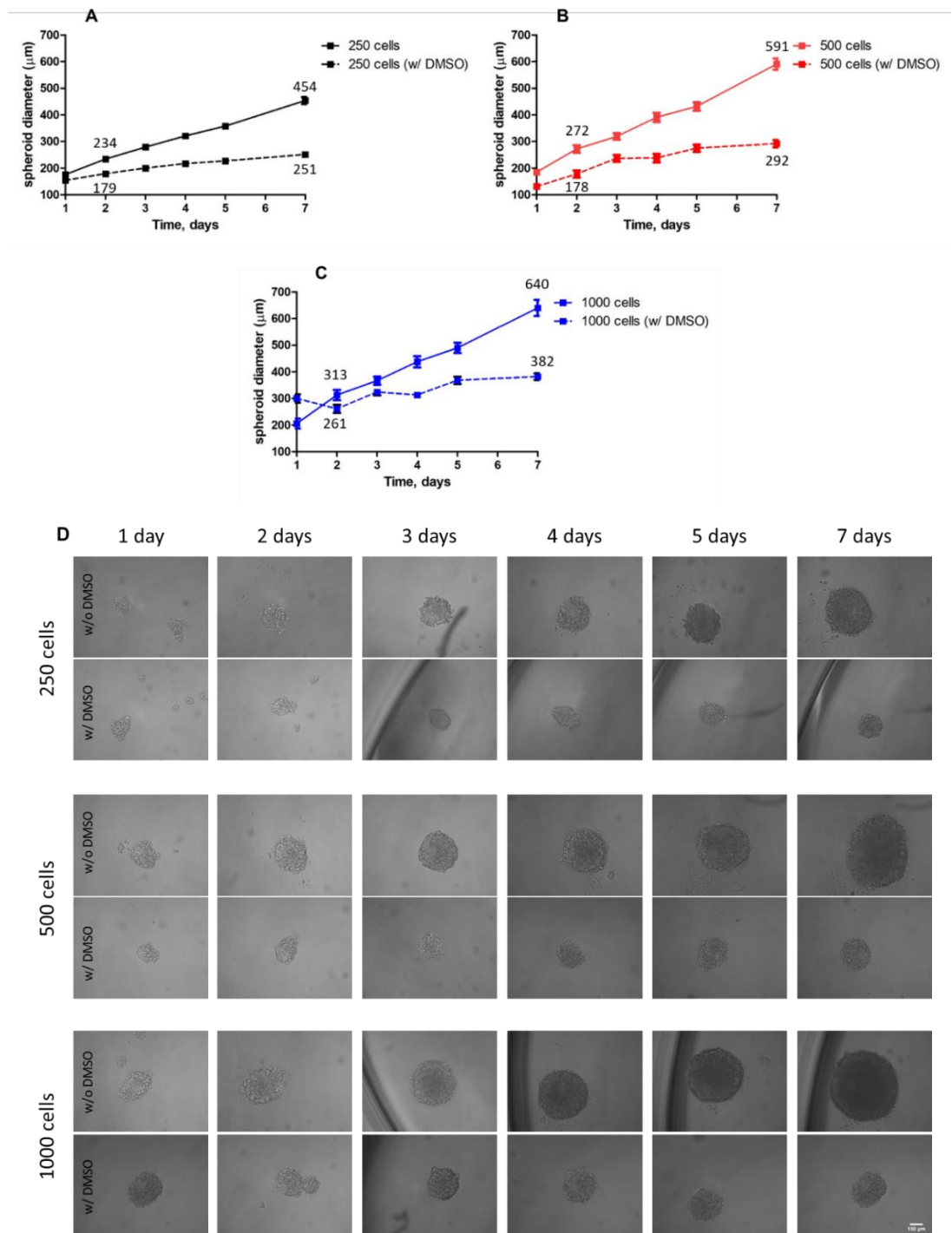
Figure 5.5: U-87 spheroid formation and growth using the Nunclon Sphera low attachment 96-well plate from different initial number of cells in the presence or absence of 1% DMSO: **A-** 250 cells. **B-** 500 cells. **C-** 1000 cells. **D-** Representative images of spheroids morphology in the first 7 days of culture (scale bar 100 µm).

Similar growth curves for U-87 cell spheroids were reported by Stein *et al.*[348], although the growth was in a collagen gel using 500 cells initially. Gao *et al.*[351] prepared U-87 cell spheroids with 2 x 10³ cells initially and seemed to have

spheroids of 1000 μm after 7 days. This correlates well with our curves if we take into account that we used half of the number of cells to start the spheroids.

The initial number of cells is important not only for the initial formation and uniformity of the spheroids but also for the following analysis. Some cell viability tests recommend a limit of detection (LOD) of at least one thousand cells. In fact, the viability measurement of the spheroids through an acid phosphatase assay[183] proved to be impossible with the 500-cell spheroids.

The 1000-cell spheroids presented a uniform spheroid formation in 2 days and a consistent growth curve generating bigger spheroids compared to the other two conditions, even in the presence of 1% DMSO. This may be important when we test the chemotherapeutic drug, which needs to be resuspended in this solvent. Therefore, we decided to use the 1000-cell spheroid model for our further analysis.

The study of the combination treatment (TMZ + PTX) on U-87 spheroids was based on the analysis of the *in vitro* release of both components from the hydrogel. In the GlioGel, the release *in vitro* over 14 days corresponded to 300 μM TMZ and 9.8 μM PTX. In 3 days, the same 300 μM TMZ were already released and small release increments continues up to 14 days and 7 μM PTX were released. Based on these results, we studied the effect of the formulation components, separately or in combination, on spheroids grown for 2 days or 4 days for 72 h.

Firstly, the average spheroid diameter at day 2 was 313 ± 82 μm and at day 4 was 438 ± 76 μm. This difference in size is visible in the spheroid appearance as shown in **Figure 5.5D**. The spheroids grown for 4 days are much more compact and dense compared to spheroids grown for 2 days. Therefore, we hypothesised that one could represent an initial stage of tumour development where the tumour mass is less strong (2 days) and the other one could be a later stage when the tumour mass is robust and may be more resistant to any treatment (4 days).

Indeed, the MSN-PTX-PEG showed a dose-dependent effect on 2-day spheroids with 100 μg/mL, 200 μg/mL and 250 μg/mL decreasing the viability to 50%, 48% and 45%, respectively, while MSN-PEG showed viabilities higher than 80% **(Figures 5.6A and B).**
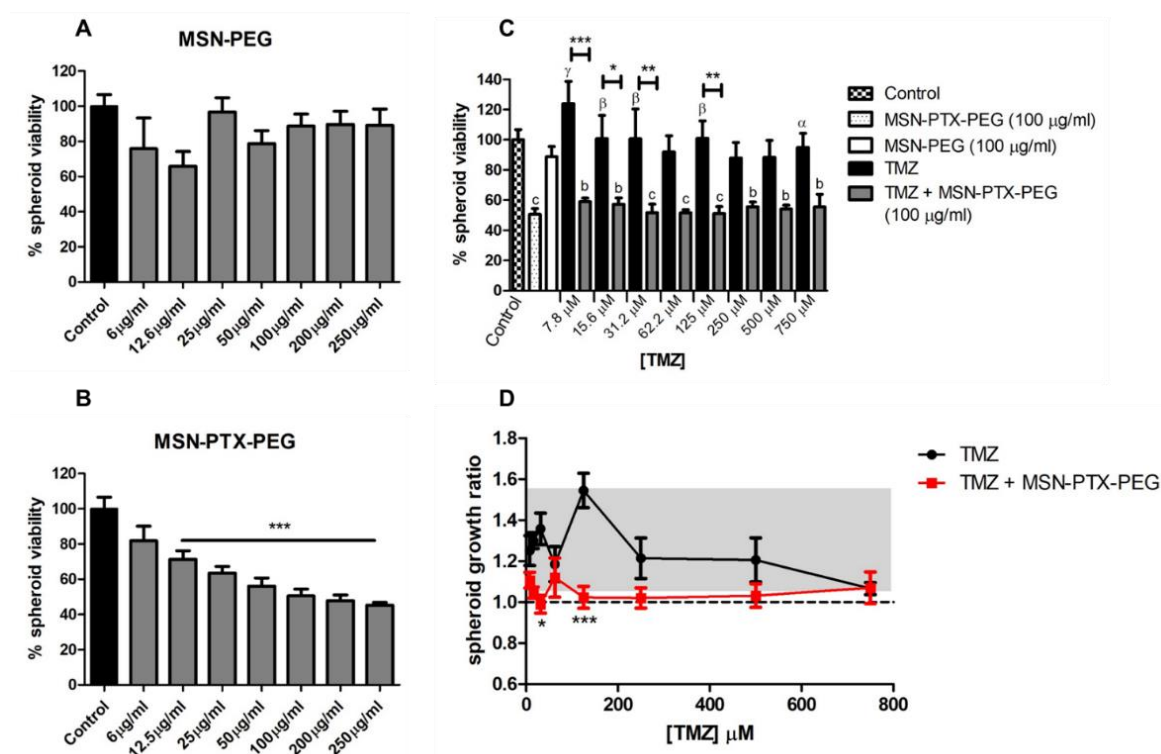
Figure 5.6: Combination treatment effect on U-87 spheroids grown for 2 days. The spheroids were treated for 72 h with different concentrations of **A-** MSN-PEG. **B-** MSN-PTX-PEG. **C-** TMZ alone and in combination with 100 µg/mL MSN-PTX-PEG. **D-** Spheroids growth ratio after treatment with different concentrations of TMZ alone and in combination with 100 µg/mL MSN-PTX-PEG. The grey area corresponds to the growth ratio ± SEM of control spheroids. One-Way ANOVA with Dunnett's post-test for **(A)** and **(B)** and Tukey's post-test for **(C)**. In **(C)**, differences to the control (spheroids without treatment) are represented as follows: $a = p < 0.05$; $b = p < 0.01$; $c = p < 0.0001$. Differences to MSN-PTX-PEG (100 µg/mL) are represented as follows: $\alpha = p < 0.05$; $\beta = p < 0.01$; $\gamma = p < 0.0001$. Differences between free TMZ and combination treatment is represented as follows: $* = p < 0.05$; $** = p < 0.01$; $*** = p < 0.0001$. Two-way ANOVA for **(D)** showing differences between the two treatments (TMZ or TMZ+MSN-PTX-PEG) at the same TMZ concentration: $* = p < 0.05$; $** = p < 0.01$; $*** = p < 0.0001$.

The spheroids observed under the microscope after the treatment confirm this result **(Figure 5.7)**. The spheroids treated with MSN-PEG are mostly intact and maintained their shape and structure while the ones treated with MSN-PTX-PEG showed signs of a slight disintegration with some small fragments or cells around them, a more loose aspect and in some cases smaller sizes.

The in vitro release of MSN-PEG from the CX gel over 3 days was calculated as 100 ug/mL **(Figure 4.9 C)**. Thus, this concentration was selected to analyse the

effect of MSN-PTX-PEG in combination with TMZ in the spheroid assay. The increasing concentrations of TMZ had almost no effect on these spheroids **(Figure 5.6C)**. The highest concentration tested (750 µM), which is near the IC50 calculated previously for the 2D culture, had an effect of only 5% on the viability of the spheroids. Hence, the TMZ IC50 was not reached on this 3D culture. At the same time, the combination of increasing concentrations of TMZ with 100 µg/mL MSN-PTX-PEG decreased the viability to a similar extent compared to MSN-PTX-PEG alone, indicating an effect exclusively by the nanoparticles. The highest effect observed in the combination treatment was from 125 µM TMZ + 100 µg/mL MSN-PTX-PEG corresponding to 1: 18 (µM) PTX to TMZ. This was 51% spheroid viability compared to 50% of nanoparticles only and no effect for TMZ alone.

The same aspects observed on the appearance of the spheroids after the treatment with MSN-PTX-PEG were observed for the combined treatment (TMZ + MSN-PTX-PEG). In all combination ratios, small fragments and individual cells detached from spheroids **(Figure 5.7).** Although this cell detachment was not enough to substantially decrease the size of the spheroids, it inhibited the growth over time. On the contrary, spheroids treated with TMZ alone grew in most of the concentrations tested **(Figure 5.6D and 5.7)**. At 125 µM and 31.2 µM TMZ, the combined treatment inhibited spheroid growth significantly compared to TMZ alone. These concentrations correspond to 1:18 and 1:4 (µM) PTX to TMZ. Moreover, even at lower combination ratios of 1:2 (15.6 µM TMZ) and 1:1 (7.8 µM), a slight inhibition of growth was observed.
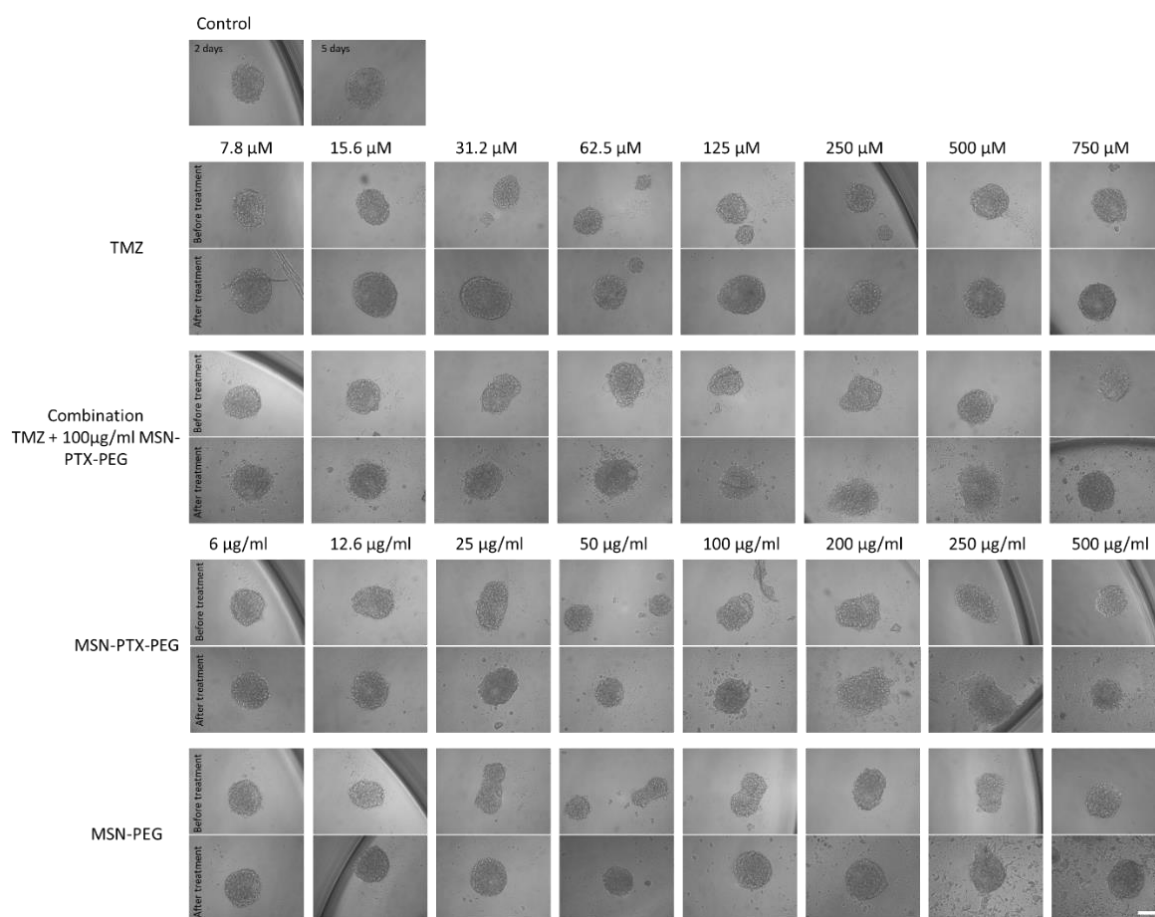
Figure 5.7: Representative images of spheroids grown for 2 days (upper panels) and treated for 72 h (lower panels) with TMZ, TMZ combined with 100 µg/mL MSN-PTX-PEG, MSN-PTX-PEG and MSN-PEG. Images (x10) are representative of three independent experiments (scale bar 200 µm).

Spheroids grown for 4 days before treatment were also mostly inert to MSN-PEG, maintaining viabilities higher than 70%, intact structure and even grow over time **(Figure 5.8A and 5.9)**. Interestingly, the effect of MSN-PTX-PEG was less concentration dependent compared to 2-day spheroids. MSN-PTX-PEG in concentrations higher than 25 µg/mL decrease the viability to 62 ± 4% in average. In these concentrations we could also observe the detachment of cells from the spheroids **(Figure 5.8B and 5.9).**

Similar to the 2-day spheroids, TMZ alone had almost no effect on these spheroids. However, the highest concentration (750 µM) decreased spheroid viability to 73%, which was the maximum effect and comparable to 125 µM TMZ (74%) **(Figure 5.8C)**. This result is very surprising since these spheroids are bigger, more compact and possibly more resistant to any treatment[367]. Nevertheless, the IC50 for TMZ was also not reached.

MSN-PTX-PEG at 100 µg/mL decreased spheroids viability to 66% **(Figure 5.8B and C)** and again the combined treatment effect was largely due to the MSN-PTX-PEG. **(Figure 5.8C)**. From 31.2 µM to 500 µM TMZ, the effect was slightly higher in the combination treatment compared to MSN-PTX-PEG (100 µg/mL), although not statistically significant.
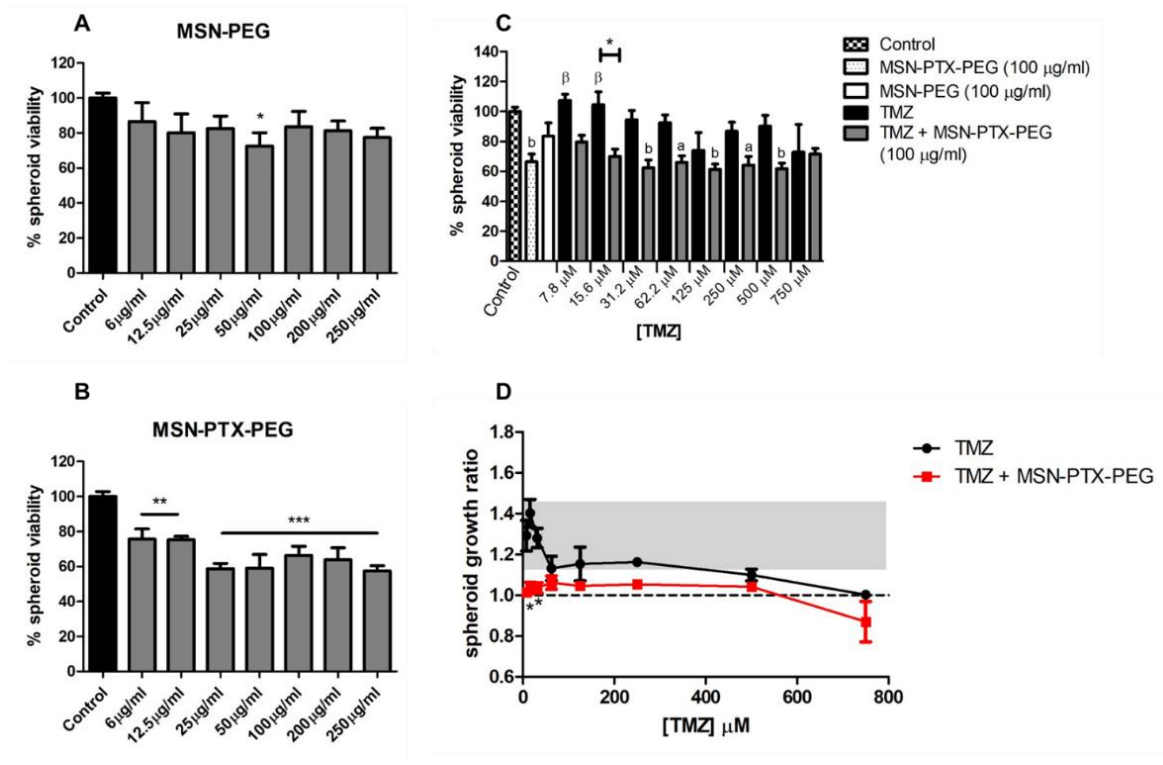
Figure 5.8: Combination treatment effect on U-87 spheroids grown for 4 days. The spheroids were treated for 72 h with increasing concentrations of **A-** MSN-PEG. **B-** MSN-PTX-PEG. **C-** TMZ alone and in combination with 100 µg/mL MSN-PTX-PEG. **D-** Spheroids growth ratio after treatment with different concentrations of TMZ alone and in combination with 100 µg/mL MSN-PTX-PEG. The grey area corresponds to the growth ratio ± SEM of control spheroids. One-Way ANOVA with Dunnett's post-test for **(A)** and **(B)** and Tukey's post-test for **(C)**. In **(C)**, differences to the control (spheroids without treatment) are represented as follows: a = p < 0.05; b = p < 0.01; c = p < 0.0001. Differences to MSN-PTX-PEG (100 µg/mL) are represented as follows: α = p < 0.05; β = p < 0.01; γ = p < 0.0001. Differences between free TMZ and combination treatment is represented as follows: * = p < 0.05; ** = p < 0.01; *** = p < 0.0001. Two-way ANOVA for **(D)** showing differences between the two treatments (TMZ or TMZ+MSN-PTX-PEG) at the same TMZ concentration: * = p < 0.05; ** = p < 0.01; *** = p < 0.0001.

Indeed, we observed the characteristic cell detachment from spheroids in all combination ratios comparable to the effect of nanoparticle alone. This was

sufficient to inhibit spheroid growth over time. Conversely, TMZ alone only slightly inhibited the growth from 62.5 µM but without visible cell detachment. Notably, the spheroids were denser when treated with TMZ alone **(Figure 5.8D and 5.9)**.
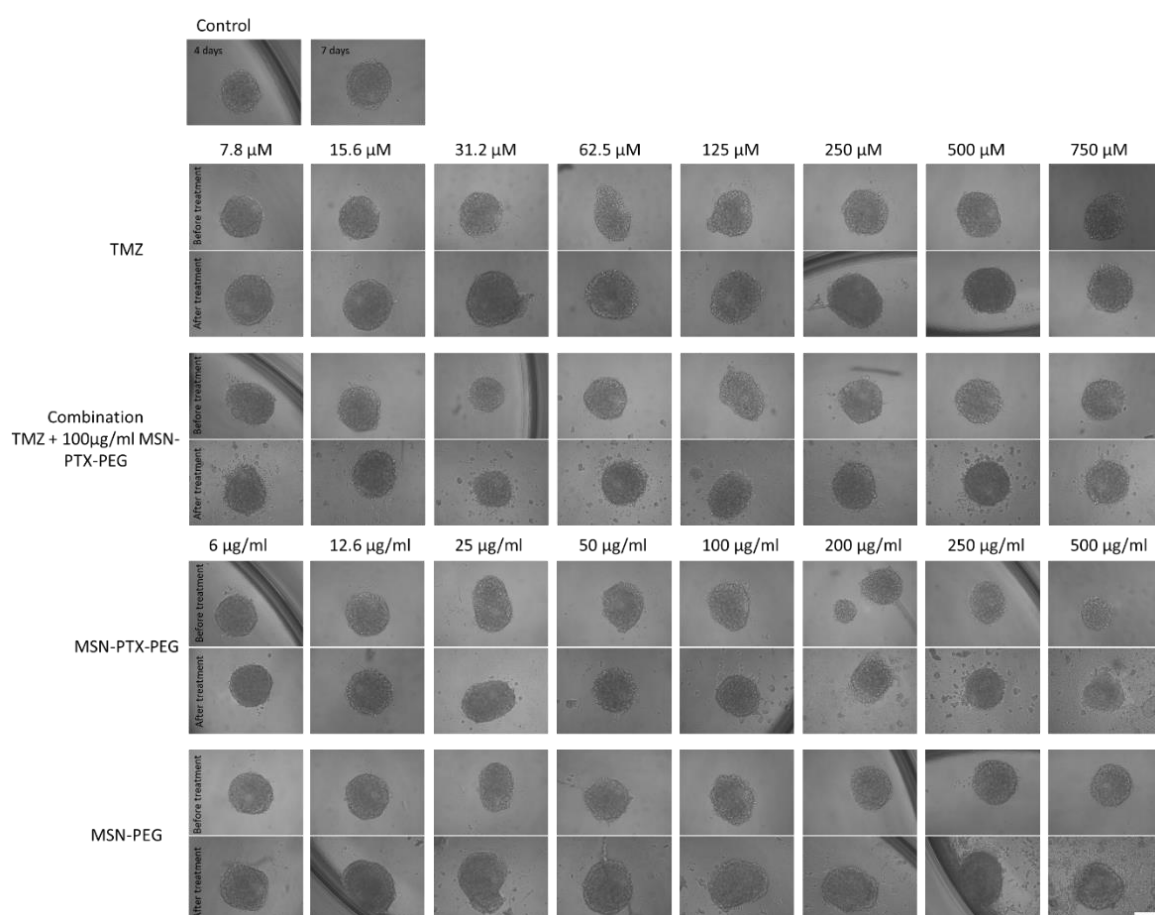
Figure 5.9: Representative images of spheroids grown for 4 days (upper panels) and treated for 72 h (lower panels) with TMZ, TMZ in combination with 100 µg/mL MSN-PTX-PEG, MSN-PTX-PEG and MSN-PEG. Images (x10) are illustrative of three independent experiments (scale bar 200 µm).

For both types of spheroids (2-day and 4-day), we observed cell detachment as a result of the treatments. Cell detachment from spheroids of different GBM cell lines, including U-87 cells, were reported upon treatment with sodium selenite[353]. This was also correlated with a decrease in the spheroid diameter and inhibition of cell dissemination and invasion both in Matrigel and in media.

Another important aspect from our analysis is the combination ratio of PTX and TMZ. Our combination strategy failed to show synergistic or additive effects on spheroids viability. However, the most pronounced effects were seen at 125 µM TMZ combined with MSN-PTX-PEG for both spheroid sizes. This combination ratio

corresponds to 1:18 (μM) PTX to TMZ. Lower combination ratios also showed effects on spheroid growth inhibition for both spheroid sizes.

Synergistic effects on U-87 cells for PTX and TMZ loaded into nanoparticles were reported for weight ratios of 1:5[368]. The combination of PTX loaded in PLGA nanoparticles and TMZ in U-87 cells showed different degrees of synergistic effect, with the largest effect at 1:2 and 1:3, and intermediate effect at 1:20 PTX to TMZ[332]. Finally, Kessel *et al.*[369] demonstrated that TMZ (200 μM) is less effective than PTX (0.5 μM) in decreasing U-87 spheroid size when treated separately. At these concentrations, free PTX decreased spheroid diameter by almost 40% while free TMZ decreased by 20%. Of note, their spheroid diameter was comparable to our 4-day spheroids, but the treatment was performed for 13 days.

The inhibition of spheroid growth upon treatment with TMZ and PTX is relevant for the effectiveness of the GlioGel treatment. This effect may be related to the nanoparticles ability to penetrate the spheroids. Therefore, this will be analysed in the following section. Moreover, this effect may also generate a decrease in tumour volume *in vivo*, which will also be analysed in the *in vivo* experiment.

5.2.3 Nanoparticles penetration into U-87 spheroids

The effect of nanoparticles on the spheroids is directly dependent on the ability to penetrate them. Therefore, we analysed the ability of MSN and MSN-PEG to penetrate spheroids grown for 2 days or 4 days after 24 h or 72 h of incubation.

In spheroids grown for 2 days, higher penetration was observed for MSN-PEG compared to MSN after both 24 h and 72 h incubation **(Figure 5.10)**. Of note, at 24 h the difference was statistically significant (p < 0.05).
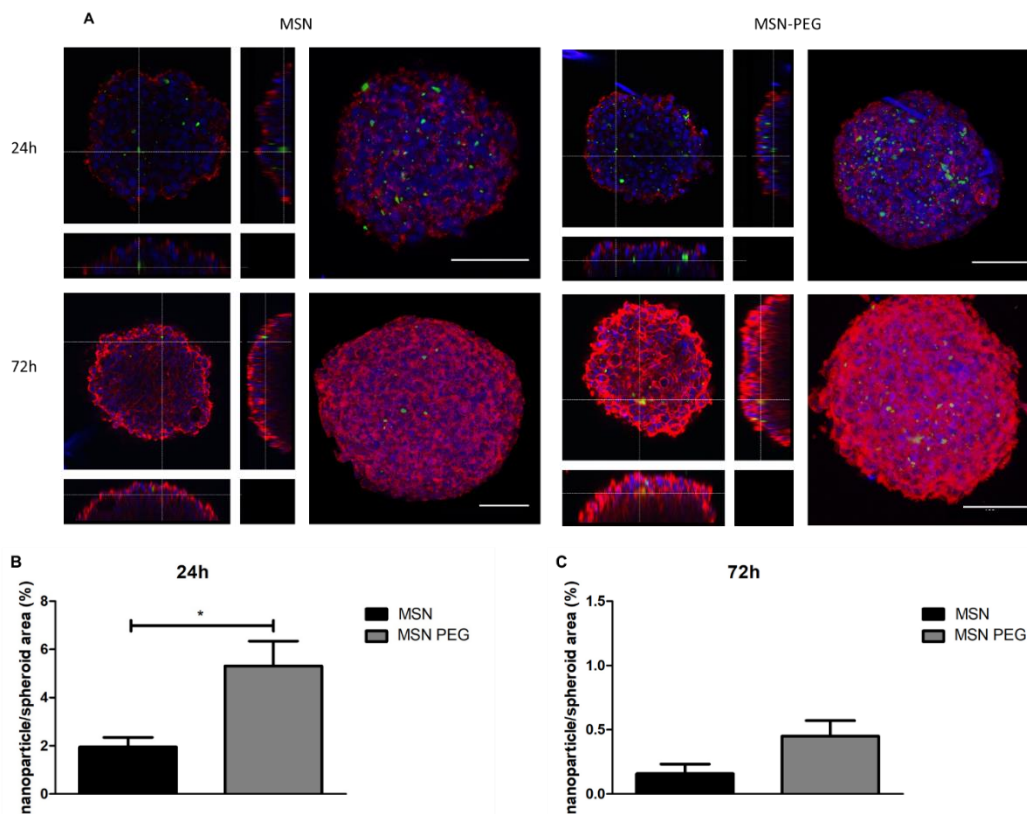
Figure 5.10: MSN-FITC and MSN-PEG-FITC penetration into spheroids grown for 2 days. **A-** Left: Orthogonal images are the combination of 10 z-stacks of 5 μm each (50 μm from the bottom to the core of the spheroid). Right: Combination of all z-stacks (up to 23 stacks). Scale bars = 100 μm. Quantification of nanoparticle (FITC) area on the combined stacks images in relation to spheroid total area after **B-** 24 h and **C-** 72 h penetration. Results are mean ± SEM of three different images. $p < 0.05$ (*).

For spheroids grown for 4 days, similar penetration was observed for MSN and MSN-PEG after 24 h. After 72 h incubation, MSN-PEG penetrated more than MSN in these spheroids.
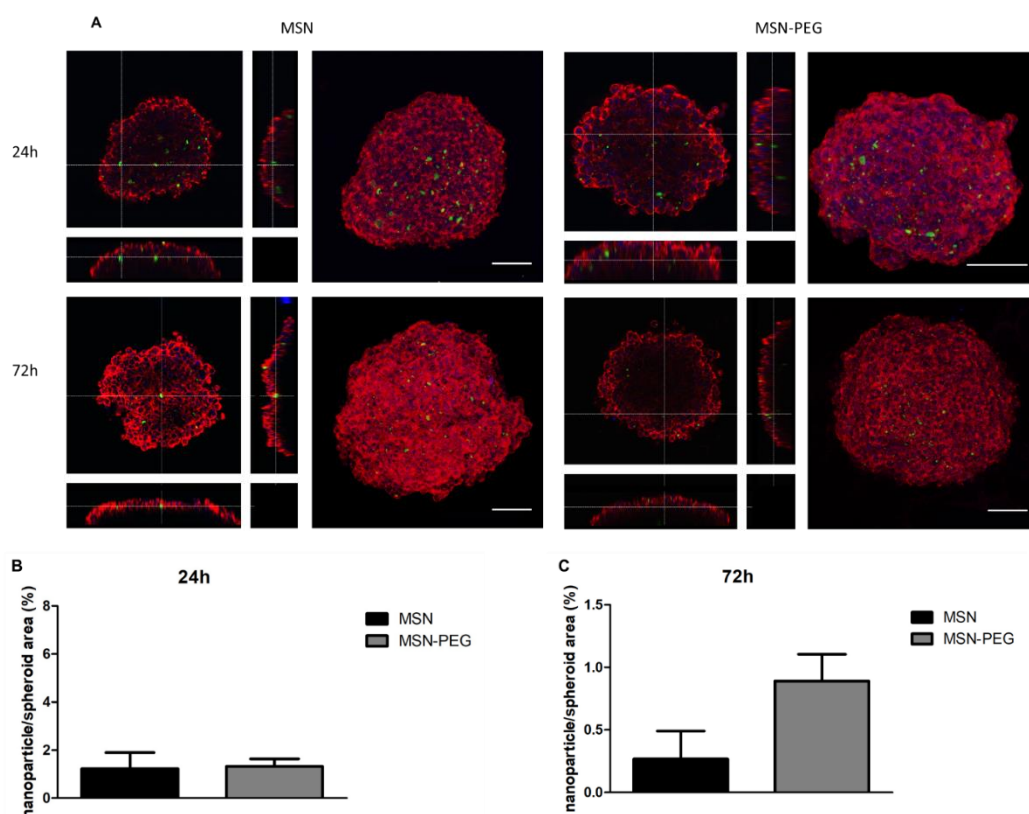
Figure 5.11: MSN-FITC and MSN-PEG-FITC penetration into spheroids grown for 4 days. **A-** Left: Orthogonal images are the combination of 10 z-stacks of 5 μm each (50 μm from the bottom to the core of the spheroid). Right: Combination of all z-stacks (up to 23 stacks). Scale bars = 100 μm. Quantification of nanoparticle (FITC) area on the combined stacks images in relation to spheroid total area after **B-** 24 h and **C-** 72 h penetration. Results are mean ± SEM of three different images.

Increasing penetration of glycosylated-dendrimers compared to unmodified dendrimers into U-87 spheroids was reported before by Dhanikula *et al.*[350] up to 24 h incubation. Our results showed that, for both types of spheroids the penetration is higher after 24 h incubation than 72 h. This observation may be related to a greater decrease in FITC fluorescence intensity in 72 h samples due to photobleaching[370]. Nevertheless, we can observe nanoparticles both in the intercellular space and in the cytoplasmic area, which suggests internalization. In this regard, Lázaro *et al.*[356] reported the penetration of graphene oxide into U-87 spheroids after 24 h, but showing that the material was mainly into the extracellular space. Overall, we can conclude that MSN-PEG tend to penetrate more the spheroids compared to MSN only. This result correlates with the MSN-PEG internalization by U-87 cells in a 2D culture confirming that the PEG not only did not impair the internalization by the cells but also facilitates the penetration into a 3D spheroid model.

The effect of PEGylation on nanoparticles ability to penetrate spheroids were previously demonstrated with polymeric nanoparticles composed of poly(glycerol-adipate)[371]. The modified nanoparticles penetrate the core of HCT116 colorectal cancer spheroids in short time frame (4 h) compared to unmodified nanoparticles. Importantly, higher penetration of PEGylated nanoparticles of several sizes (40, 100, 200 nm) into the brain tissue of humans, rats and mice is achieved when compared to non-PEGylated nanoparticles[372]. Thus, the functionalization of our nanoparticles with PEG is an important step of our design that may facilitate the penetration of these particles into the brain after release from the GlioGel formulation. Consequently, the favoured penetration of PEGylated nanoparticles loaded with PTX into the brain may result in the growth inhibition of tumours as occurred with the spheroids.

5.2.4 *In vivo* studies

5.2.4.1 U-87 tumour growth curve *in vivo*

Aiming the future clinical translation of our hydrogel formulation, an *in vivo* glioblastoma tumour model was established and used to test and validate the GlioGel performance. In our model we used the CIEA NOG immunocompromised mouse strain and injected U-87 cells into the brain establishing an orthotopic xenograft model of GBM[187].

Firstly, we monitored the tumour growth in our model through Magnetic Resonance Imaging (MRI) to establish the timeline for resection and to have similar tumour sizes in all groups. Notably, the use of tumour resection meets the clinical setting, which increases the relevance of the model.
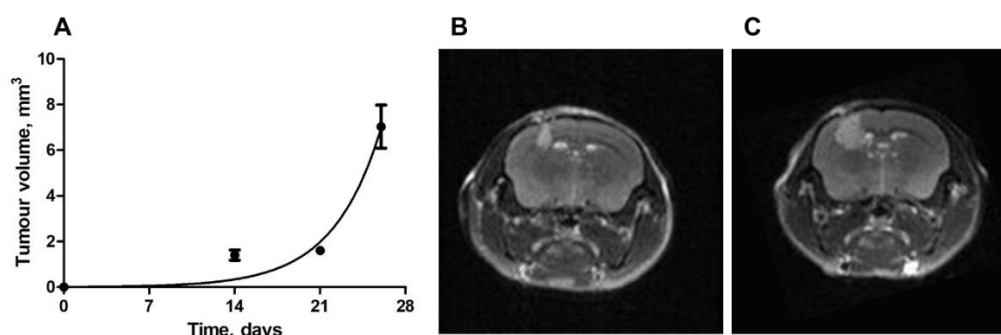
Figure 5.12: Tumour growth kinetics monitored by Magnetic Resonance Imaging (n=5). **A-** Tumour growth curve fitted with an exponential growth equation. **B-** Tumour at day 21. **C-** Tumour at day 26 after U-87 cell injection.

Previously reported glioblastoma mouse models, which we used as reference for the development of our model, recommend tumour resection at day 13 post cell injection[187,362] or when the tumour reaches a volume of 2.5 µL (or 2.5 mm^3) [373]. However, at day 14 after U-87 cell injection the average tumour volume in our model was 1.4 mm^3 **(Figure 5.12A)**. Moreover, considering that we need to perform a resection surgery to have a resection cavity where we could apply the GlioGel treatment, we established that a tumour volume around 5 mm^3 would give us enough space for hydrogel injection. At day 21, the tumour volume increased to 1.6 mm^3 and at day 26 the average volume achieved 7 mm^3 **(Figure 5.12B and C)**.

The U-87 tumour growth curve on our model was clearly slower than the rates previously reported in athymic Swiss nude mice[358]. Therefore, we estimated that between day 21 and 24 the tumour would have achieved a volume around 5 mm^3 and it would be the appropriate time for the resection surgery.

5.2.4.2 GlioGel anti-tumour effect *in vivo*

For the GlioGel anti-tumour effect evaluation, the U-87 cells were injected into the mouse brain and the tumour growth was checked at day 19 and 21 to follow with the resection surgery at day 23. Animal health and treatment effect were monitored for 5 weeks after surgery and any tumour recurrence was checked through MRI one week after surgery **(Figure 5.13)**.
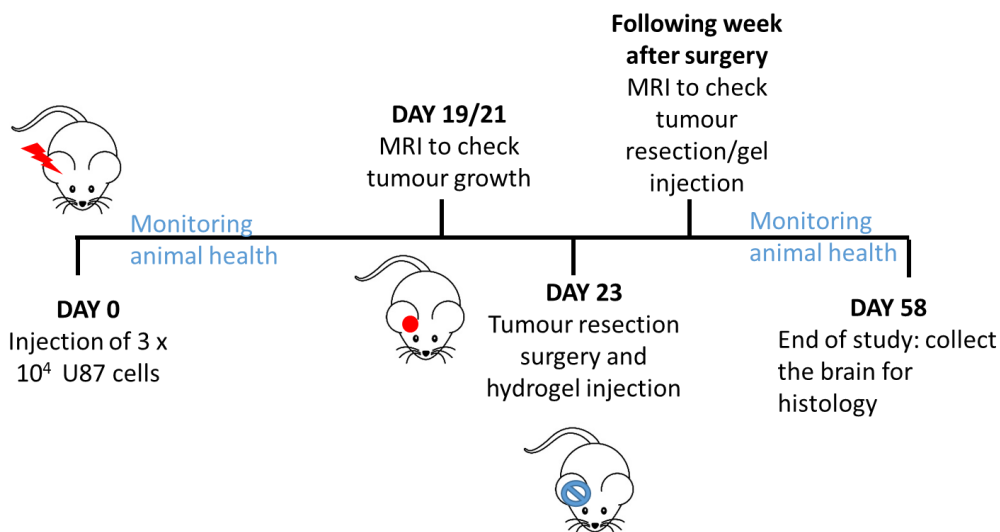
Figure 5.13: Schematic of *in vivo* protocol: timeline for tumour growth check through MRI, resection surgery and animal health monitoring. (Tumour growth (no treatment), n=5; Tumour growth + resection + hydrogel only, n=5; Tumour growth + resection + GlioGel, n=4)

At day 19 after cell injection, the average tumour volume was 1.6 mm^3 while at day 21 it increased to 4.3 mm^3. When the surgery was performed at day 23, the mice were divided in two groups, one that received only the hydrogel and another one that received the hydrogel formulated as GlioGel (0.6 mg/kg TMZ and 0.3 mg/kg PTX loaded into MSN-PEG).

The group of animals that did not undergo tumour resection started to show signs of distress and lose weight by day 27 after tumour cell injection and had a median survival of 36 days. On the contrary, the groups that had resection surgery showed stable weight up to day 44. Then, the group that received only the hydrogel, without any chemotherapy, lost weight and had a median survival of 52 days. The group that received the GlioGel formulation after resection, had a median survival of 57 days and two long-term survivals (50%) **(Figure 5.14)**. However, the median survival is statistically significant only between the tumour growth group versus the hydrogel only (p = 0.0021) and the GlioGel (p = 0.0098). Nevertheless, from day 47 a statistically significant difference in the body weight between the hydrogel only group and the GlioGel group is observed.

It is important to note that the benefit of resection surgery on the survival of GBM animal models was previously reported[187,360]. The pattern of body weight change over time showed that the welfare of the animals in the "resection + GlioGel" group was better than "resection + hydrogel only" group. The tumour regrowth rate could explain this difference. Indeed, all animals presented tumour recurrence when scanned by MRI at day 32 **(Figure 5.15)**. However, the average tumour volume for the hydrogel only group was 9.6 mm^3 compared to 2 mm^3 for the GlioGel group **(Figure 5.15E).** Moreover, in the two long term survivals the resection cavity was still visible and only a tumour border was present **(Figure 5.15C and D)**. Thus, we can conclude that the regrowth rate of the tumour was delayed due to the treatment.
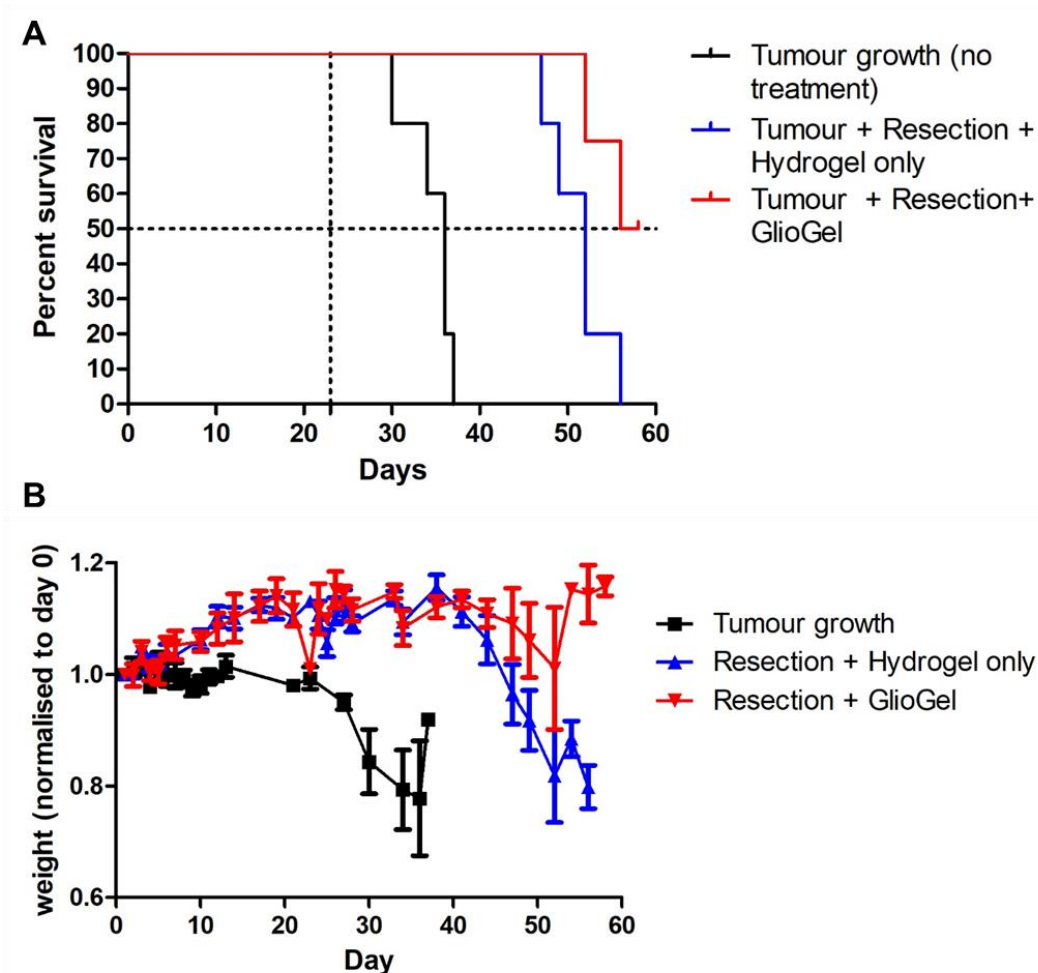
Figure 5.14: GlioGel anti-tumour effect *in vivo*. **A-** Kaplan-Meier survival curves of U-87 tumour-bearing mice. Dotted lines are the 50% survival and the day of resection surgery (day 23). The median survival for tumour growth (no treatment) is 36 days, Resection + Hydrogel only is 52 days and Resection + GlioGel is 57 days. The median survival is statistically significant only between Tumour Growth vs Resection + Hydrogel only (p = 0.0021) and Resection + GlioGel (p=0.0098). **B-** Weight change over time. From day 47 there is statistical difference between the groups Resection + Hydrogel only and Resection+ GlioGel (day 47 – p < 0.05; day 49 and day 54 – p < 0.01; day 52 and 56 – p < 0.001). (Tumour growth (no treatment), n=5; Tumour growth + resection + hydrogel only, n=5; Tumour growth + resection + GlioGel, n=4)
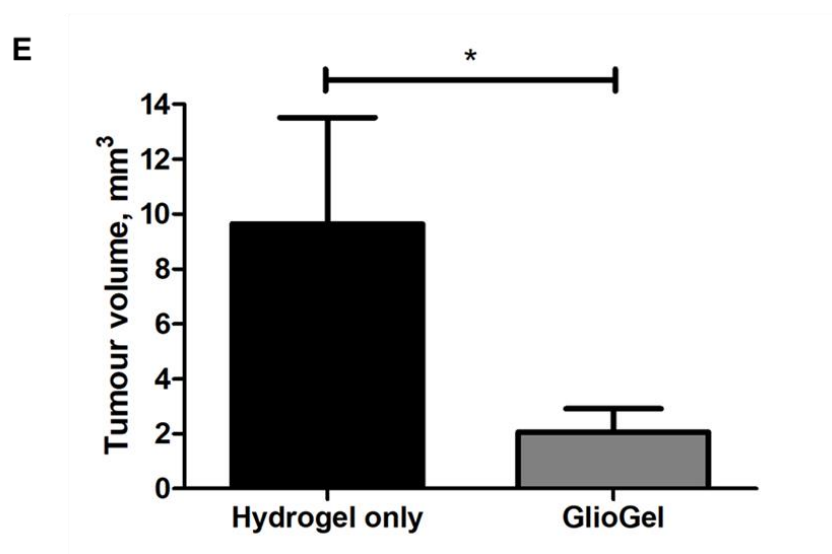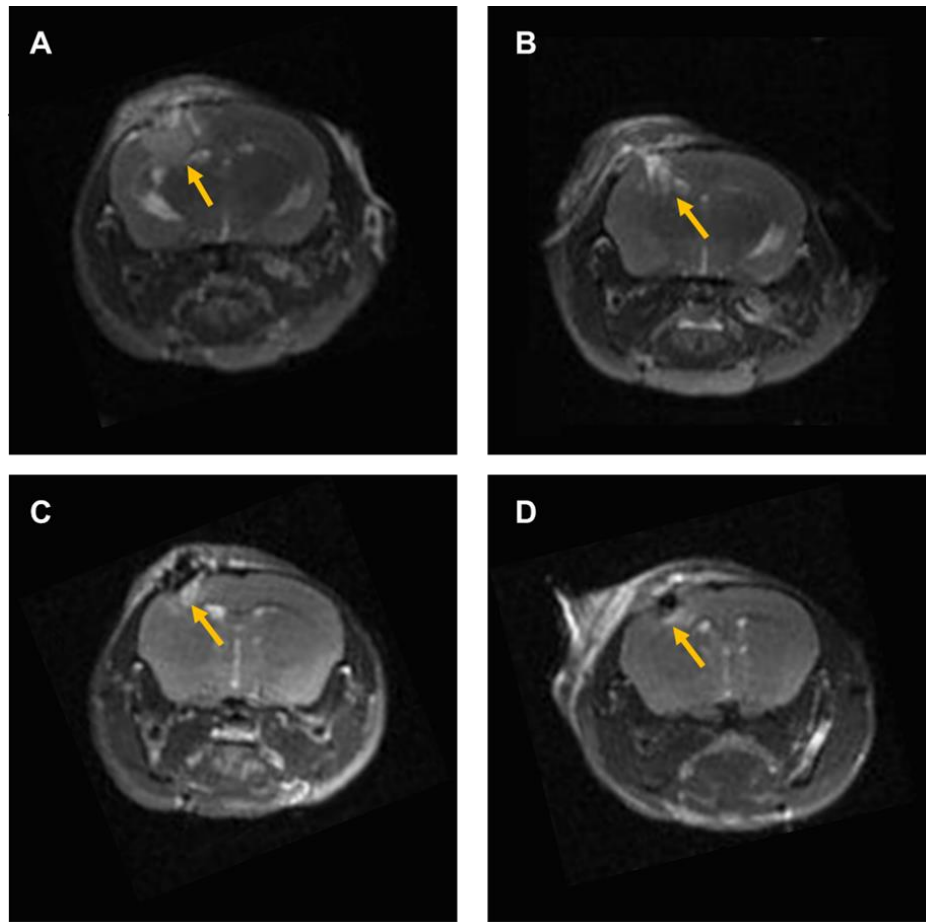
Figure 5.15: Tumour regrowth after one week of resection. **A-** Resection + Hydrogel only. **B-** Resection + GlioGel treatment. **C and D -**Tumour + GlioGel treatment long term survivals. The yellow arrows indicate the tumour regrowth (bright areas are the tumour in T1 weighted images. In D, the dark area in the brain is the cavity). **E-** Tumour volume one week after resection. Non-parametric Mann-Whitney test, $p < 0.05$ (*). (Tumour growth + resection + hydrogel only, n=5; Tumour growth + resection + GlioGel, n=4).

Histological analysis of brain tissues revealed a very dense tumour mass in the brain of the group that did not undergo surgery and the group that received only the hydrogel. For the group that received the GlioGel, although we can still observe tumour tissue, it is much less dense compared to the other groups **(Figure 5.16)**.
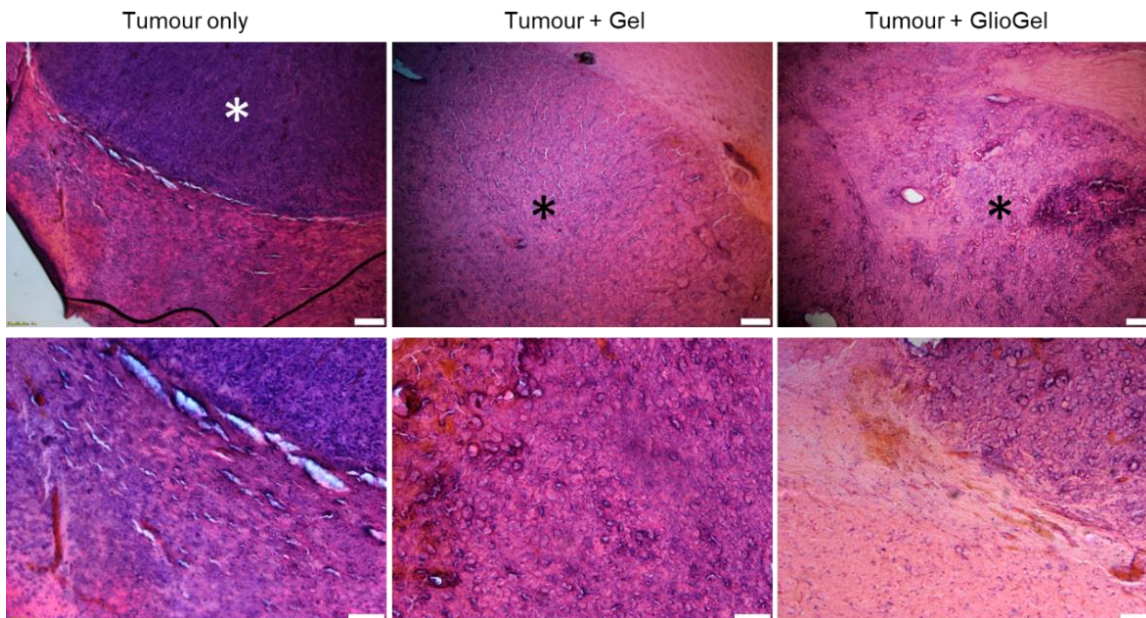
Figure 5.16: Histology analysis of brain tissue. Notice hematoxylin rich tumour area which is denser in the tumour only group (control group - without resection surgery and without treatment). White ✱ indicates dense tumour areas and black ✱ indicates less dense tumour areas. Upper panels scale bar = 200 µm; Lower panels scale bar = 100 µm.

U-87 cells are known to generate non-invasive tumours with well-defined borders in the brain of mice[374], as we observed in our model. An invasive xenograft model of GBM using immunodeficient mice implanted with D-270 MG cells in the brain presents characteristics of higher tumour invasiveness compared to U-87 cells[375].

Despite the non-invasive characteristic of our tumour model, it represents a suitable model of GBM to study the development of brain tumour and its regrowth post-resection. It is also suitable to test a new local treatment approach post-resection. As it was shown here, the local delivery of TMZ and PTX as part of the GlioGel formulation was proven effective in slowing down tumour regrowth *in vivo*. Our results are supported by previous reports showing that the local delivery of temozolomide results in improved outcomes when compared to systemic administration[376]. Furthermore, it was previously reported that local delivery of PTX-

loaded PLGA nanoparticles in PEG-DMA hydrogel prolonged the survival of U-87 tumour bearing mice with 50% long term survival until 150 days after tumour cell implantation[362]. Importantly, it is recognized that the efficacy evaluation of this treatment will be strengthened by testing it in other models of GBM.

5.3 Conclusions

The local delivery of chemotherapy to GBM tumours represents a promising approach to improve treatment outcomes for this severe disease. In this chapter, a new formulation (GlioGel) developed for the local treatment of GBM was evaluated in a 3D *in vitro* culture system and in a pre-clinical model.

Firstly, the combination of TMZ and PTX, present in the GlioGel, was evaluated in a 3D culture system of U-87 spheroids. TMZ had low effects on the spheroids viability, alone or in combination with PTX-loaded nanoparticles, over the range of concentrations tested. On the other hand, MSN-PTX-PEG demonstrated an effect on spheroids viability at concentrations as low as 12.5 µg/mL (approximately 875 nM PTX). The PEGylated nanoparticles were able to penetrate spheroids of different sizes to a higher extent as compared to non-PEGylated MSN. Furthermore, the combination of TMZ and PTX was effective in inhibiting spheroid growth over time.

To test the formulation *in vivo*, a GBM pre-clinical model that included surgical resection of the tumour and enabled a local treatment modality was established. In this model, the tumour growth was monitored by MRI and the tumours were treated (resection + GlioGel) when they reached approximately the same size.

The hydrogel formulation was implanted into the brain after resection surgery having an intimate contact with the resection cavity walls. Thus, the GlioGel components were released to cancer cells left after the surgery. The new formulation was effective in slowing down the tumour regrowth *in vivo*, increasing the survival of mice bearing U-87 tumour and improving their welfare.

In conclusion, the GlioGel formulation is a viable option to treat GBM and improves the current chemotherapy outcomes. Moreover, the GlioGel formulation opens the possibility to develop other local treatment options for GBM in the future that follow the same principle (hydrogel combined with nanoparticles).

CHAPTER 6: GENERAL DISCUSSION AND CONCLUSIONS

6.1 General discussion and conclusions

The primary aim of this project was to develop a formulation to locally treat glioblastoma multiforme after tumour resection. To achieve this, some specific objectives were determined such as the synthesis and characterization of drug-loaded stimulus-responsive nanoparticles, the evaluation and selection of the most suitable gel to be used in the formulation and the pre-clinical *in vivo* efficacy analysis of the GlioGel.

From the work described in the previous chapters, we can conclude that the project objective was achieved and an effective formulation capable of delaying tumour recurrence *in vivo* was developed. This formulation was based on free drug (TMZ) and drug-loaded nanoparticles (MSN-PTX-PEG) in a hydrogel (CX gel) that controlled their release **(Figure 6.1)**. This formulation could potentially match or even outperform standard GBM treatment outcomes. Moreover, the local administration approach for GlioGel could have the additional benefit of minimizing systemic toxicity, which is a common problem of GBM standard treatment.
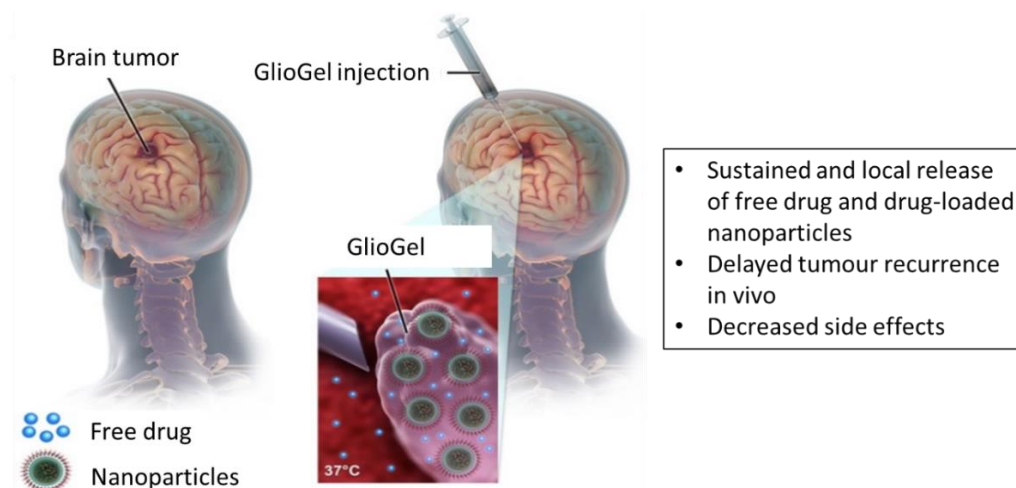
Figure 6.1: GlioGel formulation, composed of free drug and drug-loaded nanoparticles, can be injected in the tumour cavity after resection surgery and is effective in delaying tumour recurrence *in vivo*.

GBM standard therapy includes surgical resection, the use of oral TMZ combined with radiotherapy[31] and implantation of Gliadel, polymer disks of Polifeprosan 20 containing 7.7 mg of carmustine (BCNU)[45,46]. Gliadel is prescribed

for both newly diagnosed or recurrent GBM where surgery is performed to remove the tumour, and up to 8 wafer disks (61.6 mg of carmustine) can be applied in the tumour cavity[293]. According to the Food and Drug Administration (FDA) label, temozolomide (TMZ) is used in both recurrent and newly diagnosed GBM as an oral treatment. Specifically for newly diagnosed tumours, an initial dose of 75 mg/m^2 of body surface area is used with concomitant radiotherapy for 42 days. This is followed by 4 weeks interval and 6 cycles of 28 days comprising 5 days of TMZ monotherapy and 23 days interval with increasing doses (150 – 200 mg/m^2). Recurrent tumours are treated with increasing TMZ doses following the same cycle of 28 days **(Figure 6.2)**.
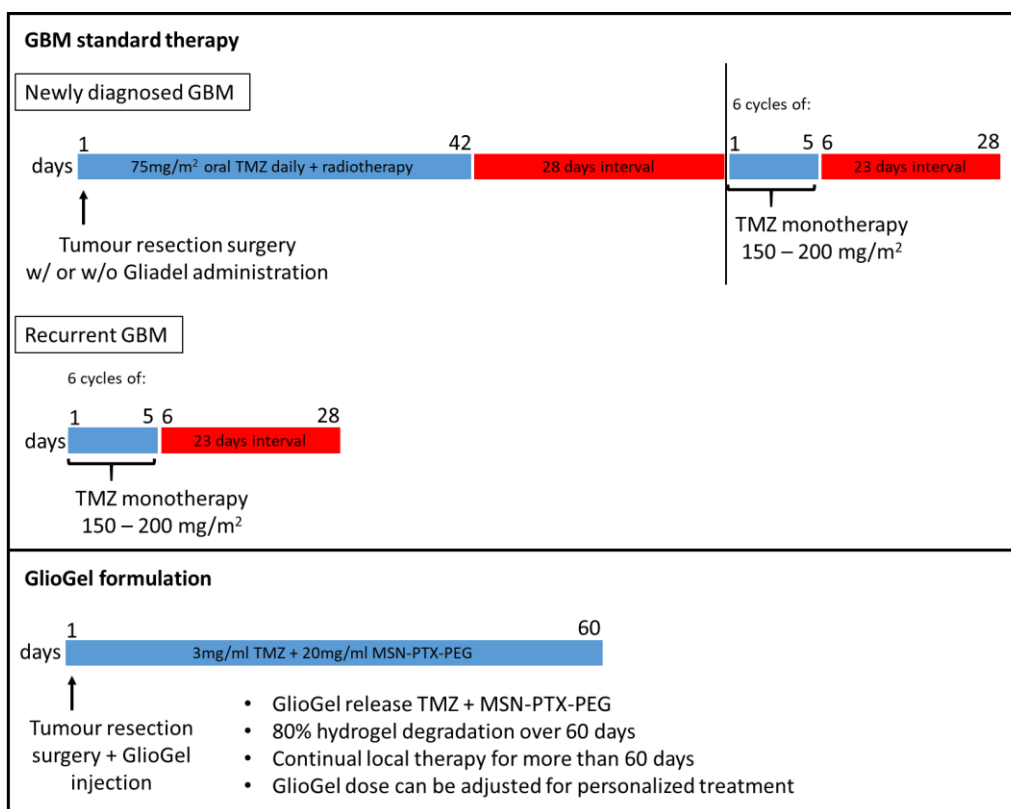
Figure 6.2: Treatment scheme for GBM standard therapy and the proposed GlioGel formulation.

A retrospective analysis has shown that the use of carmustine wafers (Gliadel) in combination with radiation therapy and concomitant systemic TMZ after tumour resection was safe to patients having a mild survival benefit[377]. Thus, the use of both TMZ and BCNU in the GlioGel formulation was considered. This was supported by a study demonstrating that the use of intracranial TMZ and BCNU combined with radiotherapy significantly prolonged survival compared to any of the

treatments alone in an F98 glioma model (median survival of 13 days BCNU, 15 days TMZ, 19 days radiotherapy and 21 days combined treatment)[376]. Moreover, in a 9L gliosarcoma model, this treatment approach improved the survival (range of 21 to 120 days and median survival not reached) even when compared with the standard treatment (oral TMZ, local BCNU and radiotherapy - median survival of 62 days)[376]. However, TMZ and BCNU are alkylating agents and share the same mechanisms of action, which can be a limiting factor for treatment success. Thus, to maximize treatment potential, the antimitotic drug PTX was also evaluated as a possibility for the final formulation.

From the *in vitro* cell assays, the high resistance of the cell model (high IC50 of 832.5 µM) to TMZ was confirmed, which limited the use of this drug loaded into MSN-PEG. On the contrary, PTX was more potent (lower IC50 of 27.7 nM) compared to TMZ, and low concentrations of MSN-PTX and MSN-PTX-PEG were able to decrease the viability of U-87 cells up to 20% and 24%, respectively. Therefore, the choice of MSN-PTX-PEG to compose the GlioGel formulation may address an important challenge in delivering drugs to tumours, namely the difficulty to reach enough concentration at the tumour site while limiting the severe side effects.

The possibility to increase drug concentration at the tumour site without increasing side effects is one of the main goals that guide the development of several nanomedicines to treat different types of cancer. Some of them have been approved by the FDA including Doxil®, the first nanomedicine available to patients, composed of doxorubicin encapsulated in PEGylated-liposomes[378]. After that, other nanotherapeutics also entered the market such as Myocet® (liposome encapsulating doxorubicin citrate)[379], Abraxane® (paclitaxel attached to albumin)[380] and Marqibo® (vincristine sulfate-loaded liposome)[381]. Specifically for GBM, NanoTherm® was approved in 2011 for use in Europe. This nanomedicine is based on drug-free magnetic nanoparticles to be injected directly into the tumour followed by magnetic field application[382]. This procedure treats the tumour by heating the area (hyperthermia therapy) and killing the cancer cells or making them more sensitive to other treatments such as chemotherapy and radiotherapy[383].

The success of the developed nanoparticle (MSN-PTX-PEG) also relies on its ability to penetrate tissues and to deliver the drug cargo mainly in the cancer cells. In fact, the internalization of MSN-PEG into U-87 cells and the ability of these particles to penetrate spheroids were demonstrated. The drug-loaded nanoparticles

were also effective in inhibiting U-87 spheroids growth (spheroids grew only 2.4% compared to 29.5% without treatment) and decreasing the viability up to 45%. Moreover, it is clear that the functionalization with PEG did not impair these processes.

The functionalization with PEG is usually applied to protect compounds from degradation and elimination, contributing to increase the biological half-life. This concept can be easily applied to nanoparticles and it was already demonstrated that MSN-PEG of different sizes were captured in a lower degree by liver, spleen and lung after intravenous administration, which correlates with less interaction with capillary cells[384]. Moreover, as previously discussed, functionalization with PEG can facilitate nanoparticle penetration into brain tissues[372].

Considering that the GlioGel formulation will be directly administered into the brain post-surgery, the lower expected interaction of MSN-PTX-PEG with endothelial cells and the reduced phagocytosis[252] would enable more time for the nanoparticles to be in contact with the tumour cells remaining in the cavity area. At the same time, it is expected that MSN will be slowly eliminated from the brain through degradation and subsequent transport of degradation products across the BBB for elimination by the systemic excretion route.

Mesoporous silica nanoparticles degrade forming soluble non-toxic orthosilicic acid, $Si(OH)_4$, which can be eliminated by renal clearance[385,386]. It is important to highlight that some factors such as concentration and functionalization of MSN may enhance or slow the degradation process[387,388]. As mentioned in Chapter 3, the relative stability of MSN combined with the degradation of its pore structure over time also plays a role in the sustained release of their cargo (PTX). In spite of the non-toxic nature of MSN degradation by-products, the interaction of MSN with cell membranes may be a factor contributing to toxicity[195]. Indeed, MSN impaired neurons complexity development while MSN-PEG compromised neither the complexity nor the viability of neurons, which supports the use of MSN-PEG in the final GlioGel formulation.

Noteworthy, the importance of these effects will be closely related to the nanoparticle doses needed to treat the tumour. In the final formulation, a dose of 0.6 mg/Kg TMZ and 0.3 mg/Kg PTX (corresponding to 4 mg/kg MSN-PTX-PEG) was used. This dose and drug combination strategy were tested before in a mice model with promising results[332] and, therefore, were selected for our formulation. Moreover, the dose of nanoparticles in the GlioGel is more than 10-times lower than

the maximum parenteral dose (50 mg/kg, intraperitoneal or intravenous) tolerated by nude mice as reported by Lu *et al.*[85].

The dose factor is also important for the free drug present in the GlioGel. Particularly, the final GlioGel formulation is adjustable to the specific doses needed. From the analysis of different gels, the CX gel was selected to be part of the lead GlioGel formulation due to the sustained release of both MSN-PEG and drugs, the maintenance of nanoparticle responsiveness after incorporation, the optimal rheologic characteristics and the inertness on healthy neurons. Considering the previous selection of MSN-PTX-PEG and the aim to have a combined therapy, the choice of TMZ to be freely dispersed in the hydrogel was clear. TMZ was released in a sustained manner by CX gel in higher proportions compared to the other gels and drugs, which is important to maintain effective drug concentrations in the tumour cavity over an extended period of time. Notably, the burst release of TMZ in the first 4 h is justifiable by the time needed for the gel to form, leaving some unencapsulated drug that is released immediately[389]. This is not necessarily a negative aspect of the formulation provided that the drug amount released in the burst is not acutely toxic. In the specific case of GlioGel, it may be even beneficial for the treatment effectivity.

In a systemic treatment, approximately 20% of the TMZ dose can cross the BBB and achieve the tumour site in the brain[390]. Several reports in the literature state that, in average, relevant TMZ concentrations in the brain of glioma patients vary between 5 and 10 µM, which are much lower than concentrations used *in vitro*[390–394]. From the *in vitro* cell assays, we can conclude that much higher concentrations (above 260 µM) are needed to exert an effect on cell viability in U-87 cell cultures. Different cell lines have different responses to chemotherapeutic drugs *in vitro*. These responses may be related to genotypic and phenotypic characteristics of GBM cells that can be more similar or different from clinic manifestations of GBM. For example, U-87 cells are considered less invasive than other human cell lines such as F98 and 9L/LacZ, and rat cell lines such as C6 cells[339]. As mentioned in Chapter 5, U-87 cells and C6 cells are classical cell lines used on GBM research. In the analysis of the effect of GlioGel components *in vitro*, priority was given to the use of a standard U-87 human cell line. However, it may be interesting to analyse other human cell lines with different characteristics both *in vitro* and *in vivo* in future studies[375]. Nevertheless, the local administration of GlioGel could facilitate the achievement of higher concentrations of TMZ in the brain capable to kill tumour cells.

Moreover, although TMZ showed almost no effect on U-87 spheroids viability, it inhibited spheroids growth at concentrations higher than 250 µM. This concentration correlates with the observed *in vitro* release of 300 µM TMZ from the GlioGel formulation used in the *in vivo* studies.

Indeed, the results from the 3D spheroids analysis regarding spheroid size, viability and nanoparticle penetration contribute to the understanding of the combination treatment and may help to predict the *in vivo* study outcomes. For example, the spheroid size can be correlated with tumour size *in vivo*. Moreover, the size of the spheroids can also have a major impact on drug cytotoxicity, and it was demonstrated that 100 µM TMZ is ineffective in reducing the size of spheroids larger than 400 µm[367]. The spheroids used here were 313 µm and 438 µm diameter in average and TMZ was effective in inhibiting spheroid growth at very high concentrations, while the toxicity effect was irrelevant.

Some reports in the literature argue about cytostatic effects of TMZ as opposed to cytotoxic effects[395,396]. A cytostatic effect may explain the inhibition of spheroid growth despite the lack of TMZ cytotoxicity. For instance, Günther *et al.*[397] showed that 100 µM TMZ induces senescence in U-87 spheroids inhibiting spheroid growth and invasion. The same effect was observed by Fehlauer *et al.* in U-87 spheroids treated with TMZ and radiotherapy showing inhibited spheroid proliferation[398].

Although TMZ inhibited spheroids growth and MSN-PTX-PEG was effective in decreasing the viability of U-87 spheroids, the overall analysis on 3D spheroids showed that the combination therapy had less than additive effects on the spheroids, which means that the effect of TMZ + 100 µg/mL MSN-PTX-PEG was smaller than the sum of the single treatments. Despite that, both components add value to the formulation considering the long term effect of a local injectable therapy.

From the work described in the previous chapters we can conclude that the combination of MSN-PTX-PEG and TMZ in the GlioGel formulation was successful in delaying tumour recurrence *in vivo*. While the hydrogel (CX gel) was effective in controlling the release of both free drug and drug-loaded nanoparticles, the MSN-PTX-PEG also controlled the release of PTX. In addition, the GlioGel showed reduced systemic side effects evidenced by the stable animal weight throughout the study. Hence the success of the GlioGel is attributed to the combined, controlled and local treatment approach.

The use of the GlioGel formulation allows the application of adjuvant chemotherapy immediately after tumour resection. It is important that this therapy includes a fast release (free drug) and a responsive delivery over time (nanoparticles) to ensure that a high sustained dose is released in the tumour area for better results. In this regard, nanoparticles embedded into hydrogels provide a more sustained release that is retained into the tumour area for longer times when compared to free nanoparticles[399,400]. Moreover, as mentioned before, the local delivery of TMZ alone or in combination with carmustine and radiotherapy was more effective than oral administration in rodent models[376,401].

Another benefit of using both nanoparticles and hydrogels in GBM treatment is the possibility to combine different drugs in the formulation. For instance, Bastiancich *et al.*[145] proposed the local delivery of lauroyl-gemcitabine loaded into a hydrogel (GemC12-LNC) and showed a delay in tumour recurrence. Then, the same hydrogel was used in combination with PTX demonstrating higher cytotoxicity to glioma cells compared to the single drug formulation[402].

Specifically, the co-delivery of PTX and TMZ from a hydrogel, reported previously by Zhao *et al.*[332], showed similar median survival for untreated and resection groups compared to the same groups in our *in vivo* experiment. Zhao *et al.* also observed a delay in tumour recurrence, although they did not reach the median survival for the combined treatment group as opposed to the GlioGel results. Of note, the GlioGel analysis *in vivo* was a pilot study and, therefore, had a small number of animals analysed. Nevertheless, the GlioGel study had two long-term survivals with less tumour recurrence as visualized by MRI. The number of animals analysed and the time of resection are different between the studies, which makes it harder to establish a comparison with the median survival observed in the GlioGel group.

The tunability of hydrogel systems makes them very versatile materials regarding not only the formulation composition but also the mode of administration. The GlioGel can be both injected or implanted into the tumour cavity. For this, the use of image techniques such as computer tomography, magnetic resonance tomography (MRT) or positron emission tomography (PET) to measure the tumour prior to the resection can guide dose determination and mode of administration.

Finally, the hydrogel characteristics, specially the rheological properties, can be modified according to the desired formulation. The CX gel showed good compatibility with healthy neurons and this may be attributed to the material

characteristics. In fact, a photopolymerizable PEG-DMA based hydrogel that shares similar rheological characteristics (viscous modulus of approximately 10kPa) with CX gel, demonstrated good *in vivo* tolerability on nude mice after injection in the brain and in situ polymerization[373].

In summary, the liquid to solid phase transition of hydrogels facilitates their administration through injection or implantation in a surgical cavity. They perfectly fill in the cavity created by the tumour resection, which means that the drugs will be closely released to residual cancer cells left post surgery, in opposition to currently used wafers. The GlioGel finds applicability in the diverse and complex scenario of GBM treatment. While we have demonstrated its efficacy in the pre-clinical evaluation against GBM, it can be optimized for other drug combinations and personalized treatments.

6.2 Main findings

- Mesoporous silica nanoparticles batches were synthetized and had comparable characteristics related to surface area (887 to 1575m^2/g), average pore diameter (2.1 to 2.7 nm) and hexagonal pore organization.

- The functionalization did not affect the morphology of MSN while the size and negative zeta potential were also comparable after the modification. The average size for MSN was 291 nm (DLS)/ 137 nm (TEM) while for MSN-PEG was 193 nm (DLS)/ 133 nm (TEM).

- The amount of PEG on the surface of MSN was estimated and the functionalization efficiency was determined as 82% ± 6% w/w. The PEG disulphide attachment successfully formed a molecular gate, which opens following the addition of reductive agents such as glutathione.

- Encapsulation efficiency of TMZ inside the MSN was improved by the use of a vacuum step in the loading process achieving 29% ± 6% and loading capacity of 22% ± 5%. Paclitaxel encapsulation efficiency was 67% ± 12% and loading capacity of 18% ± 3%. The release of both drugs was successfully controlled by the responsive molecular gate.

- From the IC50 cell assay, we observed that TMZ is not a potent drug to kill U-87 cells. The results with MSN-TMZ suggest that a lower amount of drug encapsulated into the nanoparticles is more effective in killing the cells compared to free drug. For PTX, both MSN-PTX and MSN-PTX-PEG decreased U-87 cell viability up to 20% and 24% respectively.

- MSN did not affect the viability of neurons and the PEG is protective regarding the neuron development of normal morphology.

- MSN degrades over time losing the hexagonal organization of the pores, but it did not dissolve completely after 7 days at 37 °C. The degradation also contributes to the sustained release of drug after the molecular gate is opened.

- Release profiles of three drugs (TMZ, PTX and BCNU) from three gels (LQP4, Pluronic F-127 and CX) were determined and analysed. Higher drug release proportions were observed from Pluronic F-127 and CX gels for TMZ and PTX. These releases were characterized by a burst in the first 4 h followed by a small and constant increase up to 14 days.

- The slow degradation of LQP4 may explain the low release proportion of these gels. On the other hand, both the Pluronic F-127 and CX gels initially degrade quickly in hours but maintaining the sustained release of drug through micelles incorporation (Pluronic F-127) or slow down degradation until complete dissolution or termination of the experiment.

- The CX gel presents a sustained release of both MSN and MSN-PEG, while the other gels presented a burst release (Pluronic F-127) or a very low release proportion (LQP4).

- The responsiveness of MSN-PEG is preserved after nanoparticle incorporation into the Pluronic F-127 and the CX hydrogels.

- The Pluronic F-127 hydrogel presents mild cytotoxicity effects on U-87 cells and on primary rat neurons complexity (decreased complexity measured by number of neuron branches and neuritic length) while the CX gel is mainly inert to both cell types.

- U-87 spheroids formation is impaired by the presence of 1% DMSO from day 0 of culture. The addition of 1% DMSO after the formation of the spheroid (at least 2 days from seeding) does not affect it.

- At least 2 days are needed to have uniform spheroids in culture. The final spheroid diameter is dependent on the initial number of cells, and spheroids of more than 500 µm diameter are dense and compact.

- MSN-PTX-PEG showed a concentration dependent effect on 2-day spheroids viability and inhibited spheroid growth, while TMZ had no effect

on viability. Free TMZ slightly inhibited spheroid growth in concentrations higher than 250 µM.

- Spheroids grown for 4 days were more resistant to MSN-PTX-PEG treatment compared to 2-day spheroids, and the combined treatment effect was largely due to the nanoparticle effect rather than to the presence of both components. Increased concentrations of TMZ alone or in combination with MSN-PTX-PEG showed a great inhibition of the growth of 4-day spheroids compared to 2-day spheroids.
- MSN and MSN-PEG were able to penetrate spheroids, and MSN-PTX-PEG treatment caused visible cell detachment from spheroids.
- The GlioGel treatment delayed tumour recurrence *in vivo* and improved animal welfare.

6.3 Future work

This project successfully developed and selected suitable components to build an injectable formulation aiming to treat GBM tumours. The analysis performed here proved the efficacy of the formulation while further investigations are possible.

The performance of the hydrogel combined with responsive nanoparticles and chemotherapeutic drugs was fully addressed. From this, the formulation can be optimized to have specific proportional releases of drug and nanoparticles over time. This can be achieved by analysing, for example, different hydrogel crosslinking densities. Moreover, a more comprehensive analysis of the GlioGel formulation regarding the hydrogel rheological properties could be performed with the presence of different amounts of nanoparticles incorporated into the CX gel.

Although the redox-responsive molecular gate proposed in this work is a promising and effective strategy to control the release of drugs preferentially inside cancer cells, other types of molecular gates can be considered for a targeting approach. Particularly for glioblastoma, targeting options include the use of chlorotoxin peptide[403], which binds chloride channels highly expressed in glioma cells[404]. Thus, chlorotoxin targeting may improve the selectivity of the treatment increasing nanoparticles uptake specifically by cancer cell compared to health cells[405]. Other receptors highly expressed in gliomas, such as interleukin 13 receptor alpha 2, ephrin receptor tyrosine kinases and epidermal growth factor receptor

(EGFR), can also guide the development of targeting approaches[406,407]. In addition, matrix metalloproteinase enzymes (MMP2 and MMP9), upregulated in the glioblastoma microenvironment[408], can be explored.[409]. Thus, molecular gates based on the peptides that bind receptors upregulated in glioblastoma or on specific attachments that enables the action of enzymes, such as MMP, are interesting options for a target and triggered release approach.

The evaluation of the formulation components in other cell lines and in patient-derived cells will also be relevant. These other models may highlight different levels of cytotoxicity due to different genetic characteristics of the cells, specially the patient-derived cells that more closely represent the clinical scenario compared to cell lines. On the other hand, the GlioGel formulation was analysed *in vivo* in a pilot study. To translate the use of this hydrogel formulation into clinical settings, it is imperative to compare the new formulation with the current GBM standard therapy in a complementary *in vivo* study. This would comprise different doses and comparisons of the standard treatment against the Gliadel wafers and the GlioGel, for example. In addition, it may be interesting to analyse formulation efficacy in other preclinical GBM models that present more invasive tumours than the U-87 orthotopic model. The hydrogel does not have any negative effect on animal health considering the *in vivo* analysis performed in immunocompromised mice. However, the *in vivo* biocompatibility of the CX gel can be further analysed *in vivo* in the brain of immunocompetent animals. Meanwhile, the nanoparticles biodistribution in the brain can also be addressed. For instance, fluorescent nanoparticles (MSN-FITC) could be loaded into the CX gel before injection into the brain. Thus, the nanoparticles can be tracked in the tissue using different imaging techniques both *in vivo*, such as MRI and bioluminescence[410], or through histology processing using fluorescent microscopy[384]. These analyses will be critical to evaluate the treatment response and guide the use of personalized treatment formulations in the future.

The GlioGel could enable a range of drug combinations that can be explored for personalized treatments. Thus, other combinations of drugs that have not been tested in GBM yet could be analysed in the CX gel. For instance, inhibitors of signalling pathways altered in GBM, such as the phosphoinositide 3-kinase (PI3K) and the mitogen-activated protein kinase (MAPK), may be an option to be evaluated in the GlioGel formulation[411,412]. Furthermore, some GBM patients may benefit from specific immunotherapy treatments[413], including immune checkpoint inhibitors (anti-

PDL1 and anti-CTLA)[414,415] that can also be incorporated into future versions of GlioGel.

Finally, the treatment timeline using GlioGel could be extended through the use of delivery devices similar to catheters that enable repeating doses, if needed. The use of a medical device to deliver repeated cycles of therapy in the brain after surgery may prove more effective in combating the tumour over time. Importantly, the safety of the delivery device and the 'repeating dose' approach must be assessed.

REFERENCES

1. WORLD HEALTH ORGANIZATION: REGIONAL OFFICE FOR EUROPE. *WORLD CANCER REPORT: cancer research for cancer development.* (IARC, 2020).

2. *Glioblastoma.* (Codon Publications, 2017). doi:10.15586/codon.glioblastoma.2017.

3. Urbańska, K., Sokołowska, J., Szmidt, M. & Sysa, P. Review Glioblastoma multiforme – an overview. *Contemp. Oncol* **5**, 307–312 (2014).

4. Pikor, N. B., Cupovic, J., Onder, L., Gommerman, J. L. & Ludewig, B. Stromal Cell Niches in the Inflamed Central Nervous System. *J. Immunol.* **198**, 1775–1781 (2017).

5. Purves, D. *et al. Neuroscience. 5th Edition.* (2012).

6. Neftel, C. *et al.* An Integrative Model of Cellular States, Plasticity, and Genetics for Glioblastoma. *Cell* **178**, 835–849 (2019).

7. Barker, N., Bartfeld, S. & Clevers, H. Tissue-Resident Adult Stem Cell Populations of Rapidly Self-Renewing Organs. *Cell Stem Cell* **7**, 656–670 (2010).

8. Lathia, J. D., Mack, S. C., Mulkearns-Hubert, E. E., Valentim, C. L. L. & Rich, J. N. Cancer stem cells in glioblastoma. *Genes & Development* **29**, 1203–1217 (2015).

9. Fidoamore, A. *et al.* Glioblastoma Stem Cells Microenvironment: The Paracrine Roles of the Niche in Drug and Radioresistance. *Stem Cells Int.* **2016**, 1–17 (2016).

10. Liebelt, B. D. *et al.* Glioma Stem Cells: Signaling, Microenvironment, and Therapy. *Stem Cells Int.* **2016**, 1–10 (2016).

11. Kaltschmidt, C. *et al.* A Role for NF-κB in Organ Specific Cancer and Cancer Stem Cells. *Cancers* **11**, 655 (2019).

12. Hai, L. *et al.* Notch1 is a prognostic factor that is distinctly activated in the classical and proneural subtype of glioblastoma and that promotes glioma cell survival via the NF-κB(p65) pathway. *Cell Death Dis.* **9**, 158 (2018).

13. Ma, Q. *et al.* Cancer Stem Cells and Immunosuppressive Microenvironment in Glioma. *Front. Immunol.* **9**, 2924 (2018).

14. Wu, A. *et al.* Glioma cancer stem cells induce immunosuppressive macrophages/microglia. *Neuro-Oncology* **12**, 1113–1125 (2010).

15. D'Alessio, A., Proietti, G., Sica, G. & Scicchitano, B. M. Pathological and Molecular Features of Glioblastoma and Its Peritumoral Tissue. *Cancers* **11**, 469 (2019).

16. Johanns, T. M., Bowman-Kirigin, J. A., Liu, C. & Dunn, G. P. Targeting Neoantigens in Glioblastoma: An Overview of Cancer Immunogenomics and Translational Implications. *Neurosurgery* **64**, 165–176 (2017).

17. Louis, D. N. *et al.* The 2016 World Health Organization Classification of Tumors of the Central Nervous System: a summary. *Acta Neuropathol.* **131**, 803–820 (2016).

18. Eder, K. & Kalman, B. Molecular Heterogeneity of Glioblastoma and its Clinical Relevance. *Pathol. Oncol. Res.* **20**, 777–787 (2014).

19. Brennan, C. W. *et al.* The Somatic Genomic Landscape of Glioblastoma. *Cell* **155**, 462–477 (2013).

20. Aldape, K., Zadeh, G., Mansouri, S., Reifenberger, G. & von Deimling, A. Glioblastoma: pathology, molecular mechanisms and markers. *Acta Neuropathol.* **129**, 829–848 (2015).

21. Wang, Q. *et al.* Tumor Evolution of Glioma-Intrinsic Gene Expression Subtypes Associates with Immunological Changes in the Microenvironment. *Cancer Cell* **32**, 42–56 (2017).

22. Hegi, M. E. *et al.* MGMT Gene Silencing and Benefit from Temozolomide in Glioblastoma. *New Eng. J. Med.* **352**, 997–1003 (2005).

23. Wick, W. *et al.* MGMT testing—the challenges for biomarker-based glioma treatment. *Nat. Rev. Neurol.* **10**, 372–385 (2014).

24. The Cancer Genome Atlas Research Network. Comprehensive genomic characterization defines human glioblastoma genes and core pathways. *Nature* **455**, 1061–1068 (2008).

25. An, Z., Aksoy, O., Zheng, T., Fan, Q.-W. & Weiss, W. A. Epidermal growth factor receptor and EGFRvIII in glioblastoma: signaling pathways and targeted therapies. *Oncogene* **37**, 1561–1575 (2018).

26. Balça-Silva, J. *et al.* Cellular and molecular mechanisms of glioblastoma malignancy: Implications in resistance and therapeutic strategies. *Semin. Cancer Biol.* **58**, 130–141 (2019).

27. Glunde, K., Düßmann, H., Juretschke, H.-P. & Leibfritz, D. Na+/H+ exchange subtype 1 inhibition during extracellular acidification and hypoxia in glioma cells. *J. Neurochem.* **80**, 36–44 (2002).

28. Miller, D. S. Regulation of ABC Transporters Blood–Brain Barrier. in *Advances in Cancer Research* vol. 125 43–70 (Elsevier, 2015).

29. Hubensack, M. *et al.* Effect of the ABCB1 modulators elacridar and tariquidar on the distribution of paclitaxel in nude mice. *J. Cancer Res. Clin. Oncol.* **134**, 597–607 (2008).

30. Haar, C. P. *et al.* Drug Resistance in Glioblastoma: A Mini Review. *Neurochem. Res.* **37**, 1192–1200 (2012).

31. Stupp, R. *et al.* Radiotherapy plus Concomitant and Adjuvant Temozolomide for Glioblastoma. *New Eng. J. Med.* 10 (2005).

32. Arvanitis, C. D., Ferraro, G. B. & Jain, R. K. The blood–brain barrier and blood–tumour barrier in brain tumours and metastases. *Nat. Rev. Cancer* **20**, 26–41 (2020).

33. Bruinsmann, F. A. *et al.* Nasal Drug Delivery of Anticancer Drugs for the Treatment of Glioblastoma: Preclinical and Clinical Trials. *Molecules* **24**, 4312 (2019).

34. Bailly, C. *et al.* Potential for Nuclear Medicine Therapy for Glioblastoma Treatment. *Front. Pharmacol.* **10**, 772–781 (2019).

35. Rego, G. N. A. *et al.* Therapeutic Efficiency of Multiple Applications of Magnetic Hyperthermia Technique in Glioblastoma Using Aminosilane Coated Iron Oxide Nanoparticles: In Vitro and In Vivo Study. *Int. J. Mol. Sci.* **21**, 958–989 (2020).

36. Frenster, J. D., Desai, S. & Placantonakis, D. G. In vitro evidence for glioblastoma cell death in temperatures found in the penumbra of laser-ablated tumors. *Int. J. Hyperthermia* **37**, 20–26 (2020).

37. Figueroa, J. M. *et al.* The role of neutrophil-to-lymphocyte ratio in predicting overall survival in patients undergoing laser interstitial thermal therapy for glioblastoma. *J. Clin. Neurosci.* **72**, 108–113 (2020).

38. Fabian, D. *et al.* Treatment of Glioblastoma (GBM) with the Addition of Tumor-Treating Fields (TTF): A Review. *Cancers* **11**, 174–186 (2019).

39. Parupudi, T. *et al.* Fabrication and characterization of implantable flushable electrodes for electric field-mediated drug delivery in a brain tissue-mimic agarose gel. *Electrophoresis* **39**, 2262–2269 (2018).

40. Dréan, A. *et al.* ATP binding cassette (ABC) transporters: expression and clinical value in glioblastoma. *J. Neurooncol.* **138**, 479–486 (2018).

41. Chen, Y. & Liu, L. Modern methods for delivery of drugs across the blood–brain barrier. *Adv. Drug Deliv. Rev.* **64**, 640–665 (2012).

42. Ghosh, M. *et al.* Survival and prognostic factors for glioblastoma multiforme: Retrospective single-institutional study. *Indian Journal of Cancer* **54**, 362 (2017).

43. Ganipineni, L. P., Danhier, F. & Préat, V. Drug delivery challenges and future of chemotherapeutic nanomedicine for glioblastoma treatment. *J. Control. Release* **281**, 42–57 (2018).

44. Zubair, A. & De Jesus, O. Ommaya Reservoir. in *StatPearls* (StatPearls Publishing, 2020).

45. Lin, S. H. & Kleinberg, L. R. Carmustine wafers: localized delivery of chemotherapeutic agents in CNS malignancies. *Expert Rev. Anticancer Ther.* **8**, 343–359 (2008).

46. Ashby, L. S., Smith, K. A. & Stea, B. Gliadel wafer implantation combined with standard radiotherapy and concurrent followed by adjuvant temozolomide for treatment of newly diagnosed high-grade glioma: a systematic literature review. *World J. Surg. Oncol.* **14**, 225–240 (2016).

47. Fleming, A. B. & Saltzman, W. M. Pharmacokinetics of the Carmustine Implant: *Clin. Pharmacokinet.* **41**, 403–419 (2002).

48. Samis Zella, M. A. *et al.* Evaluation of post-operative complications associated with repeat resection and BCNU wafer implantation in recurrent glioblastoma. *Acta Neurochir.* **156**, 313–323 (2014).

49. Bastiancich, C., Danhier, P., Préat, V. & Danhier, F. Anticancer drug-loaded hydrogels as drug delivery systems for the local treatment of glioblastoma. *J. Control. Release* **243**, 29–42 (2016).

50. Bobo, R. H. *et al.* Convection-enhanced delivery of macromolecules in the brain. *PNAS* **91**, 2076–2080 (1994).

51. Halle, B., Mongelard, K. & Poulsen, F. Convection-enhanced drug delivery for glioblastoma: A systematic review focused on methodological differences in the use of the convection-enhanced delivery method. *Asian J. Neurosurg.* **14**, 5–14 (2019).

52. Brown, C. B., Jacobs, S., Johnson, M. P., Southerland, C. & Threatt, S. Convection-Enhanced Delivery in the Treatment of Glioblastoma. *Semin. Oncol. Nurs.* **34**, 494–500 (2018).

53. Jahangiri, A. *et al.* Convection-enhanced delivery in glioblastoma: a review of preclinical and clinical studies. *J. Neurosurg.* **126**, 191–200 (2017).

54. Stephen, Z. R. *et al.* Time-Resolved MRI Assessment of Convection-Enhanced Delivery by Targeted and Nontargeted Nanoparticles in a Human Glioblastoma Mouse Model. *Cancer Res* **79**, 4776–4786 (2019).

55. Han, Y. & Park, J.-H. Convection-enhanced delivery of liposomal drugs for effective treatment of glioblastoma multiforme. *Drug Deliv. and Transl. Res.* **10**, 1876–1887 (2020).

56. Finbloom, J. A. *et al.* Evaluation of Three Morphologically Distinct Virus-Like Particles as Nanocarriers for Convection-Enhanced Drug Delivery to Glioblastoma. *Nanomaterials* **8**, 1007–1019 (2018).

57. Singleton, W. *et al.* Convection enhanced delivery of panobinostat (LBH589)-loaded pluronic nano-micelles prolongs survival in the F98 rat glioma model. *Int. J. Nanomedicine* **12**, 1385–1399 (2017).

58. Zhang, C. *et al.* Convection enhanced delivery of cisplatin-loaded brain penetrating nanoparticles cures malignant glioma in rats. *J Control Release* **263**, 112–119 (2017).

59. Bouras, A., Kaluzova, M. & Hadjipanayis, C. G. Radiosensitivity enhancement of radioresistant glioblastoma by epidermal growth factor receptor antibody-conjugated iron- oxide nanoparticles. *J. Neurooncol.* **124**, 13–22 (2016).

60. Pastan, I., Bigner, D. D. & Chandramohan, V. EGFR/EGFRvIII-targeted immunotoxin therapy for the treatment of glioblastomas via convection-enhanced delivery. *Receptors Clin. Investig.* **3**, 1430–1437 (2017).

61. Upadhaya, P. G., Pulakkat, S. & Patravale, V. B. Nose-to-brain delivery: exploring newer domains for glioblastoma multiforme management. *Drug Deliv. Transl. Res.* **10**, 1044–1056 (2020).

62. Ullah, I. *et al.* Nose-to-Brain Delivery of Cancer-Targeting Paclitaxel-Loaded Nanoparticles Potentiates Antitumor Effects in Malignant Glioblastoma. *Mol. Pharm.* **17**, 1193–1204 (2020).

63. Chu, L. *et al.* Nose-to-brain delivery of temozolomide-loaded PLGA nanoparticles functionalized with anti-EPHA3 for glioblastoma targeting. *Drug Deliv.* **25**, 1634–1641 (2018).

64. de Oliveira Junior, E. R. *et al.* Increased Nose-to-Brain Delivery of Melatonin Mediated by Polycaprolactone Nanoparticles for the Treatment of Glioblastoma. *Pharm. Res.* **36**, (2019).

65. Sekerdag, E. *et al.* A potential non-invasive glioblastoma treatment: Nose-to-brain delivery of farnesylthiosalicylic acid incorporated hybrid nanoparticles. *J. Control. Release* **261**, 187–198 (2017).

66. Shinde, R. L. & Devarajan, P. V. Docosahexaenoic acid–mediated, targeted and sustained brain delivery of curcumin microemulsion. *Drug Deliv.* **24**, 152–161 (2017).

67. Van Woensel, M. *et al.* Sensitization of glioblastoma tumor micro-environment to chemo- and immunotherapy by Galectin-1 intranasal knock-down strategy. *Sci. Rep.* **7**, 1217–1221 (2017).

68. Beck, J. S. *et al.* A new family of mesoporous molecular sieves prepared with liquid crystal templates. *J. Am. Chem. Soc.* **114**, 10834–10843 (1992).

69. Akinjokun, A. I., Ojumu, T. V. & Ogunfowokan, A. O. *Biomass, Abundant Resources for Synthesis of Mesoporous Silica Material.* (IntechOpen, 2016).

70. Raman, N. K., Anderson, M. T. & Brinker, C. J. Template-based approaches to the preparation of amorphous, nanoporous silicas. *Chem. Mater.* **8**, 1682–1701 (1996).

71. Kresge, C. T. & Roth, W. J. The discovery of mesoporous molecular sieves from the twenty year perspective. *Chem. Soc. Rev.* **42**, 3663–3671 (2013).

72. Bernardos, A. *et al.* Enzyme-Responsive Intracellular Controlled Release Using Nanometric Silica Mesoporous Supports Capped with "Saccharides". *ACS Nano* **4**, 6353–6368 (2010).

73. Aznar, E. *et al.* Finely Tuned Temperature-Controlled Cargo Release Using Paraffin-Capped Mesoporous Silica Nanoparticles. *Angew. Chem. Int. Ed.* **50**, 11172–11175 (2011).

74. Tarn, D., Xue, M. & Zink, J. I. pH-Responsive Dual Cargo Delivery from Mesoporous Silica Nanoparticles with a Metal-Latched Nanogate. *Inorg. Chem.* **52**, 2044–2049 (2013).

75. Radhakrishnan, K. *et al.* Protamine-Capped Mesoporous Silica Nanoparticles for Biologically Triggered Drug Release. *Part. Part. Syst. Charact.* **31**, 449–458 (2014).

76. de la Torre, C. *et al.* Temperature-controlled release by changes in the secondary structure of peptides anchored onto mesoporous silica supports. *Chem. Commun.* **50**, 3184–3186 (2014).

77. Nam, L. *et al.* Drug Delivery Nanosystems for the Localized Treatment of Glioblastoma Multiforme. *Materials* **11**, 779–808 (2018).

78. Tannock, I. F. & Rotin, D. Acid pH in Tumors and Its Potential for Therapeutic Exploitation. *Cancer Res.* **49**, 4373–4384.

79. Ahmadi Nasab, N., Hassani Kumleh, H., Beygzadeh, M., Teimourian, S. & Kazemzad, M. Delivery of curcumin by a pH-responsive chitosan mesoporous silica nanoparticles for cancer treatment. *Artif. Cells Nanomed. Biotechnol.* **46**, 75–81 (2018).

80. Li, Z.-Y. *et al.* One-pot construction of functional mesoporous silica nanoparticles for the tumor-acidity-activated synergistic chemotherapy of glioblastoma. *ACS Appl. Mater. Interfaces* **5**, 7995–8001 (2013).

81. Mo, J., He, L., Ma, B. & Chen, T. Tailoring Particle Size of Mesoporous Silica Nanosystem To Antagonize Glioblastoma and Overcome Blood–Brain Barrier. *ACS Appl. Mater. Interfaces* **8**, 6811–6825 (2016).

82. Torchilin, V. Tumor delivery of macromolecular drugs based on the EPR effect. *Adv. Drug Deliv. Rev.* **63**, 131–135 (2011).

83. Maeda, H., Wu, J., Sawa, T., Matsumura, Y. & Hori, K. Tumor vascular permeability and the EPR effect in macromolecular therapeutics: a review. *J. Control. Release* **65**, 271–284 (2000).

84. Fang, J., Nakamura, H. & Maeda, H. The EPR effect: Unique features of tumor blood vessels for drug delivery, factors involved, and limitations and augmentation of the effect. *Adv. Drug Deliv. Rev.* **63**, 136–151 (2011).

85. Lu, J., Liong, M., Li, Z., Zink, J. I. & Tamanoi, F. Biocompatibility, Biodistribution, and Drug-Delivery Efficiency of Mesoporous Silica Nanoparticles for Cancer Therapy in Animals. *Small* **6**, 1794–1805 (2010).

86. Meng, H. *et al.* Use of Size and a Copolymer Design Feature To Improve the Biodistribution and the Enhanced Permeability and Retention Effect of Doxorubicin-Loaded Mesoporous Silica Nanoparticles in a Murine Xenograft Tumor Model. *ACS Nano* **5**, 4131–4144 (2011).

87. Zentner, G. M. *et al.* Biodegradable block copolymers for delivery of proteins and water-insoluble drugs. *J. Control. Release* **72**, 203–215 (2001).

88. Ashley, G. W., Henise, J., Reid, R. & Santi, D. V. Hydrogel drug delivery system with predictable and tunable drug release and degradation rates. *PNAS* **110**, 2318–2323 (2013).

89. Huang, P. *et al.* Bridging the Gap between Macroscale Drug Delivery Systems and Nanomedicines: A Nanoparticle-Assembled Thermosensitive Hydrogel for Peritumoral Chemotherapy. *ACS Appl. Mater. Interfaces* **8**, 29323–29333 (2016).

90. Basso, J. *et al.* Hydrogel-Based Drug Delivery Nanosystems for the Treatment of Brain Tumors. *Gels* **4**, 62–90 (2018).

91. Lin, F.-W. *et al.* Rapid *In Situ* MRI Traceable Gel-forming Dual-drug Delivery for Synergistic Therapy of Brain Tumor. *Theranostics* **7**, 2524–2536 (2017).

92. Ranganath, S. H., Kee, I., Krantz, W. B., Chow, P. K.-H. & Wang, C.-H. Hydrogel matrix entrapping PLGA-paclitaxel microspheres: drug delivery with

near zero-order release and implantability advantages for malignant brain tumour chemotherapy. *Pharm. Res.* **26**, 2101–2114 (2009).

93. Ranganath, S. H. *et al.* The use of submicron/nanoscale PLGA implants to deliver paclitaxel with enhanced pharmacokinetics and therapeutic efficacy in intracranial glioblastoma in mice. *Biomaterials* **31**, 5199–5207 (2010).

94. Tsao, C.-T. *et al.* Thermoreversible Poly(ethylene glycol)- *g* -Chitosan Hydrogel as a Therapeutic T Lymphocyte Depot for Localized Glioblastoma Immunotherapy. *Biomacromolecules* **15**, 2656–2662 (2014).

95. Wang, J. *et al.* Retro-Inverso CendR Peptide-Mediated Polyethyleneimine for Intracranial Glioblastoma-Targeting Gene Therapy. *Bioconjugate Chem.* **25**, 414–423 (2014).

96. Li, J. & Mooney, D. J. Designing hydrogels for controlled drug delivery. *Nat. Rev. Mater.* **1**, 16071–16109 (2016).

97. Ahmed, E. M. Hydrogel: Preparation, characterization, and applications: A review. *J. Adv. Res.* **6**, 105–121 (2015).

98. He, C., Kim, S. W. & Lee, D. S. In situ gelling stimuli-sensitive block copolymer hydrogels for drug delivery. *J. Control. Release* **127**, 189–207 (2008).

99. Hamidi, M., Azadi, A. & Rafiei, P. Hydrogel nanoparticles in drug delivery. *Adv. Drug Deliv. Rev.* **60**, 1638–1649 (2008).

100. Caló, E. & Khutoryanskiy, V. V. Biomedical applications of hydrogels: A review of patents and commercial products. *Eur. Polym. J.* **65**, 252–267 (2015).

101. Yu, L. & Ding, J. Injectable hydrogels as unique biomedical materials. *Chem. Soc. Rev.* **37**, 1473–1481 (2008).

102. Buwalda, S. J., Vermonden, T. & Hennink, W. E. Hydrogels for Therapeutic Delivery: Current Developments and Future Directions. *Biomacromolecules* **18**, 316–330 (2017).

103. Xun, W. *et al.* Peptide-Functionalized Thermo-Sensitive Hydrogels for Sustained Drug Delivery. *Macromol. Biosci.* **9**, 1219–1226 (2009).

104. Petit, A. *et al.* Modulating rheological and degradation properties of temperature-responsive gelling systems composed of blends of PCLA–PEG–PCLA triblock copolymers and their fully hexanoyl-capped derivatives. *Acta Biomater.* **8**, 4260–4267 (2012).

105. Petit, A. *et al.* Effect of Polymer Composition on Rheological and Degradation Properties of Temperature-Responsive Gelling Systems Composed of Acyl-Capped PCLA-PEG-PCLA. *Biomacromolecules* **14**, 3172–3182 (2013).

106. Shim, W. S. *et al.* Biodegradability and biocompatibility of a pH- and thermo-sensitive hydrogel formed from a sulfonamide-modified poly(ε-caprolactone-co-lactide)–poly(ethylene glycol)–poly(ε-caprolactone-co-lactide) block copolymer. *Biomaterials* **27**, 5178–5185 (2006).

107. Shim, W. S., Kim, S. W. & Lee, D. S. Sulfonamide-Based pH- and Temperature-Sensitive Biodegradable Block Copolymer Hydrogels. *Biomacromolecules* **7**, 1935–1941 (2006).

108. Shim, W. *et al.* pH- and temperature-sensitive, injectable, biodegradable block copolymer hydrogels as carriers for paclitaxel. *Int. J. Pharm.* **331**, 11–18 (2007).

109. Elstad, N. L. & Fowers, K. D. OncoGel (ReGel/paclitaxel) — Clinical applications for a novel paclitaxel delivery system. *Adv. Drug Deliv. Rev.* **61**, 785–794 (2009).

110. Cho, H., Gao, J. & Kwon, G. S. PEG- b -PLA micelles and PLGA- b -PEG- b - PLGA sol–gels for drug delivery. *J. Control. Release* **240**, 191–201 (2016).

111. Tyler, B. *et al.* A thermal gel depot for local delivery of paclitaxel to treat experimental brain tumors in rats. *J. Neurosurg.* **113**, 210–217 (2010).

112. Vellimana, A. K. *et al.* Combination of paclitaxel thermal gel depot with temozolomide and radiotherapy significantly prolongs survival in an experimental rodent glioma model. *J. Neuro-Oncol.* **111**, 229–236 (2013).

113. Ci, T. *et al.* Development and anti- *Candida* evaluation of the vaginal delivery system of amphotericin B nanosuspension-loaded thermogel. *J. Drug Target.* **26**, 829–839 (2018).

114. Russo, E. & Villa, C. Poloxamer Hydrogels for Biomedical Applications. *Pharmaceutics* **11**, 671 (2019).

115. Mortensen, K. & Pedersen, J. S. Structural study on the micelle formation of poly (ethylene oxide)-poly (propylene oxide)-poly (ethylene oxide) triblock copolymer in aqueous solution. *Macromolecules* **26**, 805–812 (1993).

116. Anderson, B. C., Pandit, N. K. & Mallapragada, S. K. Understanding drug release from poly(ethylene oxide)-b-poly(propylene oxide)-b-poly(ethylene oxide) gels. *J. Control. Release* **70**, 157–167 (2001).

117. Batrakova, E. V. Optimal Structure Requirements for Pluronic Block Copolymers in Modifying P-glycoprotein Drug Efflux Transporter Activity in Bovine Brain Microvessel Endothelial Cells. *J. Pharmacol. Exp. Ther.* **304**, 845–854 (2003).

118. Pitto-Barry, A. & Barry, N. P. E. Pluronic® block-copolymers in medicine: from chemical and biological versatility to rationalisation and clinical advances. *Polym. Chem.* **5**, 3291–3297 (2014).

119. Kabanov, A. V., Batrakova, E. V. & Alakhov, V. Y. Pluronic® block copolymers as novel polymer therapeutics for drug and gene delivery. *J. Control. Release* **82**, 189–212 (2002).

120. Raval, A., Pillai, S. A., Bahadur, A. & Bahadur, P. Systematic characterization of Pluronic ® micelles and their application for solubilization and in vitro release of some hydrophobic anticancer drugs. *J. Mol. Liq.* **230**, 473–481 (2017).

121. Rey-Rico, A. & Cucchiarini, M. PEO-PPO-PEO Tri-Block Copolymers for Gene Delivery Applications in Human Regenerative Medicine—An Overview. *Int. J. Mol. Sci.* **19**, 775–790 (2018).

122. Batrakova, E. V. & Kabanov, A. V. Pluronic block copolymers: Evolution of drug delivery concept from inert nanocarriers to biological response modifiers. *J. Control. Release* **130**, 98–106 (2008).

123. Batrakova, E. V. *et al.* Mechanism of sensitization of MDR cancer cells by Pluronic block copolymers: Selective energy depletion. *Br. J. Cancer* **85**, 1987–1997 (2001).

124. Niu, J., Wang, A., Ke, Z. & Zheng, Z. Glucose transporter and folic acid receptor-mediated Pluronic P105 polymeric micelles loaded with doxorubicin for brain tumor treating. *J. Drug Target.* **22**, 712–723 (2014).

125. Zhang, W. *et al.* Multifunctional Pluronic P123/F127 mixed polymeric micelles loaded with paclitaxel for the treatment of multidrug resistant tumors. *Biomaterials* **32**, 2894–2906 (2011).

126. Pellosi, D. S. *et al.* Pluronic® mixed micelles as efficient nanocarriers for benzoporphyrin derivatives applied to photodynamic therapy in cancer cells. *J. Photochem. Photobiol A* **314**, 143–154 (2016).

127. Xiao, W., Ehsanipour, A., Sohrabi, A. & Seidlits, S. K. Hyaluronic-Acid Based Hydrogels for 3-Dimensional Culture of Patient-Derived Glioblastoma Cells. *JoVE* 58176 (2018) doi:10.3791/58176.

128. Heffernan, J. M., Overstreet, D. J., Le, L. D., Vernon, B. L. & Sirianni, R. W. Bioengineered Scaffolds for 3D Analysis of Glioblastoma Proliferation and Invasion. *Ann. Biomed. Eng.* **43**, 1965–1977 (2015).

129. Wang, C., Tong, X., Jiang, X. & Yang, F. Effect of matrix metalloproteinase-mediated matrix degradation on glioblastoma cell behavior in 3D PEG-based hydrogels: Effect of MMP-mediated matrix degradation on gbm cell behavior. *J. Biomed. Mater. Res.* **105**, 770–778 (2017).

130. Kaphle, P., Li, Y. & Yao, L. The mechanical and pharmacological regulation of glioblastoma cell migration in 3D matrices. *J. Cell. Physiol.* **234**, 3948–3960 (2019).

131. Chang, F.-C. *et al.* Crosslinked Chitosan-PEG Hydrogel for Culture of Human Glioblastoma Cell Spheroids and Drug Screening. *Adv. Therap.* **1**, 1800058 (2018).

132. Gao, W., Zhang, Y., Zhang, Q. & Zhang, L. Nanoparticle-Hydrogel: A Hybrid Biomaterial System for Localized Drug Delivery. *Ann. Biomed. Eng.* **44**, 2049–2061 (2016).

133. Zhao, F. *et al.* Composites of Polymer Hydrogels and Nanoparticulate Systems for Biomedical and Pharmaceutical Applications. *Nanomaterials* **5**, 2054–2130 (2015).

134. Thakor, J. *et al.* Engineered hydrogels for brain tumor culture and therapy. *Bio-des. Manuf.* **3**, 203–226 (2020).

135. Yu, F. *et al.* A pump-free tricellular blood–brain barrier on-a-chip model to understand barrier property and evaluate drug response. *Biotechnol. Bioeng.* **117**, 1127–1136 (2020).

136. Ha, J. H. *et al.* Electro-responsive hydrogel-based microfluidic actuator platform for photothermal therapy. *Lab Chip* **20**, 3354–3364 (2020).

137. Pedron, S. *et al.* Hyaluronic acid-functionalized gelatin hydrogels reveal extracellular matrix signals temper the efficacy of erlotinib against patient-derived glioblastoma specimens. *Biomaterials* **219**, 119371 (2019).

138. Civita, P., M. Leite, D. & Pilkington, G. J. Pre-Clinical Drug Testing in 2D and 3D Human In Vitro Models of Glioblastoma Incorporating Non-Neoplastic Astrocytes: Tunneling Nano Tubules and Mitochondrial Transfer Modulates Cell Behavior and Therapeutic Response. *Int. J. Mol. Sci.* **20**, 6017–6041 (2019).

139. Zhao, Z. *et al.* Injectable postoperative enzyme-responsive hydrogels for reversing temozolomide resistance and reducing local recurrence after glioma operation. *Biomater. Sci.* **8**, 5306–5316 (2020).

140. Wang, F. *et al.* Supramolecular Tubustecan Hydrogel as Chemotherapeutic Carrier to Improve Tumor Penetration and Local Treatment Efficacy. *ACS Nano* **14**, 10083–10094 (2020).

141. Garrett, M. C. *et al.* Injectable diblock copolypeptide hydrogel provides platform to deliver effective concentrations of paclitaxel to an intracranial xenograft model of glioblastoma. *PLoS ONE* **15**, e0219632 (2020).

142. Schiapparelli, P. *et al.* Self-assembling and self-formulating prodrug hydrogelator extends survival in a glioblastoma resection and recurrence model. *J. Control. Release* **319**, 311–321 (2020).

143. Arai, T. *et al.* Novel drug delivery system using thermoreversible gelation polymer for malignant glioma. *J. Neurooncol.* **77**, 9–15 (2006).

144. Akbar, U. *et al.* Delivery of temozolomide to the tumor bed via biodegradable gel matrices in a novel model of intracranial glioma with resection. *J. Neurooncol.* **94**, 203–212 (2009).

145. Bastiancich, C. *et al.* Injectable nanomedicine hydrogel for local chemotherapy of glioblastoma after surgical resection. *J. Control. Release* **264**, 45–54 (2017).

146. Bastiancich, C. *et al.* Lauroyl-gemcitabine-loaded lipid nanocapsule hydrogel for the treatment of glioblastoma. *J. Control. Release* **225**, 283–293 (2016).

147. Chen, T. *et al.* Paclitaxel loaded phospholipid-based gel as a drug delivery system for local treatment of glioma. *Int. J. Pharm.* **528**, 127–132 (2017).

148. Erkoc, P., Cingöz, A., Bagci-Onder, T. & Kizilel, S. Quinacrine Mediated Sensitization of Glioblastoma (GBM) Cells to TRAIL through MMP-Sensitive PEG Hydrogel Carriers. *Macromol. Biosci.* **17**, 1600267 (2017).

149. Ranganath, S. H., Kee, I., Krantz, W. B., Chow, P. K.-H. & Wang, C.-H. Hydrogel matrix entrapping PLGA-paclitaxel microspheres: drug delivery with near zero-order release and implantability advantages for malignant brain tumour chemotherapy. *Pharm. Res.* **26**, 2101–2114 (2009).

150. Ranganath, S. H. *et al.* The use of submicron/nanoscale PLGA implants to deliver paclitaxel with enhanced pharmacokinetics and therapeutic efficacy in intracranial glioblastoma in mice. *Biomaterials* **31**, 5199–5207 (2010).

151. Ozeki, T., Hashizawa, K., Kaneko, D., Imai, Y. & Okada, H. Treatment of rat brain tumors using sustained-release of camptothecin from poly(lactic-co-glycolic acid) microspheres in a thermoreversible hydrogel. *Chem. Pharm. Bull.* **58**, 1142–1147 (2010).

152. Ozeki, T. *et al.* Combination Therapy of Surgical Tumor Resection with Implantation of a Hydrogel Containing Camptothecin-Loaded Poly(lactic-co-glycolic acid) Microspheres in a C6 Rat Glioma Model. *Biol. Pharm. Bull.* **35**, 545–550 (2012).

153. Arai, T. *et al.* Novel local drug delivery system using thermoreversible gel in combination with polymeric microspheres or liposomes. *Anticancer Res.* **30**, 1057–1064 (2010).

154. Ding, L. *et al.* Thermoresponsive nanocomposite gel for local drug delivery to suppress the growth of glioma by inducing autophagy. *Autophagy* **13**, 1176–1190 (2017).

155. Fourniols, T. *et al.* Temozolomide-loaded photopolymerizable PEG-DMA-based hydrogel for the treatment of glioblastoma. *J. Control. Release* **210**, 95–104 (2015).

156. Thérien-Aubin, H. *et al.* Temperature-Responsive Nanofibrillar Hydrogels for Cell Encapsulation. *Biomacromolecules* **17**, 3244–3251 (2016).

157. Muraoka, D. *et al.* Nanogel-Based Immunologically Stealth Vaccine Targets Macrophages in the Medulla of Lymph Node and Induces Potent Antitumor Immunity. *ACS Nano* **8**, 9209–9218 (2014).

158. Lei, Y. *et al.* Glutathione-sensitive RGD-Poly(ethylene glycol)-SS-Polyethylenimine for intracranial glioblastoma targeted gene delivery: Glutathione-sensitive polyethylenimine for glioblastoma gene delivery. *J. Gene Med.* **15**, 291–305 (2013).

159. Kim, H. A., Park, J. H., Yi, N. & Lee, M. Delivery of Hypoxia and Glioma Dual-Specific Suicide Gene Using Dexamethasone Conjugated Polyethylenimine for Glioblastoma-Specific Gene Therapy. *Mol. Pharm.* **11**, 938–950 (2014).

160. Kim, J. I., Kim, B., Chun, C., Lee, S. H. & Song, S.-C. MRI-monitored long-term therapeutic hydrogel system for brain tumors without surgical resection. *Biomaterials* **33**, 4836–4842 (2012).

161. Lin, F.-W. *et al.* Rapid *In Situ* MRI Traceable Gel-forming Dual-drug Delivery for Synergistic Therapy of Brain Tumor. *Theranostics* **7**, 2524–2536 (2017).

162. Ozeki, T. *et al.* Improvement of survival in C6 rat glioma model by a sustained drug release from localized PLGA microspheres in a thermoreversible hydrogel. *Int. J. Pharm.* **427**, 299–304 (2012).

163. Yang, M., Oh, I. Y., Mahanty, A., Jin, W.-L. & Yoo, J. S. Immunotherapy for Glioblastoma: Current State, Challenges, and Future Perspectives. *Cancers* **12**, 2334–2356 (2020).

164. Thomas, S. & Prendergast, G. C. Cancer Vaccines: A Brief Overview. in *Vaccine Design* (ed. Thomas, S.) vol. 1403 755–761 (Springer New York, 2016).

165. Fu, B. *et al.* Application of multifunctional nanomaterials in cancer vaccines. *Oncol. Rep.* **39**, 893–900 (2018).

166. Kane, J. R. *et al.* Sui generis: gene therapy and delivery systems for the treatment of glioblastoma. *Neuro-Oncol.* **17**, ii24–ii36 (2015).

167. Ma, D., Tian, S., Baryza, J., Luft, J. C. & DeSimone, J. M. Reductively Responsive Hydrogel Nanoparticles with Uniform Size, Shape, and Tunable Composition for Systemic siRNA Delivery *in Vivo*. *Mol. Pharm.* **12**, 3518–3526 (2015).

168. Bertucci, A. *et al.* Combined Delivery of Temozolomide and Anti-miR221 PNA Using Mesoporous Silica Nanoparticles Induces Apoptosis in Resistant Glioma Cells. *Small* **11**, 5687–5695 (2015).

169. He, Y., Liang, S., Long, M. & Xu, H. Mesoporous silica nanoparticles as potential carriers for enhanced drug solubility of paclitaxel. *Mater. Sci. Eng., C* **78**, 12–17 (2017).

170. Giménez, C. *et al.* Gated Mesoporous Silica Nanoparticles for the Controlled Delivery of Drugs in Cancer Cells. *Langmuir* **31**, 3753–3762 (2015).

171. Kim, H. *et al.* High-performance liquid chromatographic analysis and stability of anti-tumor agent temozolomide in human plasma. *J. Pharm. Biomed. Anal.* **24**, 461–468 (2001).

172. Yeager, R. L., Oldfield, E. H. & Chatterji, D. C. Quantitation of 1, 3-bis (2-chloroethyl)-1-nitrosourea in plasma using high-performance liquid chromatography. *J. Chromatogr. B Biomed. Sci. Appl.* **305**, 496–501 (1984).

173. Danhier, F. *et al.* Paclitaxel-loaded PEGylated PLGA-based nanoparticles: In vitro and in vivo evaluation. *J. Control. Release* **133**, 11–17 (2009).

174. Nag, A., Mitra, G. & Ghosh, P. C. A Colorimetric Assay for Estimation of Polyethylene Glycol and Polyethylene Glycolated Protein Using Ammonium Ferrothiocyanate. *Anal. Biochem.* **237**, 224–231 (1996).

175. Brunauer, S., Emmett, P. H. & Teller, E. Adsorption of Gases in Multimolecular Layers. *J. Am. Chem. Soc.* **60**, 309–319 (1938).

176. Barrett, E. P., Joyner, L. G. & Halenda, P. P. The Determination of Pore Volume and Area Distributions in Porous Substances. I. Computations from Nitrogen Isotherms. *J. Am. Chem. Soc.* **73**, 373–380 (1951).

177. Day, J. S. *et al.* Noradrenaline acting on astrocytic β2-adrenoceptors induces neurite outgrowth in primary cortical neurons. *Neuropharmacology* **77**, 234–248 (2014).

178. McNamee, E. N. *et al.* Noradrenaline acting at β-adrenoceptors induces expression of IL-1β and its negative regulators IL-1ra and IL-1RII, and drives

an overall anti-inflammatory phenotype in rat cortex. *Neuropharmacology* **59**, 37–48 (2010).

179. Srivastava, G. K. *et al.* Trypan Blue staining method for quenching the autofluorescence of RPE cells for improving protein expression analysis. *Exp. Eye Res.* **93**, 956–962 (2011).

180. Miliukiené, V. V., Biziulevičiené, G. J., Chaustova, L. P., Pilinkiené, A. V. & Biziulevičius, G. A. Determination of quantitative parameters of Escherichia coli phagocytosis by mouse peritoneal macrophages. *Cell tissue biol.* **1**, 446–450 (2007).

181. Sholl, D. A. Dendritic organization in the neurons of the visual and motor cortices of the cat. *J. Anat.* **87**, 387–406 (1953).

182. Gutierrez, H. & Davies, A. M. A fast and accurate procedure for deriving the Sholl profile in quantitative studies of neuronal morphology. *J. Neurosci. Methods* **163**, 24–30 (2007).

183. Friedrich, J. *et al.* A Reliable Tool to Determine Cell Viability in Complex 3-D Culture: The Acid Phosphatase Assay. *J. Biomol. Screen* **12**, 925–937 (2007).

184. Friedrich, J., Seidel, C., Ebner, R. & Kunz-Schughart, L. A. Spheroid-based drug screen: considerations and practical approach. *Nat. Protoc.* **4**, 309–324 (2009).

185. Russell, W. M. S. & Burch, R. L. The Principles of Humane Experimental Technique. *Johns Hopkins Bloomberg School of Public Health* https://caat.jhsph.edu/principles/the-principles-of-humane-experimental-technique (1959).

186. Tannenbaum, J. & Bennett, B. T. Russell and Burch's 3Rs Then and Now: The Need for Clarity in Definition and Purpose. *J. Am. Assoc. Lab. Anim. Sci.* **54**, 120–132 (2015).

187. Bianco, J. *et al.* Novel model of orthotopic U-87 MG glioblastoma resection in athymic nude mice. *J. Neurosci. Methods* **284**, 96–102 (2017).

188. An ad hoc committee of the National Cancer Research Institute *et al.* Guidelines for the welfare and use of animals in cancer research. *Br. J. Cancer* **102**, 1555–1577 (2010).

189. Xie, J., Lee, S. & Chen, X. Nanoparticle-based theranostic agents. *Adv. Drug Deliv. Rev.* **62**, 1064–1079 (2010).

190. Li, Z., Barnes, J. C., Bosoy, A., Stoddart, J. F. & Zink, J. I. Mesoporous silica nanoparticles in biomedical applications. *Chem. Soc. Rev.* **41**, 2590 (2012).

191. Van Elk, M. *et al.* Nanomedicines for advanced cancer treatments: Transitioning towards responsive systems. *Int. J. Pharm.* **515**, 132–164 (2016).

192. Dhande, R., Patel, A. & Thakkar, H. *Nanopharmaceuticals: A Boon or Bane*. (2015).

193. ALOthman, Z. A Review: Fundamental Aspects of Silicate Mesoporous Materials. *Materials* **5**, 2874–2902 (2012).

194. Meynen, V., Cool, P. & Vansant, E. F. Verified syntheses of mesoporous materials. *Microporous Mesoporous Mater.* **125**, 170–223 (2009).

195. Tarn, D. *et al.* Mesoporous Silica Nanoparticle Nanocarriers: Biofunctionality and Biocompatibility. *Acc. Chem. Res.* **46**, 792–801 (2013).

196. M. Rosenholm, J., Sahlgren, C. & Linden, M. Multifunctional Mesoporous Silica Nanoparticles for Combined Therapeutic, Diagnostic and Targeted Action in Cancer Treatment. *Curr. Drug Targets* **12**, 1166–1186 (2011).

197. Shevtsov, M. A. *et al.* Zero-valent Fe confined mesoporous silica nanocarriers (Fe(0) @ MCM-41) for targeting experimental orthotopic glioma in rats. *Sci. Rep.* **6**, 29247 (2016).

198. Zhang, H., Zhang, W., Zhou, Y., Jiang, Y. & Li, S. Dual Functional Mesoporous Silicon Nanoparticles Enhance the Radiosensitivity of VPA in Glioblastoma. *Transl. Oncol.* **10**, 229–240 (2017).

199. You, Y., Yang, L., He, L. & Chen, T. Tailored mesoporous silica nanosystem with enhanced permeability of the blood–brain barrier to antagonize glioblastoma. *J. Mater. Chem. B* **4**, 5980–5990 (2016).

200. Heggannavar, G. B., Hiremath, C. G., Achari, D. D., Pangarkar, V. G. & Kariduraganavar, M. Y. Development of Doxorubicin-Loaded Magnetic Silica–Pluronic F-127 Nanocarriers Conjugated with Transferrin for Treating Glioblastoma across the Blood–Brain Barrier Using an in Vitro Model. *ACS Omega* **3**, 8017–8026 (2018).

201. Goel, S. *et al.* VEGF $_{121}$ -Conjugated Mesoporous Silica Nanoparticle: A Tumor Targeted Drug Delivery System. *ACS Appl. Mater. Interfaces* **6**, 21677–21685 (2014).

202. Yang, Q. *et al.* Evading Immune Cell Uptake and Clearance Requires PEG Grafting at Densities Substantially Exceeding the Minimum for Brush Conformation. *Mol. Pharmaceutics* **11**, 1250–1258 (2014).

203. Cui, Y., Dong, H., Cai, X., Wang, D. & Li, Y. Mesoporous Silica Nanoparticles Capped with Disulfide-Linked PEG Gatekeepers for Glutathione-Mediated Controlled Release. *ACS Appl. Mater. Interfaces* **4**, 3177–3183 (2012).

204. Wang, Y.-C., Wang, F., Sun, T.-M. & Wang, J. Redox-Responsive Nanoparticles from the Single Disulfide Bond-Bridged Block Copolymer as

Drug Carriers for Overcoming Multidrug Resistance in Cancer Cells. *Bioconjugate Chem.* **22**, 1939–1945 (2011).

205. Koo, A. N. *et al.* Disulfide-cross-linked PEG-poly(amino acid)s copolymer micelles for glutathione-mediated intracellular drug delivery. *Chem. Commun.* 6570–6572 (2008).

206. Wang, K. *et al.* Novel shell-cross-linked micelles with detachable PEG corona for glutathione-mediated intracellular drug delivery. *Soft Matter* **9**, 692–699 (2013).

207. Thambi, T., Deepagan, V. G., Ko, H., Lee, D. S. & Park, J. H. Bioreducible polymersomes for intracellular dual-drug delivery. *J. Mater. Chem.* **22**, 22028–22037 (2012).

208. Hong, R. *et al.* Glutathione-Mediated Delivery and Release Using Monolayer Protected Nanoparticle Carriers. *J. Am. Chem. Soc.* **128**, 1078–1079 (2006).

209. Mortera, R. *et al.* Cell-induced intracellular controlled release of membrane impermeable cysteine from a mesoporous silica nanoparticle-based drug delivery system. *Chem. Commun.* 3219–3221 (2009).

210. Singh, R. & Whitesides, G. M. Thiol-disulfide interchange. in *Sulphur-Containing Functional Groups* 633–658 (John Wiley & Sons, Inc., 1993).

211. Estrela, J. M., Ortega, A. & Obrador, E. Glutathione in Cancer Biology and Therapy. *Crit. Rev. Clin. Lab. Sci.* **43**, 143–181 (2006).

212. Bansal, A. & Simon, M. C. Glutathione metabolism in cancer progression and treatment resistance. *J. Cell. Biol.* **217**, 2291–2298 (2018).

213. Finsy, R. & Jaeger, N. D. Particle Sizing by Photon Correlation Spectroscopy. Part II: Average values. *Part. Part. Syst. Charact.* **8**, 187–193 (1991).

214. Kaasalainen, M. *et al.* Size, Stability, and Porosity of Mesoporous Nanoparticles Characterized with Light Scattering. *Nanoscale Res. Lett.* **12**, 74–83 (2017).

215. Cauda, V., Argyo, C. & Bein, T. Impact of different PEGylation patterns on the long-term bio-stability of colloidal mesoporous silica nanoparticles. *J. Mater. Chem.* **20**, 8693–8699 (2010).

216. Di Martino, A., Kucharczyk, P., Capakova, Z., Humpolicek, P. & Sedlarik, V. Enhancement of temozolomide stability by loading in chitosan-carboxylated polylactide-based nanoparticles. *J. Nanopart. Res.* **19**, 71–87 (2017).

217. Xu, X. *et al.* Folate-Functionalized Mesoporous Silica Nanoparticles as a Liver Tumor-Targeted Drug Delivery System to Improve the Antitumor Effect of Paclitaxel. *J. Nanomater.* **2017**, 1–13 (2017).

218. Fang, C. *et al.* Temozolomide Nanoparticles for Targeted Glioblastoma Therapy. *ACS Appl. Mater. Interfaces* **7**, 6674–6682 (2015).

219. Kumari, S., Ahsan, S. M., Kumar, J. M., Kondapi, A. K. & Rao, N. M. Overcoming blood brain barrier with a dual purpose Temozolomide loaded Lactoferrin nanoparticles for combating glioma (SERP-17-12433). *Sci. Rep.* **7**, 6602–6615 (2017).

220. Jain, D. S. *et al.* Unraveling the cytotoxic potential of Temozolomide loaded into PLGA nanoparticles. *J. Pharm. Sci.* **22**, 18–26 (2014).

221. Lee, C. & Ooi, I. Preparation of Temozolomide-Loaded Nanoparticles for Glioblastoma Multiforme Targeting—Ideal Versus Reality. *Pharmaceuticals* **9**, 54–64 (2016).

222. Yang, T. *et al.* Enhanced solubility and stability of PEGylated liposomal paclitaxel: In vitro and in vivo evaluation. *Int. J. Pharm.* **338**, 317–326 (2007).

223. Ganipineni, L. P. *et al.* Paclitaxel-loaded multifunctional nanoparticles for the targeted treatment of glioblastoma. *J. Drug Target.* **27**, 614–623 (2019).

224. Gupta, B. *et al.* Polyamino Acid Layer-by-Layer (LbL) Constructed Silica-Supported Mesoporous Titania Nanocarriers for Stimuli-Responsive Delivery of microRNA 708 and Paclitaxel for Combined Chemotherapy. *ACS Appl. Mater. Interfaces* **10**, 24392–24405 (2018).

225. Wen, J. *et al.* In Situ Formation of Homogeneous Tellurium Nanodots in Paclitaxel-Loaded MgAl Layered Double Hydroxide Gated Mesoporous Silica Nanoparticles for Synergistic Chemo/PDT/PTT Trimode Combinatorial Therapy. *Inorg. Chem.* **58**, 2987–2996 (2019).

226. Lin, J. *et al.* PEGylated Lipid bilayer coated mesoporous silica nanoparticles for co-delivery of paclitaxel and curcumin: Design, characterization and its cytotoxic effect. *Int. J. Pharm.* **536**, 272–282 (2018).

227. Qiu, Y. *et al.* Lipid-coated hollow mesoporous silica nanospheres for co-delivery of doxorubicin and paclitaxel: Preparation, sustained release, cellular uptake and pharmacokinetics. *Mater. Sci. Eng., C* **71**, 835–843 (2017).

228. Fu, Q., Hargrove, D. & Lu, X. Improving paclitaxel pharmacokinetics by using tumor-specific mesoporous silica nanoparticles with intraperitoneal delivery. *Nanomedicine* **12**, 1951–1959 (2016).

229. Jia, L. *et al.* In vitro and in vivo evaluation of paclitaxel-loaded mesoporous silica nanoparticles with three pore sizes. *Int. J. Pharm.* **445**, 12–19 (2013).

230. Lu, J., Liong, M., Zink, J. I. & Tamanoi, F. Mesoporous Silica Nanoparticles as a Delivery System for Hydrophobic Anticancer Drugs. *Small* **3**, 1341–1346 (2007).

231. Lopes, I. C., de Oliveira, S. C. B. & Oliveira-Brett, A. M. Temozolomide chemical degradation to 5-aminoimidazole-4-carboxamide – Electrochemical study. *J. Electroanal. Chem.* **704**, 183–189 (2013).

232. Maggini, L. *et al.* Breakable mesoporous silica nanoparticles for targeted drug delivery. *Nanoscale* **8**, 7240–7247 (2016).

233. Amini-Fazl, M. S., Mobedi, H. & Barzin, J. Investigation of aqueous stability of taxol in different release media. *Drug Dev. Ind. Pharm.* **40**, 519–526 (2014).

234. Wieland, T. Chemistry and Properties of Glutathione. in *Glutathione* 45–57 (Elsevier, 1954). doi:10.1016/B978-1-4832-2900-3.50008-0.

235. Tian, J. & Stella, V. J. Degradation of Paclitaxel and Related Compounds in Aqueous Solutions II: Nonepimerization Degradation Under Neutral to Basic pH Conditions. *J. Pharm. Sci.* **97**, 3100–3108 (2008).

236. Tian, J. & Stella, V. J. Degradation of Paclitaxel and Related Compounds in Aqueous Solutions III: Degradation Under Acidic pH Conditions and Overall Kinetics. *J. Pharm. Sci.* **99**, 1288–1298 (2010).

237. Andrasi, M., Bustos, R., Gaspar, A., Gomez, F. A. & Klekner, A. Analysis and stability study of temozolomide using capillary electrophoresis. *J. Chromatogr. B Biomed. Appl.* **878**, 1801–1808 (2010).

238. Estrella, V. *et al.* Acidity Generated by the Tumor Microenvironment Drives Local Invasion. *Cancer Res.* **73**, 1524–1535 (2013).

239. Schornack, P. A. & Gillies, R. J. Contributions of Cell Metabolism and H+ Diffusion to the Acidic pH of Tumors. *Neoplasia* **5**, 135–145 (2003).

240. Yeh, C.-C. *et al.* A study of glutathione status in the blood and tissues of patients with breast cancer. *Cell Biochem.* **24**, 555–559 (2006).

241. Luo, Z. *et al.* Mesoporous Silica Nanoparticles End-Capped with Collagen: Redox-Responsive Nanoreservoirs for Targeted Drug Delivery. *Angew. Chem. Int. Ed.* **50**, 640–643 (2011).

242. Lee, S. Y. Temozolomide resistance in glioblastoma multiforme. *Genes & Diseases* **3**, 198–210 (2016).

243. Munoz, J. L., Walker, N. D., Scotto, K. W. & Rameshwar, P. Temozolomide competes for P-glycoprotein and contributes to chemoresistance in glioblastoma cells. *Cancer Lett.* **367**, 69–75 (2015).

244. Zhang, J. *et al.* Co-delivery of paclitaxel and tetrandrine via iRGD peptide conjugated lipid-polymer hybrid nanoparticles overcome multidrug resistance in cancer cells. *Sci. Rep.* **7**, (2017).

245. Xue, H. *et al.* Delivery of miR-375 and doxorubicin hydrochloride by lipid-coated hollow mesoporous silica nanoparticles to overcome multiple drug resistance in hepatocellular carcinoma. *Int. J. Nanomedicine* **12**, 5271–5287 (2017).

246. Huang, W. *et al.* Surfactin-based nanoparticles loaded with doxorubicin to overcome multidrug resistance in cancers. *Int. J. Nanomedicine* **13**, 1723–1736 (2018).

247. Yin, J., Deng, X., Zhang, J. & Lin, J. Current Understanding of Interactions between Nanoparticles and ABC Transporters in Cancer Cells. *Curr. Med. Chem.* **25**, 5930–5944 (2018).

248. Yi, G. *et al.* Acquired temozolomide resistance in MGMT-deficient glioblastoma cells is associated with regulation of DNA repair by DHC2. *Brain* **142**, 2352–2366 (2019).

249. Baer', J. C., Freeman', A. A. & Newlands', E. S. Depletion of 06-alkylguanine-DNA alkyltransferase correlates with potentiation of temozolomide and CCNU toxicity in human tumour cells. *Br. J. Cancer* **67**, 1299–1302 (1993).

250. Chen, L. *et al.* Overcoming acquired drug resistance in colorectal cancer cells by targeted delivery of 5-FU with EGF grafted hollow mesoporous silica nanoparticles. *Nanoscale* **7**, 14080–14092 (2015).

251. Liebmann, J. E. *et al.* Cytotoxic studies of pacfitaxel (Taxol®) in human tumour cell lines. 6.

252. He, Q. *et al.* The effect of PEGylation of mesoporous silica nanoparticles on nonspecific binding of serum proteins and cellular responses. *Biomaterials* **31**, 1085–1092 (2010).

253. Liu, D. *et al.* In Vitro and in Vivo Studies on the Transport of PEGylated Silica Nanoparticles across the Blood–Brain Barrier. *ACS Appl. Mater. Interfaces* **6**, 2131–2136 (2014).

254. Binley, K. E. Sholl analysis: A quantitative comparison of semi-automated methods. *J. Neurosci. Methods* **225**, 65–70 (2014).

255. Orlando, A. *et al.* Mesoporous silica nanoparticles trigger mitophagy in endothelial cells and perturb neuronal network activity in a size- and time-dependent manner. *Int. J. Nanomedicine* **12**, 3547–3559 (2017).

256. Sun, B. *et al.* Nerve Growth Factor-Conjugated Mesoporous Silica Nanoparticles Promote Neuron-Like PC12 Cell Proliferation and Neurite Growth. *J. Nanosci. Nanotechnol.* **16**, 2390–2393 (2016).

257. Kim, M. S. *et al.* Nanotherapeutics of PTEN Inhibitor with Mesoporous Silica Nanocarrier Effective for Axonal Outgrowth of Adult Neurons. *ACS Appl. Mater. Interfaces* **8**, 18741–18753 (2016).

258. Cheng, C.-S. *et al.* Codelivery of Plasmid and Curcumin with Mesoporous Silica Nanoparticles for Promoting Neurite Outgrowth. *ACS Appl. Mater. Interfaces* **11**, 15322–15331 (2019).

259. Chang, J.-H. *et al.* Generation of Functional Dopaminergic Neurons from Reprogramming Fibroblasts by Nonviral-based Mesoporous Silica Nanoparticles. *Sci. Rep.* **8**, 11 (2018).

260. Tononi, G., Sporns, O. & Edelman, G. M. A measure for brain complexity: relating functional segregation and integration in the nervous system. *PNAS* **91**, 5033–5037 (1994).

261. Timme, N. M. & Marshall, N. J. Criticality Maximizes Complexity in Neural Tissue. *Front. Physiol.* **7**, 19 (2016).

262. Muotri, A. R. & Gage, F. H. Generation of neuronal variability and complexity. *Nature* **441**, 1087–1093 (2006).

263. Venkataramani, V. *et al.* Glutamatergic synaptic input to glioma cells drives brain tumour progression. *Nature* **573**, 532–538 (2019).

264. Zeng, Q. *et al.* Synaptic proximity enables NMDAR signalling to promote brain metastasis. *Nature* **573**, 526–531 (2019).

265. Bass, J. D. *et al.* Stability of Mesoporous Oxide and Mixed Metal Oxide Materials under Biologically Relevant Conditions. *Chem. Mater.* **19**, 4349–4356 (2007).

266. Cauda, V., Schlossbauer, A. & Bein, T. Bio-degradation study of colloidal mesoporous silica nanoparticles: Effect of surface functionalization with organo-silanes and poly(ethylene glycol). *Microporous Mesoporous Mater.* **132**, 60–71 (2010).

267. Fuentes, C., Ruiz-Rico, M., Fuentes, A., Ruiz, M. J. & Barat, J. M. Degradation of silica particles functionalised with essential oil components

under simulated physiological conditions. *J. Hazard. Mater.* **399**, 123120 (2020).

268. Havuz, E. & Gokmen, O. In-vitro dewetting properties of planned replacement and daily disposable silicone hydrogel contact lenses. *Cont. Lens Anterior Eye* (2020) doi:10.1016/j.clae.2020.10.007.

269. Reindel, W., Mosehauer, G., Rah, M., Proskin, H. & Steffen, R. Clinical Performance of Samfilcon A, a Unique Silicone Hydrogel Lens, on a 7-Day Extended Wear Basis. *Clin. Ophthalmol.* **14**, 3457–3464 (2020).

270. Bashari, A., Rouhani Shirvan, A. & Shakeri, M. Cellulose-based hydrogels for personal care products. *Polym. Adv. Technol.* **29**, 2853–2867 (2018).

271. Mitura, S., Sionkowska, A. & Jaiswal, A. Biopolymers for hydrogels in cosmetics: review. *J. Mater Sci. Mater. Med.* **31**, 50–63 (2020).

272. Sun, A. *et al.* An injectable photopolymerized hydrogel with antimicrobial and biocompatible properties for infected skin regeneration. *NPG Asia Mater.* **12**, 25–35 (2020).

273. Chen, H. *et al.* An injectable self-healing coordinative hydrogel with antibacterial and angiogenic properties for diabetic skin wound repair. *NPG Asia Mater.* **11**, 3–14 (2019).

274. Qu, J. *et al.* Antibacterial adhesive injectable hydrogels with rapid self-healing, extensibility and compressibility as wound dressing for joints skin wound healing. *Biomaterials* **183**, 185–199 (2018).

275. Askari, M. *et al.* Recent progress in extrusion 3D bioprinting of hydrogel biomaterials for tissue regeneration: a comprehensive review with focus on advanced fabrication techniques. *Biomater. Sci.* **9**, 535–573 (2020).

276. Rizzo, F. & Kehr, N. S. Recent Advances in Injectable Hydrogels for Controlled and Local Drug Delivery. *Adv. Healthcare Mater.* **10**, 2001341 (2020).

277. Parhi, R. Cross-Linked Hydrogel for Pharmaceutical Applications: A Review. *Adv. Pharm. Bull.* **7**, 515–530 (2017).

278. Frachini, E. & Petri, D. Magneto-Responsive Hydrogels: Preparation, Characterization, Biotechnological and Environmental Applications. *J. Braz. Chem. Soc.* **30**, 2010–2028 (2019).

279. Oyen, M. L. Mechanical characterisation of hydrogel materials. *Int. Mater. Rev.* **59**, 44–59 (2014).

280. Maitra, J. & Shukla, V. K. Crosslinking in hydrogels. *Am. J. Polym. Sci. Eng.* **4**, 25–31 (2014).

281. Yang, X. *et al.* Sustained release of lipophilic gemcitabine from an injectable polymeric hydrogel for synergistically enhancing tumor chemoradiotherapy. *Chem. Eng. J.* **396**, 125320 (2020).

282. Liao, J. *et al.* Polymer hybrid magnetic nanocapsules encapsulating IR820 and PTX for external magnetic field-guided tumor targeting and multifunctional theranostics. *Nanoscale* **9**, 2479–2491 (2017).

283. Adhikari, B. *et al.* The use of TMZ embedded hydrogels for the treatment of orthotopic human glioma xenografts. *J. Clin. Neurosci.* **45**, 288–292 (2017).

284. Puente, P. de la *et al.* Injectable Hydrogels for Localized Chemotherapy and Radiotherapy in Brain Tumors. *J. Pharm. Sci.* **107**, 922–933 (2018).

285. Babaei, M. *et al.* Thermosensitive composite hydrogel incorporated with curcumin-loaded nanopolymersomes for prolonged and localized treatment of glioma. *J. Drug Deliv. Sci. Technol.* **59**, 101885 (2020).

286. Wang, G., Wang, J.-J., Tang, X.-J., Du, L. & Li, F. In vitro and in vivo evaluation of functionalized chitosan–Pluronic micelles loaded with myricetin on glioblastoma cancer. *Nanomedicine* **12**, 1263–1278 (2016).

287. Chen, Y., Huang, Y., Liu, W., Gao, F. & Fang, X. c(RGDyK)-decorated Pluronic micelles for enhanced doxorubicin and paclitaxel delivery to brain glioma. *Int. J. Nanomedicine* **11**, 1629–1641 (2016).

288. Cidade, M. *et al.* Injectable Hydrogels Based on Pluronic/Water Systems Filled with Alginate Microparticles for Biomedical Applications. *Materials* **12**, 1083–1096 (2019).

289. Zhang, J., Stevens, M. F. G. & Bradshaw, T. D. Temozolomide: mechanisms of action, repair and resistance. *Curr. Mol. Pharmacol.* **5**, 102–114 (2012).

290. Weiss, R. B. & Issell, B. F. The nitrosoureas: carmustine (BCNU) and lomustine (CCNU). *Cancer Treat. Rev.* **9**, 313–330 (1982).

291. Papait, R., Magrassi, L., Rigamonti, D. & Cattaneo, E. Temozolomide and carmustine cause large-scale heterochromatin reorganization in glioma cells. *Biochem. Biophys. Res. Commun.* **379**, 434–439 (2009).

292. Wesolowski, J. R., Rajdev, P. & Mukherji, S. K. Temozolomide (Temodar). *Am. J. Neuroradiol.* **31**, 1383–1384 (2010).

293. GLIADEL® WAFER (carmustine implant), for intracranial use. (2018).

294. Horwitz, S. B. Taxol (paclitaxel): mechanisms of action. *Ann. Oncol.* **5**, S3-6 (1994).

295. Weinkam, R. J. & Lin, H.-S. Reactions of 1, 3-bis (2-chloroethyl)-1-nitrosourea and 1-(2-chloroethyl)-3-cyclohexyl-1-nitrosourea in aqueous solution. *J. Med. Chem.* **22**, 1193–1198 (1979).

296. Newlands, E. S., Stevens, M. F. G., Wedge, S. R., Wheelhouse, R. T. & Brock, C. Temozolomide: a review of its discovery, chemical properties, pre-clinical development and clinical trials. *Cancer Treat. Rev.* **23**, 35–61 (1997).

297. Mathematical models of drug release. in *Strategies to Modify the Drug Release from Pharmaceutical Systems* 63–86 (Elsevier, 2015). doi:10.1016/B978-0-08-100092-2.00005-9.

298. Siepmann, J. & Peppas, N. A. Higuchi equation: Derivation, applications, use and misuse. *Int. J. Pharm.* **418**, 6–12 (2011).

299. Bodratti, A. & Alexandridis, P. Formulation of Poloxamers for Drug Delivery. *J. Funct. Biomater.* **9**, 11–34 (2018).

300. Gioffredi, E. *et al.* Pluronic F127 Hydrogel Characterization and Biofabrication in Cellularized Constructs for Tissue Engineering Applications. *Proc. CIRP* **49**, 125–132 (2016).

301. Raval, A., Pillai, S. A., Bahadur, A. & Bahadur, P. Systematic characterization of Pluronic ® micelles and their application for solubilization and in vitro release of some hydrophobic anticancer drugs. *J. Mol. Liq.* **230**, 473–481 (2017).

302. Bedrov, D., Ayyagari, C. & Smith, G. D. Multiscale Modeling of Poly(ethylene oxide)−Poly(propylene oxide)−Poly(ethylene oxide) Triblock Copolymer Micelles in Aqueous Solution. *J. Chem. Theory Comput.* **2**, 598–606 (2006).

303. Chae, G. S. *et al.* Enhancement of the stability of BCNU using self-emulsifying drug delivery systems (SEDDS) and in vitro antitumor activity of self-emulsified BCNU-loaded PLGA wafer. *Int. J. Pharm.* **301**, 6–14 (2005).

304. Ding, L. *et al.* Thermoresponsive nanocomposite gel for local drug delivery to suppress the growth of glioma by inducing autophagy. *Autophagy* **13**, 1176–1190 (2017).

305. Peppas, N. Analysis of Fickian and non-Fickian drug release from polymers. *Pharm. Acta Helv.* **60**, 110–111 (1985).

306. Ricardo, N. M. P. S. *et al.* Effect of water-soluble polymers, polyethylene glycol and poly(vinylpyrrolidone), on the gelation of aqueous micellar solutions of Pluronic copolymer F127. *J. Colloid Interface Sci.* **368**, 336–341 (2012).

307. Zhang, W. *et al.* Multifunctional Pluronic P123/F127 mixed polymeric micelles loaded with paclitaxel for the treatment of multidrug resistant tumors. *Biomaterials* **32**, 2894–2906 (2011).

308. Niu, J., Wang, A., Ke, Z. & Zheng, Z. Glucose transporter and folic acid receptor-mediated Pluronic P105 polymeric micelles loaded with doxorubicin for brain tumor treating. *J. Drug Target.* **22**, 712–723 (2014).

309. Zuidema, J. M., Rivet, C. J., Gilbert, R. J. & Morrison, F. A. A protocol for rheological characterization of hydrogels for tissue engineering strategies: A Protocol for Rheological Characterization of Hydrogels. *J. Biomed. Mater. Res.* **102**, 1063–1073 (2014).

310. Baby, D. K. Rheology of hydrogels. in *Rheology of Polymer Blends and Nanocomposites* 193–204 (Elsevier, 2020). doi:10.1016/B978-0-12-816957-5.00009-4.

311. Cuomo, F., Cofelice, M. & Lopez, F. Rheological Characterization of Hydrogels from Alginate-Based Nanodispersion. *Polymers* **11**, 259–269 (2019).

312. Fallenstein, G. T., Hulce, V. D. & Melvin, J. W. Dynamic mechanical properties of human brain tissue. *J. Biomech.* **2**, 217–226 (1969).

313. McCracken, P. J., Manduca, A., Felmlee, J. & Ehman, R. L. Mechanical transient-based magnetic resonance elastography. *Magn. Reson. Med.* **53**, 628–639 (2005).

314. Cheng, S., Clarke, E. C. & Bilston, L. E. Rheological properties of the tissues of the central nervous system: A review. *Med. Eng. Phys.* **30**, 1318–1337 (2008).

315. Dou, Q., Abdul Karim, A. & Loh, X. J. Modification of Thermal and Mechanical Properties of PEG-PPG-PEG Copolymer (F127) with MA-POSS. *Polymers (Basel)* **8**, 341–354 (2016).

316. Fakhari, A., Corcoran, M. & Schwarz, A. Thermogelling properties of purified poloxamer 407. *Heliyon* **3**, e00390 (2017).

317. Hyun, K., Nam, J. G., Wilhellm, M., Ahn, K. H. & Lee, S. J. Large amplitude oscillatory shear behavior of PEO-PPO-PEO triblock copolymer solutions. *Rheol. Acta* **45**, 239–249 (2006).

318. Magami, S. M. & Williams, R. L. Gelation studies on acrylic acid-based hydrogels via in situ photo-crosslinking and rheology. *J. Appl. Polym. Sci.* **135**, 46691–46691 (2018).

319. Baït, N. Rheology and adhesive properties versus structure of poly(acrylamide-co-hydroxyethyl methacrylate) hydrogels. *Int. J. Adhes. Adhes.* **96**, 9 (2020).

320. Gordon, J., Amini, S. & White, M. K. General Overview of Neuronal Cell Culture. in *Neuronal Cell Culture* vol. 1078 1–8 (Humana Press, 2013).

321. Xie, L., Dai, Z., Pang, C., Lin, D. & Zheng, M. Cellular glucose metabolism is essential for the reduction of cell-impermeable water-soluble tetrazolium (WST) dyes. *Int. J. Biol. Sci.* **14**, 1535–1544 (2018).

322. Seibenhener, M. L. & Wooten, M. W. Isolation and Culture of Hippocampal Neurons from Prenatal Mice. *J. Vis. Exp.* (2012) doi:10.3791/3634.

323. Batrakova, E. V. & Kabanov, A. V. Pluronic block copolymers: Evolution of drug delivery concept from inert nanocarriers to biological response modifiers. *J. Control. Release* **130**, 98–106 (2008).

324. Pitto-Barry, A. & Barry, N. P. E. Pluronic® block-copolymers in medicine: from chemical and biological versatility to rationalisation and clinical advances. *Polym. Chem.* **5**, 3291–3297 (2014).

325. Batrakova, E. V. *et al.* Mechanism of sensitization of MDR cancer cells by Pluronic block copolymers: Selective energy depletion. *Br. J. Cancer* **85**, 1987–1997 (2001).

326. Batrakova, E. V. Optimal Structure Requirements for Pluronic Block Copolymers in Modifying P-glycoprotein Drug Efflux Transporter Activity in Bovine Brain Microvessel Endothelial Cells. *J. Pharmacol. Exp. Ther.* **304**, 845–854 (2003).

327. Balion, Z. *et al.* Cerebellar Cells Self-Assemble into Functional Organoids on Synthetic, Chemically Crosslinked ECM-Mimicking Peptide Hydrogels. *Biomolecules* **10**, 754–778 (2020).

328. Liu, W., Han, K., Sun, M. & Wang, J. Enhancement and control of neuron adhesion on polydimethylsiloxane for cell microengineering using a functionalized triblock polymer. *Lab Chip* **19**, 3162–3167 (2019).

329. Evans, M. G., Al-Shakli, A. & Chari, D. M. Electrophysiological properties of neurons grown on soft polymer scaffolds reveal the potential to develop neuromimetic culture environments. 9.

330. Sutachan, J.-J. & Recio-Pinto, E. Pluronic F-127 affects the regulation of cytoplasmic Ca2+ in neuronal cells. *Brain Res. J.* **1068**, 131–137 (2006).

331. Dancy, J. G. *et al.* Non-specific binding and steric hindrance thresholds for penetration of particulate drug carriers within tumor tissue. *J. Control. Release* **238**, 139–148 (2016).

332. Zhao, M. *et al.* Codelivery of paclitaxel and temozolomide through a photopolymerizable hydrogel prevents glioblastoma recurrence after surgical resection. *J. Control. Release* **309**, 72–81 (2019).

333. Robertson, F. L., Marqués-Torrejón, M.-A., Morrison, G. M. & Pollard, S. M. Experimental models and tools to tackle glioblastoma. *Dis. Model. Mech.* **12**, 1–12 (2019).

334. da Hora, C. C., Schweiger, M. W., Wurdinger, T. & Tannous, B. A. Patient-Derived Glioma Models: From Patients to Dish to Animals. *Cells* **8**, 1177–1195 (2019).

335. Clark, M. J. *et al.* U87MG Decoded: The Genomic Sequence of a Cytogenetically Aberrant Human Cancer Cell Line. *PLoS Genet.* **6**, e1000832 (2010).

336. Clark, M. J. *et al.* Correction: U87MG Decoded: The Genomic Sequence of a Cytogenetically Aberrant Human Cancer Cell Line. *PLoS Genet.* **14**, e1007392 (2018).

337. Kiseleva, L. N., Kartashev, A. V., Vartanyan, N. L., Pinevich, A. A. & Samoilovich, M. P. A172 and T98G cell lines characteristics. *Cell Tiss. Biol.* **10**, 341–348 (2016).

338. Torsvik, A. *et al.* U-251 revisited: genetic drift and phenotypic consequences of long-term cultures of glioblastoma cells. *Cancer Med.* **3**, 812–824 (2014).

339. Giakoumettis, D., Kritis, A. & Foroglou, N. C6 cell line: the gold standard in glioma research. *Hippokratia* **22**, 105–112 (2018).

340. Ledur, P. F., Onzi, G. R., Zong, H. & Lenz, G. Culture conditions defining glioblastoma cells behavior: what is the impact for novel discoveries? *Oncotarget* **8**, 69185–69197 (2017).

341. Pamies, D., Zurich, M.-G. & Hartung, T. Organotypic Models to Study Human Glioblastoma: Studying the Beast in Its Ecosystem. *iScience* **23**, 101633 (2020).

342. Zanoni, M. *et al.* Modeling neoplastic disease with spheroids and organoids. *J. Hematol. Oncol.* **13**, 97–111 (2020).

343. Gilazieva, Z., Ponomarev, A., Rutland, C., Rizvanov, A. & Solovyeva, V. Promising Applications of Tumor Spheroids and Organoids for Personalized Medicine. *Cancers* **12**, 2727–2745 (2020).

344. Zhang, C., Jin, M., Zhao, J., Chen, J. & Jin, W. Organoid models of glioblastoma: advances, applications and challenges. *Am. J. Cancer Res.* **10**, 2242–2257 (2020).

345. Fang, Y. & Eglen, R. M. Three-Dimensional Cell Cultures in Drug Discovery and Development. *SLAS Discov.* **22**, 456– 472 (2017).

346. Ryu, N.-E., Lee, S.-H. & Park, H. Spheroid Culture System Methods and Applications for Mesenchymal Stem Cells. *Cells* **8**, 1620–1632 (2019).

347. Goldbrunner, R. H. *et al.* Vascularization of human glioma spheroids implanted into rat cortex is conferred by two distinct mechanisms. *J. Neurosci. Res.* **55**, 486–495 (1999).

348. Stein, A. M., Demuth, T., Mobley, D., Berens, M. & Sander, L. M. A Mathematical Model of Glioblastoma Tumor Spheroid Invasion in a Three-Dimensional In Vitro Experiment. *Biophys. J.* **92**, 356–365 (2007).

349. Stein, A. M. *et al.* Estimating the cell density and invasive radius of three-dimensional glioblastoma tumor spheroids grown in vitro. *Appl. Opt.* **46**, 5110–5118 (2007).

350. Dhanikula, R. S., Argaw, A., Bouchard, J.-F. & Hildgen, P. Methotrexate Loaded Polyether-Copolyester Dendrimers for the Treatment of Gliomas: Enhanced Efficacy and Intratumoral Transport Capability. *Mol. Pharm.* **5**, 105–116 (2008).

351. Gao, H. *et al.* Whole-cell SELEX aptamer-functionalised poly(ethyleneglycol)-poly(ε-caprolactone) nanoparticles for enhanced targeted glioblastoma therapy. *Biomaterials* **33**, 6264–6272 (2012).

352. Koosha, F. *et al.* The combination of A-966492 and Topotecan for effective radiosensitization on glioblastoma spheroids. *Biochem. Biophys. Res. Commun.* **491**, 1092–1097 (2017).

353. Berthier, S. *et al.* Anticancer properties of sodium selenite in human glioblastoma cell cluster spheroids. *J. Trace Elem. Med. Biol.* **44**, 161–176 (2017).

354. Bayat, N. *et al.* Apoptotic effect of atorvastatin in glioblastoma spheroids tumor cultured in fibrin gel. *Biomedicine & Pharmacotherapy* **84**, 1959–1966 (2016).

355. Bayat, N. *et al.* Anti-inflammatory Effects of Atorvastatin by Suppressing TRAF3IP2 and IL-17RA in Human Glioblastoma Spheroids Cultured in a Three-dimensional Model: Possible Relevance to Glioblastoma Treatment. *Mol. Neurobiol.* **55**, 2102–2110 (2018).

356. Lázaro, I. *et al.* Deep Tissue Translocation of Graphene Oxide Sheets in Human Glioblastoma 3D Spheroids and an Orthotopic Xenograft Model. *Adv. Therap.* **4**, 1–15 (2020).

357. Upadhyay, U. M. *et al.* Intracranial microcapsule chemotherapy delivery for the localized treatment of rodent metastatic breast adenocarcinoma in the brain. *PNAS* **111**, 16071–16076 (2014).

358. Danhier, F., Messaoudi, K., Lemaire, L., Benoit, J.-P. & Lagarce, F. Combined anti-Galectin-1 and anti-EGFR siRNA-loaded chitosan-lipid nanocapsules decrease temozolomide resistance in glioblastoma: In vivo evaluation. *Int. J. Pharm.* **481**, 154–161 (2015).

359. Sanai, N., Polley, M.-Y., McDermott, M. W., Parsa, A. T. & Berger, M. S. An extent of resection threshold for newly diagnosed glioblastomas. *J. Neurosurg.* **115**, 3–8 (2011).

360. Sweeney, K. J. *et al.* Validation of an imageable surgical resection animal model of Glioblastoma (GBM). *J. Neurosci. Methods* **233**, 99–104 (2014).

361. Kim, W. *et al.* Real-time imaging of glioblastoma using bioluminescence in a U-87 MG xenograft model mouse. *J. Korean Soc. Appl. Biol. Chem.* **58**, 243–248 (2015).

362. Zhao, M. *et al.* Post-resection treatment of glioblastoma with an injectable nanomedicine-loaded photopolymerizable hydrogel induces long-term survival. *Int. J. Pharm.* **548**, 522–529 (2018).

363. Szatmári, T. *et al.* Detailed characterization of the mouse glioma 261 tumor model for experimental glioblastoma therapy. *Cancer Sci.* **97**, 546–553 (2006).

364. Kleijn, A. *et al.* The In Vivo Therapeutic Efficacy of the Oncolytic Adenovirus Delta24-RGD Is Mediated by Tumor-Specific Immunity. *PLoS ONE* **9**, e97495 (2014).

365. Kleijn, A. *et al.* The therapeutic efficacy of the oncolytic virus Delta24-RGD in a murine glioma model depends primarily on antitumor immunity. *OncoImmunology* **3**, e955697 (2014).

366. Riss, T. & Trask, O. J. Factors to consider when interrogating 3D culture models with plate readers or automated microscopes. *In Vitro Cell.Dev.Biol.-Animal* (2021) doi:10.1007/s11626-020-00537-3.

367. Singh, S. K. *et al.* Critical role of three-dimensional tumorsphere size on experimental outcome. *BioTechniques* **69**, 333–338 (2020).

368. Xu, Y. *et al.* The synergic antitumor effects of paclitaxel and temozolomide co-loaded in mPEG-PLGA nanoparticles on glioblastoma cells. *Oncotarget* **7**, 20890–20901 (2016).

369. Kessel, S. *et al.* High-Throughput 3D Tumor Spheroid Screening Method for Cancer Drug Discovery Using Celigo Image Cytometry. *SLAS Technol.* **22**, 454–465 (2017).

370. Santra, S. *et al.* Fluorescence lifetime measurements to determine the core–shell nanostructure of FITC-doped silica nanoparticles: An optical approach to evaluate nanoparticle photostability. *J. Lumin.* **117**, 75–82 (2006).

371. Tchoryk, A. *et al.* Penetration and Uptake of Nanoparticles in 3D Tumor Spheroids. *Bioconjugate Chem.* **30**, 1371–1384 (2019).

372. Nance, E. A. *et al.* A Dense Poly(Ethylene Glycol) Coating Improves Penetration of Large Polymeric Nanoparticles Within Brain Tissue. *Sci. Transl. Med.* **4**, 119–137 (2012).

373. Fourniols, T. *et al.* Temozolomide-loaded photopolymerizable PEG-DMA-based hydrogel for the treatment of glioblastoma. *J. Control. Release* **210**, 95–104 (2015).

374. Zhou, Z. *et al.* Glioblastoma spheroids produce infiltrative gliomas in the rat brainstem. *Childs. Nerv. Syst.* **33**, 437–446 (2017).

375. Miao, H. *et al.* EGFRvIII-Specific Chimeric Antigen Receptor T Cells Migrate to and Kill Tumor Deposits Infiltrating the Brain Parenchyma in an Invasive Xenograft Model of Glioblastoma. *PLoS ONE* **9**, e94281 (2014).

376. Recinos, V. R. *et al.* Combination of Intracranial Temozolomide With Intracranial Carmustine Improves Survival When Compared With Either Treatment Alone in a Rodent Glioma Model. *Neurosurgery* **66**, 530–537 (2010).

377. McGirt, M. J. *et al.* Gliadel (BCNU) wafer plus concomitant temozolomide therapy after primary resection of glioblastoma multiforme: Clinical article. *J. Neurosurg.* **110**, 583–588 (2009).

378. Barenholz, Y. (Chezy). Doxil® — The first FDA-approved nano-drug: Lessons learned. *J. Control. Release* **160**, 117–134 (2012).

379. Batist, G., Barton, J., Chaikin, P., Swenson, C. & Welles, L. Myocet (liposome-encapsulated doxorubicin citrate): a new approach in breast cancer therapy. *Expert Opin. Pharmacother.* **3**, 1739–1751 (2002).

380. Kundranda, M. N. & Niu, J. Albumin-bound paclitaxel in solid tumors: clinical development and future directions. *Drug Des. Devel. Ther.* **9**, 3767–3777 (2015).

381. Silverman, J. A. & Deitcher, S. R. Marqibo® (vincristine sulfate liposome injection) improves the pharmacokinetics and pharmacodynamics of vincristine. *Cancer Chemother. Pharmacol.* **71**, 555–564 (2013).

382. Maier-Hauff, K. *et al.* Intracranial thermotherapy using magnetic nanoparticles combined with external beam radiotherapy: results of a feasibility study on patients with glioblastoma multiforme. *J. Neurooncol.* **81**, 53–60 (2007).

383. Maier-Hauff, K. *et al.* Efficacy and safety of intratumoral thermotherapy using magnetic iron-oxide nanoparticles combined with external beam radiotherapy on patients with recurrent glioblastoma multiforme. *J. Neurooncol.* **103**, 317–324 (2011).

384. He, Q., Zhang, Z., Gao, F., Li, Y. & Shi, J. In vivo Biodistribution and Urinary Excretion of Mesoporous Silica Nanoparticles: Effects of Particle Size and PEGylation. *Small* **7**, 271–280 (2011).

385. Dekeyser, C. M. Degradation of bare and silanized silicon wafer surfaces by constituents of biological fluids. *J. Colloid Interface Sci.* **378**, 77–82 (2012).

386. Vallet-Regí, M., Colilla, M., Izquierdo-Barba, I. & Manzano, M. Mesoporous Silica Nanoparticles for Drug Delivery: Current Insights. *Molecules* **23**, 47–65 (2018).

387. Seré, S. *et al.* Altering the Biodegradation of Mesoporous Silica Nanoparticles by Means of Experimental Parameters and Surface Functionalization. *J. Nanomater.* **2018**, 1–10 (2018).

388. Dogra, P. *et al.* Establishing the effects of mesoporous silica nanoparticle properties on in vivo disposition using imaging-based pharmacokinetics. *Nat. Commun.* **9**, 4551–4564 (2018).

389. Huang, X. & Brazel, C. S. On the importance and mechanisms of burst release in matrix-controlled drug delivery systems. *J. Control. Release* **73**, 121–136 (2001).

390. Stepanenko, A. A. & Chekhonin, V. P. On the Critical Issues in Temozolomide Research in Glioblastoma: Clinically Relevant Concentrations and MGMT-independent Resistance. *Biomedicines* **7**, 92–96 (2019).

391. Ostermann, S. *et al.* Plasma and cerebrospinal fluid population pharmacokinetics of temozolomide in malignant glioma patients. *Clin. Cancer Res.* **10**, 3728–3736 (2004).

392. Rosso, L. *et al.* A new model for prediction of drug distribution in tumor and normal tissues: pharmacokinetics of temozolomide in glioma patients. *Cancer Res.* **69**, 120–127 (2009).

393. Portnow, J. *et al.* The neuropharmacokinetics of temozolomide in patients with resectable brain tumors: potential implications for the current approach to chemoradiation. *Clin. Cancer Res.* **15**, 7092–7098 (2009).

394. Jackson, S. *et al.* The effect of an adenosine A2A agonist on intra-tumoral concentrations of temozolomide in patients with recurrent glioblastoma. *Fluids Barriers CNS* **15**, 2–10 (2018).

395. Kaina, B. & Christmann, M. DNA repair in personalized brain cancer therapy with temozolomide and nitrosoureas. *DNA Repair* **78**, 128–141 (2019).

396. Strobel, H. *et al.* Temozolomide and Other Alkylating Agents in Glioblastoma Therapy. *Biomedicines* **7**, 69–85 (2019).

397. Günther, W., Pawlak, E., Damasceno, R., Arnold, H. & Terzis, A. J. Temozolomide induces apoptosis and senescence in glioma cells cultured as multicellular spheroids. *Br. J. Cancer* **88**, 463–469 (2003).

398. Fehlauer, F., Muench, M., Richter, E. & Rades, D. The inhibition of proliferation and migration of glioma spheroids exposed to temozolomide is less than additive if combined with irradiation. *Oncol. Rep.* **17**, 941–945 (2007).

399. McCrorie, P. *et al.* Etoposide and olaparib polymer-coated nanoparticles within a bioadhesive sprayable hydrogel for post-surgical localised delivery to brain tumours. *Eur. J. Pharm. Biopharm.* **157**, 108–120 (2020).

400. Brachi, G. *et al.* Intratumoral injection of hydrogel-embedded nanoparticles enhances retention in glioblastoma. *Nanoscale* **12**, 23838–23850 (2020).

401. Brem, S. *et al.* Local delivery of temozolomide by biodegradable polymers is superior to oral administration in a rodent glioma model. *Cancer Chemother. Pharmacol.* **60**, 643–650 (2007).

402. Bastiancich, C. *et al.* Drug combination using an injectable nanomedicine hydrogel for glioblastoma treatment. *Int. J. Pharm.* **559**, 220–227 (2019).

403. Soroceanu, L., Gillespie, Y., Khazaeli, M. B. & Sontheimer, H. Use of Chlorotoxin for Targeting of Primary Brain Tumors. *Cancer Res.* **58**, 4871–4879 (1998).

404. Lyons, S. A., O'Neal, J. & Sontheimer, H. Chlorotoxin, a scorpion-derived peptide, specifically binds to gliomas and tumors of neuroectodermal origin. *Glia* **39**, 162–173 (2002).

405. Kievit, F. M. *et al.* Chlorotoxin Labeled Magnetic Nanovectors for Targeted Gene Delivery to Glioma. *ACS Nano* **4**, 4587–4594 (2010).

406. Sharma, P. & Debinski, W. Receptor-Targeted Glial Brain Tumor Therapies. *Int. J. Mol. Sci.* **19**, (2018).

407. Liang, Y., Li, Z., Yuan, H., Wang, L. & Gao, L.-H. Poly(p-phenylenevinylene) nanoparticles modified with antiEGFRvIII for specific glioblastoma therapy. *Sci. Rep.* **11**, 4449 (2021).

408. Quesnel, A., Karagiannis, G. S. & Filippou, P. S. Extracellular proteolysis in glioblastoma progression and therapeutics. *Biochim. Biophys. Acta Rev. Cancer* **1874**, 188428 (2020).

409. Nazli, C., Demirer, G. S., Yar, Y., Acar, H. Y. & Kizilel, S. Targeted delivery of doxorubicin into tumor cells via MMP-sensitive PEG hydrogel-coated

magnetic iron oxide nanoparticles (MIONPs). *Colloids Surf. B: Biointerfaces* **122**, 674–683 (2014).

410. Yokel, R. A. Nanoparticle brain delivery: a guide to verification methods. *Nanomedicine* **15**, 409–432 (2020).

411. Renshaw, J. *et al.* Dual Blockade of the PI3K/AKT/mTOR (AZD8055) and RAS/MEK/ERK (AZD6244) Pathways Synergistically Inhibits Rhabdomyosarcoma Cell Growth *In Vitro* and *In Vivo*. *Clin. Cancer Res.* **19**, 5940–5951 (2013).

412. Shimizu, T. *et al.* The Clinical Effect of the Dual-Targeting Strategy Involving PI3K/AKT/mTOR and RAS/MEK/ERK Pathways in Patients with Advanced Cancer. *Clin. Cancer Res.* **18**, 2316–2325 (2012).

413. Jang, B.-S. & Kim, I. A. A Radiosensitivity Gene Signature and PD-L1 Status Predict Clinical Outcome of Patients with Glioblastoma Multiforme in The Cancer Genome Atlas Dataset. *Cancer Res. Treat.* **52**, 530–542 (2020).

414. Sanders, S. & Debinski, W. Challenges to Successful Implementation of the Immune Checkpoint Inhibitors for Treatment of Glioblastoma. *Int. J. Mol. Sci.* **21**, 2759 (2020).

415. Seidel, J. A., Otsuka, A. & Kabashima, K. Anti-PD-1 and Anti-CTLA-4 Therapies in Cancer: Mechanisms of Action, Efficacy, and Limitations. *Front. Oncol.* **8**, 86 (2018).

APPENDICES

Appendix 1
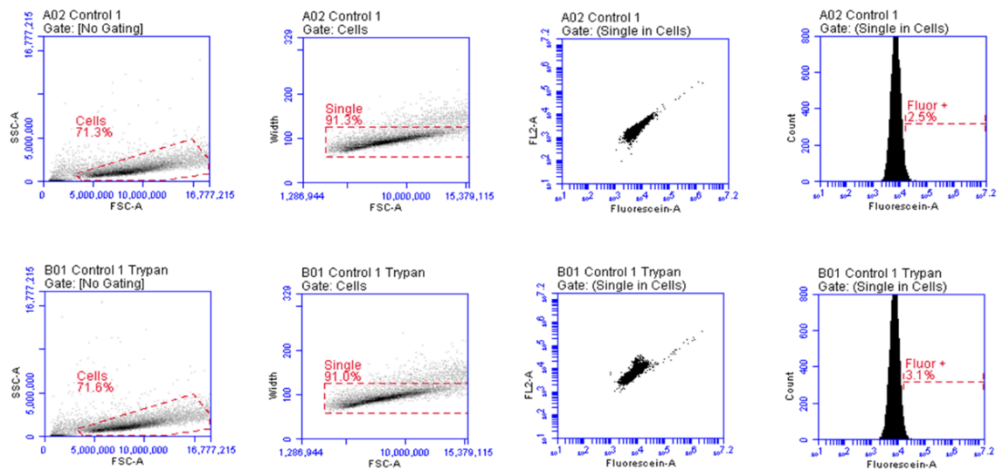
Figure A1.1: Representative graphs from the Flow cytometer analysis of control cells before and after trypan blue addition (Replicate 1).
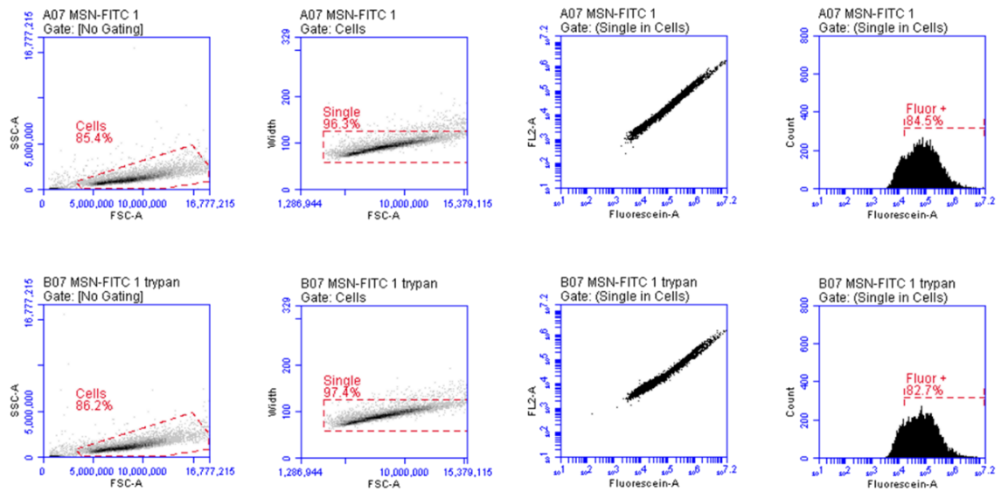
Figure A1.2: Representative graphs from the Flow cytometer analysis of MSN-FITC treated cells before and after trypan blue addition (Replicate 1).
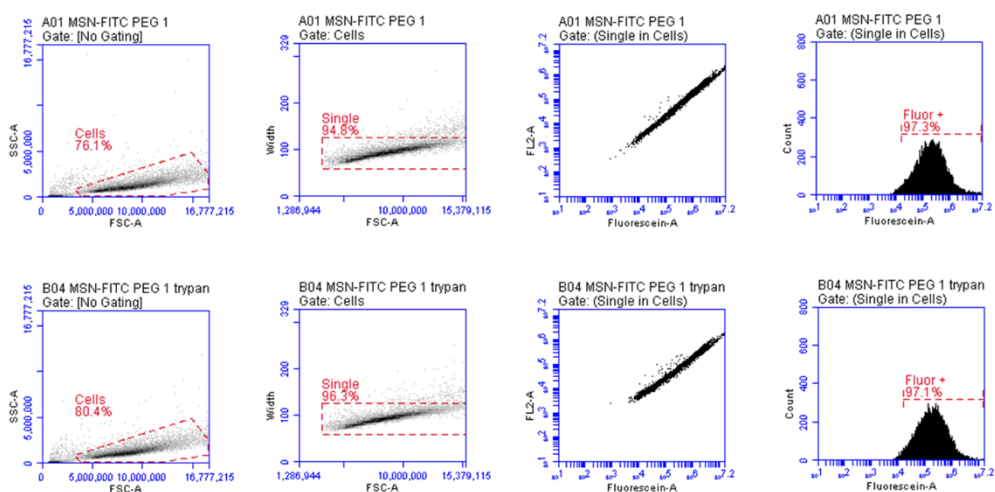
Figure A1.3: Representative graphs from the Flow cytometer analysis of MSN-FITC-PEG treated cells before and after trypan blue addition (Replicate 1).

Table A1.1: Correlation between concentrations of MSN, MSN-PEG and drugs loaded into MSNs for the *in vitro* cytotoxicity assay.

MSN (µg/mL)	MSN-PEG (µg/mL)	TMZ (µM)	PTX (µM)
1.5	5	1.5	0.35
3	10	3	0.7
5	15.5	5	1.2
15	50	15	3.5
30	100	30	7
50	175	50	12
60	200	60	14
75	250	72	17
100	350	100	23
200	700	200	46
250	875	260	58

Appendix 2
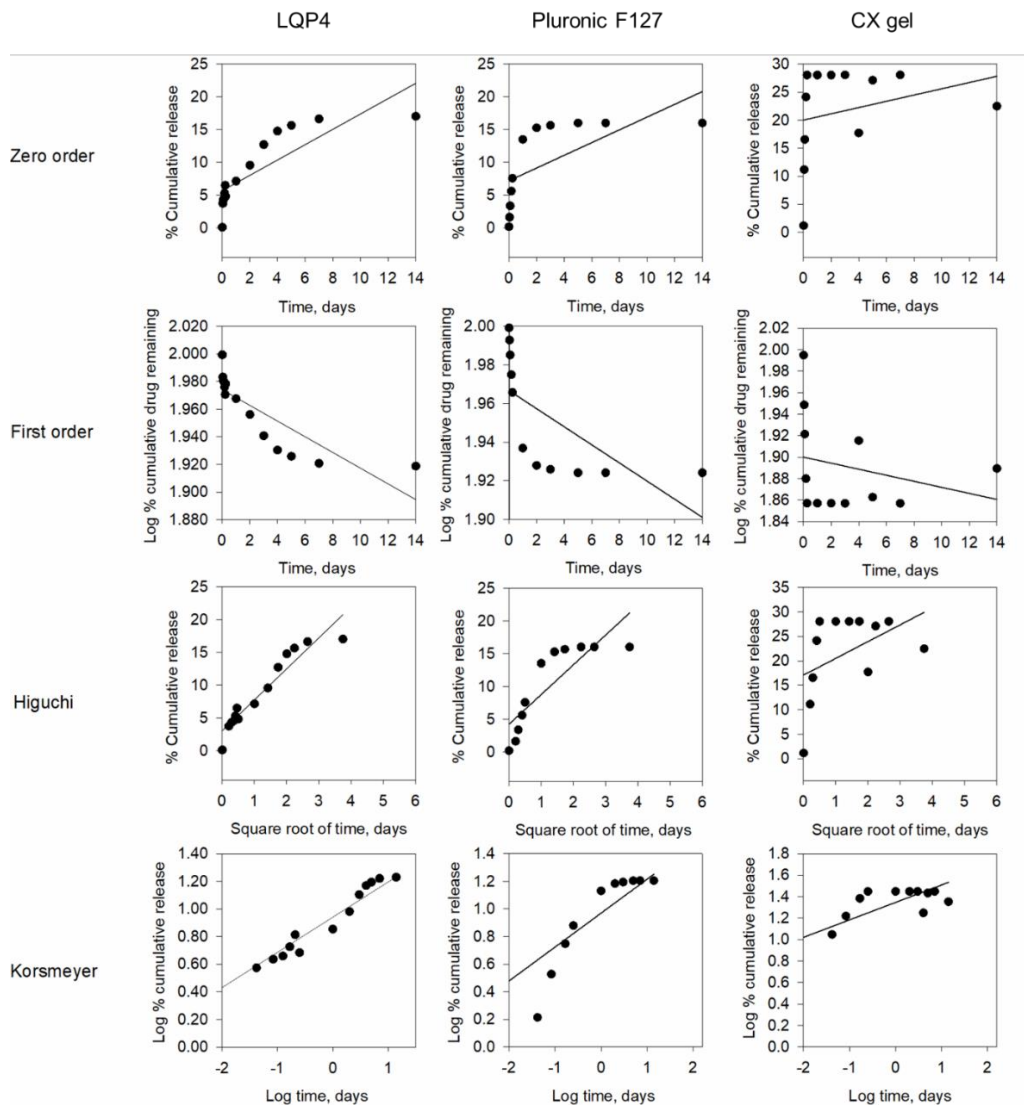
Figure A2.1: Mathematical model fitting (Zero order, First order, Higuchi and Korsmeyer-Peppas models) of TMZ release from gels (LQP4, Pluronic F-127 and CX).
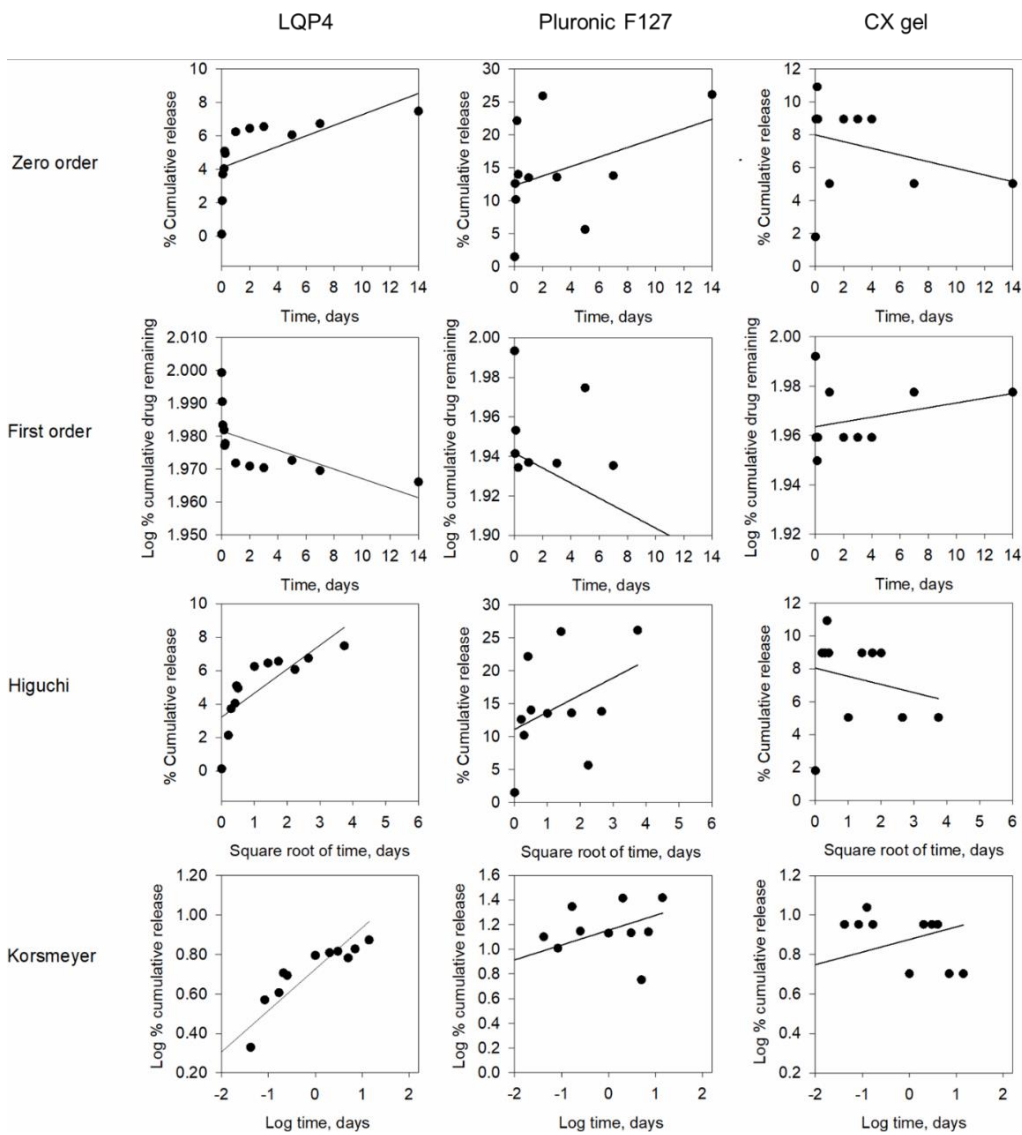
Figure A2.2: Mathematical model fitting (Zero order, First order, Higuchi and Korsmeyer-Peppas models) of BCNU release from gels (LQP4, Pluronic F-127 and CX).
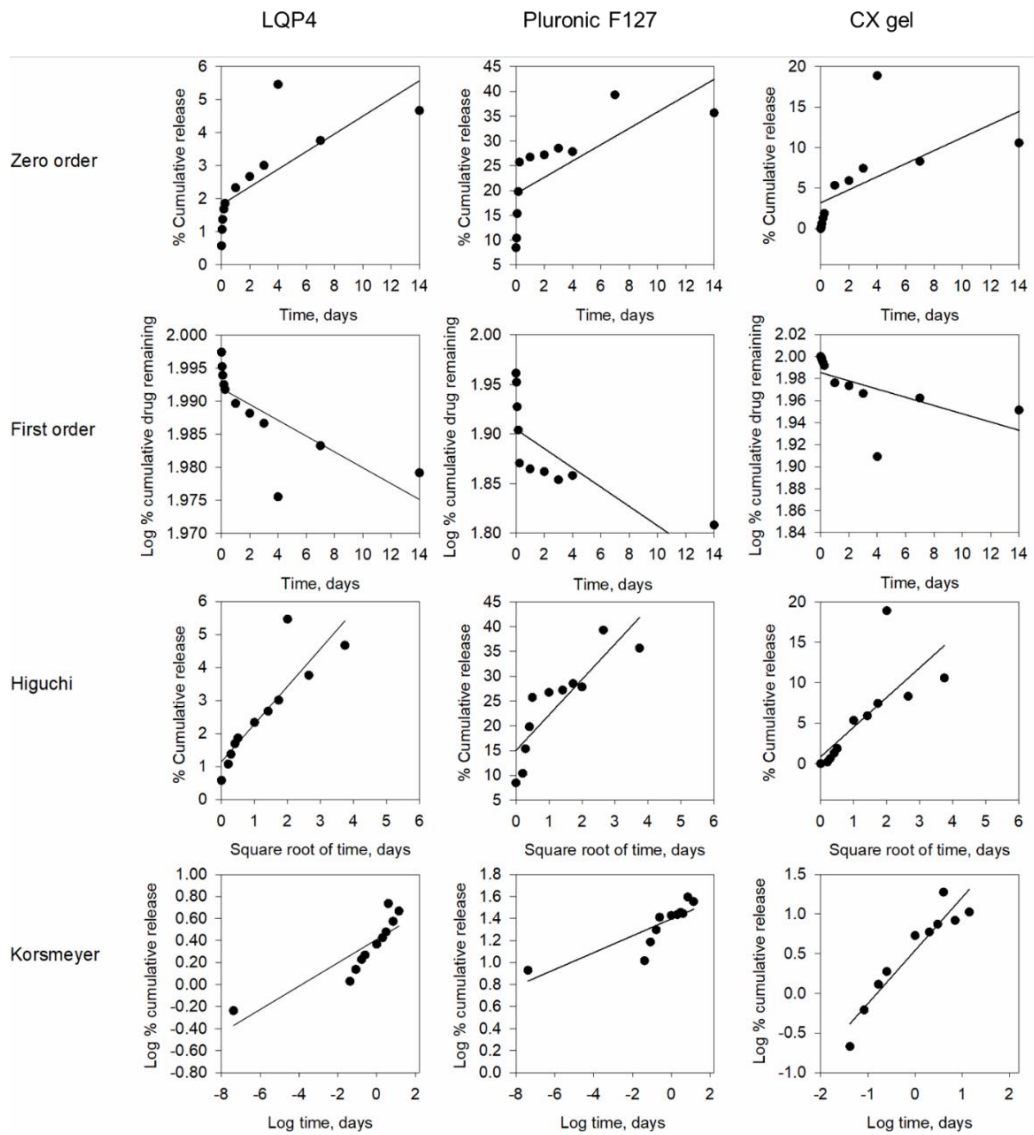
Figure A2.3: Mathematical model fitting (Zero order, First order, Higuchi and Korsmeyer-Peppas models) of PTX release from gels (LQP4, Pluronic F-127 and CX).
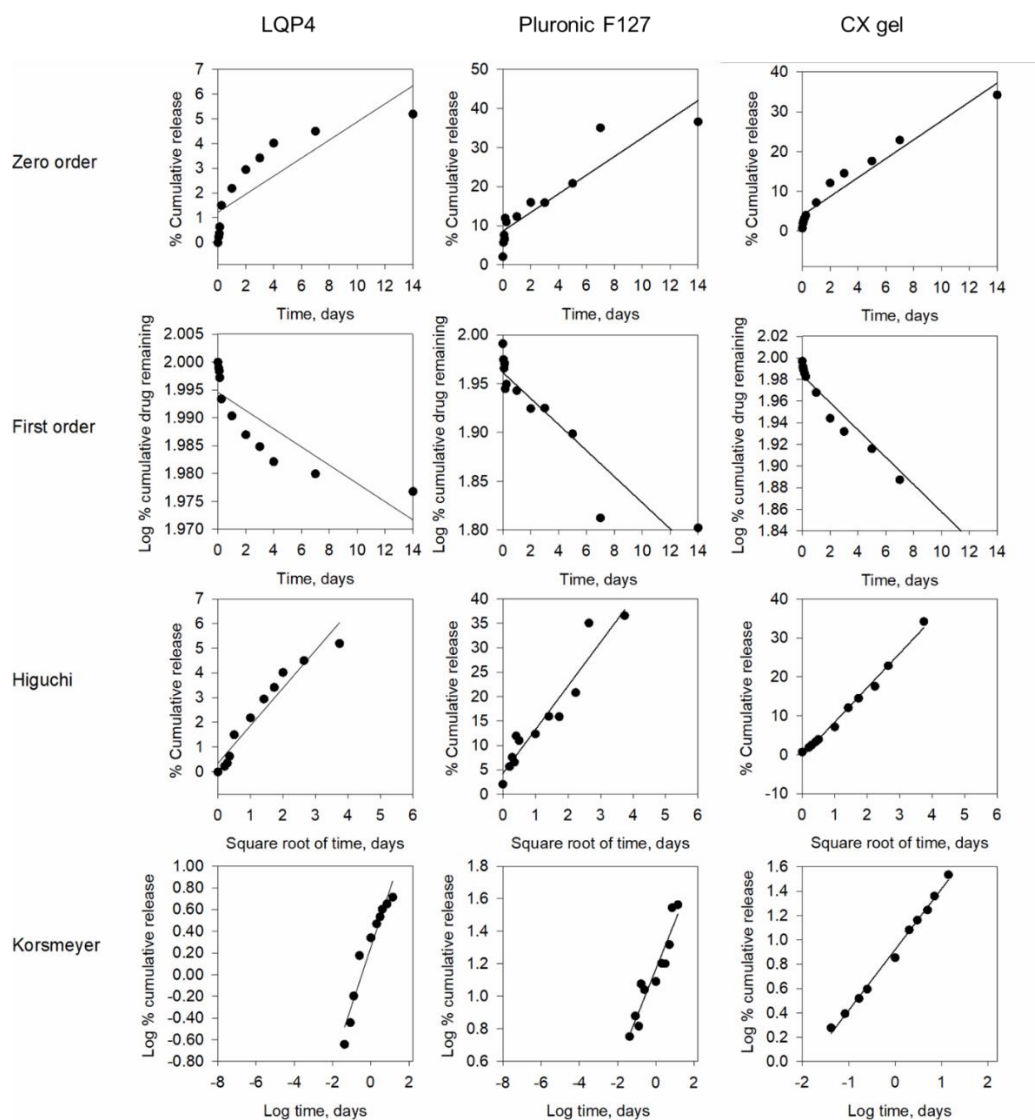
Figure A2.4: Mathematical model fitting (Zero order, First order, Higuchi and Korsmeyer-Peppas models) of MSN release from gels (LQP4, Pluronic F-127 and CX).
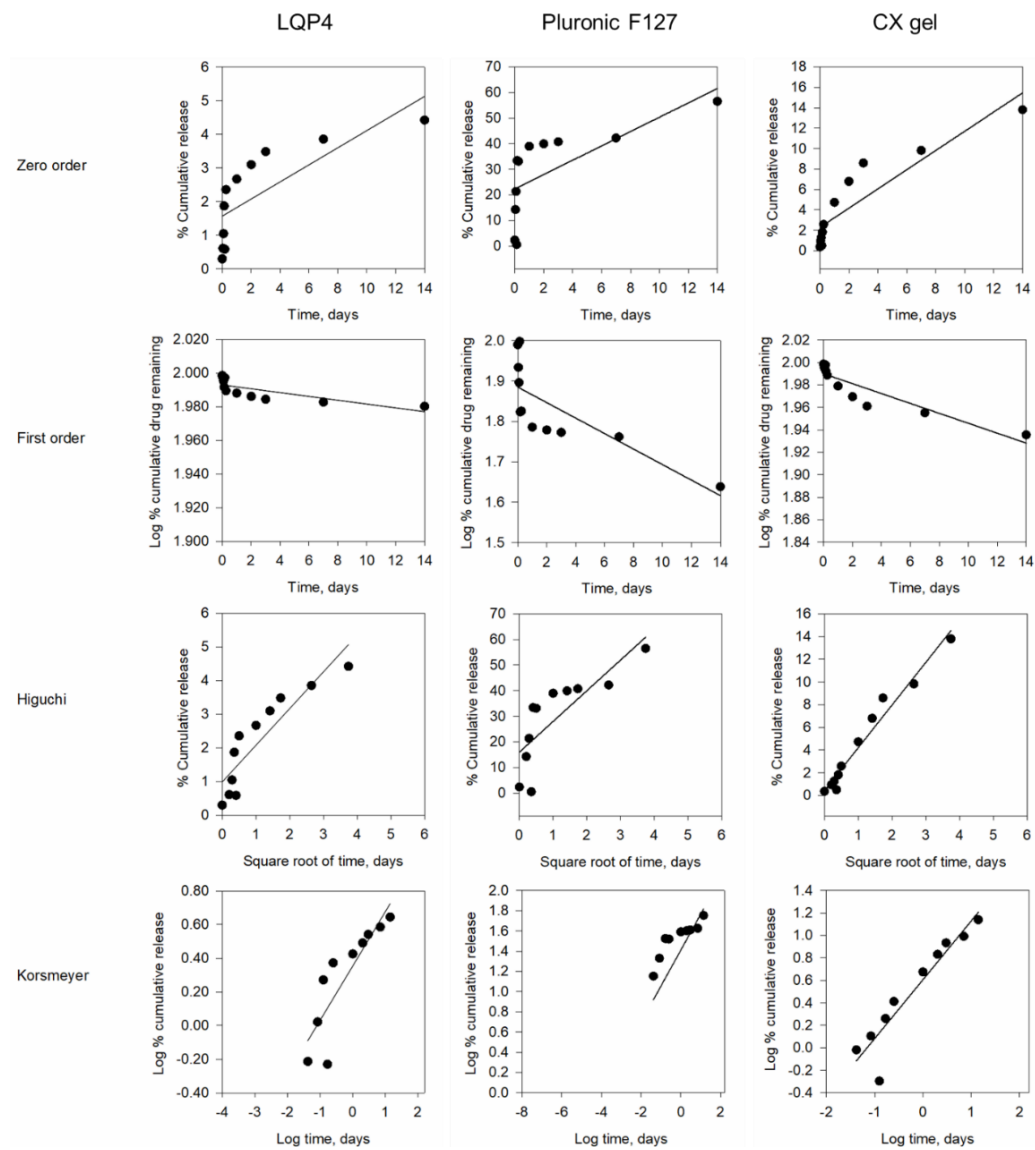
Figure A2.5: Mathematical model fitting (Zero order, First order, Higuchi and Korsmeyer-Peppas models) of MSN-PEG release from gels (LQP4, Pluronic F-127 and CX).

Appendix 3

Calculation of MSN percentage release from hydrogel

The nanoparticles/mL released were measured by Nanoparticle Tracking Analysis (NTA) for each time point and the cumulative release was calculated by progressively adding the release at increasing time points.

Using the nanoparticles diameter (MSN and MSN-PEG) determined by TEM, the nanoparticle volume was calculated.

The density of the mesoporous silica nanoparticles was assumed to be equal to commercially available mesoporous silica nanoparticles (Silica, mesostructured, MCM-41 type, hexagonal – Reference code: 643645. Sigma-Aldrich, Ireland), which have similar pore size, surface area and size. The estimated density for the commercial nanoparticle was 0.34 g/mL.

The mass (g) of one nanoparticle was calculated using the density formula:

$$d = \frac{m}{v}$$

Where,

d = nanoparticle density (g/mL)

m = nanoparticle mass (g)

v = nanoparticle volume (cm^3)

Taking the number of nanoparticles released per millilitre (N), measured by NTA, the concentration (mg/mL) of nanoparticles released at each time point was calculated as follows:

$$C = (m \times N) \times 1000$$

Where,

C = nanoparticle concentration (mg/mL)

m = nanoparticle mass (g)

N = number of nanoparticles/mL

Finally, the concentration of nanoparticles released over time was converted to percentage knowing the total weight of nanoparticles in the gel (1 mg).
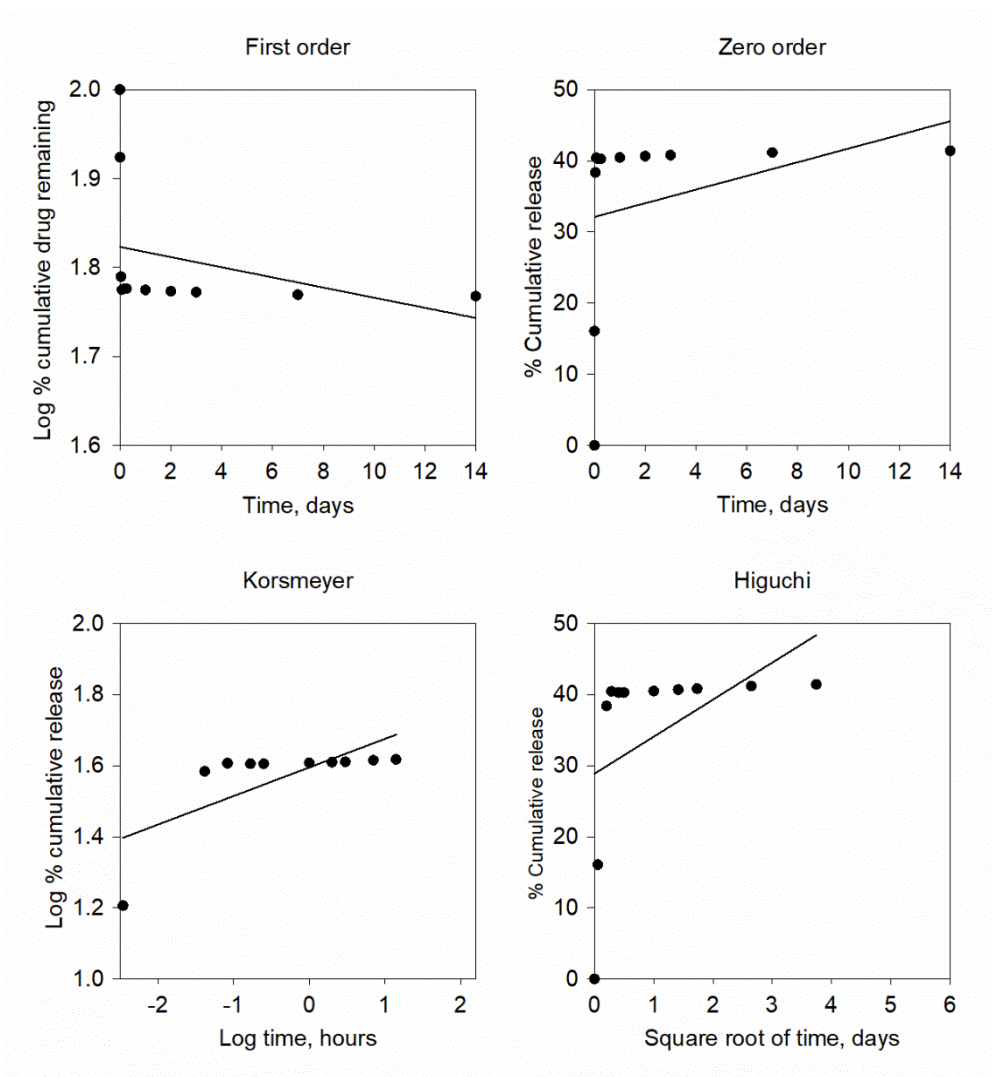
Figure A4.1: Mathematical model fitting (First order, Zero order, Korsmeyer-Peppas and Higuchi models) of TMZ release from final GlioGel formulation.

Table A4.1: Mathematical model fitting parameters of TMZ release from GlioGel at 37 °C. R^2 is the correlation coefficient. The release rate constants (K_0, K_1 and K_H) and the release exponent (n) were calculated from the slopes of the respective mathematical models.

		Zero-Order		First-Order		Higuchi		Korsmeyer-Peppas		
		R^2	K_0	R^2	K_1	R^2	K_H	R^2	n	Release mechanism
GlioGel	**TMZ**	0.0948	0.9609	0.1026	0.005	0.2118	5.207	**0.498**	**0.0803**	quasi-Fickian

Appendix 5: Score sheets *in vivo*

Observations after surgery and resection

All daily monitoring, scoring, weights, supportive care and treatment must be recorded in a monitoring log maintained by the investigator. At the time of cell implantation, each animal should be clearly labelled. Animal welfare after each procedure will be determined by observations of clinical signs or behavioural changes such as pilo-erection, oculo-nasal discharge, body temperature changes, subdued behaviour, breathing, peer interaction and transient vocalisation. For 3 days post-surgery the animals will be monitored twice a day (morning and afternoon) carefully for any sign of pain and to avoid any unexpected death. We will use the grimace score sheet to evaluate specifically their suffering post-surgery.

Instructions for the use of Grimace Scale Score Sheet post-surgery:
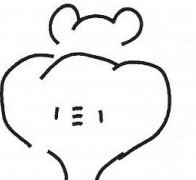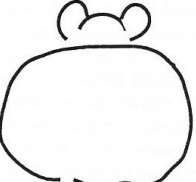
- Score animals 0, 1, 2 based on grimace scale images for facial action scores

- If an animal displays a cumulative score ≥5 they will be humanely euthanised

0	facial action not present
1	facial action moderately present
2	facial action severe

GRIMACE SCALE Score sheet (example)

Facial Action	Animal ID	Animal ID	Animal ID	Animal ID	Animal ID	Animal ID	Animal ID
Orbital Tightening							
Nose Bulge							
Cheek Bulge							
Ear position							
Whisker Change							
Total:							

Body Condition Scoring of Mice

BC 1

Mouse is emaciated.
- Skeletal structure extremely prominent; little or no flesh cover.
- Vertebrae distinctly segmented.

BC 2

Mouse is underconditioned.
- Segmentation of vertebral column evident.
- Dorsal pelvic bones are readily palpable.

BC 3

Mouse is well-conditioned.
- Vertebrae and dorsal pelvis not prominent; palpable with slight pressure.

BC 4

Mouse is overconditioned.
- Spine is a continuous column.
- Vertebrae palpable only with firm pressure.

BC 5

Mouse is obese.
- Mouse is smooth and bulky.
- Bone structure disappears under flesh and subcutaneous fat.

A "+" or a "-" can be added to the body condition score
if additional increments are necessary (i.e. ...2+, 2, 2-...)

Remarks:

The condition of the mouse is scored at defined time-points depending on the procedure.

The human endpoint is BC1

Overall condition and behaviour scoring criteria

Body Condition Score (BCS)	
0	BCS 3
1	BCS 4
1.5	BC 5
2	BCS 2
3	BCS 1
Body weight	
0	Normal
1	Weight loss >10%
2	Weight loss >15%
3	Weight loss >20%
Physical Appearance/Temperature	
0	Normal
1	Dirty (decrease in grooming behaviour)
2	Piloerection, cold when handled, oculo-nasal discharge, dehydration[1]
3	Persistent hypothermia, hunched posture[2]
Behaviour	
0	Normal
1	Decreased activity
2	Very low activity, transient vocalisation, subdued behaviour
3	Hind-limb paralysis, Immobility, Inability to obtain food & water
Wound Appearance	
0	Normal
1	Lightly red but not infected
2	Red, lightly swallowing with pus
3	Presence of large quantity of pus, important inflammation of the wound

Remarks:

Mice are humanely euthanised if they reach a score of 3 in any individual category.

Individual Score sheet (example)

Animal Identification Number:

Researcher: Individual licence #:   Procedure #:

Drug: Group #:   Dose#:

Starting date: Ending date:

Date	Body Condition Score (BCS)	Body weight	Physical Appearance Temperature	Behaviour	Grimace scale score (total)	Overall score

Remarks:

Mice are humanely euthanised if they reach a score of 3 in any individual category.

Instructions for use of the score sheet from day 3 after surgery until the end of the experiment: Each day, the animals will receive a cumulative score based on body weight, activity, appearance and behaviour (see table). Each score is associated with a specific action (see table below). For example, if an animal scores 7 (cumulative score), the appropriate care will be provided as described in the table below (Actions depending on the cumulative scores) and advice from the comparative medicine Veterinarian will be sought. Any animal scoring 10 or above should be euthanized immediately. Even without reaching a score above 4, dehydrated animals will receive an oral liquid such as NAPA nectar. If we do not see any improvement, we will also rehydrate the animal by subcutaneous injections of saline solution every 2 days (after consultation with the DV). In addition, cold animals will be placed in an individual cage with a heating pad (or a heating cabinet available in the animal house). If the wound is infected (wound appearance score 2), apply local antibiotic solution. If wound appearance scores 3, the wound will be treated with local antibiotic solution and systemic antibiotics will be administrated after consultation with the DV (we will also administrate 0.05-0.1 mg/kg of buprenorphine subcutaneously).

[1]When dehydrated the skin on the back of the neck stays tented up if pulled gently and released.

[2]head down, feet close together.

Reference: Ullman-Culleré MH, Foltz CJ. Body Condition Scoring: A rapid and Accurate Method for Assessing Health Status in mice. Laboratory Animal Science, 1999 49:319-223

Workman et al., 2010. Guidelines for the welfare and use of animals in cancer Research.

Actions depending on the cumulative scores

Cumulative Score	Care to be provided
0	Baseline weight prior injection.
1-4	Keep record in the monitoring log. Weight animal daily Mice are humanely euthanised if they reach a score of 3 in any individual category.
5-6	Provide moistened food pellets on floor of the cage. Check temperature. At this stage, we will provide oral fluid such as NAPA nectar. If we do not see any improvement, we will also rehydrate the animal with subcutaneous injections of saline every 2 days. If we suspect pain, we will administrate 0.05-0.1 mg/kg of buprenorphine subcutaneously. The animal will be monitored twice a day. Advice from the ACWO will be sought. If the wound is infected, apply local Antibiotic solution.
7-9	Separate weak mouse from stronger animals. Weight animal 2 times per day. Monitor animal through the day (4 times at least). At this stage, the animal will receive water and food to compensate the dehydration and weight loss by oral gavage. A hypothermic animal will be placed in an individual cage with a heating pad. Advice from the Designated Veterinarian will be sought. If we suspect pain, we will administrate 0.05-0.1 mg/kg of buprenorphine subcutaneously.
from 10	This animal must be euthanized immediately. It will be humanely sacrificed with CO_2 followed by post mortem analysis.

Grimace Scale Score Sheet for 3 days post-surgery:

0	facial action not present
1	facial action moderately present
2	facial action severe

Procedure: cell injection

Date of procedure: 23/10/2019

Day1 post-surgery

Facial Action	Mouse2	Mouse2	Mouse3	Mouse3	Mouse4	Mouse4
Orbital	0	0	0	0	0	0
Nose Bulge	0	0	0	0	0	0
Cheek Bulge	0	0	0	0	0	0
Ear position	0	1	1	1	1	1
Whisker	0	0	0	0	0	0
Total:	AM 0	PM 1	AM 1	PM 1	AM 1	PM 1

Day-2 post surgery

Facial Action	Mouse2	Mouse2	Mouse3	Mouse3	Mouse4	Mouse4
Orbital	0	0	0	0	0	0
Nose Bulge	0	0	0	0	0	0
Cheek Bulge	0	0	0	0	0	0
Ear position	0	0	1	0	1	0
Whisker	0	0	0	0	0	0
Total:	AM 0	PM 0	AM 1	PM 0	AM 1	PM 0

Day-3 post surgery

Facial Action	Mouse2	Mouse2	Mouse3	Mouse3	Mouse4	Mouse4
Orbital	0	0	0	0	0	0
Nose Bulge	0	0	0	0	0	0
Cheek Bulge	0	0	0	0	0	0
Ear position	1	0	0	0	0	0
Whisker	0	0	0	0	0	0
Total:	AM 1	PM 0	AM 0	PM 0	AM 0	PM 0

Grimace Scale Score Sheet for 3 days post-surgery:

0	facial action not present
1	facial action moderately present
2	facial action severe

Procedure: cell injection

Date of procedure: 24/10/2019

Day1 post-surgery

Facial Action	Mouse5	Mouse5	Mouse6	Mouse6	Mouse7	Mouse7
Orbital	0	0	0	0	0	0
Nose Bulge	0	0	0	0	0	0
Cheek Bulge	0	0	0	0	0	0
Ear position	1	1	1	1	1	1
Whisker	0	0	0	0	0	0
Total:	AM 1	PM 1	AM 1	PM 1	AM 1	PM 1

Day-2 post surgery

Facial Action	Mouse5	Mouse5	Mouse6	Mouse6	Mouse7	Mouse7
Orbital	0	0	0	0	0	0
Nose Bulge	0	0	0	0	0	0
Cheek Bulge	0	0	0	0	0	0
Ear position	0	0	1	0	1	1
Whisker	0	0	0	0	0	0
Total:	AM 0	PM	AM 1	PM 0	AM 1	PM 1

Day-3 post surgery

Facial Action	Mouse5	Mouse5	Mouse6	Mouse6	Mouse7	Mouse7
Orbital	0	0	0	0	0	0
Nose Bulge	0	0	0	0	0	0
Cheek Bulge	0	0	0	0	0	0
Ear position	0	0	1	0	1	0
Whisker	0	0	0	0	0	0
Total:	AM 0	PM 0	AM 1	PM 0	AM 1	PM 0

Grimace Scale Score Sheet for 3 days post-surgery:

0	facial action not present
1	facial action moderately present
2	facial action severe

Procedure: cell injection

Date of procedure: 24/10/2019

Day1 post-surgery

Facial Action	Mouse8	Mouse8	Mouse9	Mouse9	Mouse10	Mouse10
Orbital	0	0	0	0	0	0
Nose Bulge	0	0	0	0	0	0
Cheek Bulge	0	0	0	0	0	0
Ear position	0	0	0	0	0	0
Whisker	0	0	0	0	0	0
Total:	AM 0	PM 0	AM 0	PM 0	AM 0	PM 0

Day-2 post surgery

Facial Action	Mouse8	Mouse8	Mouse9	Mouse9	Mouse10	Mouse10
Orbital	0	0	0	0	0	0
Nose Bulge	0	0	0	0	0	0
Cheek Bulge	0	0	0	0	0	0
Ear position	1	1	0	1	1	1
Whisker	0	0	0	0	0	0
Total:	AM 1	PM 1	AM 0	PM 1	AM 1	PM 1

Day-3 post surgery

Facial Action	Mouse8	Mouse8	Mouse9	Mouse9	Mouse10	Mouse10
Orbital	0	0	0	0	0	0
Nose Bulge	0	0	0	0	0	0
Cheek Bulge	0	0	0	0	0	0
Ear position	1	0	1	0	1	0
Whisker	0	0	0	0	0	0
Total:	AM 1	PM 0	AM 1	PM 0	AM 1	PM 0

Individual Score sheet

Animal Identification Number: MOUSE 2

Researcher: Oliviero Gobbo/Luiza dos Santos   **Individual licence #:** AE1936/I104 and AE19136/I457

Procedure #: U-87 cell injection

Drug: n/a   **Group #:** n/a   **Dose#:**
n/a

Starting date: 23/10/2019

Date	Body Condition Score (BCS)	Body weight (g)	Physical Appearance Temperature	Behaviour	Grimace scale score (total)	Overall score
24-Oct	0	23.1	0	0	0	0
25-Oct	0	23.7	0	0	0	0
26-Oct	0	23.4	0	0	1	1
27-Oct	0	26.2	0	0	0	0
28-Oct	0	23.2	0	0	0	0
29-Oct	0	23.9	0	0	0	0
30-Oct	0	23.8	0	0	0	0
31-Oct	0	23.2	0	0	0	0
01-Nov	0	23.8	0	0	0	0
02-Nov	0	23.6	0	0	0	0
03-Nov	0	23.8	0	0	0	0
04-Nov	0	24	0	0	0	0
05-Nov	0	23.9	0	0	0	0
13-Nov	0	24.1	0	0	0	0
15-Nov	0	23.6	0	0	0	0
19-Nov	0	23.3	0	0	0	0
22-Nov	0	23.3	0	0	0	0
26-Nov	0	22.6	0	0	0	0
28-Nov	0	23.6	0	0	0	0
29-Nov	0	23.5	0	0	0	0

Individual Score sheet

Animal Identification Number: MOUSE 3

Researcher: Oliviero Gobbo/Luiza dos Santos   **Individual licence #:** AE1936/I104 and AE19136/I457

Procedure #: U-87 cell injection

Drug: n/a   **Group #:** n/a   **Dose#:**
n/a

Starting date: 23/10/2019

Date	Body Condition Score (BCS)	Body weight (g)	Physical Appearance Temperature	Behaviour	Grimace scale score (total)	Overall score
24-Oct	0	23.6	0	0	1	1
25-Oct	0	23.9	0	0	1	1
26-Oct	0	24	0	0	0	0
27-Oct	0	23	0	0	0	0
28-Oct	0	23	0	0	0	0
29-Oct	0	23.6	0	0	0	0
30-Oct	0	23.5	0	0	0	0
31-Oct	0	23.5	0	0	0	0
01-Nov	0	23.9	0	0	0	0
02-Nov	0	23.8	0	0	0	0
03-Nov	0	24	0	0	0	0
04-Nov	0	24	0	0	0	0
05-Nov	0	24	0	0	0	0
13-Nov	0	24.1	0	0	0	0
15-Nov	0	23	0	0	0	0
19-Nov	0	23.57	0	0	0	0
22-Nov	0	23.4	0	0	0	0
26-Nov	0	23.5	0	0	0	0
28-Nov	0	23.2	0	0	0	0
29-Nov		21.7				0

Individual Score sheet

Animal Identification Number: MOUSE 4

Researcher: Oliviero Gobbo/Luiza dos Santos   **Individual licence #:** AE1936/I104 and AE19136/I457

Procedure #: U-87 cell injection

Drug: n/a   **Group #:** n/a   **Dose#:**

n/a

Starting date: 23/10/2019

Date	Body Condition Score (BCS)	Body weight (g)	Physical Appearance Temperature	Behaviour	Grimace scale score (total)	Overall score
24-Oct	0	26.4	0	0	1	1
25-Oct	0	26.1	0	0	1	1
26-Oct	0	26.6	0	0	0	0
27-Oct	0	25.8	0	0	0	0
28-Oct	0	25	0	0	0	1
29-Oct	0	24.9	0	0	1	2
30-Oct	0	24.4	0	0	1	2
31-Oct	0	24.8	0	0	1	2
01-Nov	0	24.5	0	0	0	1
02-Nov	0	24.3	0	0	0	1
03-Nov	0	25	0	0	0	1
04-Nov	0	26	0	0	0	0
05-Nov	0	24.9	0	0	0	1
13-Nov	0	25.9	0	0	0	0
15-Nov	0	24.5	0	0	0	1
19-Nov	0	25	0	0	0	0
22-Nov	0	24.1	0	0	1	1
26-Nov	2	17.62				5

Individual Score sheet

Animal Identification Number: MOUSE 5

Researcher: Oliviero Gobbo/Luiza dos Santos   **Individual licence #:** AE1936/I104 and AE19136/I457

Procedure #: U-87 cell injection

Drug: n/a   **Group #:** n/a   **Dose#:**
n/a

Starting date: 24/10/2019

Date	Body Condition Score (BCS)	Body weight (g)	Physical Appearance Temperature	Behaviour	Grimace scale score (total)	Overall score
25-Oct	0	23.9	0	0	1	1
26-Oct	0	25.8	0	0	0	0
27-Oct	0	24.3	0	0	0	0
28-Oct	0	23.1	0	0	0	0
29-Oct	0	26.3	0	0	0	0
30-Oct	0	23.2	0	0	0	0
31-Oct	0	23.6	0	0	0	0
01-Nov	0	23.7	0	0	0	0
02-Nov	0	23	0	0	0	0
03-Nov	0	23.5	0	0	0	0
04-Nov	0	23.9	0	0	0	0
05-Nov	0	23.7	0	0	0	0
13-Nov	0	24.8	0	0	0	0
15-Nov	0	22.9	0	0	0	0
19-Nov	0	23.9	0	0	0	0
22-Nov	0	22.7	0	0	0	0
26-Nov	0	19.5	0	0	0	1
28-Nov	2	17.5	1	1	0	7
29-Nov		15.8				2

Individual Score sheet

Animal Identification Number: MOUSE 6

Researcher: Oliviero Gobbo/Luiza dos Santos   **Individual licence #:** AE1936/I104 and AE19136/I457

Procedure #: U-87 cell injection

Drug: n/a   **Group #:** n/a   **Dose#:**
n/a

Starting date: 24/10/2019

Date	Body Condition Score (BCS)	Body weight (g)	Physical Appearance Temperature	Behaviour	Grimace scale score (total)	Overall score
25-Oct	0	22.9	0	0	1	1
26-Oct	0	22.5	0	0	1	1
27-Oct	0	22.9	0	0	1	1
28-Oct	0	22.3	0	0	0	0
29-Oct	0	22.6	0	0	0	0
30-Oct	0	23.3	0	0	0	0
31-Oct	0	23.3	0	0	0	0
01-Nov	0	23	0	0	0	0
02-Nov	0	22.7	0	0	0	0
03-Nov	0	22.8	0	0	0	0
04-Nov	0	22.9	0	0	0	0
05-Nov	0	22.8	0	0	0	0
13-Nov	0	23.19	0	0	0	0
15-Nov	0	22	0	0	0	0
19-Nov	0	23.46	0	0	0	0
22-Nov	0	21.4	0	0	1	1
26-Nov	2	14.79				5

Individual Score sheet

Animal Identification Number: MOUSE 7

Researcher: Oliviero Gobbo/Luiza dos Santos   **Individual licence #:** AE1936/I104 and AE19136/I457

Procedure #: U-87 cell injection

Drug: n/a   **Group #:** n/a   **Dose#:**
n/a

Starting date: 24/10/2019

Date	Body Condition Score (BCS)	Body weight (g)	Physical Appearance Temperature	Behaviour	Grimace scale score (total)	Overall score
25-Oct	0	24.8	0	0	1	1
26-Oct	0	24.7	0	0	1	1
27-Oct	0	24.9	0	0	1	1
28-Oct	0	24.7	0	0	0	0
29-Oct	0	26	0	0	2	2
30-Oct	0	26.5	0	0	0	0
31-Oct	0	26.4	0	0	0	0
01-Nov	0	25.6	0	0	0	0
02-Nov	0	24.3	0	0	0	0
03-Nov	0	24.8	0	0	0	0
04-Nov	0	25.15	0	0	0	0
05-Nov	0	24.7	0	0	0	0
13-Nov	0	26.33	0	0	0	0
15-Nov	0	24.3	0	0	0	0
19-Nov	0	25.8	0	0	0	0
22-Nov	0	22.8	0	0	1	1
26-Nov	0	21.1	0	0	0	2
28-Nov	0	19.26	1	1	0	7
29-Nov		17.1				2

Individual Score sheet

Animal Identification Number: MOUSE 8

Researcher: Oliviero Gobbo/Luiza dos Santos   **Individual licence #:** AE1936/I104 and AE19136/I457

Procedure #: U-87 cell injection

Drug: n/a   **Group #:** n/a   **Dose#:**
n/a

Starting date: 24/10/2019

Date	Body Condition Score (BCS)	Body weight (g)	Physical Appearance Temperature	Behaviour	Grimace scale score (total)	Overall score
25-Oct	0	24.9	0	0	0	0
26-Oct	0	24.9	0	0	1	1
27-Oct	0	25.1	0	0	1	1
28-Oct	0	24.1	0	0	0	0
29-Oct	0	24.5	0	0	0	0
30-Oct	0	24.3	0	0	0	0
31-Oct	0	24.5	0	0	0	0
01-Nov	0	24.1	0	0	0	0
02-Nov	0	24	0	0	0	0
03-Nov	0	23.5	0	0	0	0
04-Nov	0	23.8	0	0	0	0
05-Nov	0	23.2	0	0	0	1
13-Nov	0	24.64	0	0	0	0
15-Nov	0	23.4	0	0	0	0
19-Nov	0	23.7	0	0	0	0
22-Nov	0	23.3	0	0	0	0

Individual Score sheet

Animal Identification Number: MOUSE 9

Researcher: Oliviero Gobbo/Luiza dos Santos   **Individual licence #:** AE1936/I104 and AE19136/I457

Procedure #: U-87 cell injection

Drug: n/a   **Group #:** n/a   **Dose#:**
n/a

Starting date: 24/10/2019

Date	Body Condition Score (BCS)	Body weight (g)	Physical Appearance Temperature	Behaviour	Grimace scale score (total)	Overall score
25-Oct	0	23.8	0	0	0	0
26-Oct	0	24.5	0	0	0	0
27-Oct	0	24.7	0	0	1	1
28-Oct	0	23.7	0	0	0	0
29-Oct	0	23.2	0	0	0	0
30-Oct	0	23.5	0	0	0	0
31-Oct	0	24.2	0	0	0	0
01-Nov	0	23.4	0	0	0	0
02-Nov	0	22.8	0	0	0	0
03-Nov	0	22.9	0	0	0	0
04-Nov	0	23	0	0	0	0
05-Nov	0	23	0	0	0	0
13-Nov	0	23.7	0	0	0	0
15-Nov	0	22.5	0	0	0	0
19-Nov	0	22.9	0	0	0	0
22-Nov	0	23.3	0	0	0	0
26-Nov	0	23.5	0	0	0	0
28-Nov	0	23.5	0	0	0	0
29-Nov	0	23	0	0	0	0

Individual Score sheet

Animal Identification Number: MOUSE 10

Researcher: Oliviero Gobbo/Luiza dos Santos   **Individual licence #:** AE1936/I104 and AE19136/I457

Procedure #: U-87 cell injection

Drug: n/a   **Group #:** n/a   **Dose#:**
n/a

Starting date: 24/10/2019

Date	Body Condition Score (BCS)	Body weight (g)	Physical Appearance Temperature	Behaviour	Grimace scale score (total)	Overall score
25-Oct	0	24.9	0	0	0	0
26-Oct	0	24.8	0	0	1	1
27-Oct	0	24.2	0	0	1	1
28-Oct	0	23	0	0	0	0
29-Oct	0	23.5	0	0	0	0
30-Oct	0	24	0	0	0	0
31-Oct	0	24.5	0	0	0	0
01-Nov	0	24.3	0	0	0	0
02-Nov	0	24	0	0	0	0
03-Nov	0	24.5	0	0	0	0
04-Nov	0	24.8	0	0	0	0
05-Nov	0	25.2	0	0	0	0
13-Nov	0	24.1	0	0	0	0
15-Nov	0	23.4	0	0	0	0
19-Nov	0	24.2	0	0	0	0
22-Nov	0	23	0	0	1	1
27-Nov	0	18.3	0	0	0	3
28-Nov	0	19.1	0	0	0	3
29-Nov	0	19	0	0	0	3
02/12		14.95				

Grimace Scale Score Sheet for 3 days post-surgery:

0	facial action not present
1	facial action moderately present
2	facial action severe

Procedure: cell injection

Date of procedure:　　　31/01/2020

Day1 post-surgery

Facial Action	Mouse11	Mouse12	Mouse13	Mouse14	Mouse15
Orbital	0	0	0	0	0
Nose Bulge	0	0	0	0	0
Cheek Bulge	0	0	0	0	0
Ear position	0	0	0	0	0
Whisker	0	0	0	0	0
Total:	0	0	0	0	0

Day-2 post surgery

Facial Action	Mouse11	Mouse12	Mouse13	Mouse14	Mouse15
Orbital	0	0	0	0	0
Nose Bulge	0	0	0	0	0
Cheek Bulge	0	0	0	0	0
Ear position	0	0	0	1	1
Whisker	0	0	0	0	0
Total:	0	0	0	1	1

Day-3 post surgery

Facial Action	Mouse11	Mouse12	Mouse13	Mouse14	Mouse15
Orbital	0	0	0	0	0
Nose Bulge	0	0	0	0	0
Cheek Bulge	0	0	0	0	0
Ear position	0	0	0	1	0
Whisker	0	0	0	0	0
Total:	0	0	0	1	0

Grimace Scale Score Sheet for 3 days post-surgery:

0	facial action not present
1	facial action moderately present
2	facial action severe

Procedure: cell injection

Date of procedure: 31/01/2020

Day1 post-surgery

Facial Action	Mouse16	Mouse17	Mouse18	Mouse19	Mouse20
Orbital	0	0	0	0	0
Nose Bulge	0	0	0	0	0
Cheek Bulge	0	0	0	0	0
Ear position	0	0	0	0	1
Whisker	0	0	0	0	0
Total:	0	0	0	0	1

Day-2 post surgery

Facial Action	Mouse16	Mouse17	Mouse18	Mouse19	Mouse20
Orbital	0	0	0	0	0
Nose Bulge	0	0	0	0	0
Cheek Bulge	0	0	0	0	0
Ear position	0	0	1	0	1
Whisker	0	0	0	0	0
Total:	0	0	1	0	1

Day-3 post surgery

Facial Action	Mouse16	Mouse17	Mouse18	Mouse19	Mouse20
Orbital	0	0	0	0	0
Nose Bulge	0	0	0	0	0
Cheek Bulge	0	0	0	0	0
Ear position	0	0	0	0	1
Whisker	0	0	0	0	0
Total:	0	0	0	0	1

Individual Score sheet

Animal Identification Number: MOUSE 11

Researcher: Oliviero Gobbo/Luiza dos Santos   **Individual licence #:** AE1936/I104 and AE19136/I457

Procedure #: U-87 cell injection (31/01/2020) + Tumour resection (24/02/2020)

Drug: n/a   **Group #:** Gel only

Dose#: n/a

Starting date: 31/01/2020

Date	Body Condition Score (BCS)	Body weight (g)	Physical Appearance Temperature	Behaviour	Grimace scale score (total)	Overall score
01-Feb	0	19.2	0	0	0	0
02-Feb	0	19.1	0	0	0	0
03-Feb	0	19.9	0	0	0	0
04-Feb	0	19.3	0	0	0	0
05-Feb	0	19.7	0	0	0	0
06-Feb	0	19.7	0	0	0	0
07-Feb	0	20.3	0	0	0	0
10-Feb	0	20	0	0	0	0
11-Feb	0		0	0	0	0
12-Feb	0	20.8	0	0	0	0
13-Feb	0		0	0	0	0
14-Feb	0	20.9	0	0	0	0
17-Feb	0	21.4	0	0	0	0
19-Feb	0	20.8	0	0	0	0
21-Feb	0	20.7	0	0	0	0
24-Feb	0	20.5	0	0	0	0
25-Feb	0	19.1	0	0	2	2
26-Feb	0	20.2	0	0	1	1
27-Feb	0	20.1	0	1	1	2
28-Feb	0	20.3	0	0	0	0
02-Mar	0		0	0	0	0
04-Mar	0	20.9	0	0	0	0
05-Mar	0	19.4	0	0	0	0
09-Mar	0	21	0	0	0	0
12-Mar		19.7				

250

15-Mar	0	18.1	0	0	1	1
18-Mar	0	17.8	0	1	0	1
20-Mar	0	16.1	0	1	0	1
23-Mar	0	13.9	0	2		2

Individual Score sheet

Animal Identification Number: MOUSE 12

Researcher: Oliviero Gobbo/Luiza dos Santos   **Individual licence #:** AE1936/I104 and AE19136/I457

Procedure #: U-87 cell injection (31/01/2020) + Tumour resection (24/02/2020)

Drug: Temozolomide (TMZ) and Paclitaxel (PTX)   **Group #:** GlioGel

Dose#: 0.6 mg/kg free TMZ and 0.3 mg/kg PTX (loaded on MSN-PEG)

Starting date: 31/01/2020

Date	Body Condition Score (BCS)	Body weight (g)	Physical Appearance Temperature	Behaviour	Grimace scale score (total)	Overall score
01-Feb	0	19.5	0	0	0	0
02-Feb	0	19	0	0	0	0
03-Feb	0	19.8	0	1	0	1
04-Feb	0	19.3	0	0	0	0
05-Feb	0	18.8	0	0	0	0
06-Feb	0	20.8	0	0	0	0
07-Feb	0	20.4	0	1	0	1
10-Feb	0	20.5	0	0	0	0
11-Feb	0		0	0	0	0
12-Feb	0	20	0	0	0	0
13-Feb	0		0	0	0	0
14-Feb	0	20.3	0	0	0	0
17-Feb	0	20.7	0	0	0	0
19-Feb	0	21.6	0	0	0	0
21-Feb	0	20.9	0	0	0	0
24-Feb	0	22	0	0	0	0
25-Feb	0	20.7	0	0	1	1
26-Feb	0	22.5	0	0	1	1
27-Feb	0	22.1	0	1	0	1
28-Feb	0	21.8	0	0	0	0
02-Mar	0		0	0	0	0
04-Mar	0	22.3	0	0	0	0
05-Mar	0	21.6	0	0	0	0
09-Mar	0	21.9	0	0	0	0
12-Mar		22.2				

15-Mar	0	21.2	0	0	0	0
18-Mar	0	21.2	0	0	0	0
20-Mar	0	20.1	0	0	0	0
23-Mar	0	18.5	0	0	0	0
25-Mar	0	16.7	0	1	0	1
27-Mar	0	16.4	0	3	0	3

Individual Score sheet

Animal Identification Number: MOUSE 13

Researcher: Oliviero Gobbo/Luiza dos Santos   **Individual licence #:** AE1936/I104 and AE19136/I457

Procedure #: U-87 cell injection (31/01/2020) + Tumour resection (24/02/2020)

Drug: n/a   **Group #:** Gel only

Dose#: n/a

Starting date: 31/01/2020   **Ending date:**

Date	Body Condition Score (BCS)	Body weight (g)	Physical Appearance Temperature	Behaviour	Grimace scale score (total)	Overall score
01-Feb	0	18.7	0	0	0	0
02-Feb	0	19.1	0	0	0	0
03-Feb	0	19.9	0	0	0	0
04-Feb	0	18.5	0	0	1	1
05-Feb	0	18.4	0	0	0	0
06-Feb	0	19	0	0	0	0
07-Feb	0	19.4	0	0	0	1
10-Feb	0	19.3	0	0	0	0
11-Feb	0		0	0	0	0
12-Feb	0	21.1	0	0	0	0
13-Feb	0		0	0	0	0
14-Feb	0	19.7	0	0	0	0
17-Feb	0	21.6	0	0	0	0
19-Feb	0	21.3	0	0	0	0
21-Feb	0	20.7	0	0	0	0
24-Feb	0	21	0	0	0	0
25-Feb	0	20.1	0	0	2	2
26-Feb	0	21.4	0	0	2	2
27-Feb	0	22.6	0	0	0	0
28-Feb	0	21	0	0	0	0
02-Mar	0		0	0	0	0
04-Mar	0	21.2	0	0	0	0
05-Mar	0	20.2	0	0	0	0
09-Mar	0	20.7	0	0	0	0
12-Mar		20.1				

254

15-Mar	0	18.3	0	0	1	1
18-Mar	0	15.6	0	0	3	3

Individual Score sheet

Animal Identification Number: MOUSE 14

Researcher: Oliviero Gobbo/Luiza dos Santos   **Individual licence #:** AE1936/I104 and AE19136/I457

Procedure #: U-87 cell injection (31/01/2020) + Tumour resection (23/02/2020)

Drug: Temozolomide (TMZ) and Paclitaxel (PTX)   **Group #:** GlioGel

Dose#: 0.6 mg/kg free TMZ and 0.3 mg/kg PTX (loaded on MSN-PEG)

Starting date: 31/01/2020

Date	Body Condition Score (BCS)	Body weight (g)	Physical Appearance Temperature	Behaviour	Grimace scale score (total)	Overall score
01-Feb	0	20	0	0	0	0
02-Feb	0	20	0	0	1	1
03-Feb	0	20	0	0	1	1
04-Feb	0	20.1	0	0	1	1
05-Feb	0	20.2	0	0	0	0
06-Feb	0	21	0	0	0	0
07-Feb	0	21.7	0	0	0	0
10-Feb	0	21.2	0	0	0	0
11-Feb	0		0	0	0	0
12-Feb	0	20.3	0	0	0	0
13-Feb	0		0	0	0	0
14-Feb	0	21.8	0	0	0	0
17-Feb	0	21.2	0	0	0	0
19-Feb	0	22.3	0	0	0	0
21-Feb	0	21.1	0	0	0	0
23-Feb	0	22	0	0	0	0
24-Feb	1	18.2	0	1	2	4
25-Feb	1	19.3	0	1	1	3
26-Feb	0	21	0	0	0	0
27-Feb	0	21.4	1	0	0	1
28-Feb	0	20.8	1	0	0	1
02-Mar	0		0	0	0	0
04-Mar	0	22	0	0	0	0
05-Mar	0	21.1	0	0	0	0

256

| 09-Mar | 0 | 21.9 | 1 | 0 | 0 | 1 |
| 12-Mar | | 17.6 | | | | |

Individual Score sheet

Animal Identification Number: MOUSE 15

Researcher: Oliviero Gobbo/Luiza dos Santos   **Individual licence #:** AE1936/I104 and AE19136/I457

Procedure #: U-87 cell injection (31/01/2020) + Tumour resection (24/02/2020)

Drug: Temozolomide (TMZ) and Paclitaxel (PTX)   **Group #:** GlioGel

Dose#: 0.6 mg/kg free TMZ and 0.3 mg/kg PTX (loaded on MSN-PEG)

Starting date: 31/01/2020

Date	Body Condition Score (BCS)	Body weight (g)	Physical Appearance Temperature	Behaviour	Grimace scale score (total)	Overall score
01-Feb	0	18.5	0	0	0	0
02-Feb	0	18.2	0	0	1	1
03-Feb	0	19	0	0	0	0
04-Feb	0	18.6	0	0	0	0
05-Feb	0	19	0	0	0	0
06-Feb	0	19	0	0	0	0
07-Feb	0	19.5	0	0	0	0
10-Feb	0	19.5	0	0	0	0
11-Feb	0		0	0	0	0
12-Feb	0	21	0	0	0	0
13-Feb	0		0	0	0	0
14-Feb	0	21.5	0	0	0	0
17-Feb	0	21.6	0	0	0	0
19-Feb	0	22.4	0	0	0	0
21-Feb	0	21.6	0	0	0	0
24-Feb	0	22	0	0	0	0
25-Feb	0	20.5	0	0	3	3
26-Feb	0	20.7	0	0	1	1
27-Feb	0	21.5	0	0	0	0
28-Feb	0	20.7	0	0	0	0
02-Mar	0		0	0	0	0
04-Mar	0	21.4	0	0	0	0
05-Mar	0	20.7	0	0	0	0

09-Mar	0	21.2	0	0	0	0
12-Mar		20.7				
15-Mar	0	20.4	0	0	0	0
18-Mar	0	20.5	0	0	0	0
20-Mar	0	21	0	0	0	0
23-Mar	0	21.2	0	0	0	0
25-Mar	0	21.2	0	0	0	0
27-Mar	0	20.2	0	0	0	0
29-Mar	0	21.1	0	0	0	0

Individual Score sheet

Animal Identification Number: MOUSE 16

Researcher: Oliviero Gobbo/Luiza dos Santos   **Individual licence #:** AE1936/I104 and AE19136/I457

Procedure #: U-87 cell injection (31/01/2020) + Tumour resection (24/02/2020)

Drug: n/a   **Group #:** Gel only

Dose#: n/a

Starting date: 31/01/2020

Date	Body Condition Score (BCS)	Body weight (g)	Physical Appearance Temperature	Behaviour	Grimace scale score (total)	Overall score
01-Feb	0	18.6	0	0	0	0
02-Feb	0	18.4	0	0	0	0
03-Feb	0	19.3	0	0	0	0
04-Feb	0	19.1	0	0	0	0
05-Feb	0	19.3	0	0	0	0
06-Feb	0	20	0	0	0	0
07-Feb	0	19.3	0	0	0	0
10-Feb	0	20.5	0	0	0	0
11-Feb	0		0	0	0	0
12-Feb	0	20.9	0	0	0	0
13-Feb	0		0	0	0	0
14-Feb	0	20.5	0	0	0	0
17-Feb	0	21.3	0	0	0	0
19-Feb	0	21.6	0	0	0	0
21-Feb	0	21	0	0	0	0
24-Feb	0	21.7	0	0	0	0
25-Feb	0	20.6	0	0	2	2
26-Feb	0	21.5	0	0	1	1
27-Feb	0	21.1	0	0	0	0
28-Feb	0	20.8	0	0	0	0
02-Mar	0		0	0	0	0
04-Mar	0	21.3	0	0	0	0
05-Mar	0	21.2	0	0	0	0
09-Mar	0	22.3	0	0	0	0
12-Mar		21.3				

15-Mar	0	21	0	0	0	0
18-Mar	0	18.2	0	1	0	1
20-Mar	0	15.9	0	3	0	3

Individual Score sheet

Animal Identification Number: MOUSE 17

Researcher: Oliviero Gobbo/Luiza dos Santos   **Individual licence #:** AE1936/I104 and AE19136/I457

Procedure #: U-87 cell injection (31/01/2020) + Tumour resection (23/02/2020)

Drug: Temozolomide (TMZ) and Paclitaxel (PTX)   **Group #:** GlioGel

Dose#: 0.6 mg/kg free TMZ and 0.3 mg/kg PTX (loaded on MSN-PEG)

Starting date: 31/01/2020

Date	Body Condition Score (BCS)	Body weight (g)	Physical Appearance Temperature	Behaviour	Grimace scale score (total)	Overall score
01-Feb	0	20.8	0	0	0	0
02-Feb	0	19.9	0	0	0	0
03-Feb	0	20.9	0	0	0	0
04-Feb	0	20	0	0	0	0
05-Feb	0	19.8	0	0	0	0
06-Feb	0	21.4	0	0	0	0
07-Feb	0	20.4	0	0	0	0
10-Feb	0	21	0	0	0	0
11-Feb	0		0	0	0	0
12-Feb	0	21.2	0	0	0	0
13-Feb	0		0	0	0	0
14-Feb	0	20.7	0	0	0	0
17-Feb	0	22.1	0	0	0	0
19-Feb	0	22.1	0	0	0	0
21-Feb	0	21.6	0	0	0	0
23-Feb	0	21	0	0	0	0
24-Feb	0	20.5	0	0	2	2
25-Feb	0		0	0	2	2
26-Feb	0		0	0	1	0
27-Feb	0	22.9	0	1	0	1
28-Feb	0	22	0	1	0	1
02-Mar	0		0	0	0	0
04-Mar	0	23.2	0	0	0	0
05-Mar	0	20.7	0	0	0	0
09-Mar	0	22.2	0	0	0	0

262

12-Mar		22.9				
15-Mar	0	21.8	0	0	0	0
18-Mar	0	19.1	0	0	0	0
20-Mar	0	18.2	0	1	0	1
21-Mar	0	14.9	0	3	0	3

Individual Score sheet

Animal Identification Number: MOUSE 18

Researcher: Oliviero Gobbo/Luiza dos Santos   **Individual licence #:** AE1936/I104 and AE19136/I457

Procedure #: U-87 cell injection (31/01/2020) + Tumour resection (23/02/2020)

Drug: n/a   **Group #:** Gel only

Dose#: n/a

Starting date: 31/01/2020

Date	Body Condition Score (BCS)	Body weight (g)	Physical Appearance Temperature	Behaviour	Grimace scale score (total)	Overall score
01-Feb	0	19.1	0	0	0	0
02-Feb	0	19.3	0	0	1	1
03-Feb	0	20.7	0	1	0	1
04-Feb	0	20.5	0	0	0	0
05-Feb	0	20.1	0	0	0	0
06-Feb	0	20.4	0	0	0	0
07-Feb	0	19.6	0	0	0	0
10-Feb	0	21.2	0	0	0	0
11-Feb	0		0	0	0	0
12-Feb	0	21.8	0	0	0	0
13-Feb	0		0	0	0	0
14-Feb	0	22.4	0	0	0	0
17-Feb	0	21.4	0	0	0	0
19-Feb	0	21.9	0	0	0	0
21-Feb	0	20.8	0	0	0	0
23-Feb	0	21.6	0	0	0	0
24-Feb	0	19.7	0	0	2	2
25-Feb	0		0	0	2	2
26-Feb	0		0	0	2	2
27-Feb	0	20.6	0	0	0	0
28-Feb	0	20.2	0	0	0	0
02-Mar	0		0	0	0	0

04-Mar	0	22	0	0	0	0
05-Mar	0	21.3	0	0	0	0
09-Mar	0	22.8	0	0	0	0
12-Mar		22				
15-Mar	0	22.3	0	0	0	0
18-Mar	0	22.1	0	0	0	0
20-Mar	0	20.5	0	0	0	0
23-Mar	0	18.8	0	1	0	1
25-Mar	0	17.5	0	1	0	1
27-Mar	0	14.5	0	3	0	3

Individual Score sheet

Animal Identification Number: MOUSE 19

Researcher: Oliviero Gobbo/Luiza dos Santos   **Individual licence #:** AE1936/I104 and AE19136/I457

Procedure #: U-87 cell injection (31/01/2020) + Tumour resection (24/02/2020)

Drug: Temozolomide (TMZ) and Paclitaxel (PTX)   **Group #:** GlioGel

Dose#: 0.6 mg/kg free TMZ and 0.3 mg/kg PTX (loaded on MSN-PEG)

Starting date: 31/01/2020

Date	Body Condition Score (BCS)	Body weight (g)	Physical Appearance Temperature	Behaviour	Grimace scale score (total)	Overall score
01-Feb	0	18.9	0	0	0	0
02-Feb	0	19.9	0	0	0	0
03-Feb	0	20.6	0	0	0	0
04-Feb	0	19.5	0	0	0	0
05-Feb	0	19.8	1	0	0	1
06-Feb	0	19.9	0	0	0	0
07-Feb	0	20.8	0	0	0	0
10-Feb	0	20.6	0	0	0	0
11-Feb	0		0	0	0	0
12-Feb	0	21.2	0	0	0	0
13-Feb	0		0	0	0	0
14-Feb	0	22.3	0	0	0	0
17-Feb	0	22.1	0	0	0	0
19-Feb	0	21.8	0	0	0	0
21-Feb	0	21.9	0	0	0	0
24-Feb	0	21.5	0	0	0	0
25-Feb	0		0	0	2	2
26-Feb	0		0	0	2	2
27-Feb	0	21.7	0	0	1	1
28-Feb	0	21.5	0	0	1	1
02-Mar	0		0	0	0	0
04-Mar	0	21.7	0	0	0	0
05-Mar	0	20.4	0	0	0	0
09-Mar	0	21.1	0	0	0	0
12-Mar		21.7				
15-Mar	0	22.1	0	0	0	0

18-Mar	0	23.1	0	0	0	0
20-Mar	0	22.2	0	0	0	0
23-Mar	0	22.8	0	0	0	0
25-Mar	0	21.9	0	0	0	0
27-Mar	0	22.6	0	0	0	0
29-Mar	0	22.2	0	0	0	0

Individual Score sheet

Animal Identification Number: MOUSE 20

Researcher: Oliviero Gobbo/Luiza dos Santos   **Individual licence #:** AE1936/I104 and AE19136/I457

Procedure #: U-87 cell injection (31/01/2020) + Tumour resection (24/02/2020)

Drug: n/a   **Group #:** Gel only

Dose#: n/a

Starting date: 31/01/2020

Date	Body Condition Score (BCS)	Body weight (g)	Physical Appearance Temperature	Behaviour	Grimace scale score (total)	Overall score
01-Feb	0	19.6	0	0	1	1
02-Feb	0	19.4	0	0	1	1
03-Feb	0	20.1	0	0	1	1
04-Feb	0	19.6	0	0	1	1
05-Feb	0	19.8	0	0	1	1
06-Feb	0	20	0	0	0	0
07-Feb	0	19.8	0	0	0	0
10-Feb	0	20.1	0	0	0	0
11-Feb	0		0	0	0	0
12-Feb	0	20.4	0	0	0	0
13-Feb	0		0	0	0	0
14-Feb	0	21.3	0	0	0	0
17-Feb	0	21.3	0	0	0	0
19-Feb	0	20.8	0	0	0	0
21-Feb	0	21.6	0	0	0	0
24-Feb	0	22.4	0	0	0	0
25-Feb	0	20.5	0	0	2	2
26-Feb	0	21.6	0	0	1	1
27-Feb	0	22.5	0	0	1	1
28-Feb	0	21.5	0	0	0	0
02-Mar	0		0	0	0	0
04-Mar	0	22.8	0	0	0	0
05-Mar	0	22	0	0	0	0
09-Mar	0	23.2	0	0	0	0
12-Mar		22.8				
15-Mar	0	21.4	0	0	0	0

268

18-Mar	0	18.1	0	0	1	1
20-Mar	0	17.7	0	1	0	1
23-Mar	0	14.6	0	2	0	2

Grimace Scale Score Sheet for 3 days post-surgery:

0	facial action not present
1	facial action moderately present
2	facial action severe

Procedure: Tumour resection

Date of procedure: 23-24/02/2020

Day1 post-surgery

Facial Action	Mouse11	Mouse11	Mouse12	Mouse12	Mouse13	Mouse13
Orbital	0	0	0	0	0	0
Nose Bulge	0	0	0	0	0	0
Cheek	1	1	0	0	1	1
Ear position	1	1	1	1	1	1
Whisker	0	0	0	0	0	0
Total:	AM 2	PM 2	AM 1	PM 1	AM 2	PM 2

Day-2 post surgery

Facial Action	Mouse11	Mouse11	Mouse12	Mouse12	Mouse13	Mouse13
Orbital	0	0	0	0	0	0
Nose Bulge	0	0	0	0	0	0
Cheek	0	0	0	0	1	1
Ear position	1	1	1	1	1	1
Whisker	0	0	0	0	0	0
Total:	AM 1	PM 1	AM 1	PM 1	AM 2	PM 2

Day-3 post surgery

Facial Action	Mouse11	Mouse11	Mouse12	Mouse12	Mouse13	Mouse13
Orbital	0	0	0	0	0	0
Nose Bulge	0	0	0	0	0	0
Cheek	0	0	0	0	0	0
Ear position	1	1	0	0	0	0
Whisker	0	0	0	0	0	0
Total:	AM 1	PM 1	AM 0	PM 0	AM 0	PM 0

Grimace Scale Score Sheet for 3 days post-surgery:

0	facial action not present
1	facial action moderately present
2	facial action severe

Procedure: Tumour resection

Date of procedure: 23-24/02/2020

Day1 post-surgery

Facial Action	Mouse14	Mouse14	Mouse15	Mouse15	Mouse16	Mouse16
Orbital	0	0	1	0	0	0
Nose Bulge	0	0	0	0	0	0
Cheek	1	1	1	0	1	1
Ear position	1	1	1	1	1	1
Whisker	0	0	0	0	0	0
Total:	AM 2	PM 2	AM 3	PM 1	AM 2	PM 2

Day-2 post surgery

Facial Action	Mouse14	Mouse14	Mouse15	Mouse15	Mouse16	Mouse16
Orbital	0	0	0	0	0	0
Nose Bulge	0	0	0	0	0	0
Cheek	0	0	0	0	0	0
Ear position	1	1	1	1	1	1
Whisker	0	0	0	0	0	0
Total:	AM 1	PM 1	AM 1	PM 1	AM 1	PM 1

Day-3 post surgery

Facial Action	Mouse14	Mouse14	Mouse15	Mouse15	Mouse16	Mouse16
Orbital	0	0	0	0	0	0
Nose Bulge	0	0	0	0	0	0
Cheek	1	0	0	0	0	0
Ear position	1	0	0	0	0	0
Whisker	0	0	0	0	0	0
Total:	AM	PM 0	AM 0	PM 0	AM 0	PM 0

Grimace Scale Score Sheet for 3 days post-surgery:

0	facial action not present
1	facial action moderately present
2	facial action severe

Procedure: Tumour resection

Date of procedure: 23-24/02/2020

Day1 post-surgery

Facial Action	Mouse 17	Mouse 17	Mouse 18	Mouse 18	Mouse 19	Mouse 19	Mouse 20	Mouse 20
Orbital	0	0	0	0	0	0	0	0
Nose Bulge	0	0	0	0	0	0	0	0
Cheek	0	1	1	1	1	0	0	1
Ear	1	1	1	1	1	0	0	1
Whisker	0	0	0	0	0	0	0	0
Total:	AM 1	PM 2	AM 2	PM 2	AM 2	PM 0	AM 0	PM 2

Day-2 post surgery

Facial Action	Mouse 17	Mouse 17	Mouse 18	Mouse 18	Mouse 19	Mouse 19	Mouse 20	Mouse 20
Orbital	0	0	0	0	0	0	0	0
Nose Bulge	0	0	0	0	0	0	0	0
Cheek	1	0	1	1	1	0	0	0
Ear position	1	1	1	1	1	1	1	1
Whisker	0	0	0	0	0	0	0	0
Total:	AM 2	PM 1	AM 2	PM 2	AM 2	PM 1	AM 1	PM 1

Day-3 post surgery

Facial Action	Mouse 17	Mouse 17	Mouse 18	Mouse 18	Mouse 19	Mouse 19	Mouse 20	Mouse 20
Orbital	0	0	0	0	0	0	0	0
Nose Bulge	0	0	0	0	0	0	0	0
Cheek	0	0	1	0	0	0	0	0
Ear position	1	1	1	1	1	0	1	1
Whisker	0	0	0	0	0	0	0	0
Total:	AM 1	PM 1	AM 2	PM 1	AM 1	PM 0	AM 1	PM 1